
Electronic Thesis and Dissertation Repository

12-20-2013 12:00 AM


Under-Sampled Reconstruction Techniques for Accelerated Magnetic Resonance Imaging

Mohammad H. Kayvanrad
The University of Western Ontario

Supervisor
Terry Peters
The University of Western Ontario

Graduate Program in Biomedical Engineering
A thesis submitted in partial fulfillment of the requirements for the degree in Doctor of Philosophy
© Mohammad H. Kayvanrad 2013

Follow this and additional works at: <https://ir.lib.uwo.ca/etd>

 Part of the [Biomedical Commons](#), [Biomedical Engineering and Bioengineering Commons](#), and the [Medicine and Health Sciences Commons](#)

Recommended Citation

Kayvanrad, Mohammad H., "Under-Sampled Reconstruction Techniques for Accelerated Magnetic Resonance Imaging" (2013). *Electronic Thesis and Dissertation Repository*. 1880.
<https://ir.lib.uwo.ca/etd/1880>

This Dissertation/Thesis is brought to you for free and open access by Scholarship@Western. It has been accepted for inclusion in Electronic Thesis and Dissertation Repository by an authorized administrator of Scholarship@Western. For more information, please contact wlsadmin@uwo.ca.

UNDER-SAMPLED RECONSTRUCTION TECHNIQUES FOR ACCELERATED MAGNETIC RESONANCE IMAGING

(Thesis format: Integrated Article)

by

Mohammad Hosain Kayvanrad

Graduate Program in Biomedical engineering

A thesis submitted in partial fulfillment
of the requirements for the degree of
Doctor of philosophy

The School of Graduate and Postdoctoral Studies
The University of Western Ontario
London, Ontario, Canada

© Mohammad Kayvanrad, 2013

Abstract

Due to physical and biological constraints and requirements on the minimum resolution and signal-to-noise ratio (SNR), the acquisition time is relatively long in magnetic resonance imaging (MRI). Consequently, a limited number of pulse sequences can be run in a clinical MRI session because of constraints on the total acquisition time due to patient comfort and cost considerations. Therefore, it is strongly desired to reduce the acquisition time without compromising the reconstruction quality. This thesis concerns under-sampled reconstruction techniques for acceleration of MRI acquisitions, i.e., parallel imaging and compressed sensing.

While compressed sensing MRI reconstructions are commonly regularized by penalizing the decimated wavelet transform coefficients, it is shown in this thesis that the visual artifacts, associated with the lack of translation-invariance of the wavelet basis in the decimated form, can be avoided by penalizing the undecimated wavelet transform coefficients, i.e., the stationary wavelet transform (SWT). An iterative SWT thresholding algorithm for combined SWT-regularized compressed sensing and parallel imaging reconstruction is presented. Additionally, it is shown that in MRI applications involving multiple sequential acquisitions, e.g., quantitative T1/T2 mapping, the correlation between the successive acquisitions can be incorporated as an additional constraint for joint under-sampled reconstruction, resulting in improved reconstruction performance.

While quantitative measures of quality, e.g., reconstruction error with respect to the fully-sampled reference, are commonly used for performance evaluation and comparison of under-sampled reconstructions, this thesis shows that such quantitative measures do not necessarily correlate with the subjective quality of reconstruction as perceived by radiologists and other expert end users. Therefore, unless accompanied by subjective evaluations, quantitative quality measurements/comparisons will be of limited clinical impact. The results of experiments aimed at subjective evaluation/comparison of different

under-sampled reconstructions for specific clinical neuroimaging MRI applications are presented in this thesis.

One motivation behind the current work was to reduce the acquisition time for relaxation mapping techniques DESPOT1 and DESPOT2. This work also includes a modification to the Driven Equilibrium Single Pulse Observation of T1 with high-speed incorporation of RF field inhomogeneities (DESPOT1-HIFI), resulting in more accurate estimation of T1 values at high strength (3T and higher) magnetic fields.

Keywords- Magnetic resonance imaging, Sparse recovery, Compressed sensing, Parallel imaging, Quantitative MRI, Driven equilibrium single pulse observation of T1/T2 (DESPOT1/DESPOT2), Clinical MRI quality assessment

Co-Authorship

Chapters 2 and 3 are based on extensions and modifications of the following publications:

M. H. Kayvanrad, C. A. McKenzie, T. M. Peters, “MRI reconstruction from partial k-space data by iterative stationary wavelet transform thresholding,” 2012 Sparsity Techniques in Image Processing (STMI), 2012, Nice, France.

M. H. Kayvanrad, C. A. McKenzie, and T. M. Peters, “Iterative wavelet thresholding for rapid MRI reconstruction,” Proceedings of Medical Imaging 2011: Image Processing, Lake Buena Vista, Florida, USA, 2011, p. 79624S–79624S–10.

M. H. Kayvanrad, A. J. McLeod, J. S. H. Baxter, C. A. McKenzie, and T. M. Peters, “Stationary wavelet transform for under-sampled MRI reconstruction,” In submission.

The idea of stationary wavelet transform (SWT) penalized reconstruction, and the multiple-coil iterative SWT thresholding reconstruction algorithm belongs to M. H. Kayvanrad. All the coding, data acquisition, and write-up was done by M. H. Kayvanrad. A. J. McLeod, and J. S. H. Baxter helped with debugging and revisions. The manuscripts were edited and revised by T. Peters. All the work was done under the supervision of T. Peters.

Chapter 4 is based on extensions and modifications of the following publication:

M. H. Kayvanrad, A. J. McLeod, J. S. H. Baxter, C. A. McKenzie, and T. M. Peters, “T1 Map Reconstruction from Under-sampled KSpace Data using a Similarity Constraint,” in *International Society of Magnetic Resonance in Medicine*, 2012 (20), p. 15.

The idea of joint reconstruction was developed in discussions between M. H. Kayvanrad, A. J. McLeod, and J. S. H. Baxter. Coding was done by M. H. Kayvanrad and A. J.

McLeod. Data acquisition was done by M. H. Kayvanrad. Write-up was mainly done by M. H. Kayvanrad. The manuscripts were edited and revised by T. Peters. All the work was done under the supervision of T. Peters.

Chapter 5 is based on extensions and modifications of the following publication:

M. H. Kayvanrad, T. Peters, “Modification to Driven equilibrium single pulse observation of T1 with high-speed incorporation of RF field inhomogeneities (DESPOT1-HIFI),” In submission, *Magnetic resonance in medicine*.

The idea of the proposed modification belongs to M. H. Kayvanrad. All the data acquisition, coding, and write-up were done by M. H. Kayvanrad. The manuscripts were edited and revised by T. Peters. All the work was done under the supervision of T. Peters.

Chapter 5 is based on extensions and modifications of the following publication:

M. H. Kayvanrad, A. Lin, R. Joshi, J. Chiu, T. M. Peters, “Subjective quality assessment of under-sampled compressed sensing and parallel imaging MRI reconstructions,” Submitted to *International Society of Magnetic Resonance in Medicine*, 2014 (ISMRM 4765).

The idea of perceptual quality measurement of under-sampled reconstructions was developed by M. H. Kayvanrad. Data acquisition, experimental design and coding, and write-up was done by M. H. Kayvanrad. A. A. Lin was actively involved in the experimental design and provided valuable feedback in the write-up. The manuscripts were edited and revised by T. Peters. All the work was done under the supervision of T. Peters.

Dedication

Mom and Dad

Acknowledgments

I would like to start by quoting my supervisor, Terry Peters, that a PhD is not solely centred around solving a research problem, but it is also a path for skills and personal development. During the course of my PhD, I could not have asked for, or thought of, a better supervision model that would let me follow my interests and develop a broad range of skills. To Terry Peters: thank you for providing me with this great opportunity. Also, thank you for your patience, understanding, and encouragement, when I followed unreasonable paths, or faced roadblocks.

I would also like to acknowledge my advisory committee members, Charlie McKenzie, Rob Bartha, and Sandrine de Ribaupierre.

Jonathan McLeod is a great friend, who was always available for exchange of ideas, but also for a game of tennis in a summer afternoon, or camping in a snowy winter. Several sections of this thesis have been done with his help.

Amy Lin spent a great amount of her precious time during her residency to develop several experiments reported in this thesis, most of which wouldn't have been possible without her insight and assistance.

Last but not definitely least, I would like to thank J. Baxter, John Moore, Elvis Chen, David Tessier, and all the lab members that made this experience a memorable one for me.

Table of Contents

Abstract.....	ii
Co-Authorship.....	iv
Acknowledgments.....	vii
Table of Contents.....	viii
List of symbols.....	xiii
List of acronyms.....	xv
List of figures.....	xviii
List of tables.....	xxv
1 Introduction.....	1
1.1 Thesis objectives.....	4
1.2 Introduction to magnetic resonance imaging (MRI).....	5
1.2.1 Basic nuclear magnetic resonance (NMR) physics.....	5
1.2.2 Spatial encoding.....	7
1.2.3 K-space.....	9
1.2.4 $T1/T2$ contrast.....	10
1.2.5 Magnetic resonance imaging.....	12
1.3 Quantitative MRI: $T1/T2$ mapping.....	14

1.3.1	DESPOT1/DESPOT2 T1 and T2 mapping	15
1.4	Parallel imaging.....	16
1.4.1	SENSE	16
1.4.2	GRAPPA.....	18
1.5	Compressed sensing.....	20
1.6	Thesis outline	21
1.6.1	Chapter 2- Iterative stationary wavelet transform thresholding reconstruction.....	21
1.6.2	Chapter 3- Stationary wavelet transform for under-sampled MRI reconstruction.....	22
1.6.3	Chapter 4- Similarity-based joint reconstruction in multiple acquisition problems with application to DESPOT1 T1 mapping	22
1.6.4	Chapter 5- Driven equilibrium single pulse observation of T1 with high-speed incorporation of RF field inhomogeneities (DESPOT1-HIFI).....	23
1.6.5	Chapter 6- Subjective reconstruction quality assessment. Error! Bookmark not defined.	
1.7	References	24
2	Iterative stationary wavelet transform thresholding reconstruction.....	28
2.1	Introduction	28
2.1.1	Papoulis-Gerchberg reconstruction.....	28
2.1.2	Under-sampled MRI reconstruction	29

2.2	Iterative stationary wavelet transform thresholding.....	30
2.2.1	Multiple coil data and combination with parallel imaging.....	32
2.3	Methods.....	33
2.4	Results.....	36
2.5	Discussion.....	41
2.6	Conclusion.....	43
2.7	References.....	43
3	Stationary wavelet transform for under-sampled MRI reconstruction.....	45
3.1	Introduction.....	45
3.2	Stationary wavelet transform sparse recovery.....	51
3.3	Methods.....	55
3.4	Results.....	60
3.5	Discussion and conclusion.....	70
3.6	References.....	72
4	Similarity-based joint reconstruction in multiple acquisition problems with application to DESPOT1 T1 mapping.....	74
4.1	Introduction.....	75
4.2	Theory.....	76
4.2.1	Similarity-promoting operation.....	79
4.2.2	Iterative reconstruction.....	80

4.3	Methods.....	82
4.4	Results.....	84
4.5	Discussion.....	92
4.6	Conclusion.....	93
4.7	References.....	94
5	Driven equilibrium single pulse observation of T1 with high-speed incorporation of RF field inhomogeneities (DESPOT1-HIFI).....	96
5.1	Introduction.....	96
5.2	Theory.....	98
5.3	Materials and Methods.....	100
5.4	Results.....	101
5.5	Discussion and conclusion.....	102
5.6	References.....	106
6	Subjective reconstruction quality assessment.....	108
6.1	Introduction.....	108
6.2	Methods.....	109
6.2.1	Study design.....	109
6.3	Results.....	114
6.3.1	Detection of white matter lesions.....	114
6.3.2	Cranial nerve imaging.....	117

6.3.3	Magnetic resonance angiography (MRA).....	118
6.4	Discussion and conclusion	122
6.5	Reference.....	124
7	Summary and future directions.....	126
7.1	Thesis summary.....	126
7.1.1	Stationary wavelet transform penalization.....	128
7.1.2	Joint under-sampled reconstruction of multiple-acquisition datasets.....	129
7.1.3	Driven equilibrium single pulse observation of T1 with high-speed incorporation of RF field inhomogeneities (DESPOT1-HIFI).....	131
7.1.4	Subjective quality assessment of under-sampled reconstructions	131
7.2	Future work	133
7.2.1	Computation time.....	133
7.2.2	Other clinical applications	134
7.2.3	Cardiac Cine MRI.....	134
7.3	Reference.....	135
	Appendix A: Erroneous DESPOT-HIFI equation	138
	Reference	139
	Appendix B: Human ethics approval.....	140
	Curriculum Vitae	172

List of symbols

T_1	Spin-lattice relaxation time
T_2	Spin-spin relaxation time
ω_0	Larmor frequency
γ	Gyro-magnetic ratio
B_0	Static magnetic field
M_0	Equilibrium magnetization
B_1	RF magnetic field
G_x	Magnetic gradient in the x direction
G_y	Magnetic gradient in the y direction
$\Delta\phi$	Phase difference
$\Delta\omega$	Frequency difference
M_z	Longitudinal magnetization component
M_{xy}	Transverse magnetization component
k_x	Readout direction
k_y	Phase-encode direction
T_2^*	Apparent T_2

α	Flip angle
N_c	Number of coils
\mathcal{F}	Fourier transform
B_1	Radio frequency field

List of acronyms

2D	2 dimensional
3D	3 dimensional
BW	Bandwidth
CNR	Contrast-to-noise ratio
CS	Compressed sensing
CSF	Cerebrospinal fluid
CT	Computed tomography
DESPOT1	Driven equilibrium single pulse observation of T1
DESPOT1-HIFI	Driven equilibrium single pulse observation of T1 with high-speed incorporation of RF field inhomogeneities
DESPOT2	Driven equilibrium single pulse observation of T2
DTI	Diffusion tensor imaging
DWT	Decimated wavelet transform
DWTRS	Decimated wavelet transform with random shifts
EPI	Echo planar imaging
ETL	Echo train length
FIESTA	Fast imaging employing steady state acquisition

FLAIR	Fluid attenuated inversion recovery
fMRI	Functional magnetic resonance imaging
FSE	Fast spin echo
GM	Grey matter
GPU	Graphical processing unit
GRAPPA	Generalized auto calibrating partially parallel acquisition
GRE	Gradient recalled echo
IR-FSE	Inversion recovery fast spin echo
IR-SPGR	Inversion recovery spoiled gradient recalled
MRI	Magnetic Resonance Imaging
NEX	Number of excitations
NMR	Nuclear magnetic resonance
NRMSE	Normalized root mean square error
P-G	Papoulis-Gerchberg
PI	Parallel imaging
POCS	Projections onto convex sets
PSF	Point spread function
RF	Radio frequency
ROI	Region of interest

SENSE	Sensitivity encoding
SMASH	Simultaneous acquisition of spatial harmonics
SNR	Signal-to-noise ratio
SOS	Sum of squares
SPGR	Spoiled gradient echo
SPIRiT	Iterative self-consistent parallel imaging reconstruction
SSFP	Steady-state free precession
SWT	Stationary wavelet transform
TE	Echo time
TI	Inversion time
TLE	Temporal lobe epilepsy
TOF	Time of flight
TR	Repetition time
TV	Total variation
WM	White matter

List of figures

Figure 1.1- A typical Gradient Recalled Echo (GRE) brain image and its echo train version known as Echo Planar Imaging (EPI). The entire EPI image is acquired with a single echo train. The images illustrate quality losses due to echo train imaging. (Figure from [7] with permission from the publisher [doi:10.1088/0031-9155/52/7/R01](https://doi.org/10.1088/0031-9155/52/7/R01))..... 2

Figure 1.2- Pictorial illustration of under-sampled k-space reconstruction. Reconstruction by simple zero-padding in k-space results in aliasing artifacts in the spatial domain image. Nevertheless, the missing k-space data can be interpolated based on *a priori* constraints in order to obtain reasonable reconstructions. 3

Figure 1.3- The magnetization vector is tilted away from the longitudinal equilibrium in the B_0 direction towards the transverse plane by the application of an RF pulse, B_1 , at the Larmor (resonance) frequency. 7

Figure 1.4- Frequency/phase encoding of the image position by the application of a linear gradient magnetic field. Left: B_0 only- all nuclei precess at the same frequency. Right: $B_0 + xG_x$ - the precession frequency is linearly dependent on the position. 8

Figure 1.5- The RF signal is usually sampled while the G_x gradient is on, therefore filling in k-space point along the readout (k_x) direction..... 11

Figure 1.6- With the duration of the gradient pulse held constant, the phase-encode position is controlled by varying the strength of the gradient. 13

Figure 1.7- Schematic diagram of the RF spin echo pulse sequence..... 13

Figure 1.8- Schematic illustration of the formation of a gradient echo. 14

Figure 1.9- Pictorial illustration of equation (1.16) for two coils and $R = 2$. Each point on the aliased image for each coil (left column) is the superposition of the corresponding

point on the original image modulated by the coil sensitivity (middle column) and a point at half of field of view, $L2$, shift (right column). 18

Figure 1.10- Pictorial illustration of GRAPPA reconstruction with two coils and $R = 2$. Auto-calibration data are shown in red. Blue represents sampled k-space data points and unsampled points are shown in grey. Once the kernel weights are found based on the auto-calibration data (red arrows), they can be used to fill in the missing data based on the neighboring sampled points (black arrows). In this example a 3×2 kernel is used (red box). 19

Figure 2.1- Mean NRMSE values with the corresponding error bars of one standard deviation for the reconstruction of 15 different SPGR images from under-sampled k-space data with the same under-sampling pattern. For clarity, the error bars are shown at increments of 0.5. However, the growth in the error bars follows a consistent trend. 36

Figure 2.2- Mean NRMSE values with the corresponding error bars of one standard deviation for the reconstruction of a SPGR image from 15 sets of independently under-sampled k-space data. For clarity, the error bars are shown at increments of 0.5. However, the growth in the error bars follows a consistent trend. 38

Figure 2.3- Visual comparison of different reconstructions of an under-sampled SPGR dataset. K-space data are randomly under-sampled in the two phase-encode directions by a factor of 4. The reconstructed images and the corresponding difference images with respect to the fully-sampled image are shown. 40

Figure 2.4- Sum of squares (SOS) of the reconstructed multiple coil data. The normalized root mean square errors (NRMSE) are computed with respect to the fully-sampled SOS after 40 iterations. 41

Figure 2.5- Normalized RMSE vs. iteration number for the reconstruction of the under-sampled 32-channel brain data. The proposed iterative SWT thresholding reconstruction is compared with l1SPIRiT at under-sampling factor of 6. 42

Figure 3.1-Illustration of the lack of translation invariance of DWT and the resulting thresholding artifacts: A simple test image- an 8x8 square in the middle of a 16x16 black background (a) and a shifted version of it (b) are decomposed with the Haar wavelet to 1 level. The original image is deliberately chosen to align with the wavelet basis, resulting in a very sparse decomposition. The shift, however, results in a misalignment between the image features and those of the wavelet basis functions, which, consequently, results in noticeable loss of the sparsity of the decomposition. In each case, the decomposition coefficients are hard thresholded and a wavelet reconstruction (IDWT) is performed on the thresholded coefficients. Dashed circles highlight the reconstruction artifacts. 46

Figure 3.2- Shift-localization tree for a three level stationary wavelet transform (SWT) decomposition. Each node is indexed by parameters (j, p) , where j is the decomposition level and p is the shift. For clarity, the binary representation of p is shown in brackets. 50

Figure 3.3- Point spread functions (PSF) resulting from k-space under-sampling followed by the application of DWT and SWT soft thresholding. An example of the reduction of the artifacts by SWT thresholding compared to DWT thresholding is highlighted. 52

Figure 3.4- Reconstruction of the Shepp-Logan phantom from Cartesian under-sampled frequency data by DWT/SWT- l_1 (+TV) penalized optimization. 54

Figure 3.5- Flowchart of the multiple-coil iterative thresholding reconstruction algorithm 57

Figure 3.6- Reconstruction of under-sampled SGPR data (under-sampling factor 3) by l_1 + TV penalized optimization. The arrows point examples of the artifacts present in the DWT reconstruction that are absent in the corresponding SWT reconstruction. 60

Figure 3.7- Mean NRMSE and the corresponding error bars of one standard deviation for the reconstruction of the under-sampled 32-channel FSE data by the multiple-coil iterative thresholding algorithm. 61

Figure 3.8- Reconstruction of under-sampled 32-channel FSE data (under-sampling factor 5) by the multiple-coil iterative thresholding algorithm. Arrows point to examples of DWT reconstruction artifacts that are absent or greatly reduced in the corresponding SWT reconstruction. 63

Figure 3.9- Convergence plot of the multiple-coil iterative thresholding reconstruction algorithm, in terms of NRMSE vs. iteration number, corresponding to the reconstructions of Figure 3.8. 64

Figure 3.10- Effect of the choice of the threshold on the convergence of the multiple-coil iterative SWT/DWT soft thresholding algorithm for the reconstruction of under-sampled data (under-sampling factor 5) with SWT (a) and DWT (b, c). The convergence of the algorithms, in terms of the reconstruction NRMSE vs. iteration number, is shown for several variations of a base threshold, T , by multiplicative factors. Since the DWT reconstruction requires far more iterations to converge than the SWT reconstruction, an extended plot over 10000 iterations is shown in (c) for the DWT reconstruction. 66

Figure 3.11- Mean NRMSE and the error bars of one standard deviation for the reconstruction of the under-sampled 32-channel FSE data by DWT/DWTRS/SWT SPIRiT. 67

Figure 3.12- Reconstruction of the under-sampled 32-channel FSE data (under-sampling factor 5) by SWT/DWTRS/DWT SPIRiT. The arrows point to examples of DWT/DWTRS reconstruction artifacts that are absent in the corresponding SWT reconstruction. 69

Figure 3.13- Effect of the choice of the regularization parameter on the convergence of the SPIRiT reconstruction algorithm for the reconstruction of under-sampled data (under-sampling factor 5) with several variations of the discrete wavelet transform, i.e., SWT, DWTRS, and DWT. The convergence of the algorithm, in terms of the reconstruction NRMSE vs. iteration number, is shown for several variations of a base threshold, T , by multiplicative factors. 71

Figure 4.1- Effect of random and independent k-space under-sampling in terms of point spread functions (PSF) and joint intensity distributions. 78

Figure 4.2- Mean NRMSE values and corresponding error bars of one standard deviation for the reconstruction of 15 SPGR pairs from under-sampled k-space data and derived T1 map. For clarity, the error bars are shown at increments of 0.5. However, the growth in the error bars follows a consistent trend. 86

Figure 4.3- Mean NRMSE values and corresponding error bars of one standard deviation for the reconstruction of SPGR images and derived T1 maps of one healthy volunteer from 15 independently under-sampled datasets. For clarity, the error bars are shown at increments of 0.5. However, the growth in the error bars follows a consistent trend. 88

Figure 4.4- The DESPOT1 T1 error is shown as a function of the error in the intensity images in (a) and the distribution of errors in the intensity images is shown for individual reconstruction (b), joint reconstruction (c) and low resolution image (d) acquired with an under-sampling ratio of 4. 89

Figure 4.5- Reconstruction of SPGR images at flip angles 4° and 18° with an under-sampling factor of 4, and T1 map computed using DESPOT1. The zooming area is shown by the white box. The arrowhead points to an example of aliasing artifacts present in individual reconstruction that are removed by the joint reconstruction. 90

Figure 4.6- Box plots of T1 values over three local ROIs (shown in Figure 4.7) on the WM, GM, and CSF, at an under-sampling factor of 4. The central mark in each box is the median and the edges of the box are the 25th and 75th percentiles. 91

Figure 4.7- Three ROIs representative of white matter (green), gray matter (blue), and cerebrospinal fluid (red), over which the distribution of the T1 values are computed. 92

Figure 5.1- Comparison of the original and the modified IR-SPGR equations for three T1 values representative of the white matter (T1=900ms), grey matter (T1=1500ms), and the

cerebrospinal fluid ($T_1=3000\text{ms}$) at 3T. The longitudinal magnetization normalized by M_0 is plotted for different values of TI for each case..... 99

Figure 5.2- Mean T1 values for each tube in the agarose phantom, computed by conventional DESPOT1 and by the original and modified DESPOT1-HIFI versus reference values determined by IR-FSE. The errorbars denote one standard deviation. Linear regressions and the line of unity with the reference T1 values are also shown... 102

Figure 5.3- Mean T1 values, computed by the conventional DESPOT1, the original and modified DESPOT1-HIFI, and the IR-FSE reference, for each tube in the agarose phantom, versus nickel chloride concentration of the tube..... 103

Figure 5.4- Mean T1 values computed by the conventional DESPOT and by the original and modified DESPOT-HIFI versus reference values computed based on IR-FSE acquisitions over three regions of interests (ROI) on white matter (WM), grey matter (GM) and cerebrospinal fluid (CSF). WM ROI includes areas on the frontal lobe, parietal lobe, and corpus callosum, GM ROI includes areas on the cerebral cortex and the caudate nucleus, and CSF ROI includes areas on the lateral ventricle. The errorbars denote one standard deviation. Linear regressions and the line of unity with the reference T1 values are also shown..... 104

Figure 5.5- Mean T1 values with the errorbars of one standard deviation computed by the conventional DESPOT1, the original and modified DESPOT1-HIFI, and the IR-FSE reference over some anatomies of interest..... 105

Figure 6.1- Sample white matter lesion artificially incorporated in a FLAIR image. 110

Figure 6.2- Sample multiacquisition SSFP image (fully-sampled reconstruction). 112

Figure 6.3- Lesion detection performance (pooled) for the compressed sensing (CS) and low-resolution (lowres) reconstructions. 114

Figure 6.4- ROC curves corresponding to the lesion detection task (pooled results)..... 116

Figure 6.5- Area under ROC curves (AUC) versus average normalized root mean square error for each under-sampling factor for the lesion detection task with compressed sensing (CS) and low-resolution (lowres) reconstructions. 117

Figure 6.6- Average score (given by three participants) versus the normalized root mean square error (NRMSE) for the cranial nerve imaging scoring task. The error bars show one standard deviation, if non-zero. 119

Figure 6.7- Maximum intensity projection- Axial view: (a) fully-sampled (b,c,d) 5x under-sampled. 121

Figure 6.8- Average score (given by three participants) versus the normalized root mean square error (NRMSE) for the MRA scoring task. The error bars show one standard deviation, if non-zero. 122

Figure 6.9- Compressed sensing (a) and low-resolution (b) reconstruction of a simple test image by under-sampling in the frequency domain (under-sampling factor 5). While compressed sensing results in higher resolution (finer lines are resolved in the left image) it also results in some aliasing visual artifacts. The arrows point to examples of aliasing artifacts on the compressed sensing reconstruction and loss of resolution in the lowres reconstruction. 123

Figure 7.1- Reconstruction of 8-channel spoiled gradient recalled foot images at x3 under-sampling. 134

List of tables

Table 2.1- Iterative SWT thresholding reconstruction algorithm.....	31
Table 2.2- Multiple-coil iterative thresholding reconstruction algorithm.	33
Table 2.3- Mean and the 95% confidence interval of the paired NRMSE differences (i.e., the NRMSE of the second reconstruction in each pair subtracted from that of the first) for the reconstruction of 15 different SPGR images. All the findings in this table are statistically significant under the Bonferroni correction, except those denoted by an asterisk (*).....	37
Table 2.4- Mean and the 95% confidence interval of the paired NRMSE differences (i.e., the NRMSE of the second reconstruction in each pair subtracted from that of the first) for the reconstruction of a SPGR image from 15 sets of independently under-sampled k-space data. All findings in this table are statistically significant after the Bonferroni correction.	39
Table 3.1- Signal-to-alias ratios corresponding to the point spread functions (PSF) in Figure 3.3.	53
Table 3.2- Multiple-coil iterative thresholding reconstruction algorithm. \mathcal{F} and Γ denote the Fourier transform and wavelet thresholding operations, respectively.	56
Table 3.3- Mean and its 95% confidence interval of the paired NRMSE differences (i.e., NRMSE of the DWT reconstruction subtracted from that of the corresponding SWT reconstruction) for the reconstructions by the multiple-coil iterative thresholding algorithm with soft and hard thresholding for different under-sampling factors (U.F.). The numbers in brackets show the percentage of mean improvement with SWT over DWT. All findings in this table are statistically significant after the Bonferroni correction.....	62

Table 3.4- Mean and its 95% confidence interval of the paired NRMSE differences (i.e., NRMSE of the DWT/DWTRS reconstruction subtracted from that of the corresponding SWT reconstruction) for the reconstruction of the 32-channel FSE data by SWT/DWTRS/DWT SPIRiT for different under-sampling factors (U.F.). The numbers in brackets show the percentage of mean improvement with SWT over the corresponding DWT reconstruction. All findings are significant after the Bonferroni correction.....	68
Table 4.1- Joint reconstruction algorithm.....	81
Table 4.2- Statistical significance of NRMSE comparisons for the reconstruction of 15 different datasets. The results of paired t-tests for image 1, image 2, and the T1 map are shown.	85
Table 4.3- Statistical significance of NRMSE comparisons for the reconstructions with 15 different sets of under-sampling patterns. The results of paired t-tests for image 1, image 2, and the T1 map are shown.	87
Table 5.1- Sample T1 maps computed by the original and modified DESPOT-HIFI and by the conventional DESPOT1 for a healthy volunteer.....	106
Table 6.1- Multiple-coil iterative thresholding reconstruction algorithm. \mathcal{F} and Γ denote the Fourier transform and wavelet thresholding operations, respectively.	113
Table 6.2- Area under ROC curves (AUC) and the average normalized mean square error (NRMSE) for different under-sampling factors (UF) in the lesion detection task (pooled results). Corresponding ROC curves are shown in Figure 6.4.	115
Table 6.3- Statistical comparison of the low-resolution (lowres) and compressed sensing (CS) reconstruction errors (NRMSE) in terms of the confidence intervals and the p-values corresponding to a two-sample t test, for different under-sampling factors.	116
Table 6.4- Results of the cranial nerve imaging ranking task for three participants.	118

Table 6.5- Average scores given by three participants for the cranial nerve imaging scoring task and the normalized root mean square error (NRMSE) of the corresponding reconstructions.	119
Table 6.6- Results of the MRA ranking task for three participants.	120
Table 6.7- Average scores given by three participants for the MRA scoring task and the normalized root mean square error (NRMSE) of the corresponding reconstructions.	120

1 Introduction

Patient comfort and cost considerations limit the total acceptable acquisition time in magnetic resonance imaging (MRI). On the other hand, it is often desired to have high-resolution images with high signal-to-noise ratio (SNR). However, the SNR in MRI is proportional to the voxel volume and the square root of the acquisition time [1].

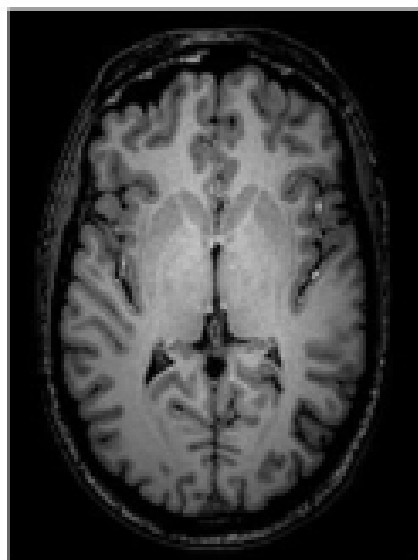
Consequently, this requirement limits the number of pulse sequences that can be run on a patient in a clinical examination without the scan time becoming excessive. Therefore, it is strongly desired to reduce the acquisition time without compromising the resolution and the SNR.

Furthermore, rapid acquisitions are often desirable to reduce motion artifacts, particularly in applications such as pediatric imaging or cardiac MRI.

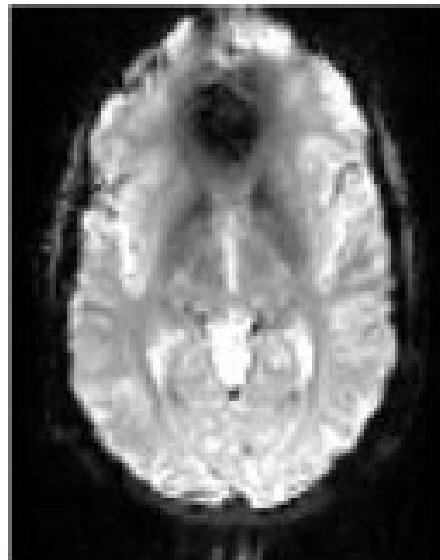
There exist several MRI applications that require multiple acquisitions of an object, e.g., T1/T2 mapping [2]–[5], in which maintaining an acceptable acquisition time, while also maintaining an acceptable resolution and SNR, may become of particular concern. For example, a typical study for surgical treatment of epilepsy with image guidance may consist of several acquisitions for T1 and T2 mapping, diffusion tensor imaging (DTI), and fMRI, in addition to regular clinical acquisitions. While each of these datasets can be acquired in about 10 minutes, which is acceptable for an MRI scan if it was the only pulse sequence to be run, once other acquisitions are added the total time may become excessive. Indeed, this work was partly motivated by the excessive pre-operative image acquisition time for the surgical treatment planning of epilepsy.

Accelerating MR acquisitions has been a primary goal of research since the introduction of this modality. Pulse sequences have been modified ever since in an effort to shorten the acquisition time. The simplest modification is to shorten the repetition time, TR, by using stronger gradients (and small flip angles) [6]. However, not only is the gradient strength limited by engineering limitations but also there are physiological considerations

associated with the rate of switching of the gradients due to the possibility of peripheral nerve stimulation [7].



(a) Gradient recalled echo (GRE)



(b) Echo planar imaging (EPI)

Figure 1.1- A typical Gradient Recalled Echo (GRE) brain image and its echo train version known as Echo Planar Imaging (EPI). The entire EPI image is acquired with a single echo train. The images illustrate quality losses due to echo train imaging. (Figure from [7] with permission from the publisher [doi:10.1088/0031-9155/52/7/R01](https://doi.org/10.1088/0031-9155/52/7/R01))

Another complementary approach is the acquisition of more than one phase-encode line after each excitation during each repetition time. Such pulse sequences are commonly known as echo train sequences [8]–[14]. While echo train imaging results in impressive reductions in the acquisition time, these reductions are often achieved at the expense of compromising the contrast and in some cases introducing image distortions. For example, [Figure 1.1](#) shows a brain image acquired using a Gradient Recalled Echo (GRE) pulse sequence and an echo train version of this pulse sequence, known as Echo Planar Imaging (EPI). The images illustrate the loss of quality with echo train imaging.

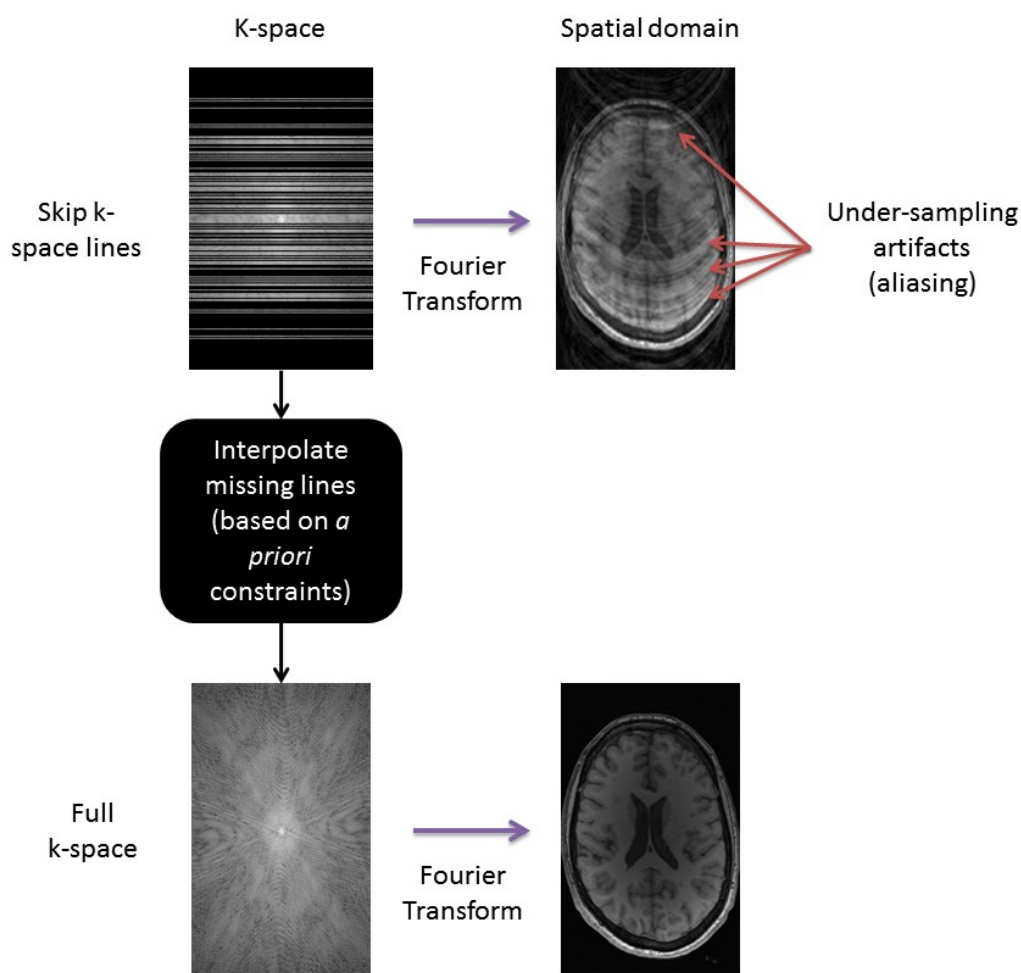


Figure 1.2- Pictorial illustration of under-sampled k-space reconstruction. Reconstruction by simple zero-padding in k-space results in aliasing artifacts in the spatial domain image. Nevertheless, the missing k-space data can be interpolated based on *a priori* constraints in order to obtain reasonable reconstructions.

Another class of accelerating approaches reduces the acquisition time by acquiring under-sampled data and reconstructing the missing data based on *a priori* knowledge or constraints on the data. The procedure is pictorially illustrated in [Figure 1.2](#). [Parallel imaging](#) [7] and [Compressed sensing](#) [15], [16] are two major categories of such

approaches, where the former is based on the knowledge of the coil sensitivity profiles and the latter is based on the sparsity of the image in a transform domain. In this thesis both approaches are considered, individually and in combination.

The aforementioned concepts of compressed sensing and parallel imaging are briefly introduced in sections 1.4 and 1.5, respectively. Before that, however, due to the importance of a general knowledge of the physics of MRI for following the rest of this thesis, a brief introduction to MRI physics is provided in sections 1.2 and 1.3.

1.1 Thesis objectives

One of the main objectives of this work is to introduce under-sampled MRI reconstruction techniques for accelerating MRI acquisitions. To this end, various reconstruction constraints are employed, depending on the application, to regularize the inverse problem. The following constraints are particularly considered:

1. **Sparsity in a transform domain:** Sparse representations of MR images can be obtained in appropriate transform domains. A reconstruction can therefore be obtained by regularizing the inverse problem by penalizing the sparsity in the sparse transform domain ([Compressed sensing](#)).
2. **Coil sensitivity profiles:** If data are acquired with multiple receive coils, the sensitivity profiles can be used for under-sampled reconstruction with [Parallel imaging](#). In multiple-coil acquisitions the best reconstruction performance is achieved by simultaneously incorporating coil sensitivities and sparsity constraints.
3. **Structural similarity between multiple sequential acquisitions:** In applications involving multiple sequential acquisitions, e.g., [Quantitative MRI: T1/T2 mapping](#), the structural similarity between sequential acquisitions can be incorporated as an additional reconstruction constraint to achieve improved reconstruction performance.

Furthermore, an important aspect of under-sampled reconstructions is the assessment of the reconstruction quality. While quantitative quality measures such as the reconstruction error with respect to the fully-sampled reference or the signal-to-noise ratio (SNR) are commonly used, these measures do not always correlate with the perceptual quality judgment of radiologists and other end users with respect to employing the images for diagnostic purposes (see chapter 5). Therefore, unless accompanied by subjective measurements, such quantitative measures are of limited clinical impact. Subjective quality assessment of under-sampled reconstructions is another major objective of this thesis.

1.2 Introduction to magnetic resonance imaging (MRI)

1.2.1 Basic nuclear magnetic resonance (NMR) physics

Magnetic resonance imaging is based on the interaction of a nuclear spin with external magnetic fields. All atomic nuclei consist of nucleons (protons and neutrons) that possess a quantum mechanical property called *spin*. If the nucleus consists of an odd number of nucleons, the nuclear spin is greater than zero, the nucleus is NMR-active, and a *magnetic dipole moment*, or simply a magnetic moment, can be associated with the nucleus. The dominant nucleus in biological tissues is the proton in hydrogen. The interaction of the NMR-active nuclei, e.g., the proton, with the external magnetic field results in the precession¹ of the spin about the external field direction, which is called the *Larmor precession*.

The Larmor precession occurs at a specific frequency, called the *Larmor frequency*, which depends on the strength of the external magnetic field and the characteristics of the nucleus:

$$\omega_0 = \gamma B_0 \quad (1.1)$$

¹ By definition, precession is the circular motion of the axis of rotation of a spinning body around another fixed axis caused by the application of a torque in the direction of precession [17].

where ω_0 is the Larmor frequency, B_0 is the external magnetic field, and γ is a constant called the *gyro-magnetic ratio*, which depends on the nucleus involved. $\gamma = 2.68 \times 10^8 \text{ rad/s/Tesla}$ for hydrogen [17].

In a classical picture, the precession of the spins around the magnetic field occurs out of phase with each other in the presence of a static external magnetic field, B_0 . This out-of-phase precession results in a net macroscopic magnetization in the direction of the external magnetic field, i.e., the longitudinal direction, since the transverse magnetization components cancel out due to the out-of-phase precession². This is usually referred to as the *equilibrium magnetization*, denoted by M_0 . Note that, by definition, magnetization is a vector field equal to the volume density of permanent or induced magnetic dipole moments in a magnetic material.

To detect this magnetization, it can be rotated away from its alignment along the B_0 axis by applying a radio frequency (RF) magnetic field for a short time, i.e., an RF pulse, with its frequency tuned to the Larmor frequency, i.e., the resonance frequency (Figure 1.3). The RF pulse is produced by an RF transmit coil, which is often used as the receive coil as well. The RF magnetic field is also referred to as the B_1 field. The duration and power of the RF pulse determines the *flip angle* by which the magnetization is rotated.

The application of the RF pulse tilts the net macroscopic magnetization away from the B_0 direction, resulting in a net (macroscopic) transverse magnetization component precessing at the Larmor frequency. The produced magnetic field precesses along with the magnetization, yielding a changing flux in the receive coil and therefore a current based on the Faraday's law.

² The B_0 direction is referred to as the longitudinal direction and is often assumed to be in the direction of the z-axis. Perpendicular to the B_0 direction is the transverse plane, i.e., the xy-plane.

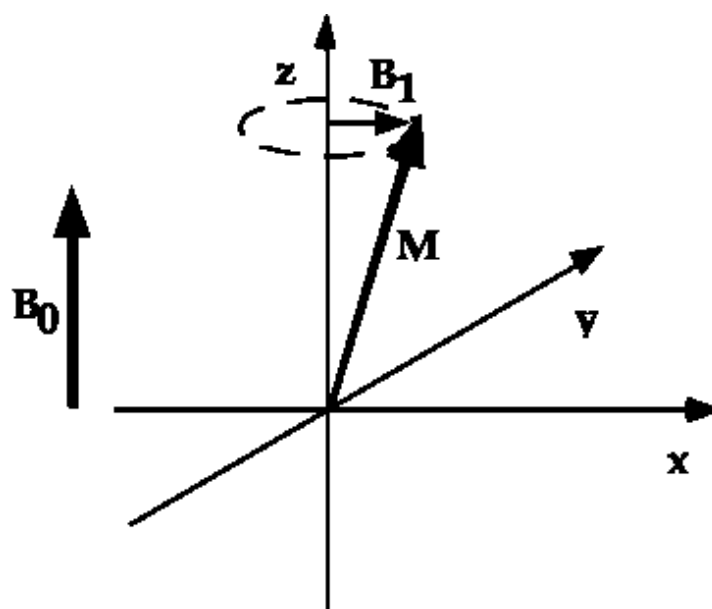


Figure 1.3- The magnetization vector is tilted away from the longitudinal equilibrium in the B_0 direction towards the transverse plane by the application of an RF pulse, B_1 , at the Larmor (resonance) frequency.

1.2.2 Spatial encoding

The goal of imaging is to correlate a series of signal measurements with the spatial locations of the various sources [17]. This can be achieved by the addition of a spatially changing magnetic field across the sample to produce a signal with varying frequency components according to

$$\omega(x) = \gamma B(x) \quad (1.2)$$

where x denotes the spatial coordinate along the direction of the gradient of the field. This makes it possible to localize the source by encoding the source location into the frequency or phase. This encoding is carried out by constructing *gradient coils* that change the original field B_0 linearly in the gradient directions (Figure 1.4). That is,

$$B(x) = B_0 + xG_x \quad (1.3)$$

where G_x is the gradient of the field in the direction of the applied gradient field.

Therefore:

$$\omega(x) = \underbrace{\gamma B_0}_{\omega_0} + \underbrace{\gamma x G_x}_{\Delta\omega} \quad (1.4)$$

Or, noting that the first term, γB_0 , is a constant independent of the location, equation 1.4 can be expressed in terms of a continuous accumulation of phase difference:

$$\Delta\phi(x, t) = \int_0^t \Delta\omega(x, t') dt' = \gamma x \int_0^t G_x(t') dt' \quad (1.5)$$

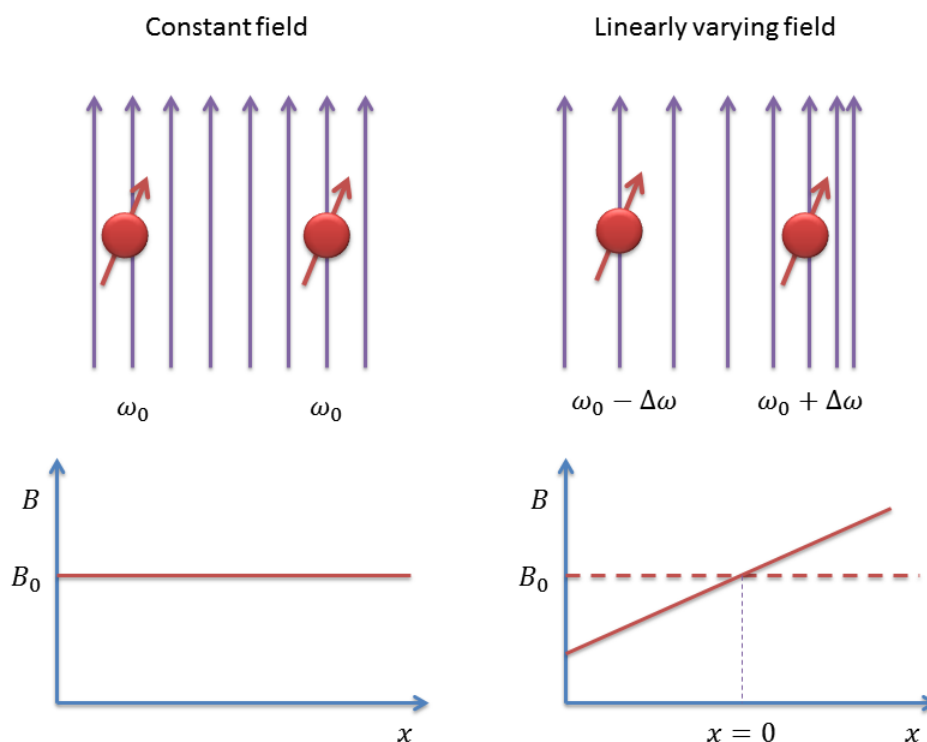


Figure 1.4- Frequency/phase encoding of the image position by the application of a linear gradient magnetic field. Left: B_0 only- all nuclei precess at the same frequency. Right: $B_0 + xG_x$ - the precession frequency is linearly dependent on the position.

As described later in section 1.2.3, such linear encoding simplifies the mapping between the signal space and the image position space to taking a Fourier transform.

The Fourier transform of the detected signal is a projection of the object onto the x axis. Therefore, a projection reconstruction of the object can theoretically be obtained by repeating the acquisitions while applying gradients at different orientations.

1.2.3 K-space

The frequency domain is often referred to as *k-space* in the MRI literature. While based on the above discussion it is possible to acquire projections through the object by changing the direction of the gradient and reconstruct the image similar to computed tomography (CT)³, in practice the image is often reconstructed by filling in a grid of 2D Fourier data and taking the inverse Fourier transform:

Assume a 2D grid in the xy direction, corresponding to the 2D Fourier data of a 2D image or a slice of the 3D object. As described above, a phase-encoded signal can be acquired by applying a gradient in the x direction during the signal acquisition. Nevertheless, while this phase encoding results in localization in the x direction, the detected signal does not contain any localization information in the direction of the y coordinate.

Consider applying a second gradient G_y along the y axis (perpendicular to the x direction) for a short period just before G_x . The resonance frequency of the nuclei will be altered depending on their position along the y axis, which results in the accumulation of a phase difference during the period that G_y is on. The phase incurred depends on the strength of the gradient and the time during which G_y was on, and can provide localization information along the y direction. The signal is then “read” while G_x is on.

³ In theory, projection reconstruction can be done either using filtered-back projection or, based on the central section theorem, by re-binning the frequency domain data and taking an inverse Fourier transform.

The direction of G_y is often called the *phase-encode* direction and the direction of G_x the *readout* direction.

The received RF signal is the superposition of all the precessing magnetization vectors within the sensitivity range of the RF coil:

$$S(t) = \iint_{xy \text{ plane}} m(x, y) e^{-i\phi(x, y, t)} dx dy \quad (1.6)$$

Note that what can be measured is the difference in phase, $\Delta\phi$, rather than the absolute phase. Similar to equation (1.5), $\Delta\phi$ can be written in terms of the spatial location and the magnetic gradients:

$$\Delta\phi(x, y, t) = \int_0^t \gamma x G_x(t') dt' + \int_0^t \gamma y G_y(t') dt' \quad (1.7)$$

Letting $k_x(t) = \gamma \int_0^t G_x(t') dt'$, and $k_y(t) = \gamma \int_0^t G_y(t') dt'$, equation (1.6) becomes:

$$S(t) = \iint_{xy \text{ plane}} m(x, y) e^{-i(xk_x + yk_y)} dx dy \quad (1.8)$$

which is essentially the Fourier transform of $m(x, y)$. In other words, the RF signal gives us a point in $M(k_x, k_y)$ - the Fourier transform of $m(x, y)$.

As described in section 1.2.5, by changing k_x and k_y through manipulation of the gradients, all the points on k-space can be filled.

1.2.4 T_1/T_2 contrast

Once the RF pulse is turned off, the spins return to the lower energy state, i.e., equilibrium. Macroscopically, this is modeled by an exponential recovery of the longitudinal component towards the equilibrium state:

$$M_z(t) = M_z(0) e^{-\frac{t}{T_1}} + M_0 (1 - e^{-\frac{t}{T_1}}) \quad (1.9)$$

where M_z is the longitudinal magnetization component.

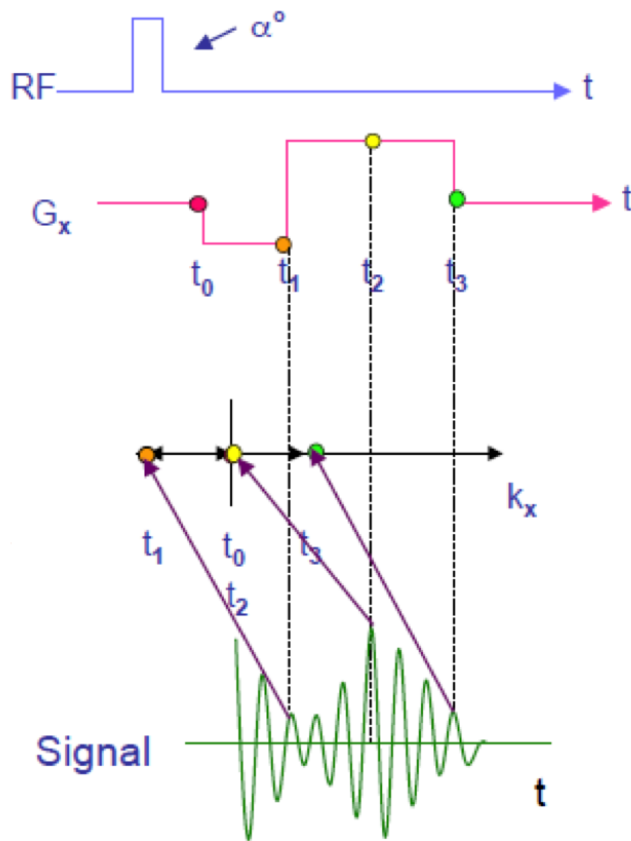


Figure 1.5- The RF signal is usually sampled while the G_x gradient is on, therefore filling in k-space point along the readout (k_x) direction.

Furthermore, the spin-spin interactions cause slight differences in the net magnetic field, which result in different precession frequencies and, consequently, dephasing of the spins, which, in turn, results in a decay of the transverse magnetic field. The transverse decay also follows an exponential curve:

$$M_{xy}(t) = M_{xy}(0)e^{-t/T_2} \quad (1.10)$$

where M_{xy} is the transverse magnetization component.

T_1 and T_2 are the longitudinal and transverse relaxation time constants, also known as the *spin-lattice* and *spin-spin relaxation time*, respectively.

These time constants are intrinsic properties of the material and, since the signal is read during the relaxation, the difference in the relaxation time constants in different tissues produces some contrast. In general, depending on the imaging pulse sequence, one relaxation may become more dominant in terms of producing the contrast, and therefore the image may be T_1 - or T_2 - or M_0 weighted.

1.2.5 Magnetic resonance imaging

As described previously, **K-space** is filled by sampling the RF signal while changing k_x and k_y . The samples are usually acquired while k_x is on, therefore filling in k-space points along one line in the readout (k_x) direction ([Figure 1.5](#)).

To advance though different location in the phase-encode (k_y) direction, a gradient in the y direction, G_y , is usually applied prior to readout. With the duration of the gradient pulse held constant, the phase-encode position is controlled by varying the strength of the gradient ([Figure 1.6](#)).

Typically after each RF excitation pulse, one or more k-space lines are acquired in the readout direction. The entire k-space is filled by repeating this sequence.

1.2.5.1 Pulse sequence parameters

As an example, [Figure 1.7](#) shows a schematic diagram of an RF spin echo pulse sequence [18], in which 90° excitation pulses are used. The time between consecutive excitation pulses is often referred to as the *repetition time (TR)*. Note that in addition to the spin-spin interactions described in section 1.2.4, local inhomogeneities of the main magnetic field can result in additional dephasing. The overall effect results in a larger time constant T_2^* , often called the *apparent T_2* . Nevertheless, the latter effects can be reversed by the application of a 180° RF pulse, resulting in the formation of a *spin echo*. The time from

the excitation pulse (the 90° pulse in this case) to the formation of an echo is called the *echo time (TE)*.

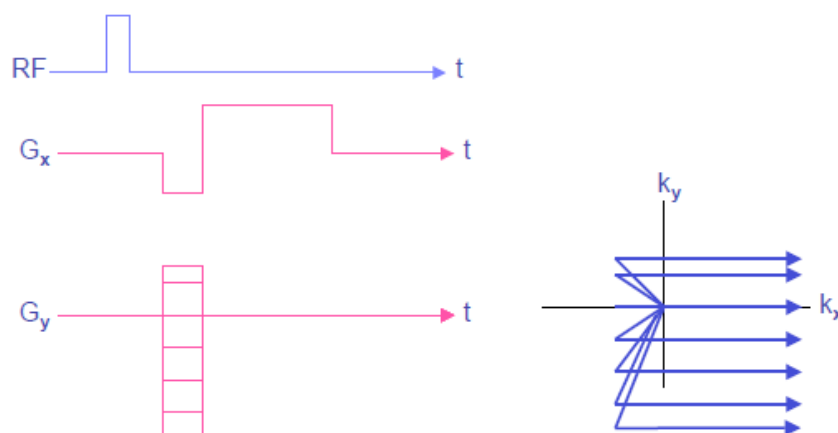


Figure 1.6- With the duration of the gradient pulse held constant, the phase-encode position is controlled by varying the strength of the gradient.

In addition, any magnetic field gradient results in additional dephasing of the spins, which can be counteracted by the application of an inverse gradient, resulting in the formation of a *gradient echo* (Figure 1.8). An RF spin echo pulse sequence is deliberately designed so that the RF spin echo and the gradient echo occur simultaneously.

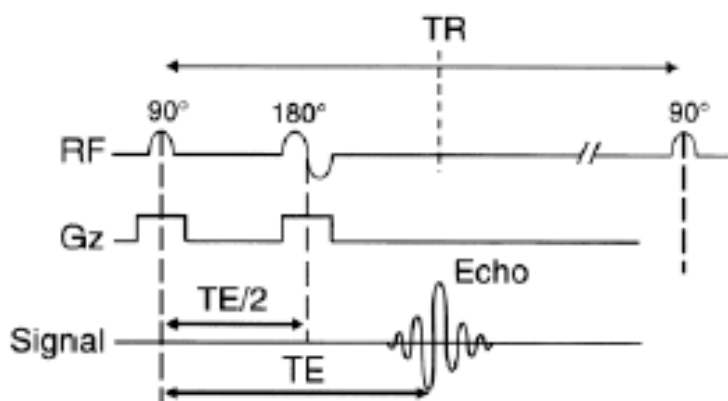


Figure 1.7- Schematic diagram of the RF spin echo pulse sequence.

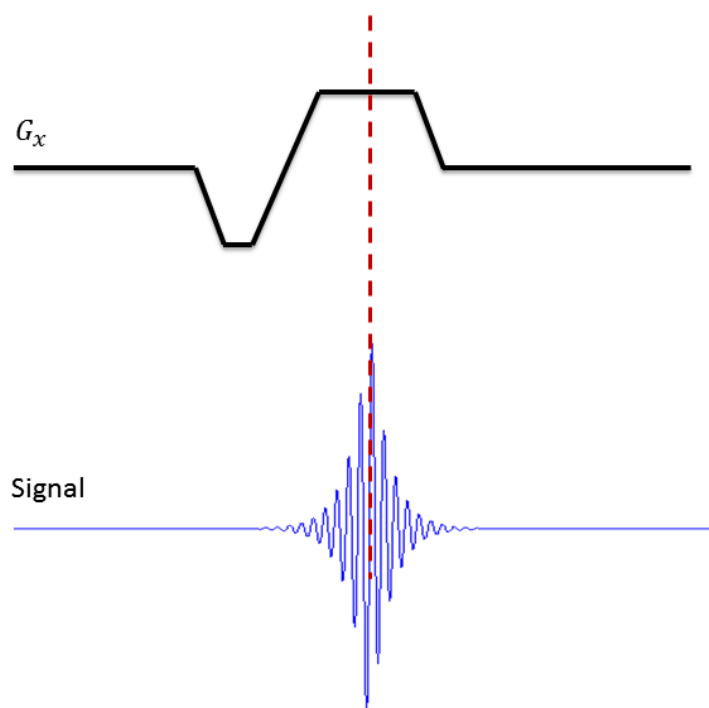


Figure 1.8- Schematic illustration of the formation of a gradient echo.

Not all pulse sequences involve a 180° RF refocussing pulse, in which case the decay of the measured signal occurs with time constant T_2^* .

The reader is referred to [17], [19], [20] for a more thorough explanation of different aspects of magnetic resonance imaging.

1.3 Quantitative MRI: T1/T2 mapping

While the contrast in an MR image may be due to the difference in T_1/T_2 contrast of different tissues, the intensity image does not necessarily provide the quantitative values of the relaxation time constants T_1 and T_2 . Having a quantitative map of the relaxation time constants T_1 and T_2 has immediate clinical applicability [21]. Such quantitative T_1/T_2 maps are often estimated by acquiring multiple points on the exponential

recovery/relaxation curves through multiple acquisitions, and fitting an exponential function onto the acquired data points [22]. This procedure is usually referred to as T_1/T_2 mapping.

1.3.1 DESPOT1/DESPOT2 T_1 and T_2 mapping

Although several T_1/T_2 techniques have been proposed [2]–[4], [22], [23], the T_1 and T_2 mapping techniques DESPOT1 and DESPOT2 developed by Deoni et al [5], which are currently the most efficient quantitative mapping techniques [24], were particularly considered in this thesis. Since DESPOT1 is employed in the future chapters, here a brief overview is provided below.

1.3.1.1 DESPOT1

DESPOT1 T_1 mapping is based on the acquisition of two spoiled gradient recalled (SPGR) images at the *optimal* flip angles [5].

The SPGR signal intensity, S_{SPGR} , is a function of the longitudinal relaxation time, T_1 , repetition time, TR , flip angle, α . At steady state:

$$S_{SPGR} = \frac{\rho(1-E_1) \sin \alpha}{1-E_1 \cos \alpha} \quad (1.11)$$

where $E_1 = \exp\left(-\frac{TR}{T_1}\right)$, and ρ is a factor proportional to the equilibrium longitudinal magnetization, M_0 .

By holding TR constant and incrementally increasing α , a curve characterized by T_1 is generated, which can be represented in a linear form ($Y = mX + b$) as:

$$\frac{S_{SPGR}}{\sin \alpha} = E_1 \frac{S_{SPGR}}{\tan \alpha} + \rho(1 - E_1) \quad (1.12)$$

The slope, m , can be estimated by linear regression, from which T_1 can be extracted:

$$T_1 = -TR/\ln(m) \quad (1.13)$$

It has also been suggested that improved T_1 accuracy can be achieved using weighted linear regression [25], [26].

1.4 Parallel imaging

Parallel imaging is the use of multi-coil arrays (also called phased array coils) to accelerate the MRI acquisition by acquiring under-sampled k-space data and filling in the un-sampled points using the redundant data acquired by multiple coils and the coil sensitivity profiles.

Parallel imaging techniques can be divided into two categories based on whether the reconstruction takes place in the spatial domain or in the Fourier domain, i.e., in k-space. SENSE (*Sensitivity encoding*) [27] is an example of the former where coil sensitivity profiles are used to unfold under-sampling aliasing artifacts in the spatial domain after taking the Fourier transform, and GRAPPA (*generalized auto calibrating partially parallel acquisition*) [28] exemplifies the latter where coil sensitivity profiles are used to fill in the missing k-space data before taking the Fourier transform.

Another categorization of parallel imaging techniques is based on whether the sensitivities are measured directly or indirectly. In the direct approach, coil sensitivities are explicitly calculated from the calibration data. In the indirect approach, however, coil sensitivities are not explicitly calculated but rather the calibration data are used to determine weights based on which the unknown k-space samples can be estimated from the known samples. This inevitably requires a k-space based reconstruction. GRAPPA is an example of calibration based on indirect sensitivity measurement. SENSE and SMASH (*simultaneous acquisition of spatial harmonics*) [29] exemplify direct sensitivity measurement where in SMASH reconstruction takes place in k-space.

1.4.1 SENSE

In SENSE coil sensitivities are directly used to unwrap the under-sampling aliasing artifacts in the spatial domain. In the simplest form, k-space is under-sampled by

increasing the distance between adjacent k-space lines in the phase-encode⁴ direction by a factor R (the acceleration ratio), while maintaining the maximum extent of k-space. Since field of view is inversely proportional to line spacing in k-space, this results in an R fold reduction in field of view resulting in an aliased image. Mathematically, the under-sampled image is a superposition of shifted replicas of the original image:

$$I^{\text{aliased}}(x, y) = \sum_{n=0}^{R-1} I(x, y + nL/R) \quad (1.14)$$

where L is the original field of view.

With phased array coils, the signal produced by each coil is the signal from the object, ρ , modulated by the coil sensitivity, c_i :

$$s_j(x, y) = c_j(x, y)\rho(x, y) \quad (1.15)$$

Therefore, assuming N_c receive coils and acceleration factor of R , the signal measured by each coil is given by:

$$\begin{aligned} s_1(x, y) &= c_1(x, y)\rho(x, y) + \dots + c_1(x, y + \frac{(R-1)L}{R})\rho(x, y + \frac{(R-1)L}{R}) \\ &\quad \vdots \\ s_{N_c}(x, y) &= c_{N_c}(x, y)\rho(x, y) + \dots + c_{N_c}(x, y + \frac{(R-1)L}{R})\rho(x, y + \frac{(R-1)L}{R}) \end{aligned} \quad (1.16)$$

Or in matrix form:

$$\mathbf{s} = \mathbf{c}\rho \quad (1.17)$$

Figure 1.9 pictorially shows equations (1.16) (or (1.17)) for two coils with $R = 2$.

⁴ Based on the discussion in section 1.2.3, in practice it is not possible to move from one readout (k_x) position to another without passing through the intervening positions and, therefore, k-space under-sampling is carried out in the phase-encode (k_y) direction only.

$$\begin{array}{ccccccc}
 \text{Image} & = & \text{Image} & \text{Image} & + & \text{Image} & \text{Image} \\
 s_1(x, y) & & c_1(x, y) & \rho(x, y) & & c_1\left(x, y + \frac{L}{2}\right) & \rho\left(x, y + \frac{L}{2}\right) \\
 \\
 \text{Image} & = & \text{Image} & \text{Image} & + & \text{Image} & \text{Image} \\
 s_2(x, y) & & c_2(x, y) & \rho(x, y) & & c_2\left(x, y + \frac{L}{2}\right) & \rho\left(x, y + \frac{L}{2}\right)
 \end{array}$$

Figure 1.9- Pictorial illustration of equation (1.16) for two coils and $R = 2$. Each point on the aliased image for each coil (left column) is the superposition of the corresponding point on the original image modulated by the coil sensitivity (middle column) and a point at half of field of view, $L/2$, shift (right column).

In general, equations (1.16) or (1.17) form a system of linear equations, which can be solved for ρ provided $N_c > R$.

1.4.2 GRAPPA

In GRAPPA calibration data are used to obtain a kernel relating k-space points on each coil to neighboring points over all coils. This kernel is then used to estimate un-sampled points based on the neighboring sampled points.

Calibration data are obtained integral to the scan (and therefore called auto-calibration) often by acquiring fully-sampled data at the center of k-space, amounting to a low resolution fully-sampled acquisition, for all coils. The kernel, consisting of reconstruction weights w , is obtained based on the following expression:

$$s_j(k_x, k_y + m\Delta k_y) = \sum_l \sum_a \sum_b w(j, l, a, b, m) s_l(k_x + a \Delta k_x, k_y + bR \Delta k_y) \quad (1.18)$$

The size of the kernel is chosen by the user. A larger kernel results in increased estimation accuracy at the expense of longer computation time. Figure 1.10 shows a GRAPPA reconstruction with a 3x2 kernel.

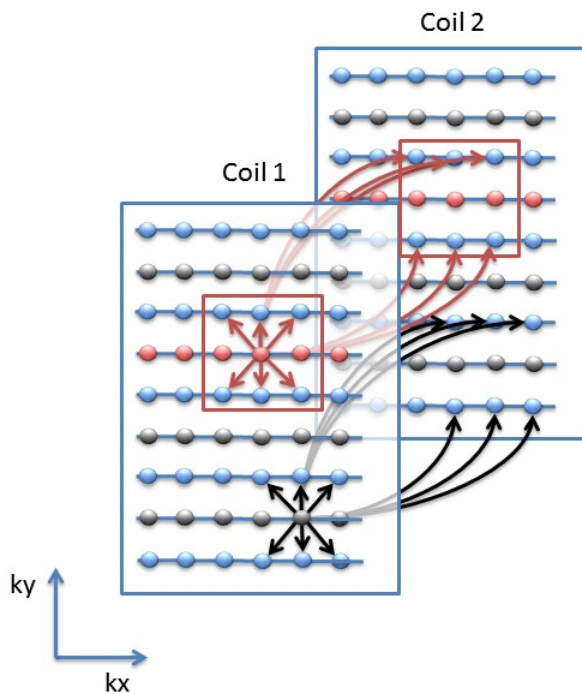


Figure 1.10- Pictorial illustration of GRAPPA reconstruction with two coils and $R = 2$. Auto-calibration data are shown in red. Blue represents sampled k-space data points and unsampled points are shown in grey. Once the kernel weights are found based on the auto-calibration data (red arrows), they can be used to fill in the missing data based on the neighboring sampled points (black arrows). In this example a 3x2 kernel is used (red box).

1.5 Compressed sensing

Many natural images, including MR images, are compressible based on their sparsity in a transform domain. In other words, there exist transform domains in which a large number of the transformation coefficients are zero or negligibly small and the energy of the image is concentrated in a few large coefficients. The small coefficients can be discarded without noticeable loss in the quality of the image and the image can be represented by a noticeably smaller number of coefficients (compression). Such transform-domain sparsity has been commonly used as regularization constraint for under-sampled MR imaging [15], [16]. These techniques are commonly known as compressed sensing (CS) [30], [31].

In traditional compressed sensing, a convex norm⁵ is minimized constrained by adherence to sampled k-space data. Traditional sparse reconstruction problems are often formulated as an optimization problem:

$$\min_{f^*} \|\psi f^*\|_{l_1} \text{ s.t. } \|U_F \mathcal{F} f^* - F_u\|_{l_2} < \varepsilon \quad (1.19)$$

Where ψ denotes a sparsifying transform, f^* the reconstructed image, \mathcal{F} the Fourier transform, U_F the under-sampling operation in the Fourier domain, and F_u the observed or sampled k-space data. The l_1 norm is often chosen as it is convex and promotes sparsity. In the absence of noise, and assuming sufficient sparsity in the underlying image, the solution to this problem is equivalent to minimizing the l_0 pseudo-norm [32]. Frequently, total variation, the l_1 norm of the finite differences, is also included as another convex cost function [33]:

$$\min_{f^*} \|\psi f^*\|_{l_1} + \alpha TV(f^*) \text{ s.t. } \|U_F \mathcal{F} f^* - F_u\|_{l_2} < \varepsilon \quad (1.20)$$

⁵ In a Euclidean space, an object is convex if for every pair of points within the object, every point on the straight line segment that joins the pair of points is also within the object.

Many techniques have been used for solving these minimization problems including interior point methods [34], conjugate gradient [15] and iterative soft thresholding [35]. More theoretical discussions on the application of iterative soft and hard thresholding for solving optimization problems can be found in [35]–[37]. Furthermore, projections onto convex sets (POCS) [38] algorithms have also been used to find the solution to this problem [39].

Traditional POCS methods solve equation (1.19) by iteratively projecting the solution onto convex sets in the Fourier and wavelet domains, where consistency with the acquired k-space data and the wavelet sparsity are respectively re-enforced. Wavelet sparsity is often re-enforced through the convex soft thresholding. In chapter 2 a similar approach is used with stationary wavelet transform (SWT) [40], [41], which provides superior reconstructions compared to the regular decimated wavelet transform (DWT).

POCS algorithms have been used for image restoration from partial data with nonlinear constraints [42]. In [39], [43] the authors propose POCS-based parallel imaging MRI reconstruction algorithms, which also allow the integration of additional constraints, where in [39] the authors explicitly explore the -wavelet regularization.

1.6 Thesis outline

1.6.1 Chapter 2- Iterative stationary wavelet transform thresholding reconstruction

In chapter 2 the reconstruction of a single under-sampled k-space dataset based on the [Sparsity in a transform domain](#) and the [Coil sensitivity profiles](#) constraints described in section 1.1 are considered. An [Iterative stationary wavelet transform thresholding](#) algorithm is developed whereby the image is reconstructed by alternating between the spatial, wavelet, and frequency domains, in which the coil sensitivity, wavelet sparsity, and sampled k-space data consistency constraints are respectively re-enforced. While the rationale behind the use of [Iterative stationary wavelet transform thresholding](#) for [Compressed sensing](#) is more thoroughly explored in chapter 3, chapter 2 demonstrates

how it can be incorporated in an [Iterative stationary wavelet transform thresholding](#) for [Under-sampled MRI reconstruction](#).

1.6.2 Chapter 3- Stationary wavelet transform for under-sampled MRI reconstruction

As described in section 1.5, sparsity constraints are often incorporated as an l_p -penalty⁶ to regularize the [Under-sampled MRI reconstruction](#) inverse problem. While conventionally the aforementioned l_p -penalty is imposed on the decimated wavelet transform (DWT) coefficients, chapter 3 shows that this may result in visual artifacts, e.g., pseudo-Gibbs ringing, most of which can be avoided by penalizing the stationary wavelet transform (SWT) coefficients instead. It is shown that this holds with various additional constraints, e.g., coil sensitivities and total variation, which may additionally be assumed depending on the application. Furthermore, SWT-penalized reconstructions generally result in lower error values and faster convergence compared to the DWT-penalized counterparts.

1.6.3 Chapter 4- Similarity-based joint reconstruction in multiple acquisition problems with application to DESPOT1 T1 mapping

Chapter 4 demonstrates that in applications involving multiple acquisitions, e.g., [Quantitative MRI: T1/T2 mapping](#), the similarity between consecutive acquisitions can be used as an additional reconstruction constraint to achieve improved reconstruction performance. To this end, an [Iterative reconstruction](#) algorithm is developed incorporating both the similarity and wavelet sparsity constraints for under-sampled data reconstruction.

Without loss of generality, the methods and results are demonstrated for human brain [DESPOT1 T1 mapping](#). It is shown that joint reconstruction based on the similarity in addition to individual sparsity constraints results in reduced visual artifacts and

⁶ I.e., penalizing an l_p -norm, which is defined as:

$$\|x\|_p = \left(\sum_i |x_i|^p \right)^{\frac{1}{p}}$$

significantly lower reconstruction error compared to the traditional sparsity-based individual reconstruction of the images. Additionally, while the individual reconstruction fails to produce T1 maps even as accurate as a simple low-resolution acquisition, joint reconstruction results in significantly lower T1 map errors than both the individual and the low resolution reconstructions.

1.6.4 Chapter 5- Driven equilibrium single pulse observation of T1 with high-speed incorporation of RF field inhomogeneities (DESPOT1-HIFI)

Frequent uses of the [DESPOT1/DESPOT2 \$T_1\$ and \$T_2\$ mapping](#) techniques during the course of the work presented in this thesis, led to a closer inspection of these techniques and the pulse sequences involved. This resulted in a modification to an extension of DESPOT known as *DESPOT-HIFI*, which addresses some of the limitations of the conventional DESPOT due to RF field inhomogeneities at high (3T and above) magnetic fields (see section 5.1). The aforementioned modification is presented and validated on phantom and *in vivo* human data in chapter 5.

1.6.5 Chapter 6- Subjective reconstruction quality assessment

While quantitative quality measures, e.g., normalized root mean square error (NRMSE), contrast-to-noise ratio (CNR), and signal-to-noise ratio (SNR), are commonly used to assess the quality of reconstruction and to compare different reconstructions with each other, such quantitative measures do not necessarily correlated with perceptual quality judgments made by radiologists and other end users of the medical images. Therefore, to be of clinical impact, any quantitative quality assessment/comparison should be accompanied by subjective evaluations that rate the reconstruction techniques in terms of their ability to produce diagnostically meaningful images. In chapter 5, the results of a number of experiments, carried out with the help of collaborating radiologists in order to subjectively assess the quality of different under-sampled reconstructions, are presented and compared against each other for specific applications. This chapter also demonstrates the dependence of the reconstruction performance on the particular application involved.

1.7 References

- [1] A. Macovski, "Noise in MRI," *Magn. Reson. Med.*, vol. 36, no. 3, pp. 494–497, 1996.
- [2] C. Y. Tong and F. S. Prato, "A novel fast T1-mapping method," *J. Magn. Reson. Imaging*, vol. 4, no. 5, pp. 701–708, 1994.
- [3] Z. Chen, F. S. Prato, and C. McKenzie, "T1 fast acquisition relaxation mapping (T1-FARM): an optimized reconstruction," *IEEE Trans. Med. Imaging*, vol. 17, no. 2, pp. 155–160, Apr. 1998.
- [4] C. A. McKenzie, Z. Chen, D. J. Drost, and F. S. Prato, "Fast acquisition of quantitative T2 maps," *Magn. Reson. Med. Off. J. Soc. Magn. Reson. Med. Soc. Magn. Reson. Med.*, vol. 41, no. 1, pp. 208–212, Jan. 1999.
- [5] S. C. L. Deoni, B. K. Rutt, and T. M. Peters, "Rapid combined T1 and T2 mapping using gradient recalled acquisition in the steady state," *Magn. Reson. Med.*, vol. 49, no. 3, pp. 515–526, Mar. 2003.
- [6] A. Haase, J. Frahm, D. Matthaei, W. Hanicke, and K.-D. Merboldt, "FLASH imaging. Rapid NMR imaging using low flip-angle pulses," *J. Magn. Reson.* 1969, vol. 67, no. 2, pp. 258–266, Apr. 1986.
- [7] D. J. Larkman and R. G. Nunes, "Parallel magnetic resonance imaging," *Phys. Med. Biol.*, vol. 52, no. 7, pp. R15–55, Apr. 2007.
- [8] P. Mansfield, "Multi-planar image formation using NMR spin echoes," *J. Phys. C Solid State Phys.*, vol. 10, no. 3, p. L55, Feb. 1977.
- [9] D. A. Feinberg and K. Oshio, "GRASE (gradient- and spin-echo) MR imaging: a new fast clinical imaging technique.," *Radiology*, vol. 181, no. 2, pp. 597–602, Nov. 1991.
- [10] K. Oshio and D. A. Feinberg, "GRASE (Gradient-and Spin-Echo) imaging: A novel fast MRI technique," *Magn. Reson. Med.*, vol. 20, no. 2, pp. 344–349, 1991.
- [11] C. T. W. Moonen, G. Liu, P. V. Gelderen, and G. Sobering, "A fast gradient-recalled MRI technique with increased sensitivity to dynamic susceptibility effects," *Magn. Reson. Med.*, vol. 26, no. 1, pp. 184–189, 1992.
- [12] G. Liu, G. Sobering, A. W. Olson, P. Van Gelderen, and C. T. W. Moonen, "Fast echo-shifted gradient-recalled MRI: Combining a short repetition time with variable T2* weighting," *Magn. Reson. Med.*, vol. 30, no. 1, pp. 68–75, 1993.

- [13] J. Hennig, "Multiecho imaging sequences with low refocusing flip angles," *J. Magn. Reson.* 1969, vol. 78, no. 3, pp. 397–407, Jul. 1988.
- [14] J. Hennig, A. Nauerth, and H. Friedburg, "RARE imaging: A fast imaging method for clinical MR," *Magn. Reson. Med.*, vol. 3, no. 6, pp. 823–833, 1986.
- [15] M. Lustig, D. Donoho, and J. M. Pauly, "Sparse MRI: The application of compressed sensing for rapid MR imaging," *Magn. Reson. Med.*, vol. 58, no. 6, pp. 1182–1195, Dec. 2007.
- [16] M. Lustig, D. L. Donoho, J. M. Santos, and J. M. Pauly, "Compressed Sensing MRI," *IEEE Signal Process. Mag.*, vol. 25, no. 2, pp. 72–82, Mar. 2008.
- [17] E. M. Haacke, R. W. Brown, M. R. Thompson, and R. Venkatesan, *Magnetic Resonance Imaging: Physical Principles and Sequence Design*. Wiley, 1999.
- [18] E. L. Hahn, "Spin Echoes," *Phys. Rev.*, vol. 80, no. 4, pp. 580–594, Nov. 1950.
- [19] D. W. McRobbie, E. A. Moore, M. J. Graves, and M. R. Prince, *MRI from Picture to Proton*. Cambridge University Press, 2006.
- [20] M. A. Bernstein, K. F. King, and X. J. Zhou, *Handbook of MRI Pulse Sequences*. Elsevier, 2004.
- [21] S. C. L. Deoni, M. J. C. Josseau, B. K. Rutt, and T. M. Peters, "Visualization of thalamic nuclei on high resolution, multi-averaged T1 and T2 maps acquired at 1.5 T," *Hum. Brain Mapp.*, vol. 25, no. 3, pp. 353–359, 2005.
- [22] S. Meiboom and D. Gill, "Modified Spin-Echo Method for Measuring Nuclear Relaxation Times," *Rev. Sci. Instrum.*, vol. 29, no. 8, pp. 688–691, Aug. 1958.
- [23] S. C. L. Deoni, "High-resolution T1 mapping of the brain at 3T with driven equilibrium single pulse observation of T1 with high-speed incorporation of RF field inhomogeneities (DESPOT1-HIFI)," *J. Magn. Reson. Imaging JMRI*, vol. 26, no. 4, pp. 1106–1111, Oct. 2007.
- [24] D. Ma, V. Gulani, N. Seiberlich, K. Liu, J. L. Sunshine, J. L. Duerk, and M. A. Griswold, "Magnetic resonance fingerprinting," *Nature*, vol. 495, no. 7440, pp. 187–192, Mar. 2013.
- [25] S. C. L. Deoni, T. M. Peters, and B. K. Rutt, "Determination of optimal angles for variable nutation proton magnetic spin-lattice, T1, and spin-spin, T2, relaxation times measurement," *Magn. Reson. Med.*, vol. 51, no. 1, pp. 194–199, 2004.

- [26] L.-C. Chang, C. G. Koay, P. J. Basser, and C. Pierpaoli, "Linear least-squares method for unbiased estimation of T1 from SPGR signals," *Magn. Reson. Med.*, vol. 60, no. 2, pp. 496–501, 2008.
- [27] K. P. Pruessmann, M. Weiger, M. B. Scheidegger, and P. Boesiger, "SENSE: Sensitivity encoding for fast MRI," *Magn. Reson. Med.*, vol. 42, no. 5, pp. 952–962, 1999.
- [28] M. A. Griswold, P. M. Jakob, R. M. Heidemann, M. Nittka, V. Jellus, J. Wang, B. Kiefer, and A. Haase, "Generalized autocalibrating partially parallel acquisitions (GRAPPA)," *Magn. Reson. Med.*, vol. 47, no. 6, pp. 1202–1210, 2002.
- [29] D. K. Sodickson and W. J. Manning, "Simultaneous acquisition of spatial harmonics (SMASH): Fast imaging with radiofrequency coil arrays," *Magn. Reson. Med.*, vol. 38, no. 4, pp. 591–603, 1997.
- [30] E. J. Candes and M. B. Wakin, "An Introduction To Compressive Sampling," *Signal Process. Mag. IEEE*, vol. 25, no. 2, pp. 21–30, 2008.
- [31] D. L. Donoho, "Compressed sensing," *IEEE Trans. Inf. Theory*, vol. 52, no. 4, pp. 1289–1306, Apr. 2006.
- [32] D. L. Donoho, "For most large underdetermined systems of equations, the minimal l_1 -norm near-solution approximates the sparsest near-solution," *Commun. Pure Appl. Math.*, vol. 59, no. 7, pp. 907–934, 2006.
- [33] E. J. Candes, J. Romberg, and T. Tao, "Robust uncertainty principles: exact signal reconstruction from highly incomplete frequency information," *Inf. Theory IEEE Trans. On*, vol. 52, no. 2, pp. 489–509, 2006.
- [34] S. S. Chen, D. L. Donoho, and M. A. Saunders, "Atomic Decomposition by Basis Pursuit," *SIAM Rev.*, vol. 43, no. 1, pp. 129–159, Jan. 2001.
- [35] I. Daubechies, M. Defrise, and C. De Mol, "An iterative thresholding algorithm for linear inverse problems with a sparsity constraint," *Commun. Pure Appl. Math.*, vol. 57, no. 11, pp. 1413–1457, Nov. 2004.
- [36] M. Fornasier and H. Rauhut, "Iterative thresholding algorithms," *Appl. Comput. Harmon. Anal.*, vol. 25, no. 2, pp. 187–208, Sep. 2008.
- [37] T. Blumensath and M. E. Davies, "Iterative hard thresholding for compressed sensing," *Appl. Comput. Harmon. Anal.*, vol. 27, no. 3, pp. 265–274, Nov. 2009.
- [38] L. G. Gubin, B. T. Polyak, and E. V. Raik, "The method of projections for finding the common point of convex sets," *USSR Comput. Math. Math. Phys.*, vol. 7, no. 6, pp. 1–24, 1967.

- [39] M. Lustig and J. M. Pauly, "SPIRiT: Iterative self-consistent parallel imaging reconstruction from arbitrary k-space," *Magn. Reson. Med.*, vol. 64, no. 2, pp. 457–471, 2010.
- [40] G. P. Nason and B. W. Silverman, "The Stationary Wavelet Transform and some Statistical Applications," in *Wavelets and Statistics*, A. Antoniadis and G. Oppenheim, Eds. Springer New York, 1995, pp. 281–299.
- [41] J. Pesquet, H. Krim, and H. Carfantan, "Time-invariant orthonormal wavelet representations," *IEEE Trans. Signal Process.*, vol. 44, no. 8, pp. 1964–1970, 1996.
- [42] D. C. Youla and H. Webb, "Image Restoration by the Method of Convex Projections: Part 1 #2014;Theory," *Med. Imaging IEEE Trans. On*, vol. 1, no. 2, pp. 81–94, Oct. 1982.
- [43] A. A. Samsonov, E. G. Kholmovski, D. L. Parker, and C. R. Johnson, "POCSense: POCS-based reconstruction for sensitivity encoded magnetic resonance imaging," *Magn. Reson. Med.*, vol. 52, no. 6, pp. 1397–1406, 2004.

2 Iterative stationary wavelet transform thresholding reconstruction

In this chapter, an iterative stationary wavelet transform (SWT) [1], [2] thresholding algorithm for [Under-sampled MRI reconstruction](#) based on wavelet sparsity [3], [4] and coil sensitivity profiles in multiple coil acquisitions [5] is developed. SWT penalized reconstructions are more thoroughly investigated in the next chapter, where I show that SWT penalized reconstructions result in improved reconstruction performance compared to the corresponding reconstruction obtained by penalizing the decimated wavelet transform (DWT) coefficients. In particular, it is shown that some reconstruction artifacts attributed to the translation-variance of DWT can be eliminated by SWT, which is a translation-invariant wavelet transform [6]. In this chapter, however, SWT thresholding is incorporated in an iterative thresholding algorithm [7] to obtain an [Iterative stationary wavelet transform thresholding](#) reconstruction algorithm by alternating between the frequency domain, in which the k-space data constraint is re-enforced, and the SWT domain, in which the sparsity constraint is re-enforced. For more background on SWT and the rationale behind the proposition to use SWT thresholding in the iterative reconstruction algorithm, the reader is referred to the [Introduction](#) section of the next chapter.

2.1 Introduction

2.1.1 Papoulis-Gerchberg reconstruction

The Papoulis-Gerchberg (P-G) reconstruction algorithm was originally developed for reconstruction from partial spatial or frequency domain data with a finite support constraint in the other domain. The signal is reconstructed by alternating between these domains to re-enforce the data and support constraints in the corresponding domains.

This algorithm has been also used for MRI reconstruction from limited k-space

observations with the assumption of a finite spatial support constraint on the image [9], [10], [11].

As described in the methods section, a similar reconstruction can be obtained with the assumption of a wavelet sparsity constraint (equivalent to the support constraint in P-G). Similar to the P-G algorithm, the image is reconstructed by alternating between the frequency domain and the wavelet domain to re-enforce the known k-space data and sparsity constraints, respectively. Nevertheless, in addition to the domain on which these constraints are defined (wavelet vs. spatial), they also differ in the sense that while a known finite support can be considered a *hard* constraint, a sparsity constraint on the unknown wavelet coefficients is a *soft* constraint.

2.1.2 Under-sampled MRI reconstruction

Assume Cartesian k-space trajectories and assume any point on the k-space grid is either sampled or replaced by zero. K-space under-sampling can, therefore, be denoted by a linear operation, U_F , defined in Fourier space. The relationship between the fully-sampled k-spaced data, F , and the under-sampled k-space data, F_u , can be expressed as:

$$F_u = U_F F \quad (2.1)$$

Under-sampling is usually assumed to be random to achieve incoherent under-sampling artifacts [3], [12].

Also, with many pulse sequences one may not achieve further time savings by under-sampling in the readout (k_x) direction, since in practice it is not possible to move from one k_x position to another without passing through the intervening positions. Therefore, assuming full sampling in the readout direction, the problem reduces to a 1D (for 2D MRI) or 2D (for 3D MRI) interpolation problem in the phase-encode directions.

Our objective is to reconstruct F , or equivalently in the spatial domain, f , from the under-sampled k-space data, F_u , based on an *a priori* sparsity constraint, where $f = \mathcal{F}^{-1}F$ is the

spatial domain representation of F , where \mathcal{F} is the Fourier transform operation and $*$ denotes the adjoint operation.

2.2 Iterative stationary wavelet transform thresholding

Assume an under-sampled image f_u corresponding to an under-sampled k-space dataset F_u . Consider the SWT decomposition of f_u : $C_{SWT} = \psi_{SWT} f_u$, where ψ_{SWT} is the stationary wavelet transforms, and C_{SWT} contains the corresponding wavelet decomposition coefficients. Assume a thresholding operation, γ , acting on the decomposition coefficients: $\tilde{C}_{SWT} = \gamma\{C_{SWT}\}$. The SWT thresholded image is obtained by SWT reconstruction of the thresholded coefficients: $\tilde{f}_{SWT} = \psi_{SWT}^* \tilde{C}_{SWT}$. In order to simplify our notation, define a SWT thresholding operation, Γ , such that

$$\tilde{f} = \Gamma\{f_u\} = \psi_{SWT}^* \gamma\{\psi_{SWT} f_u\} \quad (2.2)$$

Beginning with f_u as the initial estimate to the solution, a better estimate is achieved by removing some of the aliasing artifacts by the thresholding (sparsity-promoting) operation: $g^{(1)} = \Gamma\{f_u\}$. The superscript denotes the iteration number.

However, both under-sampling (U_F) and thresholding (Γ) operations reduce the energy of the image. Consequently, $g^{(1)}$ has reduced energy compared to f_u and f_u has reduced energy compared to f .⁷

In addition, while thresholding should have revealed more features of the image by removing some of the aliasing artifacts, it may as well have affected the known k-space samples. Mathematically, $F_u = U_f F \neq U_f G^{(1)}$, where $G^{(1)} = \mathcal{F} g^{(1)}$ is the Fourier transform of $g^{(1)}$. In other words, if $G^{(1)}$ is under-sampled in the same manner k-space was, the resulting under-sampled data will not necessarily be consistent with the original under-sampled k-space data.

⁷ In fact, $f_u = \mathcal{F}^{-1} F_u$ has the minimum energy among all the solutions consistent with the k-space data since we assume the unobserved k-space samples are simply replaced by zero in F_u . This is usually called a minimum-energy reconstruction.

Iterative SWT thresholding reconstruction algorithm

Inputs:

 F_u : Under-sampled k-space data U_F : Under-sampling operation selecting k-space data

Output:

 F_{rec} : Reconstructed k-space data

Algorithm:

// Initialize to the minimum energy reconstruction

 $F_{rec} \leftarrow F_{u,1}$

//Reconstruct through iterative thresholding

while *not converged* do $f_{rec} \leftarrow \mathcal{F}^{-1}F_{rec}$ //sum of squares $\tilde{f} = \Gamma f_{rec}$ //thresholding

//data consistency

 $\tilde{F} \leftarrow \mathcal{F}\tilde{f}$ $F_{rec} \leftarrow \tilde{F} - U_f\tilde{F} + F_u$

end

Table 2.1- Iterative SWT thresholding reconstruction algorithm

Therefore, before further progress, the known k-space samples are recovered by replacing the corrupted values with those originally observed: $F^{(1)} = G^{(1)} - U_F G^{(1)} + F_u$.

Note that $F^{(1)}$ has higher energy than F_u since some of the unknown coefficients, which are replaced by zero in F_u , take an estimated value in $F^{(1)}$.

Since $f^{(1)}$ is a better estimate of f than f_u , this estimate can potentially be improved by repeating the above procedure in an iterative manner, where, at the n th iteration, starting with the latest estimate at the previous iteration, $f^{(n-1)}$, the next estimate is achieved by a sparsity-promoting operation,

$$g^{(n)} = \Gamma\{f^{(n-1)}\}, \quad (2.3)$$

followed by recovery of the known k-space samples,

$$F^{(n)} = G^{(n)} - U_F G^{(n)} + F_u \quad (2.4)$$

Combining these two operations, and noting $f^{(n)} = \mathcal{F}^* F^{(n)}$, the iterative process can be expressed as

$$f^{(n)} = \Gamma\{f^{(n-1)}\} - \mathcal{F}^* U_F \mathcal{F} \Gamma\{f^{(n-1)}\} + \mathcal{F}^* F_u \quad (2.5)$$

The iterations are initialized with the minimum-energy reconstruction, $f^{(0)} = f_u$, and continue until a convergence criterion is reached. E.g., changes between iterations of less than a certain threshold are recorded, $|f^{(n)} - f^{(n-1)}|/|f^{(n)}| < \epsilon$, or a maximum number of iterations is reached.

Table 2.1 summarizes the iterative SWT thresholding reconstruction algorithm.

2.2.1 Multiple coil data and combination with parallel imaging

Extension of this algorithm to multiple coil acquisitions is straightforward. Assuming under-sampled coil data $F_{u,i}; i = 1, 2, \dots, N_c$, where N_c is the number of coils, at each iteration the enforcer, e.g., wavelet thresholding, is applied to the combined-channels image, $f_{opt} = \sum_{i=1}^{N_c} \omega_i \frac{f_{u,i}}{s_i}$, where $\omega_i = \frac{s_i^2}{\sum_{j=1}^{N_c} s_j^2}$, and s_i is the sensitivity profile of the i th coil:

$$\tilde{f} = \Gamma\{f_{opt}\} \quad (2.6)$$

In order to ensure consistency between the acquired data and the reconstructed image, the image estimate is modulated by the sensitivity profiles of the coils [13]. The data consistency operation then becomes:

$$F_i = \tilde{F}_i - U_F \tilde{F}_i + F_{u,i} \quad (2.7)$$

where $\tilde{F}_i = \mathcal{F} s_i \tilde{f}$, and s_i is the sensitivity profile of the i th coil. In practice, the sensitivity profiles can be acquired either by a separate pre-calibration reference acquisition or by fully sampling the center of k-space to be used as low-resolution auto-calibration reference data. This approach to incorporating coil sensitivity data in the

reconstruction algorithm is similar to the POCS-based parallel imaging reconstruction algorithm described by Samsonov et al [13].

Table 2.2 summarizes the multiple-coil iterative reconstruction algorithm.

Multiple-coil iterative thresholding reconstruction algorithm

Inputs:

$F_{u,i}$: Under-sampled k-space data ($i = 1, \dots, N_c$, where N_c is the number of coils)

s_i : Coil sensitivities

U_F : Under-sampling operations selecting k-space data

Output:

F_i : Reconstructed k-space data

Algorithm:

```

// Initialize to the minimum energy reconstruction
for  $i \leftarrow 1:N_c$  do
     $F_i \leftarrow F_{u,i}$ 
end

//Reconstruct through iterative thresholding
while not converged do
//combine multiple channel data
 $f_{opt} \leftarrow \sum_{i=1}^{N_c} \omega_i \frac{f_i}{s_i}$  //where  $f_i = \mathcal{F}^{-1}F_i$  and  $\omega_i = \frac{s_i^2}{\sum_{j=1}^{N_c} s_j^2}$ 

//thresholding
 $\tilde{f} \leftarrow \Gamma(f_{opt})$  // where the nonlinear thresholding operation  $\Gamma$  is
defined as:  $\Gamma(f) = \psi^* \gamma(\psi f)$ , where  $\psi$  denotes wavelet transform and  $\gamma$  denotes
thresholding.

//data consistency
for  $i \leftarrow 1:N_c$  do
     $\tilde{F}_i \leftarrow \mathcal{F}(s_i \tilde{f})$ 
     $F_i \leftarrow \tilde{F}_i - U_F \tilde{F}_i + F_{u,i}$ 
end
end

```

Table 2.2- Multiple-coil iterative thresholding reconstruction algorithm.

2.3 Methods

Brain MR images of volunteers and patients were acquired at 3T using a GE scanner (Discovery 750, software revision 22M32, General Electric Healthcare, Waukesha, WI)

with spoiled gradient echo (SPGR). The parameters used for the SPGR acquisitions are as follows: matrix: 256x256x160, resolution = 1mm isotropic, TE/TR = 3.71ms/8.36ms, flip angle = 18°, BW = ±19.23 kHz, NEX=1. Human data used in this work were acquired using a protocol approved by the University of Western Ontario Office of Research Ethics.

SPGR datasets of a total of 5 healthy volunteers and 10 temporal lobe epilepsy (TLE) patients were used in the first set of experiments, with the fully-sampled datasets being employed as the gold standard. Independent 2D random under-sampling was achieved by selecting phase-encodes (k_y and k_z) by drawing samples from a Gaussian distribution with a zero mean (corresponding to the center of k-space, i.e., the zero frequency) and a standard deviation of 0.25mm^{-1} . To eliminate the dependence of the reconstructions on the under-sampling pattern, the same randomly selected under-sampling patterns were used for all datasets in this set of experiments.

Each set of under-sampled data was reconstructed by both iterative soft and hard wavelet thresholding using both the SWT and DWT, and by $l_1 + TV$ norm optimization [3], [4] (i.e., $\min_{f^*} \|\psi f^*\|_{l_1} + \alpha TV(f^*)$ s.t. $\|U_F \mathcal{F} f^* - F_u\|_{l_2} < \varepsilon$, where ψ is the wavelet transform operation) for comparison. $l_1 + TV$ norm optimization was performed by the conjugate gradient method, using the code supplement to [3]. The results were also compared with low-resolution sampling (acquired by zero-padding in the phase-encode directions in k-space, i.e., interpolation by a sinc kernel in the spatial domain) with the same under-sampling factor. These experiments were repeated for under-sampling factors from 1.5 to 4.

Another set of experiments was performed to study the sensitivity of the reconstruction to the randomly generated under-sampling pattern. In these experiments, a single dataset from a healthy volunteer was under-sampled with 15 different under-sampling patterns generated independently based on the Gaussian distribution.

To evaluate these algorithms on multiple coil data, brain images of a healthy volunteer were acquired by FSE using a 32-channel head coil with the following parameters: matrix

matrix: 256x256, resolution = 1mm, slice thickness = 2mm, TR/TE = 3600ms/80ms, ETL = 15, BW = ± 15.63 kHz, NEX = 1. A portion of k-space at the center was fully-sampled to generate the low-resolution auto-calibration reference data and the rest of k-space was under-sampled as described previously. The under-sampled data achieved in this manner were reconstructed by iterative SWT thresholding using coil sensitivity profiles computed from the auto-calibration reference data. For comparison, the under-sampled data were also reconstructed by the POCS-based *II-SPiRiT* (iterative self-consistent parallel imaging reconstruction) method described in [14] using the code provided by the authors. In order to draw conclusions with statistical significance and to eliminate possible dependence of the conclusions on the choice of the under-sampling pattern, the experiments were repeated with 15 independent random under-sampling patterns.

However, there are a few considerations that should be taken into account when under-sampling an echo train pulse sequence in practice. While under-sampled k-space data can be acquired by reducing the echo train length (ETL), this may not reduce the acquisition time since longitudinal recovery requires a minimum time interval between successive excitations. On the other hand, under-sampling by maintaining the ETL requires that the total number of phase-encode lines to be evenly divisible by the ETL since acquisition of a partial echo train is not practical. Nevertheless, in this article we follow the conventional evaluation approach of acquiring fully-sampled k-space data, which are then under-sampled by assuming a specific under-sampling factor.

All the algorithms were implemented in MATLAB (MathWorks, Inc., Natick, MA). In all the experiments, reconstruction quality was measured in terms of the normalized root mean square error (NRMSE) with respect to the fully-sampled data. The statistical significance of the findings was evaluated by paired comparisons of the NRMSE values based on paired t-tests under the null hypothesis that the mean NRMSE of the second reconstruction in each pair is smaller than or equal to that of the first one. Since several such t-tests were performed, the comparisons were corrected by the Bonferroni correction where each individual hypothesis is tested at a statistical significance level of α/n to

achieve the desired significance level of α for the whole set of experiments, where n is the total number of tests. In this thesis we used $\alpha = 0.05$.

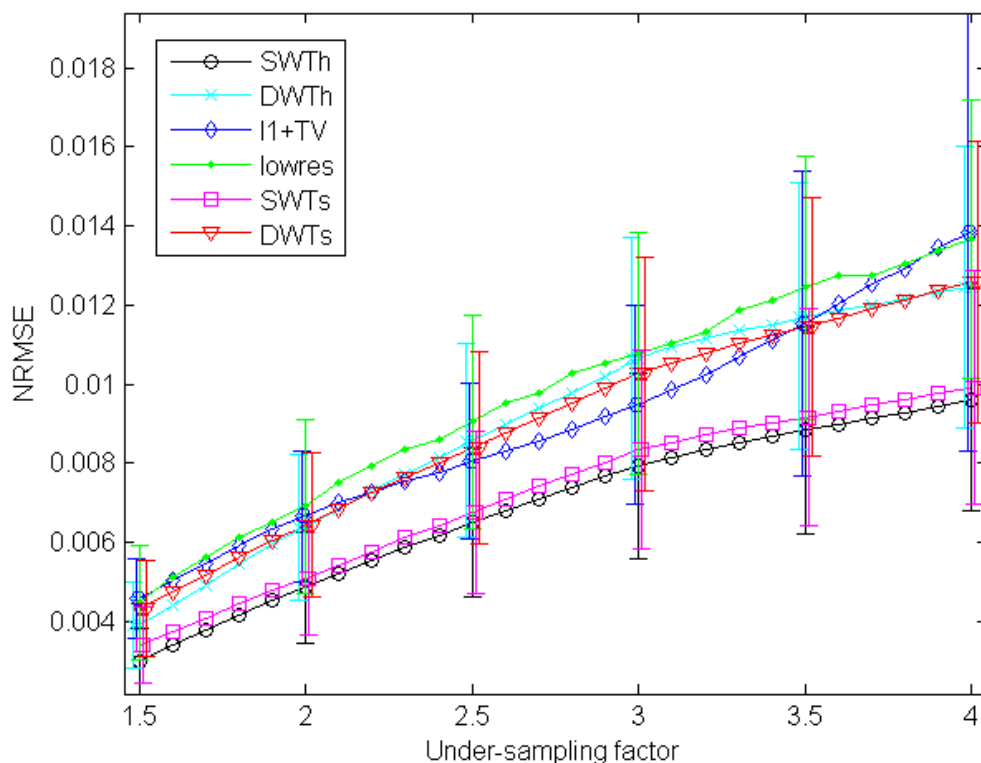


Figure 2.1- Mean NRMSE values with the corresponding error bars of one standard deviation for the reconstruction of 15 different SPGR images from under-sampled k-space data with the same under-sampling pattern. For clarity, the error bars are shown at increments of 0.5. However, the growth in the error bars follows a consistent trend.

2.4 Results

Figure 2.1 shows the mean NRMSE and the corresponding error bars of one standard deviation for the reconstruction of 15 SPGR images with the same k-space under-sampling. Reconstructions by SWT hard and soft thresholding (SWTh and SWTs respectively) are compared with the reconstructions by DWT hard and soft thresholding (DWTh and DWTs respectively) as well as the reconstructions by l1+TV norm optimization (l1+TV) and the low-resolution (lowres) reconstructions. The mean and

95% confidence interval of the paired NRMSE differences are shown in Table 2.3.

Negative NRMSE difference means and confidence intervals that do not include zero indicate that the first method produced lower reconstruction errors than the second one. After the Bonferroni correction all entries were significant except for the two denoted by asterisks.

The results indicate that SWT soft/hard thresholding significantly improves the reconstruction quality, measured in terms of NRMSE, compared to DWT soft/hard thresholding. Furthermore, SWTh results in lower NRMSE values compared to SWTs. Also, SWTh results in lower NRMSE values compared to the l1+TV and lowres reconstructions. The same trend is seen for SWTs with the exception that no statistical significance is observed at the intermediate under-sampling factors for comparison with l1+TV (p-values in the order of 5×10^{-3} at these under-sampling factors, which are insignificant after the Bonferroni correction).

(x10 ⁻⁴)						
U.F.	1.5	2	2.5	3	3.5	4
SWTh-	-9.0e-4 ±	-1.5e-3 ±	-2.1e-3 ± 3.4e-	-2.7e-3 ± 4.2e-	-2.9e-3 ±	-2.9e-3 ±
DWTh	1.4e-4	2.5e-4	4	4	4.6e-4	4.5e-4
SWTs-	-9.2e-4 ±	-1.3e-3 ±	-1.6e-3 ± 2.6e-	-1.9e-3 ± 2.9e-	-2.3e-3 ±	-2.7e-3 ±
DWTs	1.4e-4	2.1e-4	4	4	3.4e-4	3.8e-4
SWTh-SWTs	-4.1e-4 ±	-2.4e-4 ±	-2.7e-4 ± 1.2e-	-4.1e-4 ± 1.2e-	-3.3e-4 ±	-3.1e-4 ±
	8.8e-5	5.3e-5	4	4	1.1e-4	1.2e-4
SWTh-	-1.6e-3 ±	-1.8e-3 ±	-1.5e-3 ± 7.8e-	-1.5e-3 ± 8.3e-	-2.7e-3 ±	-4.3e-3 ±
l1+TV	4.0e-4	7.7e-4	4	4	1.4e-3	2.2e-3
SWTs-	-1.2e-3 ±	-1.6e-3 ±	-1.3e-3 ± 8.1e-	-1.1e-3 ± 8.2e-	-2.4e-3 ±	-4.0e-3 ±
l1+TV	4.2e-4	7.8e-4	4*	4*	1.4e-3	2.2e-3
SWTh-	-1.5e-3 ±	-2.1e-3 ±	-2.6e-3 ± 5.9e-	-2.8e-3 ± 5.5e-	-3.6e-3 -5.5e-	-4.1e-3 -5.3e-
lowres	4.9e-4	5.8e-4	4	4	4	4
SWTs-	-1.1e-3 ±	-1.8e-3 ±	-2.3e-3 ± 5.2e-	-2.4e-3 ± 4.8e-	-3.3e-3 ±	-3.8e-3 ±
lowres	4.9e-4	5.9e-4	4	4	4.9e-4	4.8e-4

Table 2.3- Mean and the 95% confidence interval of the paired NRMSE differences (i.e., the NRMSE of the second reconstruction in each pair subtracted from that of the first) for the reconstruction of 15 different SPGR images. All the findings in this table are statistically significant under the Bonferroni correction, except those denoted by an asterisk (*).

* No statistical significance after the Bonferroni correction.

Figure 2.2 shows the mean NRMSE values along with the corresponding error bars for the reconstruction of a SPGR image from 15 sets of independently under-sampled k-space data. The mean and the 95% confidence interval of the paired NRMSE differences are shown in Table 2.4. Similar to the previous set of experiments, negative NRMSE difference means and confidence intervals that do not include zero indicate that the first method produced lower reconstruction errors than the second one. Furthermore, after the Bonferroni correction all entries were significant.

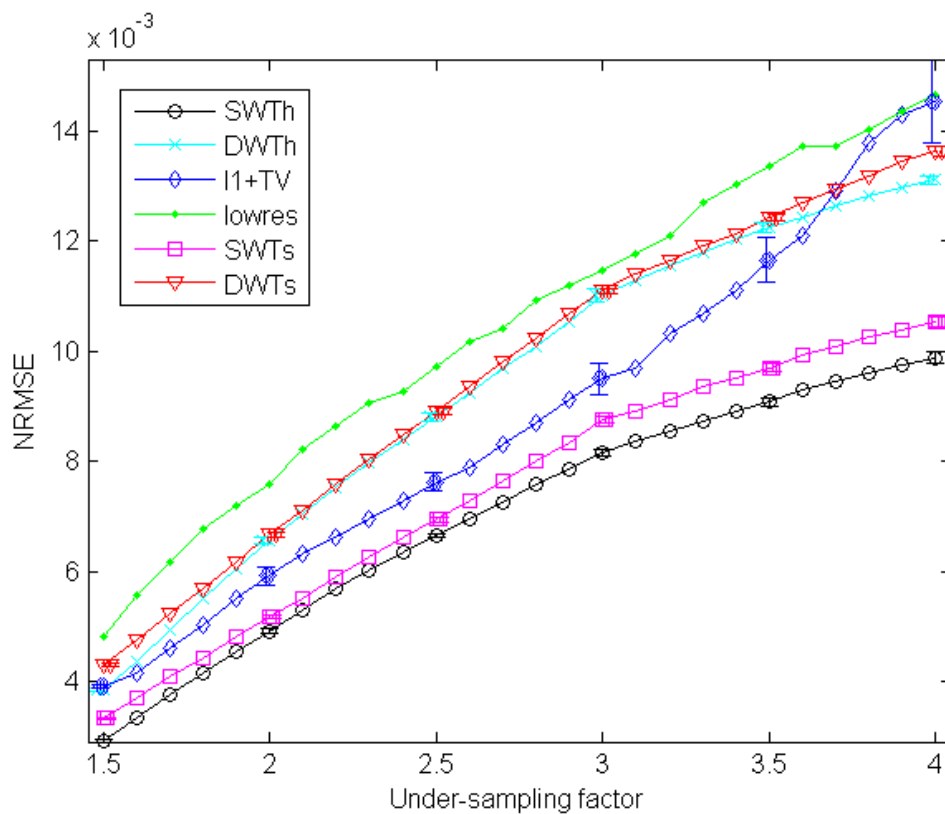


Figure 2.2.- Mean NRMSE values with the corresponding error bars of one standard deviation for the reconstruction of a SPGR image from 15 sets of independently under-sampled k-space data. For clarity, the error bars are shown at increments of 0.5. However, the growth in the error bars follows a consistent trend.

The findings are similar to the previous set of experiments in terms of the relative performance of the different reconstruction techniques. However, the variance in the

reconstruction error is much smaller than in the previous experiments. This indicates that the reconstruction methods are relatively insensitive to variations in the randomly generated under-sampling patterns.

UF	1.5	2	2.5	3	3.5	4
SWTh-DWTh	-9.2e-4 ± 1.9e-5	-1.6e-3 ± 3.0e-5	-2.1e-3 -4.2e-5	-2.9e-3 ± 7.8e-5	-3.2e-3 ± 5.3e-5	-3.2e-3 ± 6.3e-5
SWTs-DWTs	-9.7e-4 ± 9.7e-6	-1.5e-3 ± 1.9e-5	-2.0e-3 ± 2.9e-5	-2.3e-3 ± 3.6e-5	-2.7e-3 ± 5.4e-5	-3.1e-3 ± 6.5e-5
SWTh-SWTs	-4.1e-4 ± 1.3e-5	-2.6e-4 ± 3.7e-5	-2.9e-4 ± 2.9e-5	-6.0e-4 ± 5.2e-5	-6.1e-4 ± 5.1e-5	-6.5e-4 ± 6.1e-5
SWTh-l1+TV	-9.9e-4 ± 2.5e-5	-1.0e-3 ± 8.9e-5	-9.7e-4 ± 8.3e-5	-1.3e-3 ± 1.6e-4	-2.6e-3 ± 2.5e-4	-4.6e-3 ± 4.2e-4
SWTs-l1+TV	-5.8e-4 ± 2.1e-5	-7.4e-4 ± 8.0e-5	-6.8e-4 ± 9.3e-5	-7.5e-4 ± 1.5e-4	-2.0e-3 ± 2.3e-4	-4.0e-3 ± 4.3e-4

Table 2.4- Mean and the 95% confidence interval of the paired NRMSE differences (i.e., the NRMSE of the second reconstruction in each pair subtracted from that of the first) for the reconstruction of a SPGR image from 15 sets of independently under-sampled k-space data. All findings in this table are statistically significant after the Bonferroni correction.

Figure 2.3 provides a visual comparison of the different reconstructions of the SPGR data at an under-sampling factor of 4. Note the increased visual artifacts in the DWT reconstructions. Also, the l1+TV reconstruction results in over-smoothing of the image. The visual comparison of the images conforms to the NRMSE values.

Figure 2.4 shows the sum of squares (SOS) of the reconstructed under-sampled (under-sampling factor 6) multiple coil FSE data. Reconstruction by SWTh is compared to the l1SPIRiT reconstruction described in [14] and the low-resolution sampling with the same under-sampling factor. The progress of the reconstruction algorithms is shown in Figure 2.5 in terms of the normalized RMSE vs. iteration number. The plots indicate that SWTh stabilizes after fewer iterations than l1SPIRiT.

Although the images and NRMSE values of Figure 2.4 correspond to a specific under-sampling pattern, repeating the experiment with 15 independent random under-sampling patterns suggests that the SWTh reconstruction results in significantly lower NRMSE values than l1SPIRiT.

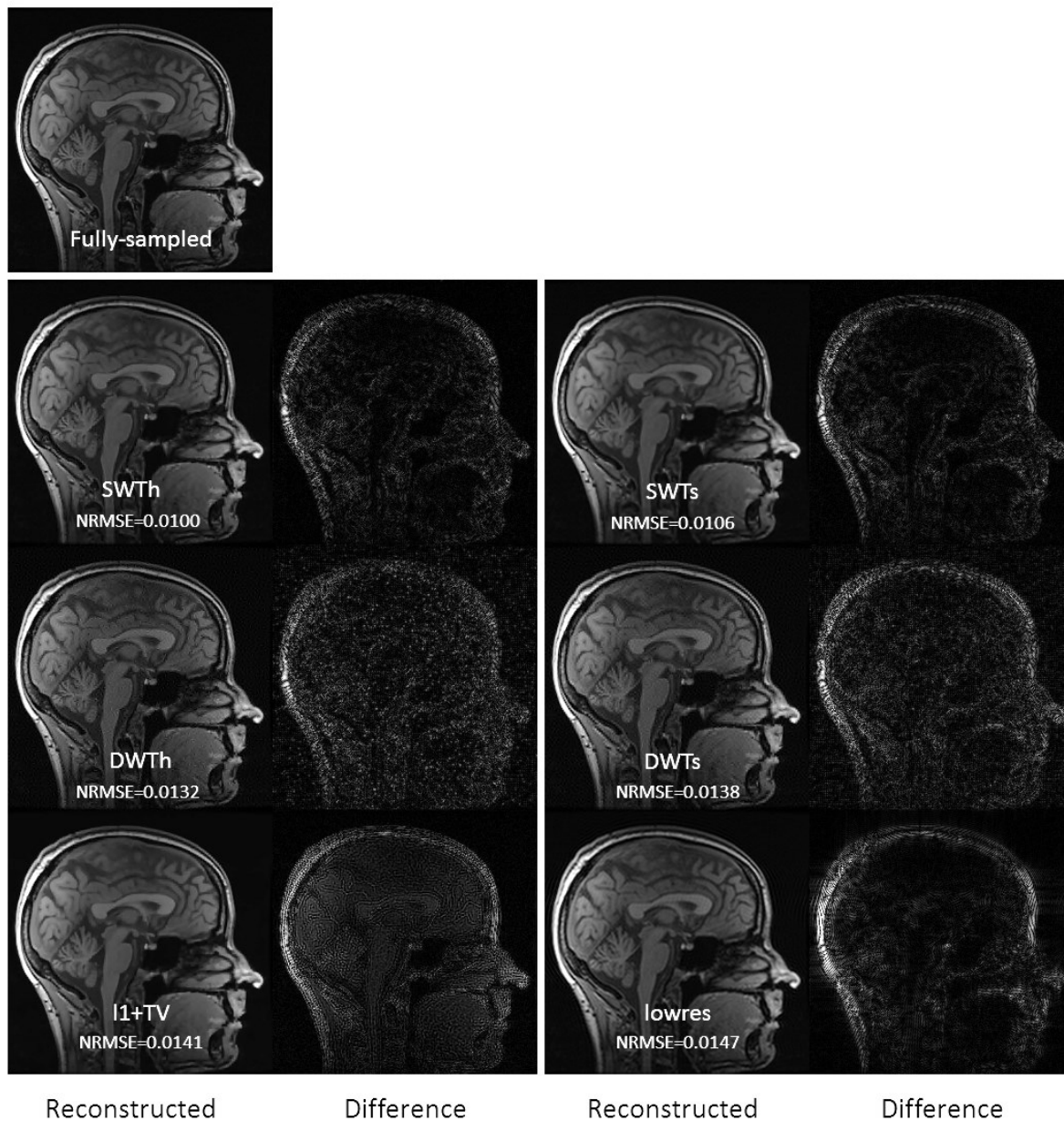


Figure 2.3- Visual comparison of different reconstructions of an under-sampled SPGR dataset. K-space data are randomly under-sampled in the two phase-encode directions by a factor of 4. The reconstructed images and the corresponding difference images with respect to the fully-sampled image are shown.

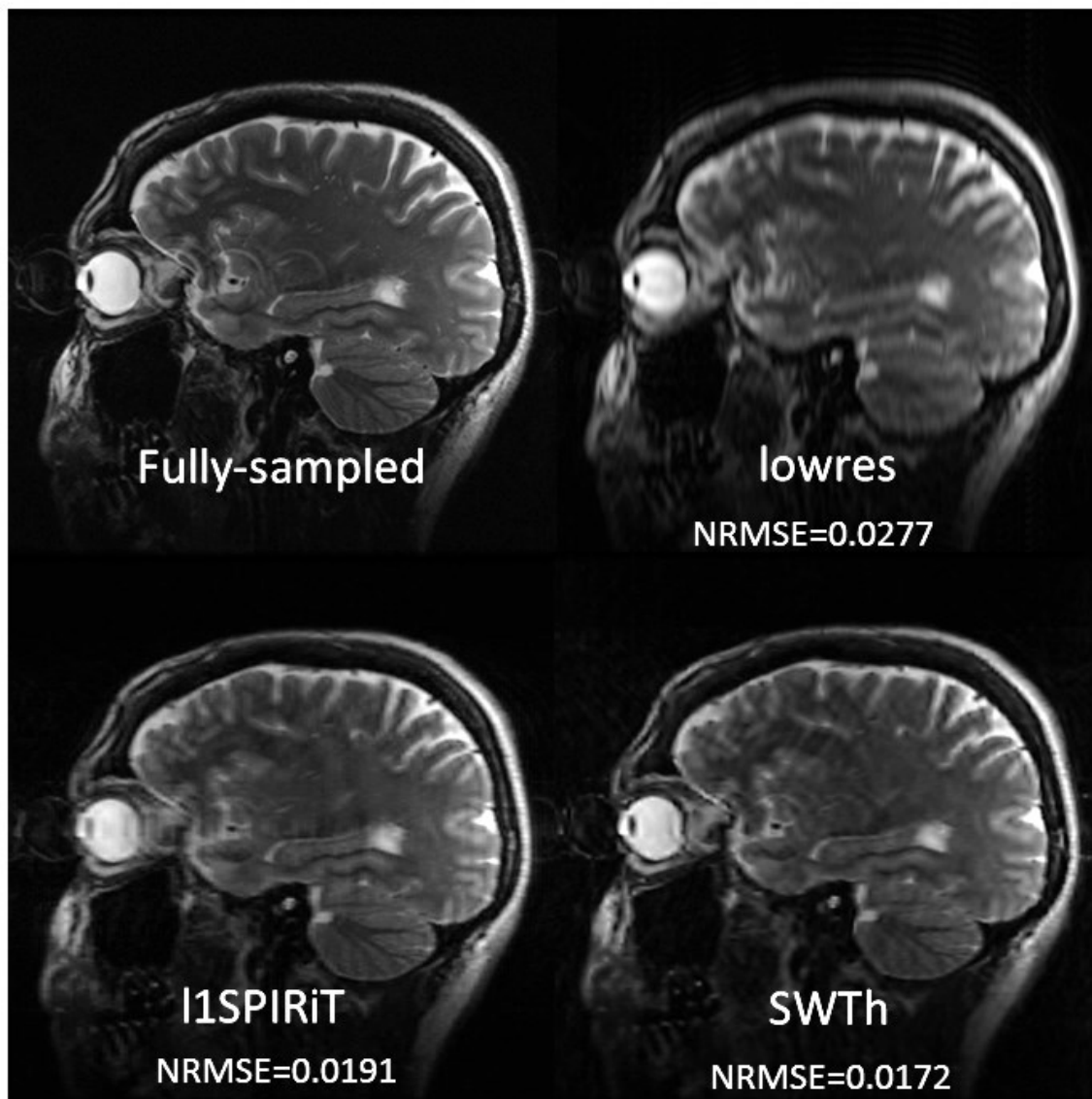


Figure 2.4- Sum of squares (SOS) of the reconstructed multiple coil data. The normalized root mean square errors (NRMSE) are computed with respect to the fully-sampled SOS after 40 iterations.

2.5 Discussion

The results show that iterative SWT thresholding significantly reduces the reconstruction error compared to iterative DWT thresholding and $l1+TV$ norm optimization.

Furthermore, we demonstrated that the non-convex hard SWT thresholding results in significantly lower reconstruction error values than the convex soft SWT thresholding at all the under-sampling factors. This suggests that use of other non-convex enforcers iteratively could improve the reconstruction quality.

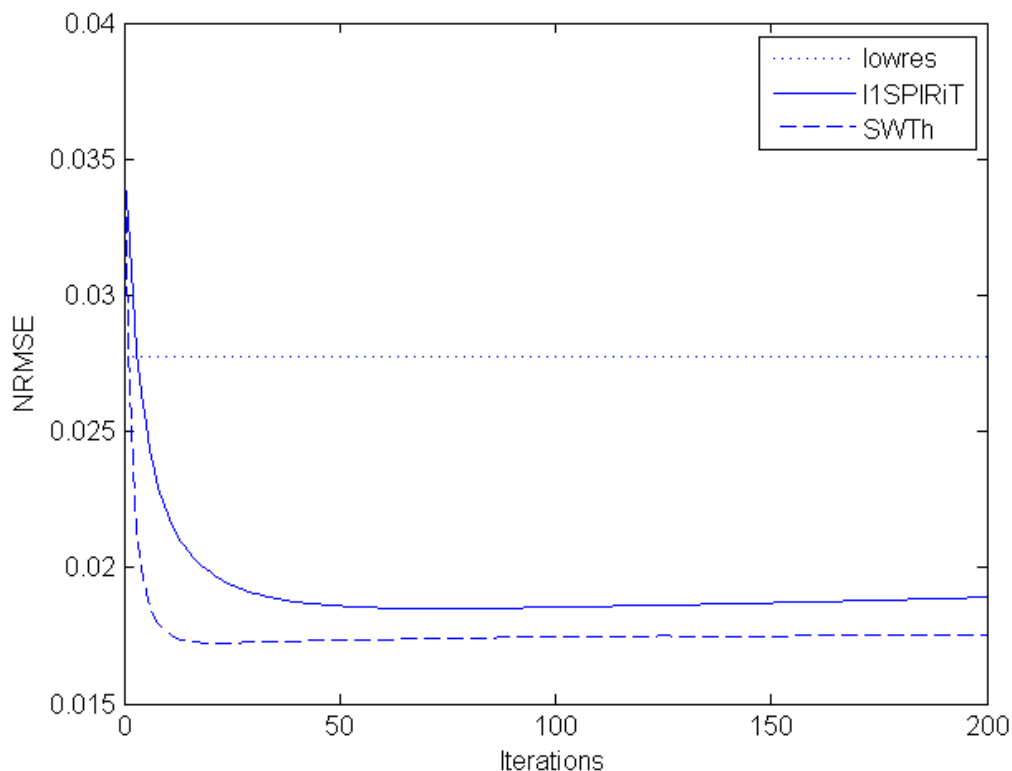


Figure 2.5- Normalized RMSE vs. iteration number for the reconstruction of the under-sampled 32-channel brain data. The proposed iterative SWT thresholding reconstruction is compared with l1SPIRiT at under-sampling factor of 6.

As noted, reconstruction by soft thresholding consists of iterative projections onto convex sets, for which convergence to a point in the intersection of those convex sets is guaranteed [15]. While convergence is not guaranteed for SWT hard reconstruction, my observations indicate that the reconstruction stabilizes to an acceptable solution after a reasonable number of iterations. In practice, the reconstruction algorithm may be terminated after a certain number of iterations.

2.6 Conclusion

I demonstrated an iterative stationary wavelet transform (SWT) thresholding algorithm for the reconstruction of under-sampled k-space data based on the wavelet sparsity of MR images and coil sensitivity profiles in case of multiple coil acquisitions. In addition to developing a reconstruction algorithm based on the translation-invariant SWT thresholding, we explored the effects of both hard and soft thresholding.

Iterative SWT reconstruction was compared with the iterative DWT reconstruction as well as the reconstruction by $l_1 + TV$ norm minimization and low-resolution sampling. Iterative SWT reconstruction of multiple coil data was compared with l_1 SPIRiT reconstruction. The experiments were performed on *in vivo* brain data. The results show that both hard and soft SWT thresholding result in significantly better reconstruction quality compared with DWT thresholding as well as the reconstruction by l_1+TV norm optimization and low-resolution sampling. Also, significantly better results were achieved by SWT thresholding compared to l_1 SPIRiT for multiple coil data reconstruction.

Since soft thresholding is a convex enforcer, the reconstruction through iterative soft thresholding is a projections onto convex sets (POCS) algorithm, guaranteeing convergence. Hard thresholding, being non-convex, has no such theoretical convergence guarantee, but we found that it stabilizes quickly and produces lower errors.

2.7 References

- [1] G. P. Nason and B. W. Silverman, "The Stationary Wavelet Transform and some Statistical Applications," in *Wavelets and Statistics*, A. Antoniadis and G. Oppenheim, Eds. Springer New York, 1995, pp. 281–299.
- [2] J. Pesquet, H. Krim, and H. Carfantan, "Time-invariant orthonormal wavelet representations," *Ieee Trans. Signal Process.*, vol. 44, no. 8, pp. 1964–1970, 1996.
- [3] M. Lustig, D. Donoho, and J. M. Pauly, "Sparse MRI: The application of compressed sensing for rapid MR imaging," *Magn. Reson. Med.*, vol. 58, no. 6, pp. 1182–1195, Dec. 2007.

- [4] M. Lustig, D. L. Donoho, J. M. Santos, and J. M. Pauly, "Compressed Sensing MRI," *Ieee Signal Process. Mag.*, vol. 25, no. 2, pp. 72–82, Mar. 2008.
- [5] D. J. Larkman and R. G. Nunes, "Parallel magnetic resonance imaging," *Phys. Med. Biol.*, vol. 52, no. 7, pp. R15–55, Apr. 2007.
- [6] R. R. Coifman and D. L. Donoho, "Translation-invariant de-noising," *Wavelets Stat. Springer Lect. Notes Stat.*, vol. 103, pp. 125–150, 1995.
- [7] I. Daubechies, M. Defrise, and C. De Mol, "An iterative thresholding algorithm for linear inverse problems with a sparsity constraint," *Commun. Pure Appl. Math.*, vol. 57, no. 11, pp. 1413–1457, Nov. 2004.
- [8] A. Papoulis, "A new algorithm in spectral analysis and band-limited extrapolation," *Circuits Syst. Ieee Trans.*, vol. 22, no. 9, pp. 735–742, 1975.
- [9] A. B. Cheryauka, J. N. Lee, A. A. Samsonov, M. Defrise, and G. T. Gullberg, "MRI diffusion tensor reconstruction with PROPELLER data acquisition," *Magn. Reson. Imaging*, vol. 22, no. 2, pp. 139–148, Feb. 2004.
- [10] C. I. Haupt, N. Schuff, M. W. Weiner, and A. A. Maudsley, "Removal of lipid artifacts in 1H spectroscopic imaging by data extrapolation," *Magn. Reson. Med. Off. J. Soc. Magn. Reson. Med. Soc. Magn. Reson. Med.*, vol. 35, no. 5, pp. 678–687, May 1996.
- [11] S. K. Plevritis and A. Macovski, "Spectral extrapolation of spatially bounded images [MRI application]," *Med. Imaging Ieee Trans.*, vol. 14, no. 3, pp. 487–497, Sep. 1995.
- [12] E. J. Candes and M. B. Wakin, "An Introduction To Compressive Sampling," *Signal Process. Mag. Ieee*, vol. 25, no. 2, pp. 21–30, 2008.
- [13] A. A. Samsonov, E. G. Kholmovski, D. L. Parker, and C. R. Johnson, "POCSense: POCS-based reconstruction for sensitivity encoded magnetic resonance imaging," *Magn. Reson. Med.*, vol. 52, no. 6, pp. 1397–1406, 2004.
- [14] M. Lustig and J. M. Pauly, "SPIRiT: Iterative self-consistent parallel imaging reconstruction from arbitrary k-space," *Magn. Reson. Med.*, vol. 64, no. 2, pp. 457–471, 2010.
- [15] L. G. Gubin, B. T. Polyak, and E. V. Raik, "The method of projections for finding the common point of convex sets," *Ussr Comput. Math. Math. Phys.*, vol. 7, no. 6, pp. 1–24, 1967.

3 Stationary wavelet transform for under-sampled MRI reconstruction

In addition to coil sensitivity data ([Parallel imaging](#)), sparsity constraints are often used as an additional l_p -penalty for under-sampled MRI reconstruction ([Compressed sensing](#)). Penalizing the traditional decimated wavelet transform (DWT) coefficients, however, results in visual pseudo-Gibbs artifacts, some of which are attributed to the lack of translation invariance of the wavelet basis. I show that these artifacts can be greatly reduced by penalizing the translation-invariant stationary wavelet transform (SWT) coefficients. This holds with various additional reconstruction constraints, including coil sensitivity profiles and total variation. Additionally, SWT reconstructions result in lower error values and faster convergence compared to DWT. These concepts are illustrated with extensive experiments on *in vivo* MRI data with particular emphasis on multiple-channel acquisitions.

3.1 Introduction

Cost considerations and patient comfort limit the total acceptable acquisition time in magnetic resonance imaging (MRI). On the other hand, it is necessary to acquire high-resolution images with high signal-to-noise ratio (SNR) for some applications. However, the SNR in MRI is proportional to the voxel volume and the square root of the acquisition time [1], which implies that high resolution and SNR are only achieved at the expense of long acquisition times. This in turn limits the number of pulse sequences that can be run in a clinical examination, which consequently limits the information that can be obtained. Therefore, there has been a strong motivation to reduce the acquisition time without compromising the resolution or the SNR of the MR images, since the introduction of this modality.

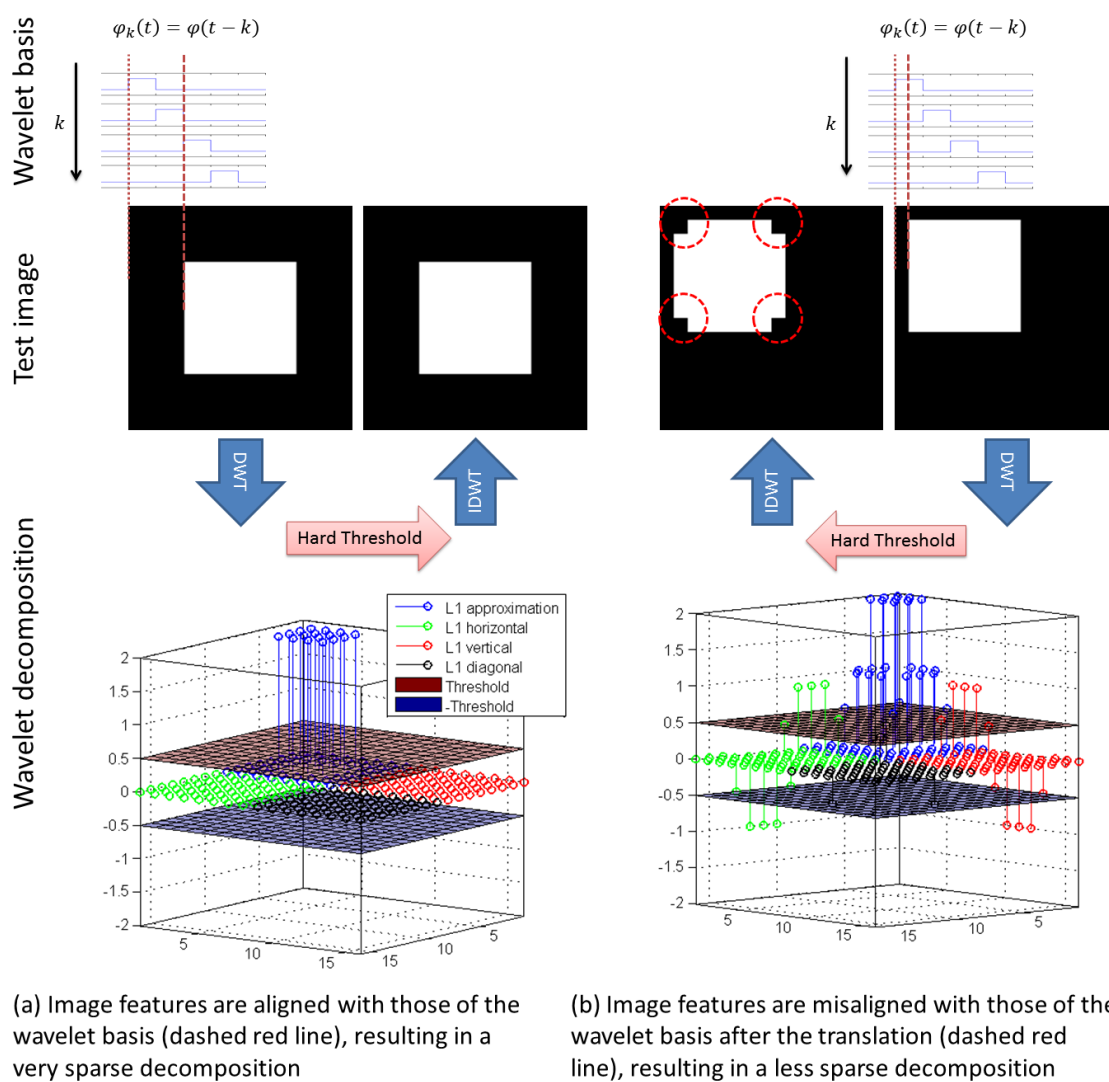


Figure 3.1-Illustration of the lack of translation invariance of DWT and the resulting thresholding artifacts: A simple test image- an 8x8 square in the middle of a 16x16 black background (a) and a shifted version of it (b) are decomposed with the Haar wavelet to 1 level. The original image is deliberately chosen to align with the wavelet basis, resulting in a very sparse decomposition. The shift, however, results in a misalignment between the image features and those of the wavelet basis functions, which, consequently, results in noticeable loss of the sparsity of the decomposition. In each case, the decomposition coefficients are hard thresholded and a wavelet reconstruction (IDWT) is performed on the thresholded coefficients. Dashed circles highlight the reconstruction artifacts.

In addition to [Parallel imaging](#) techniques [2]–[4], another approach to improving the trade-off between the acquisition time and the resolution is the acquisition of under-sampled k-space data and the use of the sparsity of the image in a transform domain, as an *a priori* reconstruction constraint, to interpolate the missing data. This approach is commonly referred to as [Compressed sensing](#) or compressive sampling (CS) [5]–[8] and can be used in conjunction with parallel imaging [9].

Wavelet sparsity is commonly used as a reconstruction constraint in compressed sensing and sparse recovery applications. Conventionally, a weighted l_p -penalty on the decimated wavelet transform (DWT⁸) coefficients is used as a regularization term and the reconstruction problem is generally formulated as a constrained optimization- see [6]–[8], [10] and references therein.

It is well established in thresholding-based denoising that thresholding with the traditional DWT often results in pseudo-Gibbs artifacts, which are connected to the misalignment between the image features and the features of the wavelet basis [11]. For example, in [Figure 3.1](#) a shift in the image results in misalignment between the image features and those of the wavelet basis after the shift ([Figure 3.1\(b\)](#)), which consequently results in a less sparse wavelet decomposition than the original image where the image features are deliberately chosen to match those of the wavelet basis ([Figure 3.1\(a\)](#)). Note that the shift does not change the energy of signal but after the shift the energy is spread over more [smaller] coefficients. A sparse decomposition is desirable in denoising as well as in sparse recovery applications since it allows the original features of the image to be distinguished from the noise or under-sampling artifacts (and therefore enabling us to efficiently remove noise/artifacts, e.g., by thresholding) [7], [11]. This is pictorially shown in [Figure 3.1](#) where thresholding results in visual reconstruction artifacts in

⁸ DWT is also used to abbreviate *discrete wavelet transform*. Since in this article we are essentially considering discrete cases only, any mention of the wavelet transform refers to the discrete wavelet transform (either decimated or undecimated). We use the abbreviation DWT to distinguish the decimated [discrete] wavelet transform from its undecimated version, i.e., SWT.

Figure 3.1(b) due to the removal of a number of wavelet coefficients that fall below the threshold in the less sparse representation. (Obviously, in this example one can avoid the artifacts by choosing a smaller threshold that maintains all the coefficients, but in practice a too small threshold fails to remove the noise/artifacts resulting in poor denoising/reconstruction. In this example the threshold is chosen to be 1/4 of the largest coefficient, for the sake of illustration.) The effect of the choice of the threshold in practice is more thoroughly investigated in the Results section.

One could possibly avoid the misalignment between the image features and those of the wavelet basis by shifting the image or the basis functions to make them aligned. However, this requires *a priori* knowledge of the best aligning shift. Furthermore, when the image contains several discontinuities, there may not be a single shift that works for all the discontinuities- the best shift for one may be the worst for the other. Consequently, Coifman and Donoho proposed the idea of “translation-invariant denoising,” i.e., average[shift-denoise-unshift] for several (or all possible) shifts [11]. This, in practice, is often achieved by stationary wavelet transform (SWT) thresholding, which provides a translation-invariant basis [12], [13]. For the sake of completeness, a brief description of SWT based on [12] follows. For simplicity, let us consider the 1D discrete case only- extension to 2D is straight forward.

DWT decomposition of a signal $x(t)$ results in the scaling (approximation) and wavelet (detail) coefficients:

$$c_j^k = \langle x(t), 2^{-j/2} \varphi\left(\frac{t}{2^j} - k\right) \rangle \quad (3.1)$$

$$d_j^k = \langle x(t), 2^{-j/2} \psi\left(\frac{t}{2^j} - k\right) \rangle \quad (3.2)$$

where $\varphi(t)$, and $\psi(t)$, are the scaling and wavelet functions, respectively, and j and k amount to the scaling and translation of the wavelet basis, respectively.

For SWT, a redundant decomposition can be obtained as,

$$\tilde{c}_{2^j}^{2^j k+p} = \langle x(t), 2^{-j/2} \varphi\left(\frac{t-p}{2^j} - k\right) \rangle \quad (3.3)$$

$$\tilde{d}_{2^j}^{2^j k+p} = \langle x(t), 2^{-j/2} \psi\left(\frac{t-p}{2^j} - k\right) \rangle \quad (3.4)$$

where $p \in \{0, \dots, 2^j - 1\}$ allows for all the possible shifts in a discrete setting.

For decomposition to j_m levels, 2^{j_m} different orthogonal bases can be generated. The different possible choices can be illustrated by a binary tree in the form of [Figure 3.2](#). Each node in this tree is indexed by parameters (j, p) , to which the set of coefficients $\{\tilde{c}_{2^j}^{2^j k+p}\}_{k \in \mathbb{Z}}$ is associated. Each path from the root of the tree to a leaf corresponds to the set of functions $\{2^{-j/2} \psi[(t - p_j)/2^j - k], k \in \mathbb{Z}, 1 \leq j \leq j_m\} \cup \{2^{-j_m/2} \varphi[(t - p_{j_m})/2^{j_m} - k], k \in \mathbb{Z}\}$, which forms an orthogonal wavelet basis, resulting in a standard wavelet reconstruction. The inverse SWT is often defined as the average of all the 2^{j_m} different reconstructions obtained in this manner.

While SWT is predominantly used in denoising, to the best of my knowledge, the use of SWT in compressed sensing and sparse recovery applications, particularly in under-sampled MRI reconstruction, has not been explored before. The key idea here is that the l_p -penalty on the DWT coefficients may essentially result in the same sort of artifacts described above, which can be avoided or reduced by penalizing the SWT coefficients.

The intent of this chapter is to call attention to the benefits of the use of SWT in place of DWT for compressed sensing and sparse recovery, with particular focus on MRI reconstruction from under-sampled k-space data. Although use of SWT for such applications may seem counter intuitive, since it is a redundant transform, it is shown that significant improvement in reconstruction quality is achieved by replacing the l_p -penalty on the DWT coefficients with one on the SWT coefficients. This holds even with additional constraints, including total variation (TV) penalties or coil sensitivity constraints when compressed sensing is combined with parallel imaging.

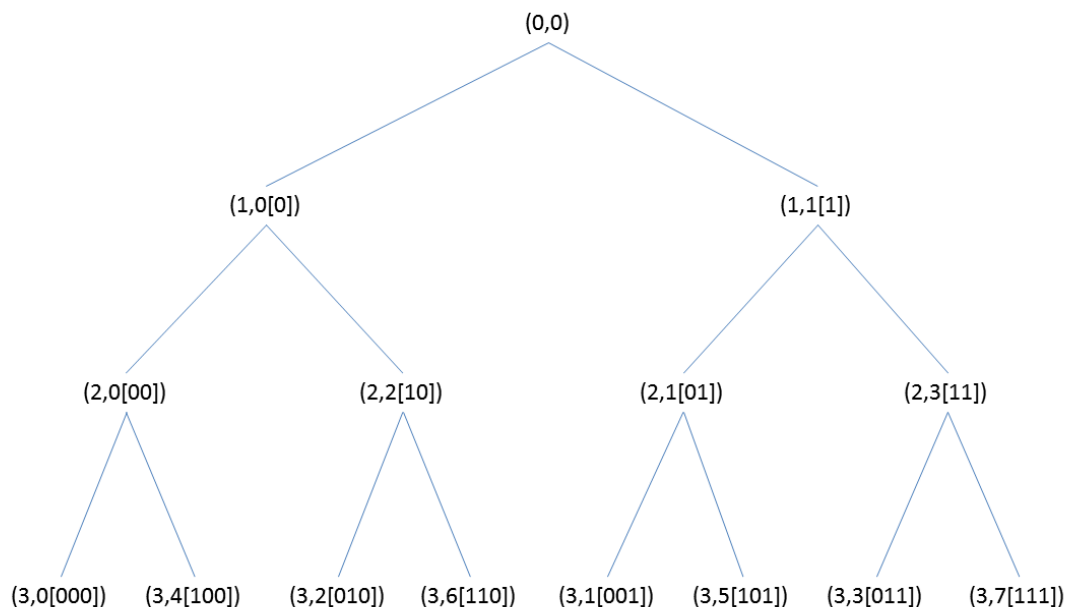


Figure 3.2- Shift-localization tree for a three level stationary wavelet transform (SWT) decomposition. Each node is indexed by parameters (j, p) , where j is the decomposition level and p is the shift. For clarity, the binary representation of p is shown in brackets.

Furthermore, a few authors have recently reported the use of DWT with random shifts [14] to address the DWT translation variance problem for compressed sensing and sparse recovery applications [15], [16]. In this chapter, use of random shifts with decimated wavelet transform will also be considered in comparison with the conventional decimated wavelet transform as well as its undecimated version, i.e., SWT.

In addition to reduced visual artifacts, SWT results in significantly lower reconstruction errors as well as faster convergence. Furthermore, despite its redundancy, it can be computed rapidly- in $n \log(n)$ time [11].

All these concepts are illustrated by extensive experiments with different reconstruction techniques, all of which are reproducible using the supplementary code provided with this thesis or the code supplied by the authors cited in this thesis.

3.2 Stationary wavelet transform sparse recovery

In the discussion that follows we perform a point spread function (PSF)⁹ analysis to demonstrate the advantage of SWT thresholding over DWT thresholding for removing under-sampling aliasing artifacts. A computational experiment with the Shepp-Logan phantom is also presented to illustrate the visual artifacts in the DWT reconstruction compared with those in the SWT reconstruction.

Let $f(m, n) = \delta(m, n)$ be an impulse input in the spatial domain, where $\delta(m, n) = \begin{cases} 1 & m = 0, n = 0 \\ 0 & \text{otherwise} \end{cases}$. Transforming f to the Fourier domain, under-sampling, and transforming back to the spatial domain results in the k-space under-sampling PSF, f_u (Figure 3.3):

$$f_u = \mathcal{F}^{-1}U_F\mathcal{F}f \quad (3.5)$$

where U_F is the Fourier (k-space) under-sampling operation and \mathcal{F} is the Fourier transform.

Now consider the wavelet decomposition of f_u using DWT and SWT: $C_{DWT} = \psi_{DWT}f_u$, and $C_{SWT} = \psi_{SWT}f_u$, where ψ_{DWT} and ψ_{SWT} are the decimated and stationary wavelet transforms, and C_{DWT} and C_{SWT} are the corresponding wavelet decomposition coefficients. Assume a thresholding operation, γ , acting on the decomposition coefficients: $\tilde{C}_{DWT} = \gamma(C_{DWT})$, and $\tilde{C}_{SWT} = \gamma(C_{SWT})$. The corresponding PSFs are computed by wavelet reconstruction of the thresholded coefficients: $\tilde{f}_{DWT} = \psi_{DWT}^*\tilde{C}_{DWT}$, and $\tilde{f}_{SWT} = \psi_{SWT}^*\tilde{C}_{SWT}$. Figure 3.3 shows the DWT and SWT soft thresholding PSFs. The same threshold, chosen using the Birgé-Massart strategy [17], is used with both DWT and SWT. (The choice of the threshold and its effect on the reconstruction is more thoroughly investigated in the Results section.)

⁹ A linear shift-invariant imaging system can completely be described in terms of its point spread function (PSF). Although thresholding is a non-linear operation, we still use the PSF for illustration/comparison of the artifacts.

Note that with the assumption of under-sampling in the phase-encode (k_y) direction only, the point spread functions can be sufficiently illustrated with 1D plots. An example of the reduction of the artifacts by SWT thresholding compared to DWT thresholding is highlighted. Several such reductions can be easily identified on the PSFs. As illustrated in Figure 3.3, SWT thresholding results in noticeably fewer artifacts than the corresponding DWT thresholding.

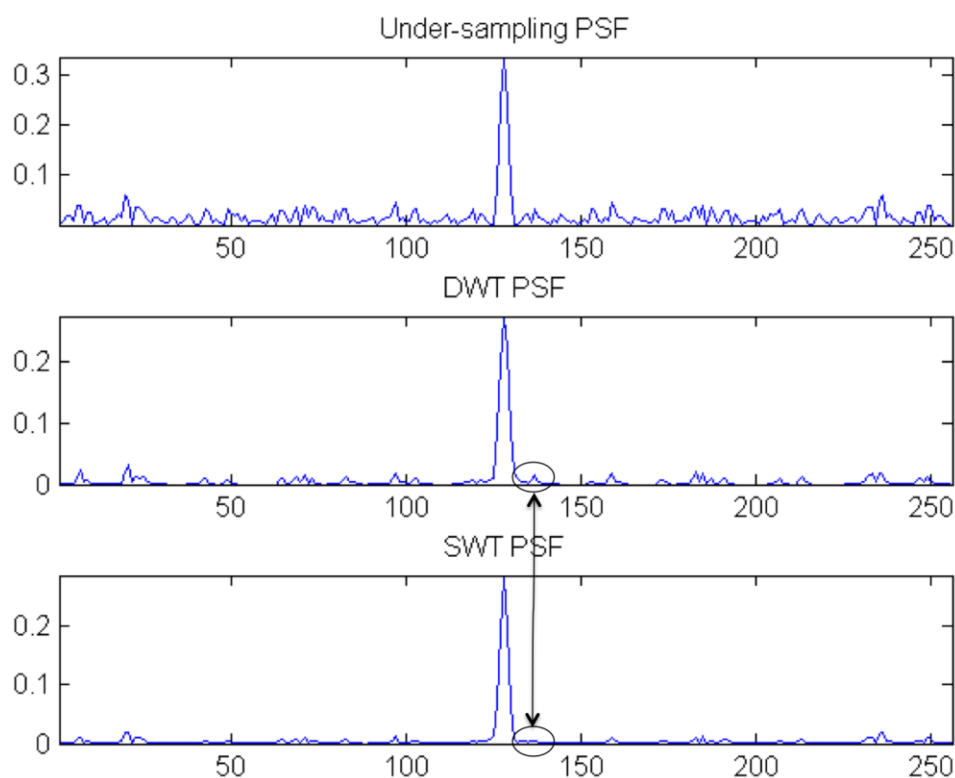


Figure 3.3- Point spread functions (PSF) resulting from k-space under-sampling followed by the application of DWT and SWT soft thresholding. An example of the reduction of the artifacts by SWT thresholding compared to DWT thresholding is highlighted.

Since the aliasing artifacts are effectively incoherent¹⁰, the signal-to-alias ratio, defined as the energy of the signal (i.e., the peak in this case) to the energy of the alias (i.e., the side-lobes in this case) of the PSFs, provides a quantitative means of comparing these PSFs with each other and with the under-sampling PSF (Table 3.1). The higher signal-to-alias ratio achieved by SWT thresholding also indicates less aliasing interference.

Signal-to-alias ratio	
Under-sampling PSF	0.506
DWT thresholding PSF	0.647
SWT thresholding PSF	0.912

Table 3.1- Signal-to-alias ratios corresponding to the point spread functions (PSF) in Figure 3.3.

In order to illustrate the nature of the artifacts associated with the DWT reconstruction, consider the computational experiment of reconstruction of the Shepp-Logan phantom (Figure 3.4a) from under-sampled frequency domain data. For the sake of illustration, and since Cartesian sampling is by far the most common way of acquiring k-space data in MRI, we assume Cartesian under-sampling in the y direction (corresponding to under-sampling in the phase-encode direction in an MRI application).

Figure 3.4(b,c) show the reconstruction of the under-sampled frequency domain data based on an l_1 penalized optimization, i.e., $\min_{f^*} \|\psi f^*\|_{l_1}$ s.t. $\|U_F \mathcal{F} f^* - F_u\|_{l_2} < \varepsilon$, where the reconstruction in Figure 3.4(b) is achieved when $\psi = \psi_{DWT}$ is a decimated wavelet transform and that of Figure 3.4(c) is achieved when $\psi = \psi_{SWT}$ is the corresponding stationary wavelet transform. Here f^* denotes the reconstructed image, \mathcal{F} the Fourier transform, U_F the under-sampling operation in the frequency domain, and F_u the acquired frequency data. As shown in Figure 3.4(b,c), most of the artifacts present in the DWT reconstruction are absent in the SWT reconstruction.

¹⁰ In compressed sensing, it is desired to have incoherent (noise-like) under-sampling artifacts so that they can be distinguished from the original signal/image features in the sparse domain [7]. The incoherence is often achieved through random under-sampling.

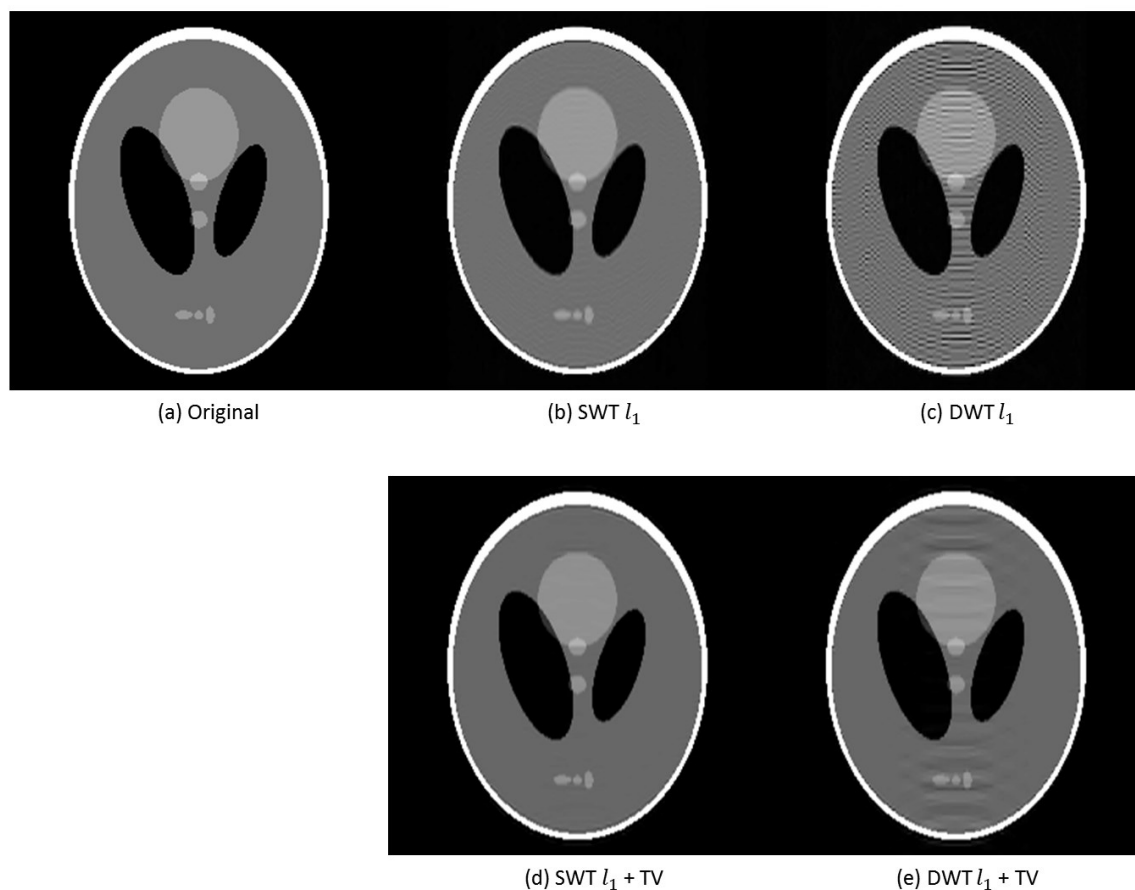


Figure 3.4- Reconstruction of the Shepp-Logan phantom from Cartesian under-sampled frequency data by DWT/SWT- l_1 (+TV) penalized optimization.

Furthermore, several authors have reported that it is often useful to include an additional total variation (TV) penalty in the reconstruction [7], [18]. Since all the previous works were based on penalizing the DWT coefficients, the TV term was needed to alleviate the associated artifacts. However, as illustrated by the above example, penalizing the SWT coefficients may reduce the need for the additional TV penalty. Nevertheless, as

illustrated in [Figure 3.4\(d,e\)](#) SWT is preferred over DWT with an additional TV penalty, i.e., $\min_{f^*} \|\psi f^*\|_{l_1} + \alpha TV(f^*)$ s.t. $\|U_F \mathcal{F} f^* - F_u\|_{l_2} < \varepsilon$, also¹¹.

3.3 Methods

Single channel spoiled gradient recalled (SPGR) data of a healthy volunteer were acquired at 3T using a GE scanner (Discovery 750, software revision 22M32, General Electric Healthcare, Waukesha, WI) with the following parameters: matrix: 256x256, resolution = 0.86mm isotropic, slice thickness = 1mm, TE/TR = 4.1ms/8.9ms, BW = ± 19.23 kHz, flip angle = 18°, NEX = 1. Human data used in this work were acquired using a protocol approved by the University Of Western Ontario Office Of Research Ethics.

k-space data were retrospectively under-sampled in the phase-encode direction and the under-sampled data were reconstructed by SWT $l_1 + TV$ penalized and DWT $l_1 + TV$ penalized optimization, i.e.,

$$\min_{f^*} \|\psi f^*\|_{l_1} + \alpha TV(f^*) \text{ s.t. } \|U_F \mathcal{F} f^* - F_u\|_{l_2} < \varepsilon \quad (3.6)$$

with $\psi = \psi_{SWT}$ and $\psi = \psi_{DWT}$, respectively. The optimization was performed using the code provided by Lustig for [7].

In practice it is expected to achieve the best under-sampled reconstruction performance by the combined application of compressed sensing and parallel imaging. Iterative thresholding reconstruction [10] can be modified to directly incorporate the coil sensitivity profiles.

The multiple-coil iterative thresholding reconstruction algorithm is shown in [Figure 3.5](#).

¹¹ It should be noted that the Shepp-Logan phantom heavily favors a TV penalty (perfect reconstruction has been demonstrated for the Shepp-Logan phantom with a TV penalty with radial under-sampling [5]). Such drastic improvement with an additional TV term may not be observed with real MR images though.

A flow chart of the multiple-coil reconstruction procedure is shown in Figure 3.5. In Step 1 the combined-channels image is modulated by the coil sensitivity profile of each channel in order to make the combined-channels estimate consistent with the coil data before the data projection in Step 2, which enforces the data consistency constraint for each channel by projecting the current estimate onto the corresponding coil data [19].

Multiple-coil iterative thresholding reconstruction algorithm

Inputs:

$F_{u,i}$: Under-sampled k-space data ($i = 1, \dots, N_c$, where N_c is the number of coils)

s_i : Coil sensitivities

U_F : Under-sampling operations selecting k-space data

Output:

F_i : Reconstructed k-space data

Algorithm:

```

// Initialize to the minimum energy reconstruction
for  $i \leftarrow 1:N_c$  do
     $F_i \leftarrow F_{u,i}$ 
end

//Reconstruct through iterative thresholding
while not converged do
//combine multiple channel data
 $f_{opt} \leftarrow \sum_{i=1}^{N_c} \omega_i \frac{f_i}{s_i}$  //where  $f_i = \mathcal{F}^{-1}F_i$  and  $\omega_i = \frac{s_i^2}{\sum_{j=1}^{N_c} s_j^2}$ 

//thresholding
 $\tilde{f} \leftarrow \Gamma(f_{opt})$  // where the nonlinear thresholding operation  $\Gamma$  is
defined as:  $\Gamma(f) = \psi^* \gamma(\psi f)$ , where  $\psi$  denotes wavelet transform and  $\gamma$  denotes
thresholding.

//data consistency
for  $i \leftarrow 1:N_c$  do
     $\tilde{F}_i \leftarrow \mathcal{F}(s_i \tilde{f})$ 
     $F_i \leftarrow \tilde{F}_i - U_F \tilde{F}_i + F_{u,i}$ 
end
end

```

Table 3.2- Multiple-coil iterative thresholding reconstruction algorithm. \mathcal{F} and Γ denote the Fourier transform and wavelet thresholding operations, respectively.

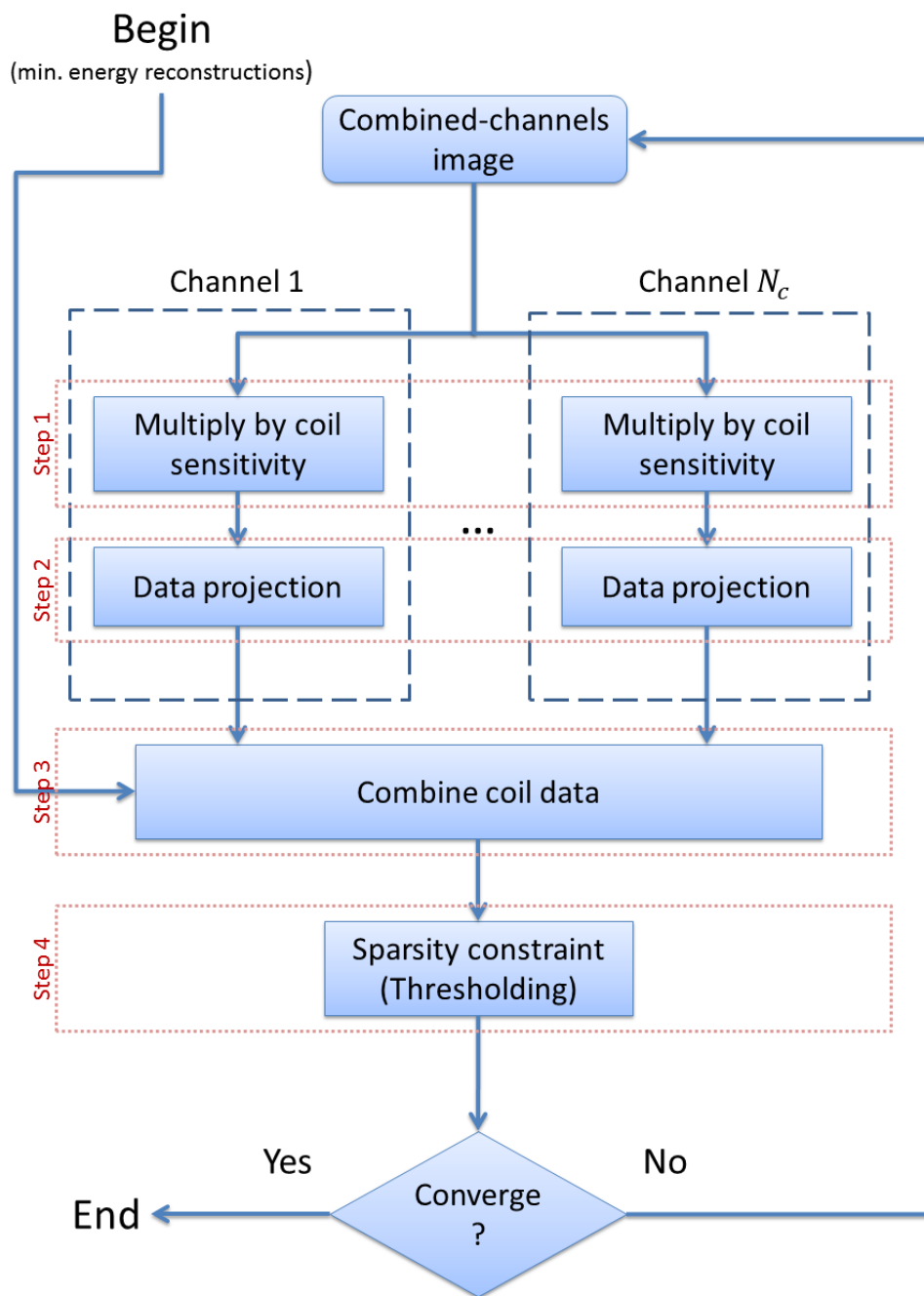


Figure 3.5- Flowchart of the multiple-coil iterative thresholding reconstruction algorithm

In Step 3 data from multiple channels are combined to obtain a combined-channels estimate image. If coil sensitivities are explicitly available, an optimal combination has been shown by Roemer to be [20]:

$$f_{opt} = \sum_{i=1}^{N_c} \omega_i \frac{f_i}{s_i} \quad \text{where } \omega_i = \frac{s_i^2}{\sum_{j=1}^{N_c} s_j^2} \quad (3.7)$$

where f_i is the image from the i th coil and s_i is the corresponding coil sensitivity profile. In practice, the coil sensitivities are commonly extracted from fully-sampled low-resolution reference data¹², which can be acquired prior to the main scan (pre-calibration) or integral to the main scan (auto-calibration) by fully sampling a region over the center of k-space [21]. We use the latter approach to estimate the coil sensitivities.

Finally, in Step 4, the sparsity constraint is enforced through a thresholding operation.

The approach to incorporating coil sensitivity data in the reconstruction algorithm is similar to the POCS-based parallel imaging reconstruction algorithm described by Samsonov et al [19]. Note that this approach does not impose any constraint on the k-space under-sampling pattern.

The multiple-coil reconstruction algorithm amounts to thresholded Landweber iterations, which has been proved to converge with soft thresholding by Daubechies [10]. Nevertheless, we also experimentally investigate reconstruction by hard thresholding to show the effectiveness of SWT with both soft and hard thresholding. Soft thresholding is

¹² A simple approach to computing the sensitivity profiles from reference data, which is commonly used in practice, is to divide each native coil image by the sum of squares [21].

defined as: $\gamma_{\mu}(x) = \begin{cases} x + \frac{\mu}{2} & \text{if } x \leq -\frac{\mu}{2} \\ 0 & \text{if } |x| < \frac{\mu}{2} \\ x - \frac{\mu}{2} & \text{if } x \geq \frac{\mu}{2} \end{cases}$, where μ is the threshold. Similarly, hard

thresholding is defines as: $\gamma_{\mu}(x) = \begin{cases} x & \text{if } x \leq -\frac{\mu}{2} \\ 0 & \text{if } |x| < \frac{\mu}{2} \\ x & \text{if } x \geq \frac{\mu}{2} \end{cases}$.

Brain images of a healthy volunteer were acquired at 3T using a 32-channel head coil with a fast spin echo (FSE) pulse sequence with the following parameters: matrix: 256x256, resolution = 1mm, slice thickness = 2mm, TR/TE = 3600ms/80ms, ETL = 15, BW = ± 15.63 kHz, NEX = 1. A portion of k-space at the center was fully sampled to generate the low-resolution auto-calibration data with the rest of k-space under-sampled with variable density in the phase-encode direction. K-space data were then reconstructed by the multiple-coil iterative thresholding reconstruction algorithm with SWT ($\Gamma = \Gamma_{SWT}$) and DWT ($\Gamma = \Gamma_{SWT}$). The experiments were repeated for a range of under-sampling factors from 2 to 6, each with 15 sets of random under-sampling patterns generated independently.

To further examine the applicability of SWT to multiple-coil reconstructions, the aforementioned under-sampled data were reconstructed by the *Iterative self-consistent parallel imaging reconstruction (SPIRiT)* reconstruction method described in [9], where the reconstruction problem is formulated as an optimization with calibration and DWT/SWT l_1 penalties, subject to consistency with the acquired data:

$$\min_{f^*} \|\psi f^*\|_{l_1} + \lambda \|(G - I)\mathcal{F}f^*\|_{l_2} \text{ s.t. } \|U_F \mathcal{F}f^* - F_u\|_{l_2} < \varepsilon \quad (3.8)$$

Where f^* is now the solution consisting of every and each individual coil. Similarly F_u consists of under-sampled data acquisition for all coils. G is the SPIRiT calibration operator and I is the unitary matrix. The difference between the SPIRiT calibration operator and that of the traditional GRAPPA [3] is that in SPIRiT the calibration operator is a “full” kernel independent of the under-sampling pattern, which is the same for all k-

space positions. For more details refer to [9]. Reconstruction was performed using the code provided by the authors with SWT, DWT, and DWT with random shifts (here after denoted DWTRS).

Reconstruction quality was measured in terms of the normalized root mean square error (NRMSE) with respect to the fully-sampled data. The statistical significance of the findings was evaluated by paired comparisons of the NRMSE values based on paired t-tests under the null hypothesis that the mean NRMSE of the DWT reconstruction in each pair is smaller than or equal to that of SWT. Since several such t-tests were performed, the comparisons were corrected by the Bonferroni correction with a significance level of $\alpha = 0.05$.

3.4 Results

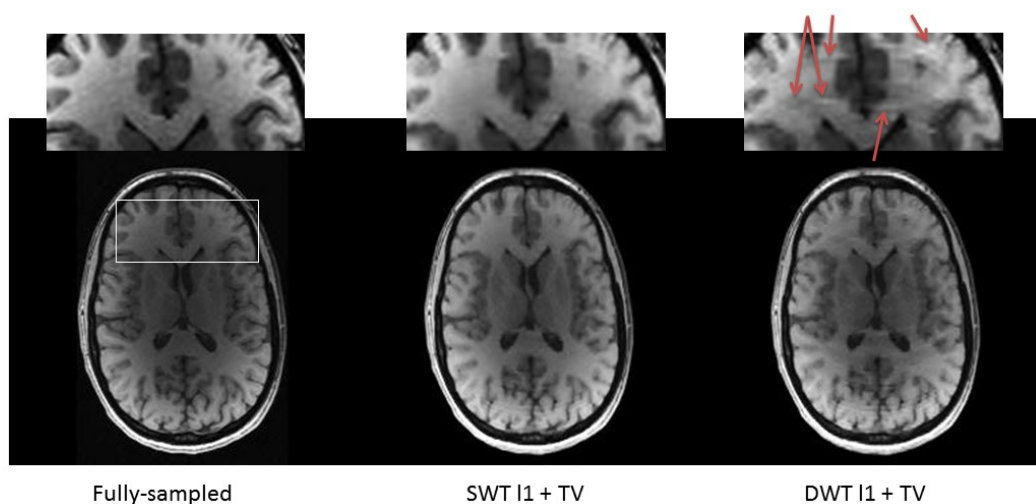


Figure 3.6- Reconstruction of under-sampled SGPR data (under-sampling factor 3) by $l_1 + TV$ penalized optimization. The arrows point examples of the artifacts present in the DWT reconstruction that are absent in the corresponding SWT reconstruction.

Figure 3.6 shows the reconstruction of the under-sampled SPGR data by SWT/DWT $l_1 + TV$ penalized optimization. The choice of the regularization parameter (α in equation 3.6) generally affects the reconstruction performance. In order to avoid the

possibility of giving SWT any advantage over DWT by a particular choice of α , a value optimized for the DWT reconstruction (suggested by Lustig et al in their code) was used for both reconstructions. The dependence of the SWT/DWT reconstructions on the regularization parameter is more thoroughly investigated in the next experiments. The images clearly illustrate DWT reconstruction artifacts (even with an additional TV penalty) that are absent in the SWT reconstruction.

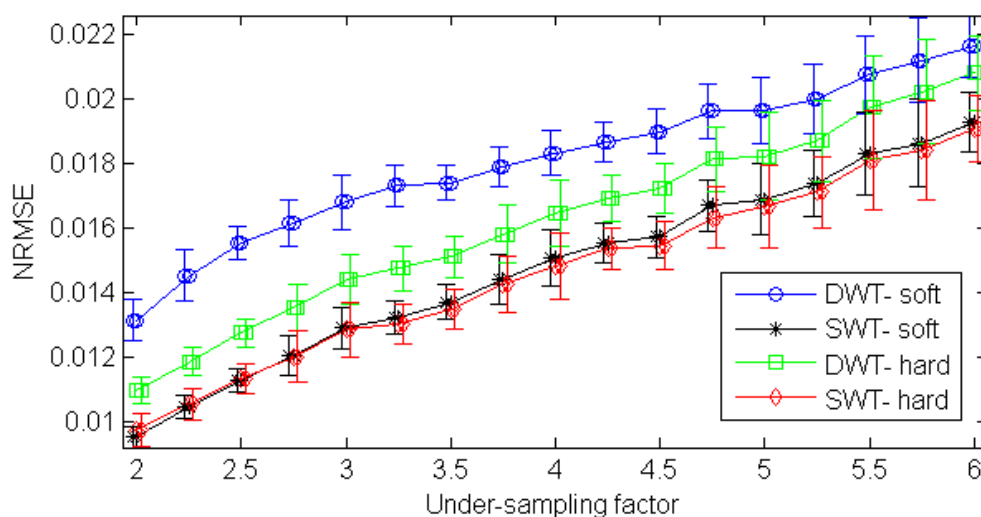


Figure 3.7- Mean NRMSE and the corresponding error bars of one standard deviation for the reconstruction of the under-sampled 32-channel FSE data by the multiple-coil iterative thresholding algorithm.

Figure 3.7 shows the results of the repeated experiments for the reconstruction of the under-sampled 32-channel FSE data by the multiple-coil iterative thresholding algorithm. Clearly, the SWT reconstructions resulted in lower mean error values than the corresponding DWT reconstructions. The mean and its 95% confidence interval of the paired NRMSE differences of the SWT and DWT reconstructions, i.e., $\text{NRMSE}_{\text{SWT}} - \text{NRMSE}_{\text{DWT}}$, for both hard and soft thresholding are shown in Table 3.3. Negative NRMSE difference means with confidence intervals that do not include zero indicate that SWT resulted in lower reconstruction errors than DWT for both soft and hard

thresholding. Furthermore, after the Bonferroni correction all the findings were significant.

NRMSE _{SWT} - NRMSE _{DWT} (x10 ⁻³)					
U.F.	2	3	4	5	6
Soft	-3.6(37%) ± 0.16	-3.9(30%) ± 0.22	-3.2(22%) ± 0.18	-2.7(16%) ± 0.17	-2.4(12%) ± 0.18
Hard	-1.2(13%) ± 0.12	-1.6(12%) ± 0.12	-1.6(11%) ± 0.24	-1.5(9%) ± 0.18	-1.7(9%) ± 0.16

Table 3.3- Mean and its 95% confidence interval of the paired NRMSE differences (i.e., NRMSE of the DWT reconstruction subtracted from that of the corresponding SWT reconstruction) for the reconstructions by the multiple-coil iterative thresholding algorithm with soft and hard thresholding for different under-sampling factors (U.F.). The numbers in brackets show the percentage of mean improvement with SWT over DWT. All findings in this table are statistically significant after the Bonferroni correction.

Figure 3.8 shows sample reconstructions by the multiple-coil iterative thresholding algorithm with SWT/DWT soft/hard thresholding. As illustrated in this figure, most of the artifacts in the DWT iterative soft/hard thresholding reconstruction are noticeably reduced in the corresponding SWT reconstructions.

The progress of the iterative reconstruction algorithms is shown in Figure 3.9. Not only do the SWT reconstructions result in lower reconstruction errors, the “over-convergence” effect¹³ in the DWT reconstructions, which results in an increase in the reconstruction error after a number of iterations before convergence, is not observed in the SWT reconstructions. This is more thoroughly investigated in Figure 3.10.

¹³ Over-convergence occurs when the optimum for the objective function being computed (in this case, the l_1 norm of the DWT coefficients) differs significantly from a desirable reference metric (such as the NRMSE between the reconstructed and fully-sampled images) often characterized by an initial, sharp decrease in the reference metric followed by a more gradual increase.

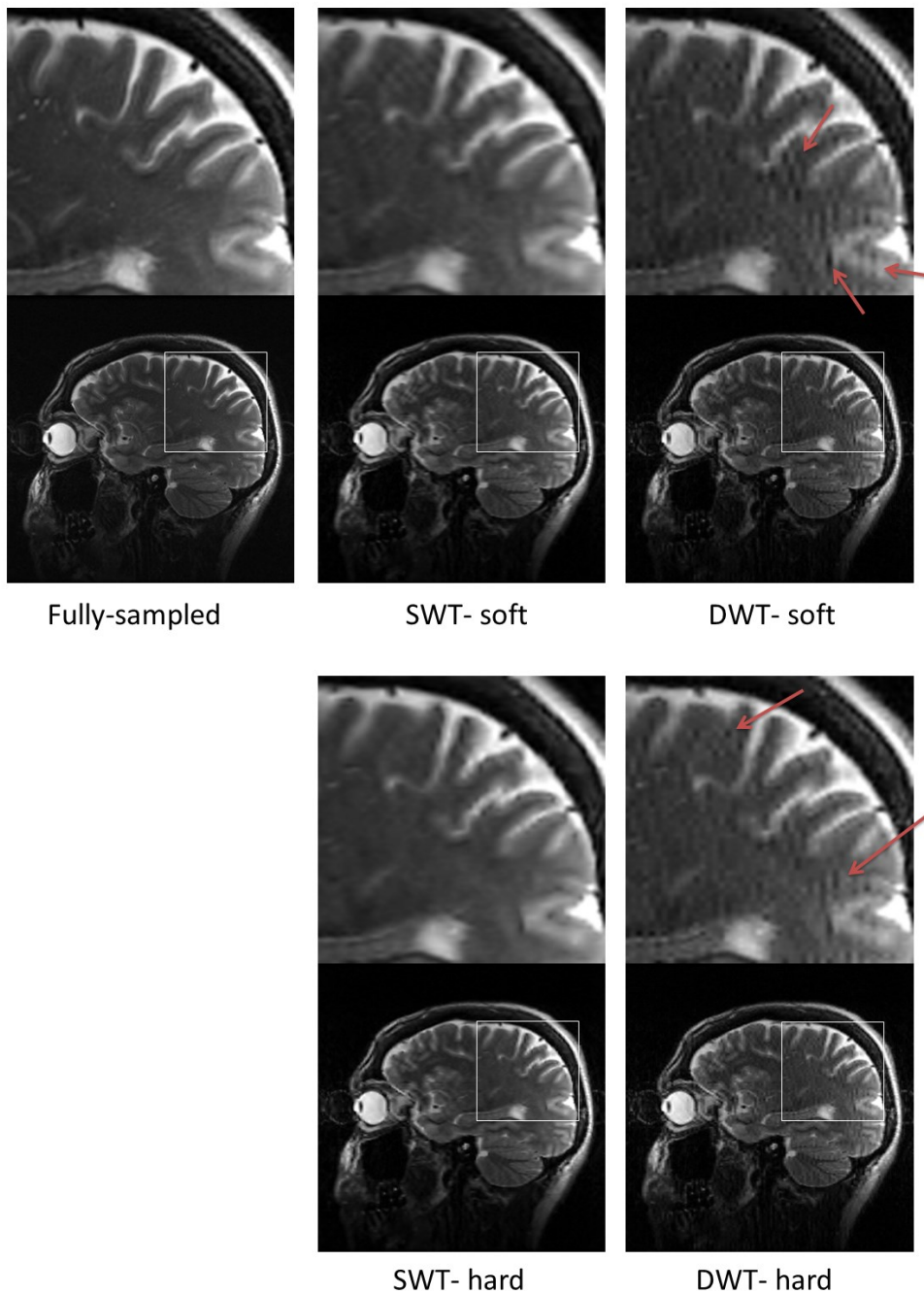


Figure 3.8- Reconstruction of under-sampled 32-channel FSE data (under-sampling factor 5) by the multiple-coil iterative thresholding algorithm. Arrows point to examples of DWT reconstruction artifacts that are absent or greatly reduced in the corresponding SWT reconstruction.

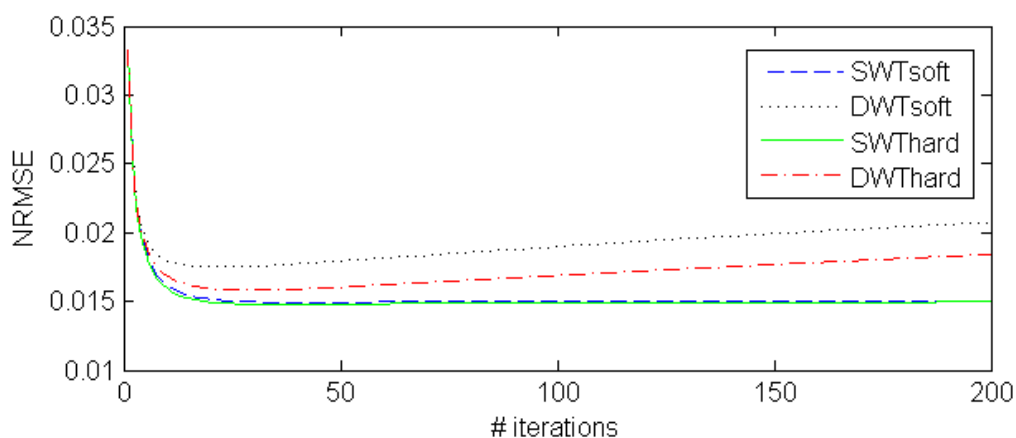


Figure 3.9- Convergence plot of the multiple-coil iterative thresholding reconstruction algorithm, in terms of NRMSE vs. iteration number, corresponding to the reconstructions of Figure 3.8.

The dependence of the iterative SWT/DWT thresholding reconstructions on the choice of the threshold is illustrated in Figure 3.10. In the interest of space, only soft thresholding reconstructions are reported. Nevertheless, the main conclusions are applicable to hard thresholding also.

An initial base threshold was obtained using the Birgé-Massart strategy [17], in which the threshold is chosen such that at each decomposition level j , from 1 to j_m , n_j largest *decimated* wavelet transform coefficients are kept, with $n_j = M/(j_m + 2 - j)^\alpha$, where M is typically assumed to be equal to the length of the coarsest approximation coefficients, and $\alpha = 3$. The convergence of the iterative SWT/DWT thresholding algorithms, in terms of the reconstruction NRMSE vs. iteration number, was studied for several variations of the base threshold by multiplicative factors.

As shown in Figure 3.10, increasing the threshold generally resulted in increased reconstruction error for both the SWT and DWT reconstructions as well as increased over-convergence for the DWT reconstruction (dotted lines on the plots). On the other hand, a moderate decrease of the threshold did not result in noticeable improvement in the reconstruction error, nor did it alleviate the over-convergence observed with DWT,

while a more aggressive decrease in the threshold resulted in increased reconstruction error due to increased over-convergence for both SWT and DWT. In general the results suggest that the Birgé -Massart strategy can be used to obtain practically optimum thresholds for both SWT and DWT.

Clearly, regardless of the threshold, SWT results in lower reconstruction errors compared to DWT. Additionally, the SWT reconstruction generally reaches convergence in far less iterations than the corresponding DWT reconstruction, with no noticeable over-convergence. (For instance compare [Figure 3.10\(a\)](#) with [Figure 3.10\(b,c\)](#): while SWT reaches convergence in about 50 iterations, it almost takes 5000 iterations for the DWT reconstruction to reach convergence.)

It should be noted that all the results in [Figure 3.7](#), [Table 3.3](#), [Figure 3.8](#), and [Figure 3.9](#) are obtained with thresholds obtained based on the Birgé -Massart strategy. Furthermore, in order to avoid giving SWT any advantage due to the over-convergence of the DWT reconstruction (see the discussion above on over-convergence, [Figure 3.9](#), and [Figure 3.10](#)), and since in practice the reconstructions can be terminated after a certain number of iterations, all the results in [Figure 3.7](#), [Table 3.3](#), and [Figure 3.8](#) were obtained with 50 iterations.

[Figure 3.11](#) shows the reconstruction performance of SWT/DWTRS/DWT SPIRiT on the same under-sampled 32-channel FSE datasets, in terms of the mean and the standard deviation of the reconstruction errors in the repeated experiments. Clearly SWT results in lower error values than DWT and DWTRS. The mean and its 95% confidence interval of the paired NRMSE differences are shown in [Table 3.4](#). Similar to the previous experiments, negative NRMSE difference means with confidence intervals that do not include zero indicate that SWT resulted in lower reconstruction errors than DWT and DWTRS with all the findings showing significance after the Bonferroni correction.

A sample reconstruction by SWT/DWTRS/DWT SPIRiT is shown in [Figure 3.12](#). This figure clearly illustrates that most of the DWT reconstruction (including DWTRS) artifacts are absent or greatly reduced in the corresponding SWT reconstruction.

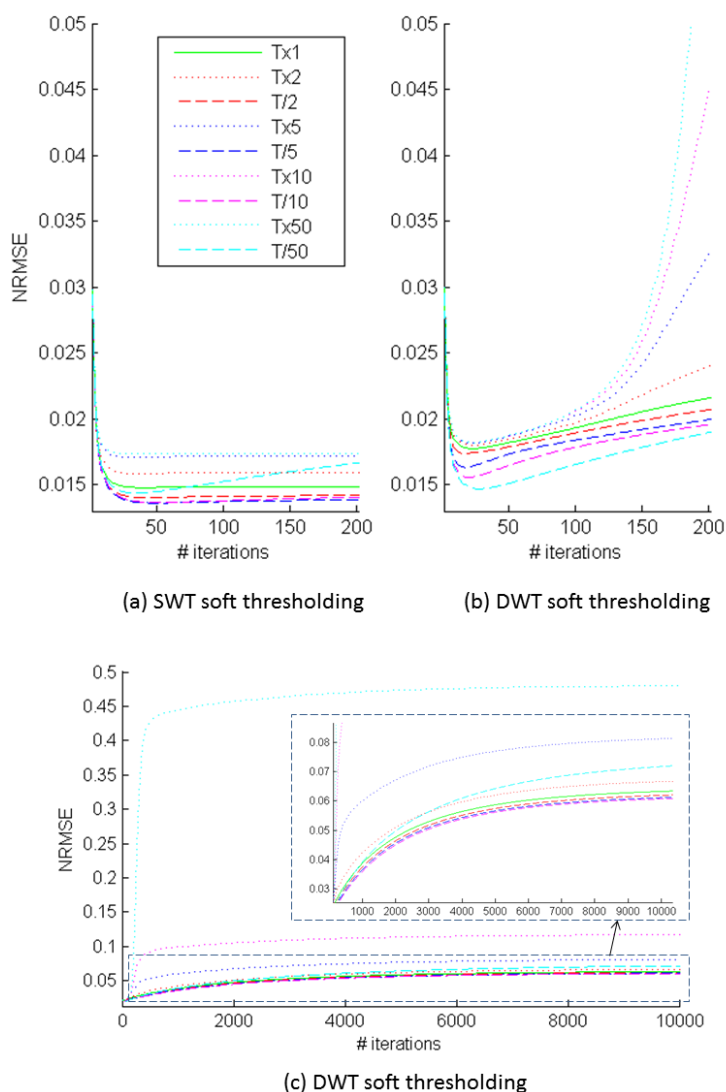


Figure 3.10- Effect of the choice of the threshold on the convergence of the multiple-coil iterative SWT/DWT soft thresholding algorithm for the reconstruction of under-sampled data (under-sampling factor 5) with SWT (a) and DWT (b, c). The convergence of the algorithms, in terms of the reconstruction NRMSE vs. iteration number, is shown for several variations of a base threshold, T , by multiplicative factors. Since the DWT reconstruction requires far more iterations to converge than the SWT reconstruction, an extended plot over 10000 iterations is shown in (c) for the DWT reconstruction.

Although reconstruction by random shifts results in reduced artifacts compared to the simple DWT with no shifts (as an example note the reduced ringing artifacts over the grey matter), many artifacts are still remaining that are completely removed or greatly reduced in the corresponding SWT reconstruction.

The progress of the SPIRiT reconstructions for various regularization parameters (λ in equation 3.8) is shown in Figure 3.13. A base value T for the regularization parameter was assumed as suggested in the code supplement to [9]. The convergence of the algorithm, in terms of the reconstruction NRMSE vs. iteration number, was studied for several variations of T by multiplicative factors.

The convergence plots generally conform to those of the multiple-coil iterative thresholding algorithms in the sense that the SWT reconstruction results in lower reconstruction error and less over-convergence. Furthermore, as expected, DWTRS falls in between DWT and SWT both in terms of the reconstruction error and over-convergence.

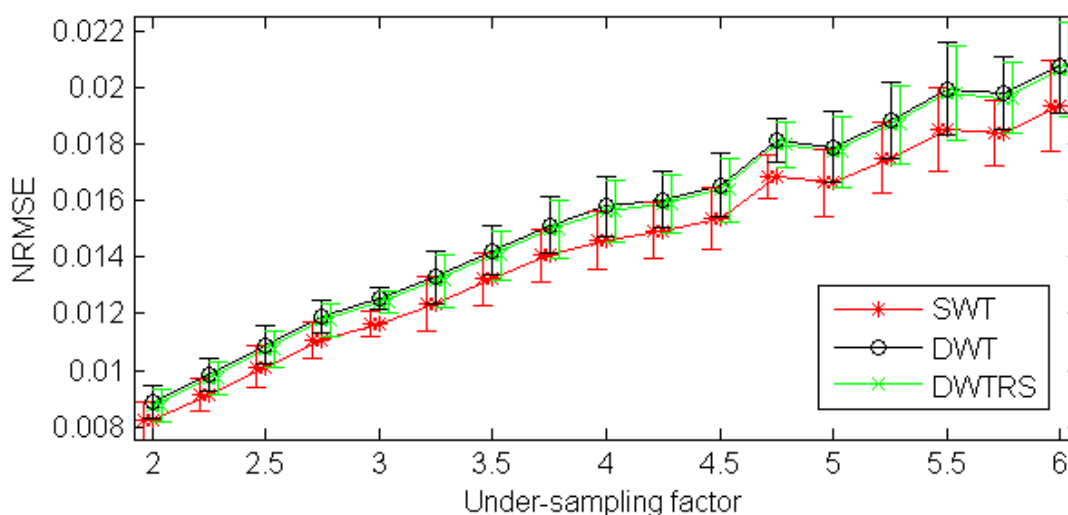


Figure 3.11- Mean NRMSE and the error bars of one standard deviation for the reconstruction of the under-sampled 32-channel FSE data by DWT/DWTRS/SWT SPIRiT.

($\times 10^{-3}$)					
U.F.	2	3	4	5	6
NRMSE_{SWT} - NRMSE_{DWT}	-0.67(8%) ± 0.067	-0.91(8%) ± 0.082	-1.2(8%) ± 0.12	-1.3(7%) ± 0.10	-1.4(7%) ± 0.090
NRMSE_{SWT} - NRMSE_{DWTRS}	-0.54(6%) ± 0.066	-0.76(6%) ± 0.090	-1.1(7%) ± 0.13	-1.1(6%) ± 0.11	-1.3(6%) ± 0.095

Table 3.4- Mean and its 95% confidence interval of the paired NRMSE differences (i.e., NRMSE of the DWT/DWTRS reconstruction subtracted from that of the corresponding SWT reconstruction) for the reconstruction of the 32-channel FSE data by SWT/DWTRS/DWT SPIRiT for different under-sampling factors (U.F.). The numbers in brackets show the percentage of mean improvement with SWT over the corresponding DWT reconstruction. All findings are significant after the Bonferroni correction.

In general, variation of the regularization parameter affects all the three variations of the discrete wavelet transform, i.e., SWT, DWTRS, and DWT, in a similar manner. That is, while reducing the regularization parameter results in lower reconstruction errors, further reduction beyond a certain limit results in over-convergence. Nevertheless, the SWT reconstruction generally results in lower error values compared to the corresponding DWT (including DWTRS) reconstructions with essentially any choice of the regularization parameter. Additionally, SWT is generally less prone to over-convergence, in the sense that lower reconstruction errors can be achieved with a smaller regularization parameter with no over-convergence. Nonetheless, in order to avoid giving the SWT reconstruction any advantage due to over-convergence, all the results reported in [Figure 3.11](#), [Table 3.4](#), and

[Figure 3.12](#) are obtained with a regularization T (corresponding to the green plot in [Figure 3.13](#)) and at 100 iterations, i.e., around the minimum of the NRMSE curves for DWT and DWTRS.

It is interesting to observe that the multiple-coil iterative SWT reconstructions and the SWT SPIRiT reconstructions result in similar reconstruction quality both visually and in terms of the reconstruction error, while the multiple-coil iterative DWT thresholding

reconstructions suffers from more artifacts than the corresponding DWT SPIRiT reconstructions.

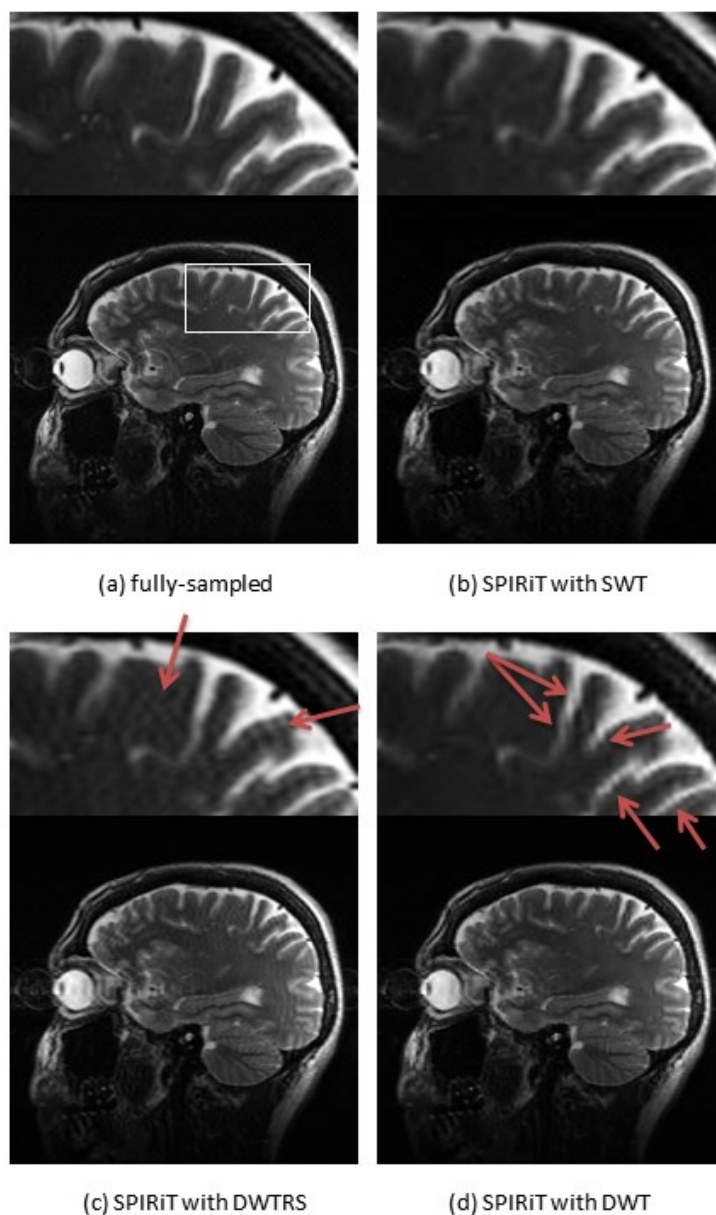


Figure 3.12- Reconstruction of the under-sampled 32-channel FSE data (under-sampling factor 5) by SWT/DWTRS/DWT SPIRiT. The arrows point to examples of DWT/DWTRS reconstruction artifacts that are absent in the corresponding SWT reconstruction.

This suggests that reasonable reconstructions can be achieved with simple [multiple-coil] [Iterative stationary wavelet transform thresholding](#), which is much less computational demanding than more complex algorithms such as SPIRiT.

Furthermore, as noted previously, despite its redundancy, the non-decimated wavelet transform can be computed very efficiently- in $O(n \log(n))$ time. While it is still more computationally demanding compared with the decimated wavelet transform or its random-shits version, which can be computed in $O(n)$, the visual and quantitative improvements are very noticeable. In addition, practical implementations show small execution time difference between SWT and DWT. (For example, the execution time for the simple multiple-coil iterative thresholding reconstructions of [Figure 3.9](#) were 33 and 37 seconds for DWT and SWT respectively, on an ordinary dual core 3.40 GHz PC using MATLAB.)

3.5 Discussion and conclusion

The most important conclusion drawn from the results presented in this article is that under-sampled MRI reconstructions based on the stationary wavelet transform (SWT) exhibit noticeably fewer visual artifacts than the corresponding decimated wavelet transform (DWT) reconstructions.

While quantitative quality measures, e.g., the normalized root mean square error (NRMSE), are commonly used to measure the reconstruction performance, these quantities do not necessarily provide a good measure of the practical quality perceived by radiologists and other expert users of these medical images. In fact, it was called to author's attention by collaborating radiologists and neurosurgeons that images with a very high quantitative reconstruction quality may still suffer from potentially critical losses that those quantitative measures fail to capture. This issue will more thoroughly investigated in chapter 5, in which we investigate the relationship between the quantitative quality measures and the perceptual quality scores, as given by radiologists and other expert users, for different reconstructions and applications.

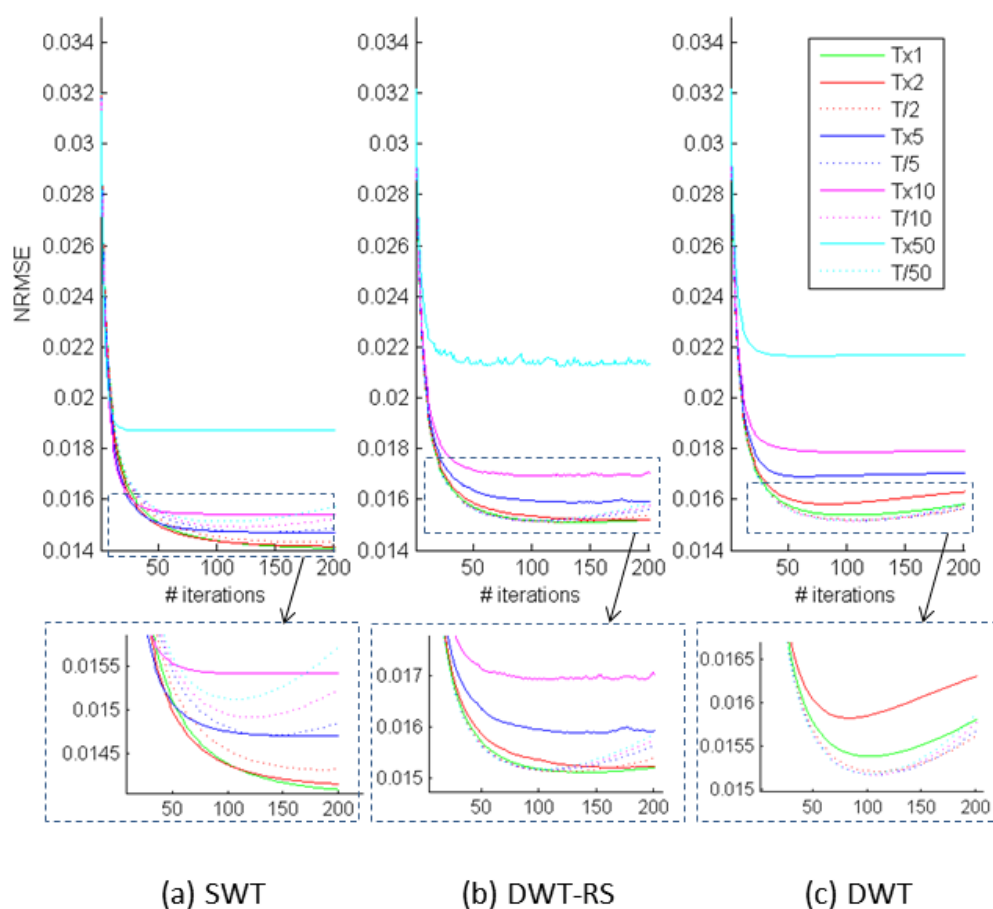


Figure 3.13- Effect of the choice of the regularization parameter on the convergence of the SPIRiT reconstruction algorithm for the reconstruction of under-sampled data (under-sampling factor 5) with several variations of the discrete wavelet transform, i.e., SWT, DWTRS, and DWT. The convergence of the algorithm, in terms of the reconstruction NRMSE vs. iteration number, is shown for several variations of a base threshold, T , by multiplicative factors.

Nevertheless, the results also indicate that SWT reconstructions result in approximately 10-30% improvement in the reconstruction error compared to the corresponding DWT reconstructions for the reconstruction of multi-channel data. This improvement is statistically significant, and is robust to the particular reconstruction algorithm chosen.

Additionally, SWT results in faster convergence than DWT. Also, the over-convergence effect in the DWT reconstruction, where the reconstruction error reaches its minimum before convergence and increases thereafter, is not observed with SWT.

3.6 References

- [1] A. Macovski, "Noise in MRI," *Magn. Reson. Med.*, vol. 36, no. 3, pp. 494–497, 1996.
- [2] K. P. Pruessmann, M. Weiger, M. B. Scheidegger, and P. Boesiger, "SENSE: Sensitivity encoding for fast MRI," *Magn. Reson. Med.*, vol. 42, no. 5, pp. 952–962, 1999.
- [3] M. A. Griswold, P. M. Jakob, R. M. Heidemann, M. Nittka, V. Jellus, J. Wang, B. Kiefer, and A. Haase, "Generalized autocalibrating partially parallel acquisitions (GRAPPA)," *Magn. Reson. Med.*, vol. 47, no. 6, pp. 1202–1210, 2002.
- [4] D. K. Sodickson and W. J. Manning, "Simultaneous acquisition of spatial harmonics (SMASH): Fast imaging with radiofrequency coil arrays," *Magn. Reson. Med.*, vol. 38, no. 4, pp. 591–603, 1997.
- [5] E. J. Candes, J. Romberg, and T. Tao, "Robust uncertainty principles: exact signal reconstruction from highly incomplete frequency information," *Inf. Theory IEEE Trans.*, vol. 52, no. 2, pp. 489–509, 2006.
- [6] E. J. Candes and M. B. Wakin, "An Introduction To Compressive Sampling," *Signal Process. Mag. IEEE*, vol. 25, no. 2, pp. 21–30, 2008.
- [7] M. Lustig, D. Donoho, and J. M. Pauly, "Sparse MRI: The application of compressed sensing for rapid MR imaging," *Magn. Reson. Med.*, vol. 58, no. 6, pp. 1182–1195, Dec. 2007.
- [8] D. L. Donoho, "Compressed sensing," *IEEE Trans. Inf. Theory*, vol. 52, no. 4, pp. 1289–1306, Apr. 2006.
- [9] M. Lustig and J. M. Pauly, "SPIRiT: Iterative self-consistent parallel imaging reconstruction from arbitrary k-space," *Magn. Reson. Med.*, vol. 64, no. 2, pp. 457–471, 2010.
- [10] I. Daubechies, M. Defrise, and C. De Mol, "An iterative thresholding algorithm for linear inverse problems with a sparsity constraint," *Commun. Pure Appl. Math.*, vol. 57, no. 11, pp. 1413–1457, Nov. 2004.

- [11] R. R. Coifman and D. L. Donoho, "Translation-invariant de-noising," *Wavelets Stat. Springer Lect. Notes Stat.*, vol. 103, pp. 125–150, 1995.
- [12] J. Pesquet, H. Krim, and H. Carfantan, "Time-invariant orthonormal wavelet representations," *IEEE Trans. Signal Process.*, vol. 44, no. 8, pp. 1964–1970, 1996.
- [13] G. P. Nason and B. W. Silverman, "The Stationary Wavelet Transform and some Statistical Applications," in *Wavelets and Statistics*, A. Antoniadis and G. Oppenheim, Eds. Springer New York, 1995, pp. 281–299.
- [14] M. A. T. Figueiredo and R. D. Nowak, "An EM algorithm for wavelet-based image restoration," *IEEE Trans. Image Process.*, vol. 12, no. 8, pp. 906–916, 2003.
- [15] M. Guerquin-Kern, M. Haberlin, K. P. Pruessmann, and M. Unser, "A Fast Wavelet-Based Reconstruction Method for Magnetic Resonance Imaging," *IEEE Trans. Med. Imaging*, vol. 30, no. 9, pp. 1649–1660, 2011.
- [16] S. S. Vasanawala, M. J. Murphy, M. T. Alley, P. Lai, K. Keutzer, J. M. Pauly, and M. Lustig, "Practical parallel imaging compressed sensing MRI: Summary of two years of experience in accelerating body MRI of pediatric patients," in *Biomedical Imaging: From Nano to Macro, 2011 IEEE International Symposium on*, 2011, pp. 1039–1043.
- [17] L. Birgé and P. Massart, "From Model Selection to Adaptive Estimation," in *Festschrift for Lucien Le Cam*, D. Pollard, E. Torgersen, and G. L. Yang, Eds. Springer New York, 1997, pp. 55–87.
- [18] Y. Tsaig and D. L. Donoho, "Extensions of compressed sensing," *Signal Process.*, vol. 86, no. 3, pp. 549–571, Mar. 2006.
- [19] A. A. Samsonov, E. G. Kholmovski, D. L. Parker, and C. R. Johnson, "POCSense: POCS-based reconstruction for sensitivity encoded magnetic resonance imaging," *Magn. Reson. Med.*, vol. 52, no. 6, pp. 1397–1406, 2004.
- [20] P. B. Roemer, W. A. Edelstein, C. E. Hayes, S. P. Souza, and O. M. Mueller, "The NMR phased array," *Magn. Reson. Med. Off. J. Soc. Magn. Reson. Med. Soc. Magn. Reson. Med.*, vol. 16, no. 2, pp. 192–225, Nov. 1990.
- [21] D. J. Larkman and R. G. Nunes, "Parallel magnetic resonance imaging," *Phys. Med. Biol.*, vol. 52, no. 7, pp. R15–R55, Apr. 2007.

4 Similarity-based joint reconstruction in multiple acquisition problems with application to DESPOT1 T1 mapping

My purpose in this chapter is to show that in MRI applications involving multiple acquisitions, e.g., [Quantitative MRI: T1/T2 mapping](#), the structural similarity between the acquisitions can be used as a reconstruction constraint, in addition to the (wavelet) sparsity, to achieve improved reconstruction performance.

Without loss of generality, human brain T1 mapping by [DESPOT1](#) based on the acquisition of two spoiled gradient recalled (SPGR) images at optimum flip angles is considered. K-space data in each acquisition are retrospectively under-sampled and then jointly reconstructed by an [Iterative reconstruction](#) incorporating an additional similarity constraint.

It is shown that joint reconstruction results in reduced visual artifacts and significantly lower reconstruction error compared to the traditional individual reconstruction for the reconstruction of SPGR images. Additionally, while the individual reconstruction fails to produce T1 maps even as accurate as just a low resolution acquisition, joint reconstruction results in significantly lower T1 map errors than both the individual and the low resolution reconstructions.

Similarity-based joint reconstruction in multiple acquisition problems results in significant visual/quantitative improvements over the traditional individual reconstructions. The improvements become more important in quantitative mapping applications that are more sensitive to reconstruction errors.

4.1 Introduction

Since signal to noise ratio (SNR) in magnetic resonance imaging (MRI) is proportional to voxel volume and the square root of the acquisition time [1], higher resolution and SNR often comes at the expense of long acquisition times and patient discomfort. This, in turn, limits how many pulse sequences can be run during a single clinical examination, which can create difficulties for applications where multiple images should be acquired in order to reconstruct a map of a parameter of interest, e.g., T1 and T2 mapping [2]–[4]. If additional sequences or maps need to be acquired, the total scanning time can quickly become excessive.

As noted in the previous chapters, one approach to reducing MRI acquisition time is to acquire under-sampled k-space data and interpolate missing data based some *a priori* reconstruction constraints, such as sparsity in a transform domain [5]. This approach is commonly known as [Compressed sensing](#) (CS) [6], [7]. CS has also been used for MR parameter mapping [8]–[11], which take advantage of the sparsity of the joint k-p data in a transform domain, where p is an added dimension of the parameter of interest, to achieve improved reconstruction quality.

In particular, Velikina et al have recently proposed to use the smoothness of the signal in the parameter (e.g., flip angle) direction as a reconstruction constraint by penalizing a hybrid $l1/l2$ norm on the first or second derivative of the signal in the parameter direction [9]. While this is an intriguing idea, it requires a relatively large number of acquisitions in the parameter direction, which can defeat the purpose of under-sampled reconstruction, especially since it has been shown that two acquisitions at optimal flip angles can result in similar accuracy as multiple acquisitions at multiple flip angles [4]. In this chapter, a joint reconstruction based on spatial similarity, i.e., joint-entropy, of the acquisitions at optimal flip angles is presented.

As noted previously, some MRI applications, e.g., [Quantitative MRI: T1/T2 mapping](#), involve sequential acquisitions of multiple images of an object where the acquisitions differ by a single [Pulse sequence parameters](#) [2]–[4]. While these differences may affect

the intensity, the resulting images carry similar structural information. We hypothesize that this similarity can be used as an additional constraint to further increase the reconstruction quality and/or k-space under-sampling factor, enabling potential savings in acquisition time.

The structural similarity between images implies a sparse joint intensity distribution of the images, and consequently a low joint-entropy. It is demonstrated that incoherent under-sampling in k-space results in a loss of sparsity of the joint intensity distribution and therefore an increase in the joint-entropy (loss of similarity), which is primarily associated with the incoherent aliasing artifacts caused by under-sampling. On these grounds, we develop a [Similarity-promoting operation](#) to restore the similarity between the images by re-enforcing the sparsity of the joint intensity distribution of the images, thereby decreasing their joint-entropy. Joint reconstruction is achieved by incorporating the [Similarity-promoting operation](#) into an [Iterative reconstruction](#) algorithm [12].

Without loss of generality, we specifically consider [DESPOT1](#) [4] T1 map reconstruction, which is currently the most efficient T1 mapping technique [13], to demonstrate my methods and results. This technique, which has been developed to accelerate the acquisition and reconstruction of T1 maps, is based on the acquisition of two spoiled gradient recalled (SPGR) images at the optimum flip angles.

4.2 Theory

In the following discussion a point spread function (PSF) analysis is performed to investigate the effect of k-space under-sampling on each image and on their joint intensity distribution.¹⁴ A [Similarity-promoting operation](#) is developed based on this

¹⁴ Based on the principle of superposition, a linear time-invariant system can be completely described by its response to an impulse input function. The response of an imaging system to such an input is often described in terms of a point spread function (PSF). Since k-space under-sampling is a linear operation [5], and with the assumption that the imaging system does not noticeably change during a set of consecutive acquisitions (time-invariance), I also describe the under-sampling operation in terms of its PSF.

analysis. This operation is then incorporated into an [Iterative reconstruction](#) algorithm to reconstruct the images based on both their wavelet sparsity and their structural similarity.

Let $f_i(m, n) = \zeta_i \delta(n)$ ($i = 1, 2$) be Kronecker delta inputs in the y direction in the spatial domain, corresponding to the phase-encode (k_y) direction in k -space, where $\delta(n) =$

$$\begin{cases} 1 & n = 0 \\ 0 & n \neq 0 \end{cases} \text{ and } \zeta_i \text{ are constants accounting for the difference in the intensity between}$$

images in multiple-acquisition problems. The structural similarity between the images in sequential acquisitions is modeled by placing the delta inputs in the same locations in each image.

Incoherent k -space under-sampling is achieved by random and independent phase-encode under-sampling operators $U_{F,i}$ ($i = 1, 2$). Transforming f_i to the Fourier domain, under-sampling, and taking the inverse Fourier transform back to the spatial domain result in an under-sampling PSFs, $f_{u,i}$:

$$f_{u,i} = \mathcal{F}^{-1} U_{F,i} \mathcal{F} f_i ; i = 1, 2 \quad (4.1)$$

where operators \mathcal{F} and \mathcal{F}^{-1} denote the Fourier transform and its inverse respectively.

[Figure 4.1](#) shows the original delta inputs, the under-sampling PSFs, and their respective joint intensity distributions. Note that since the delta inputs and the under-sampling operations are applied in the phase-encode direction only, the point spread functions can be represented by 1D functions.

The joint intensity distribution of the original delta inputs consists of two non-zero values only: a spike at $(0, 0)$ corresponding to all the zero values of f_1 and f_2 , and another at (ζ_1, ζ_2) corresponding to the peaks of f_1 and f_2 . Random and independent under-sampling of f_1 and f_2 results in a more diffuse joint intensity distribution due to the incoherence of aliasing artifacts between images, and therefore in an increase in the joint entropy ($H(f_1, f_2) = 0.037$ bits, $H(f_{u,1}, f_{u,2}) = 6.9$ bits, in the particular case of [Figure 4.1](#)), i.e., reduced similarity.

Note that the independence of the under-sampling operations is essential. While random under-sampling of each image results in incoherent artifacts on each image, which is desired in order to distinguish them from the image features, the independence of the under-sampling operations ensures that these artifacts are also incoherent between images. This incoherence results in increased joint entropy, ensuring that under-sampling artifacts are also distinguishable in the joint intensity distribution. Note that independent random under-sampling amounts to under-sampling both in the phase-encode and parameter, e.g., flip angle, direction.

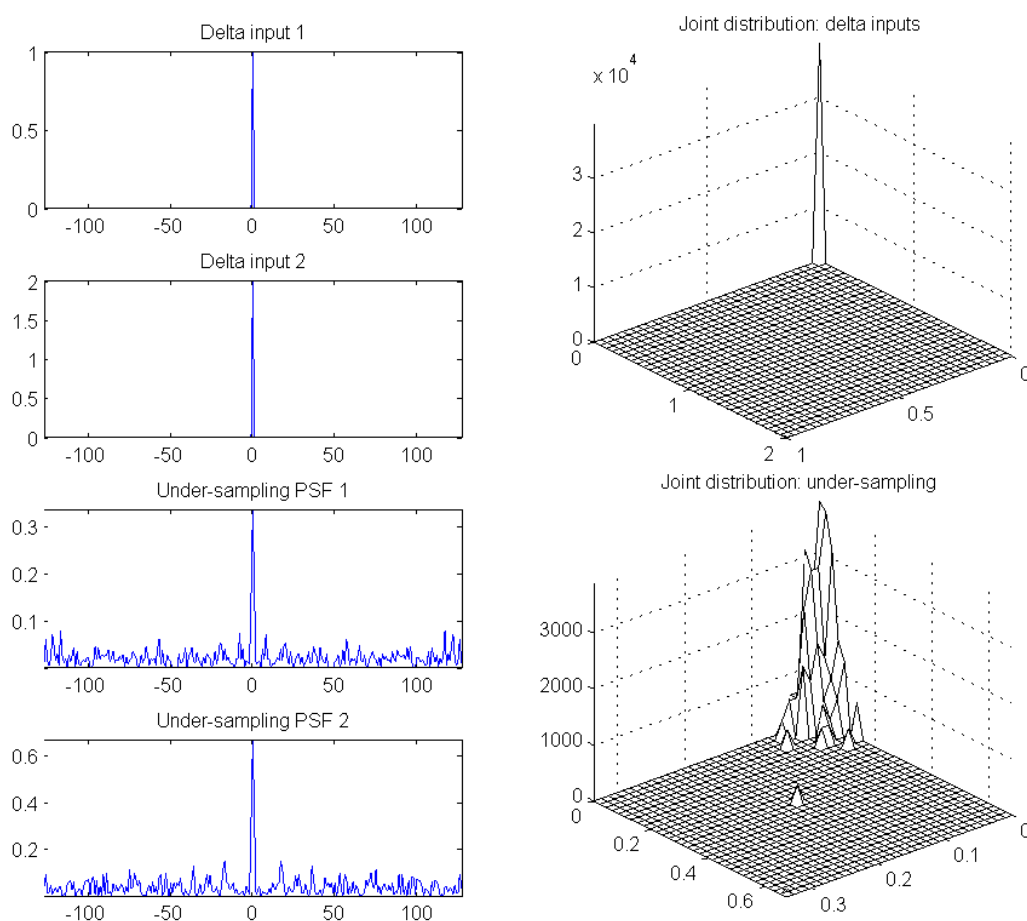


Figure 4.1- Effect of random and independent k-space under-sampling in terms of point spread functions (PSF) and joint intensity distributions.

4.2.1 Similarity-promoting operation

In general, we consider multiple acquisitions of an object resulting in images with similar structural information. Due to this similarity, the joint intensity distribution is expected to consist of a few sparsely distributed clusters (low joint entropy). However, based on the above discussion, aliasing artifacts due to incoherent under-sampling in k-space result in a loss of sparsity of the joint intensity distribution (increase in joint entropy). Therefore, one may remove some of these artifacts by re-enforcing the sparsity of the joint intensity distribution to decrease the joint entropy. This is in essence similar to noise/artifact removal, based on the loss of wavelet sparsity due to the noise/artifacts, by re-enforcing the wavelet sparsity by a wavelet thresholding operation [12], [14].

Assume under-sampled images $f_{u,1}$ and $f_{u,2}$, and the joint intensity points $p_{m,n} = (f_{u,1}(m, n), f_{u,2}(m, n))$. The mean of the neighborhood around $p_{m,n}$ can be estimated as:

$$\mu_{p_{m,n}} = \frac{\sum_{p_{i,j} \in N_{p_{m,n}}} K(p_{m,n} - p_{i,j}) p_{m,n}}{\sum_{p_{i,j} \in N_{p_{m,n}}} K(p_{m,n} - p_{i,j})} \quad (4.2)$$

where $N_{p_{m,n}} = \{\forall p_{i,j} | \|p_{m,n} - p_{i,j}\| < r\}$ is the r -neighborhood of $p_{m,n}$, and $K(p_{m,n} - p_{i,j}) = \frac{1}{\sigma\sqrt{2\pi}} e^{-\|p_{m,n} - p_{i,j}\|^2 / 2\sigma^2}$ is a Gaussian kernel function.

To sparsify the joint intensity distribution, consider shifting every point towards the mean of its neighborhood:

$$\hat{p}_{m,n} = p_{m,n} + \beta(\mu_{p_{m,n}} - p_{m,n}) \quad (4.3)$$

where $0 \leq \beta \leq 1$ is a fixed parameter determining the shift ratio. Note that with $\beta = 1$ this is equivalent to a single iteration in the mean-shift algorithm [15], [16].

Since $p_{m,n} = (f_{u,1}(m, n), f_{u,2}(m, n))$, $f_{u,1}$ and $f_{u,2}$ can be directly updated by equation (4.3). That is,

$$\begin{aligned} & \left(\hat{f}_{u,1}(m, n), \hat{f}_{u,2}(m, n) \right) = \\ & \left(f_{u,1}(m, n), f_{u,2}(m, n) \right) + \beta \left[\mu_{p_{m,n}} - \left(f_{u,1}(m, n), f_{u,2}(m, n) \right) \right] \end{aligned} \quad (4.4)$$

where $\hat{f}_{u,1}$ and $\hat{f}_{u,2}$ are the resulting images from the above operations.

These operations decrease the joint entropy of $f_{u,1}$ and $f_{u,2}$ by sparsifying their joint intensity distribution. To simplify our notations, we denote the above operations by a single *similarity-promoting* operation, Ω , such that

$$\left(\hat{f}_{u,1}, \hat{f}_{u,2} \right) = \Omega\{f_{u,1}, f_{u,2}\} \quad (4.5)$$

4.2.2 Iterative reconstruction

Assuming randomly and independently under-sampled k-space data, $F_{u,i}$ ($i = 1,2$), and beginning with $f_{u,i} = \mathcal{F}^{-1}F_{u,i}$,¹⁵ one can remove some of the aliasing artifacts and thereby improve the resulting image by the application of a wavelet sparsity, i.e., wavelet thresholding, operation, Γ :

$$\tilde{f}_i = \Gamma\{f_{u,i}\} \quad (4.6)$$

Note that this is based on the *a priori* assumption that MR images have a sparse representation in the wavelet domain [5]. In practice, the threshold can be obtained adaptively using a wavelet coefficient selection rule, e.g., the Birge-Massart strategy [17].

The aliasing artifacts can be further removed by the application of the aforementioned similarity-promoting operation:

$$\left(\hat{f}_1, \hat{f}_2 \right) = \Omega\{\tilde{f}_1, \tilde{f}_2\} \quad (4.7)$$

¹⁵ This is usually called a minimum energy reconstruction since among all the solutions matching the original k-space data $F_{u,i}$, it has the lowest energy because unobserved k-space samples are simply replaced by zero.

Joint reconstruction algorithm

Inputs:

 $F_{u,1}, F_{u,2}$: Under-sampled k-space data $U_{F,2}, U_{F,2}$: Under-sampling operations selecting k-space data

Output:

 $F_{rec,1}, F_{rec,2}$: Reconstructed k-space data

Algorithm:

// Initialize to the minimum energy reconstruction

 $F_{rec,1} \leftarrow F_{u,1}$ $F_{rec,2} \leftarrow F_{u,2}$

//Reconstruct through iterative thresholding

while *not converged* do $f_{rec,1} \leftarrow \mathcal{F}^{-1}F_{rec,1}$ $f_{rec,2} \leftarrow \mathcal{F}^{-1}F_{rec,2}$

//wavelet sparsity-promoting

 $\tilde{f}_1 = \Gamma\{f_{rec,1}\}$ $\tilde{f}_2 = \Gamma\{f_{rec,2}\}$

//similarity-promoting

 $(\hat{f}_1, \hat{f}_2) = \Omega\{\{\tilde{f}_1, \tilde{f}_2\}\}$

//data consistency

 $\hat{F}_1 \leftarrow \mathcal{F}\hat{f}_1$ $\hat{F}_2 \leftarrow \mathcal{F}\hat{f}_2$ $F_{rec,1} \leftarrow \hat{F}_1 - U_{f,1}\hat{F}_1 + F_{u,1}$ $F_{rec,2} \leftarrow \hat{F}_2 - U_{f,2}\hat{F}_2 + F_{u,2}$

end

Table 4.1- Joint reconstruction algorithm

While these operations should have revealed more features of the images by removing some of the aliasing artifacts, they may also have affected the known k-space samples as originally measured. Mathematically, $U_{F,i}\hat{F}_i \neq F_{u,i} = U_{F,i}F_i$ ($i = 1,2$), where $\hat{F}_i = \mathcal{F}\hat{f}_i$ is the Fourier transform of \hat{f}_i . In other words, if \hat{F}_i is under-sampled in the same manner that k-space data were originally acquired, the resulting under-sampled data will not necessarily be consistent with the original under-sampled k-space data. Therefore, before further progress, the known k-space samples are recovered: $F_i^{(1)} = \hat{F}_i - U_{F,i}\hat{F}_i + F_{u,i}$.

Transforming to the spatial domain, $f_i^{(1)}$ are better estimates of f_i than $f_{u,i}$, since some of the unknown Fourier coefficients, which are replaced by zero in $F_{u,i}$, take an estimated value in $F_i^{(1)}$.

These estimates can be improved by applying the above procedure in an iterative manner. The joint reconstruction algorithm is shown in [Table 4.1](#).

The algorithm is initialized with the minimum-energy reconstructions, $f_i^{(0)} = f_{u,i}$, and continues until a convergence criterion is reached, e.g., changes between iterations are below a predefined threshold, $\left| f_i^{(n)} - f_i^{(n-1)} \right| / \left| f_i^{(n)} \right| < \epsilon$, or a maximum number of iterations is reached.

4.3 Methods

SPGR brain images of healthy volunteers and temporal lobe epilepsy (TLE) patients were acquired at 3T using a GE scanner (Discovery 750, software revision 22M32, General Electric Healthcare, Waukesha, WI) with flip angles 4° and 18° , with the following parameters: matrix: 256x256, resolution = 0.86mm isotropic, slice thickness = 1mm, TE/TR = 4.1ms/8.9ms, BW = ± 19.23 kHz, flip angle = 18° , NEX = 1. Human data used in this work were acquired using a protocol approved by the Western University Office of Research Ethics.

The first set of experiments compared reconstruction methods on multiple images while keeping the under-sampling pattern constant to reduce the dependence of the comparison on the choice of under-sampling pattern. A total of 5 healthy volunteer and 10 TLE patient datasets were used. Fully-sampled k-space data were employed as the reference standard. Each dataset was then retrospectively under-sampled by randomly and independently under-sampling the k-space datasets corresponding to acquisitions at flip angles 4° and 18° , along the phase-encode direction with variable density. All datasets were under-sampled with the same randomly and independently selected under-sampling patterns.

Corresponding under-sampled slices (at flip angles 4° and 18°) were jointly reconstructed as described above, and the corresponding T1 map was computed by [DESPOT1](#). The same datasets were also reconstructed based on either wavelet sparsity only or similarity only. The former is achieved by removing the similarity-promoting operation in the

described iterative algorithm and the latter by removing the wavelet sparsity-promoting operation. For clarity, we call the former individual reconstruction and the latter entropy-only reconstruction. The reconstructions were also compared with the low resolution sampling with the same under-sampling factor, achieved by fully sampling the center of k-space and zero-padding the remainder, i.e., interpolation by a sinc kernel in the spatial domain. These experiments were repeated for a range of under-sampling factors from 2 to 6.

Another set of experiments was performed to study the effect of various under-sampling patterns. One healthy volunteer dataset was under-sampled with 15 pairs of under-sampling patterns selected independently based on a Gaussian probability density function. Similar to the previous set of experiments, the under-sampled datasets were reconstructed jointly and the results compared with individual, entropy-only, and low resolution reconstructions as described above.

All the algorithms were implemented in MATLAB (MathWorks, Inc., Natick, MA). In all the experiments the reconstruction quality was measured in terms of the normalized root mean squared error (NRMSE) of the reconstructed images and the T1 maps with respect to the fully sampled data. To eliminate error due to background noise, the NRMSE was computed over the support of the image, excluding the background. The support was computed automatically by binarizing the image based on a threshold and fitting a convex hull to the binary image. The threshold was chosen using the Otsu's method [18].

The statistical significance of the findings was evaluated using paired t-tests. Since several such t-tests were performed, the comparisons were corrected by the Bonferroni correction in which each individual hypothesis is tested at a statistical significance level of α/n to achieve the desired significance level of α for the whole set of experiments, where n is the total number of tests. In this thesis we used $\alpha = 0.05$.

Although NRMSE is a measure of the global error with respect to the reference standard, it fails to capture local artifacts, which may be of more interest in practice. To illustrate

the local effects of each under-sampled reconstruction method on the computed T1 map, we define three regions of interest (ROI) in the white matter (WM), gray matter (GM), and cerebrospinal fluid (CSF) and show the distribution of the reconstructed T1 values on each ROI and those of the reference standard using box plots.

4.4 Results

Figure 4.2 shows the mean NRMSE values along with corresponding error bars of one standard deviation for the reconstruction of the 15 SPGR datasets in the first set of experiments. Joint reconstruction is compared with both individual and entropy-only (E.O.) reconstructions. The results are also compared with low resolution reconstruction. The statistical significance of the results, determined by paired t-tests, is shown in [Table 4.2](#).

In terms of the SPGR images, joint reconstruction significantly improved the NRMSE compared to individual reconstruction at all but very low and high under-sampling factors, and both consistently outperformed all other reconstruction methods evaluated. This is expected since both methods exploit wavelet sparsity, which is a well-established in compressed sensing and sparse recovery. The entropy-only reconstruction did not perform better than low resolution reconstruction indicating that the [Similarity-promoting operation](#) by itself was not sufficient to reconstruct images. However, when combined with wavelet thresholding in joint reconstruction, the entropy promoting operation further improves the reconstruction.

In general, the T1 maps derived from the two SPGR reconstructions exhibited a higher NRMSE than either SPGR image as the DESPOT calculations are very sensitive to errors in the SPGR images. Somewhat counter-intuitively, however, the T1 map derived from the low resolution SPGR images performed better than the T1 map derived from the individual reconstructions of the SPGR images even though the individual reconstructions had a lower NRMSE than the low resolution SPGR images. Nevertheless, the joint reconstruction still obtained significantly lower T1 NRMSE values compared to all other reconstructions with the exception of low resolution reconstruction at high

under-sampling factors (4.5 and higher in Table 4.2). It is interesting to note that at an under-sampling factor of 4 the joint reconstruction resulted in an RMSE approximately 15% lower than the individual reconstruction of SPGR images but 45% in the reconstruction of a T1 map. A more thorough investigation of these findings is presented at the end of this section.

Figure 4.3 shows the mean NRMSE values along with corresponding error bars of one standard deviation for the reconstruction of one healthy volunteer dataset with 15 different sets of under-sampling patterns in the second set of experiments. The statistical significance of the results is shown in Table 4.3.

	2	2.5	3	3.5	4	4.5	5	5.5	6
	I1 I2 T1	I1 I2 T1	I1 I2 T1	I1 I2 T1	I1 I2 T1	I1 I2 T1	I1 I2 T1	I1 I2 T1	I1 I2 T1
Joint-Indiv	+	+	+	+	+	+	+	+	+
Joint-E.O.	+	+	+	+	+	+	+	+	+
Joint-Lowres	+	+	+	+	+	+	+	+	+
Indiv-E.O.	+	+	+	+	+	+	+	+	+
Indiv-Lowres	+	+	+	+	+	+	+	+	+
E.O-Lowres.	-	-	+	+	+	+	-	-	-

+ statistical significance under the null hypothesis that the NRMSE of the second reconstruction is lower than the first one in each pair;

- statistical significance under the inverse null hypothesis, i.e., the NRMSE of the first reconstruction is lower than the second one;

Otherwise, no statistical significance observed

Table 4.2- Statistical significance of NRMSE comparisons for the reconstruction of 15 different datasets. The results of paired t-tests for image 1, image 2, and the T1 map are shown.

The results generally follow the same trend as in the previous set of experiments. However, the NRMSE values generally show smaller deviation and consequently stronger statistical significance is observed. This indicates that the variation in reconstruction quality from randomly choosing the under-sampling patterns from a Gaussian probability density is relatively small compared with the variation in reconstruction quality between subjects.

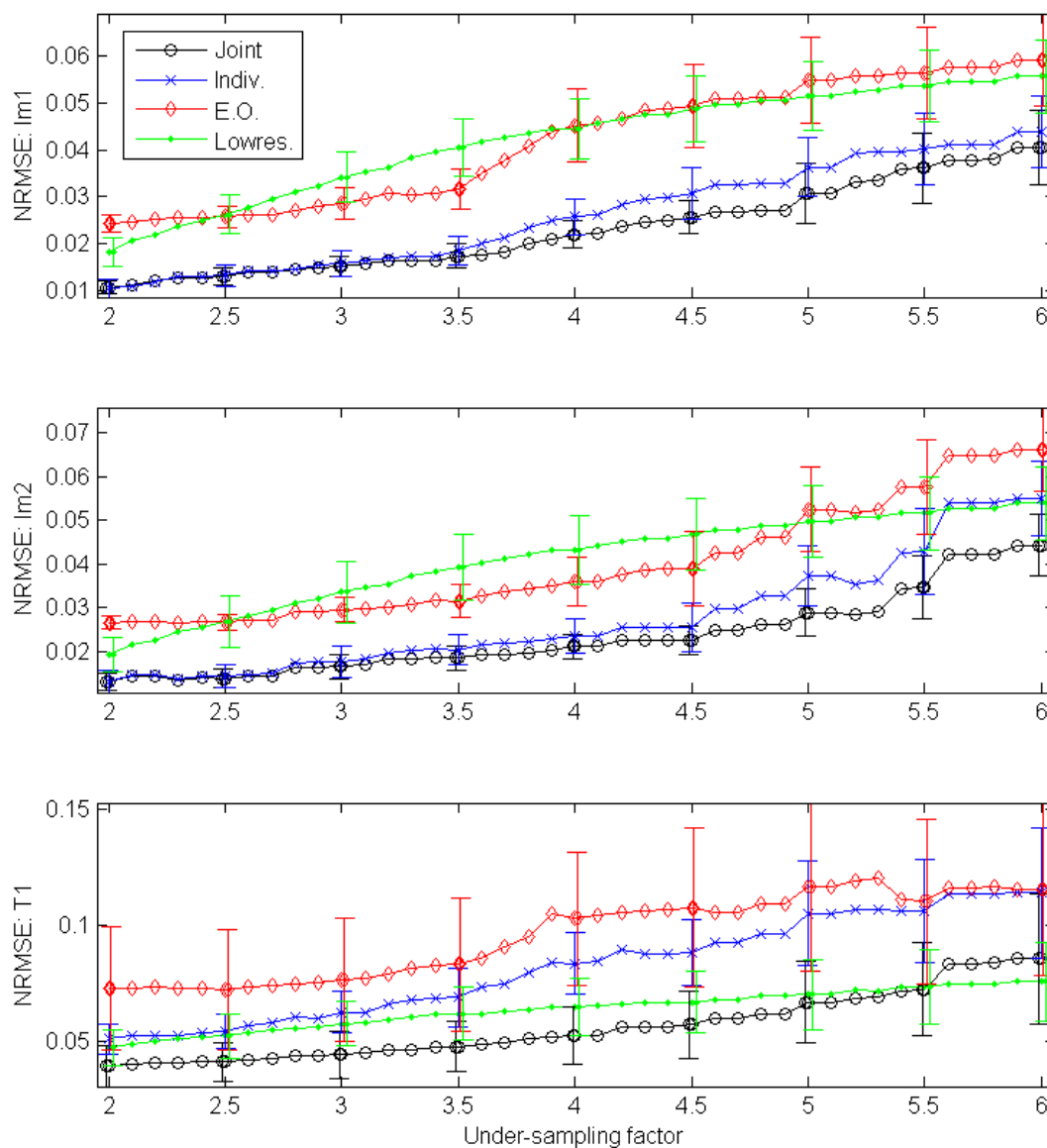


Figure 4.2- Mean NRMSE values and corresponding error bars of one standard deviation for the reconstruction of 15 SPGR pairs from under-sampled k-space data and derived T1 map. For clarity, the error bars are shown at increments of 0.5. However, the growth in the error bars follows a consistent trend.

While the NRMSE values from low resolution reconstruction of the SPGR images are higher than those of the joint and individual reconstructions, the NRMSE values of the derived T1 map is lower than those of the individual reconstructions and comparable to those of the joint reconstructions, especially at high under-sampling factors (see [Figure 4.2](#) and [Figure 4.3](#)). This behavior is unexpected, especially considering the rather well behaved NRMSE curves of the SPGR images.

	2	2.5	3	3.5	4	4.5	5	5.5	6
	I1 I2 T1	I1 I2 T1	I1 I2 T1	I1 I2 T1	I1 I2 T1	I1 I2 T1	I1 I2 T1	I1 I2 T1	I1 I2 T1
Joint-Indiv	+ +	+ + +	+ + +	+ + +	+ + +	+ + +	+ + +	+ + +	+ + +
Joint-E.O.	+ + +	+ + +	+ + +	+ + +	+ + +	+ + +	+ + +	+ + +	+ + +
Joint-Lowres	+ + +	+ + +	+ + +	+ + +	+ +	+ +	+ +	+ +	+ + -
Indiv-E.O.	+ + +	+ + +	+ + +	+ + +	+ + +	+ + +	+ + +	+ + +	+ + +
Indiv-Lowres	+ +	+ +	+ + -	+ + -	+ + -	+ + -	+ + -	+ + -	+ + -
E.O.-Lowres	- - -	- -	+ + -	+ + -	+ + -	+ + -	+ + -	+ + -	-

+ statistical significance under the null hypothesis that the NRMSE of the second reconstruction is lower than the first one in each pair;
 - statistical significance under the inverse null hypothesis, i.e., the NRMSE of the first reconstruction is lower than the second one;
 Otherwise, no statistical significance observed

Table 4.3- Statistical significance of NRMSE comparisons for the reconstructions with 15 different sets of under-sampling patterns. The results of paired t-tests for image 1, image 2, and the T1 map are shown.

This observation can be explained by looking at the effects of error in the two intensity images on the final T1 values determined by [DESPOT1](#). The T1 values are calculated from the slope of the signal intensity equations in linearized form (see the [DESPOT1](#) overview in the Introduction section). In [Figure 4.4\(a\)](#) we plot the error in [DESPOT1](#) reconstruction as a function of the percentage error in the two SPGR images using the same imaging parameters as the experiments and intensity values taken from white matter. In [DESPOT1](#), it is not the magnitude of the errors that affects the quality of the [DESPOT1](#) reconstruction, but the relationship between errors in the two images. [Figure 4.4](#) (b-d) show scatter plots showing the joint distribution of errors of intensity values in the two SPGR images as a percentage of the fully-sampled intensity values at each pixel. The error in T1 is zero along the 45° line marked on the graph, as changing

the intensity values in both images by the same factor does not affect the **DESPOT1** calculations and the error in T1 values increases with distance from this line.

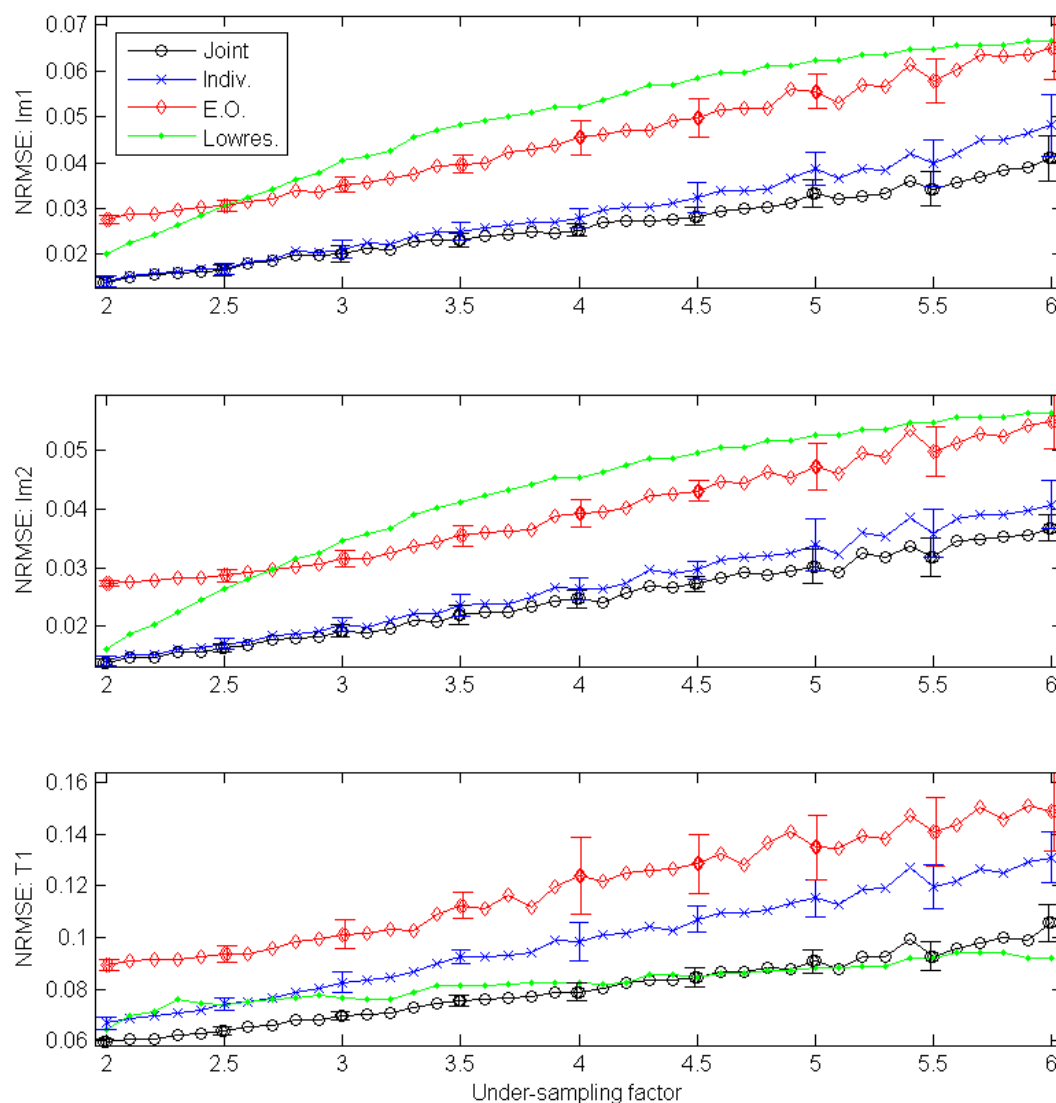


Figure 4.3- Mean NRMSE values and corresponding error bars of one standard deviation for the reconstruction of SPGR images and derived T1 maps of one healthy volunteer from 15 independently under-sampled datasets. For clarity, the error bars are shown at increments of 0.5. However, the growth in the error bars follows a consistent trend.

These plots show that the low resolution reconstruction resulted in errors in the estimated intensity values that are highly correlated between the two images. This is expected as the low resolution sampling is equivalent to smoothing the reference standard images with a sinc kernel. Although the contrast between the two intensity images is different, the basic structure, and much of the overall intensity pattern remains the same. This resulted in a distribution of the intensity errors clustered along the 45° line. On the other hand, the wavelet sparsity based reconstruction methods result in a less correlated intensity error distribution. The net result is that the errors incurred from acquiring a low resolution image, though larger than the individual wavelet reconstruction, had less impact on the computed T1 values.

The joint reconstruction technique continued to perform better than either of these methods at low and middling under-sampling factors. We observed in [Figure 4.4](#) that the errors in the joint reconstruction were more correlated than the individual reconstruction. The similarity-promoting operation was designed to cluster the SPGR intensity values to reduce the joint entropy. As the two images were very positively correlated, this clustering also increased the positive correlation between the errors in SPGR intensity values pushing them towards the 45° line.

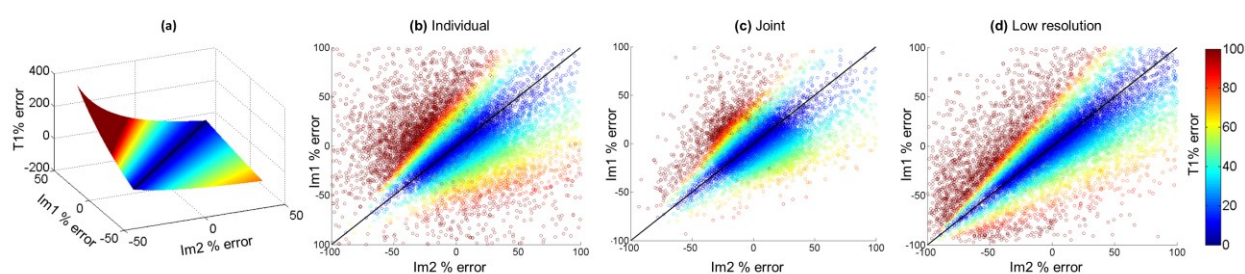


Figure 4.4- The [DESPOT1](#) T1 error is shown as a function of the error in the intensity images in (a) and the distribution of errors in the intensity images is shown for individual reconstruction (b), joint reconstruction (c) and low resolution image (d) acquired with an under-sampling ratio of 4.

[Figure 4.5](#) provides a visual illustration of a typical reconstruction of the SPGR images and derived T1 map for an under-sampling factor 4.

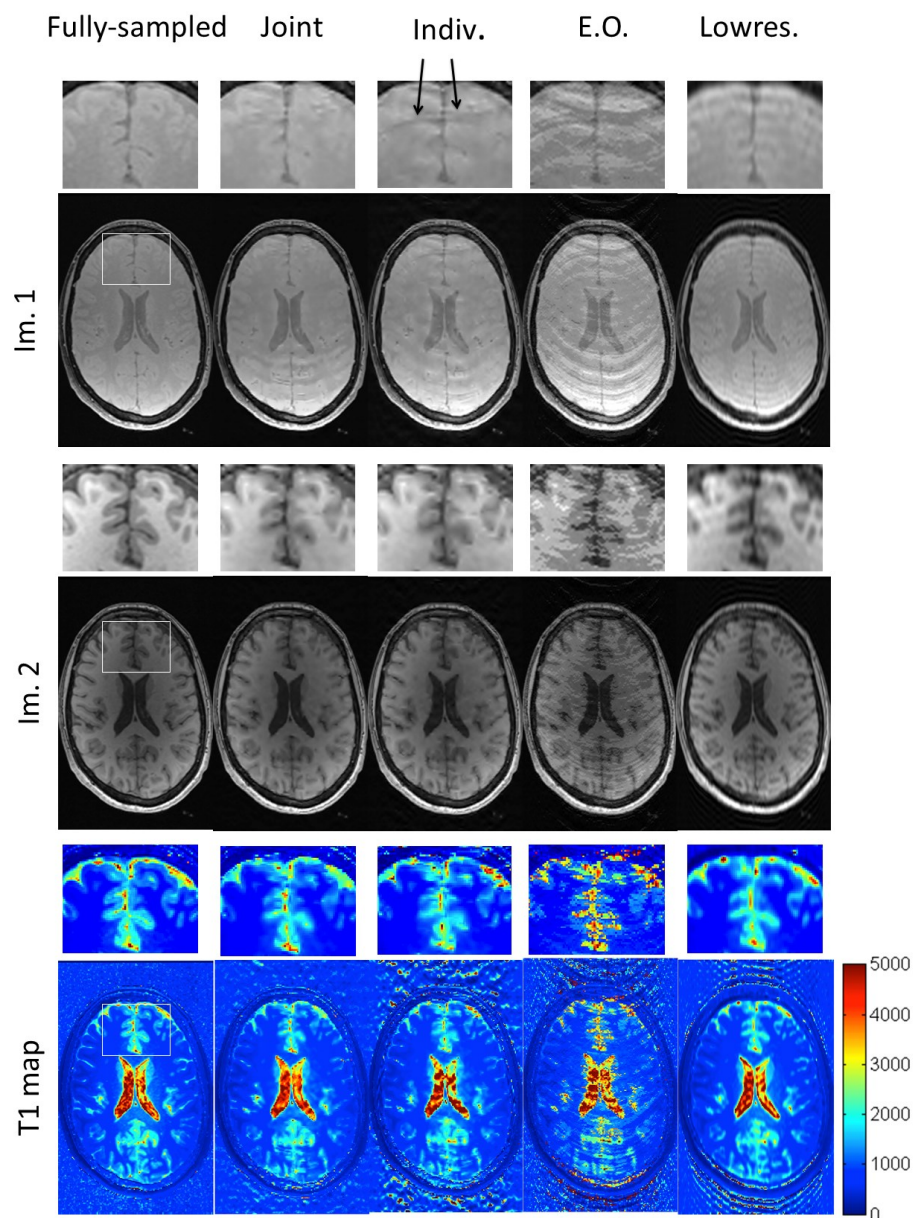


Figure 4.5- Reconstruction of SPGR images at flip angles 4° and 18° with an under-sampling factor of 4, and T1 map computed using [DESPOT1](#). The zooming area is shown by the white box. The arrowhead points to an example of aliasing artifacts present in individual reconstruction that are removed by the joint reconstruction.

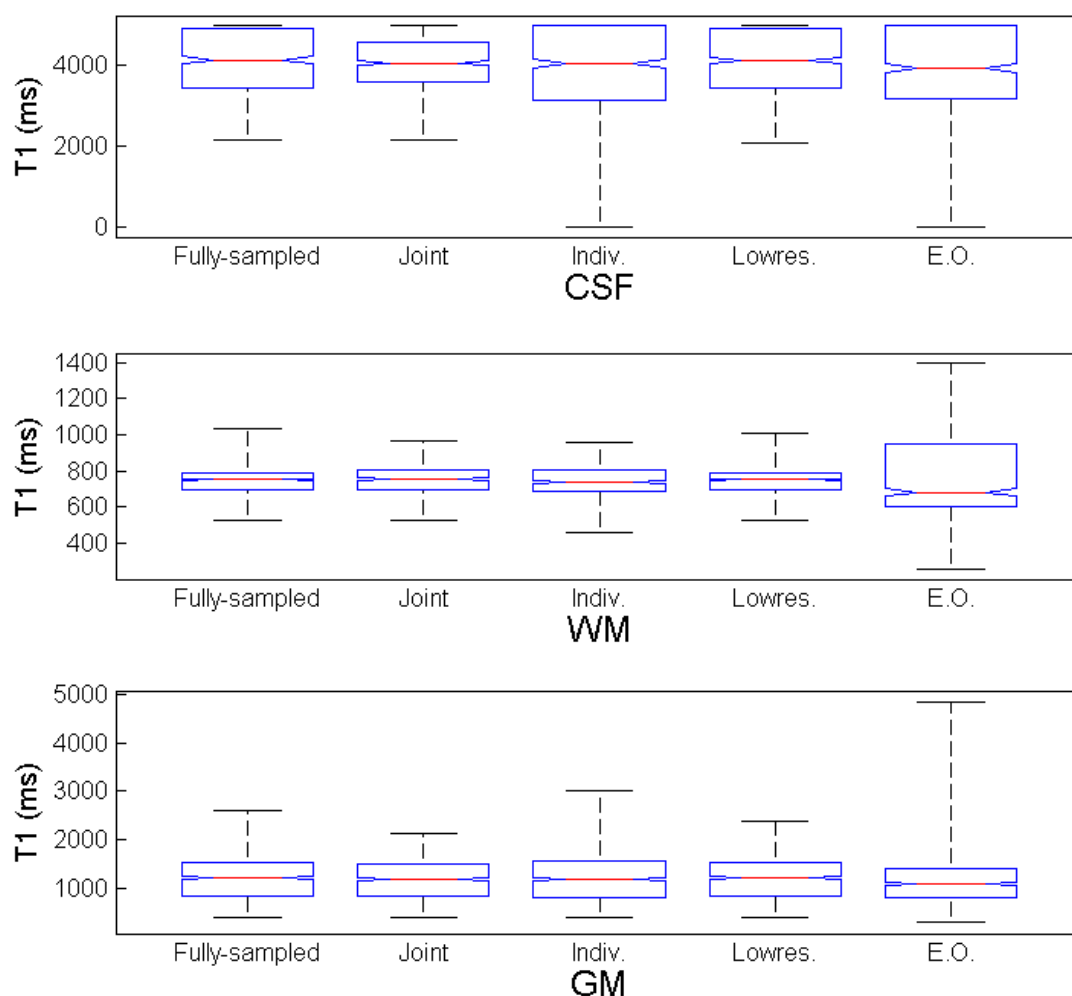


Figure 4.6- Box plots of T1 values over three local ROIs (shown in Figure 4.7) on the WM, GM, and CSF, at an under-sampling factor of 4. The central mark in each box is the median and the edges of the box are the 25th and 75th percentiles.

The box plots in Figure 4.6 show the distribution of T1 values for the different reconstruction methods and fully sampled reference standard over three local ROIs, with the ROIs shown in Figure 4.7. The individual and entropy only reconstructions resulted in wider quartiles and more variation in T1 values in CSF, white matter and grey matter. However, both the joint and low resolution reconstruction resulted in white matter and

grey matter distributions that closely matched the reference standard. For CSF, the low resolution reconstruction produced a distribution similar to the reference standard while the joint reconstructions resulted in slightly less variation as seen from the inner quartile range of the box plots. However, it should be recalled that the flip angles for [DESPOT1](#) are optimized to reconstruct T1 values for white matter and grey matter.

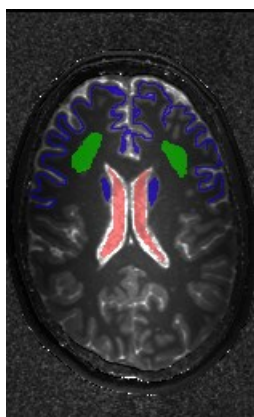


Figure 4.7- Three ROIs representative of white matter (green), gray matter (blue), and cerebrospinal fluid (red), over which the distribution of the T1 values are computed.

4.5 Discussion

The experimental results presented in the previous section confirm my hypothesis that the structural similarity between images acquired at different flip angles can be incorporated as an additional under-sampled reconstruction constraint to improve the reconstruction quality of the images. In particular, the results suggest that joint reconstruction with both similarity and wavelet sparsity constraints can significantly reduce the reconstruction error compared with individual reconstruction based on wavelet sparsity alone. This improved reconstruction quality can make higher under-sampling factors realizable.

We observed that errors in the T1 map depend not only on the errors in the reconstruction of the individual images, but also on how correlated these errors are. Consequently, while under-sampled reconstruction techniques (like those presented in chapters 2 and 3) may improve the quantitative quality metrics of single images, when these images are used for a more complicated calculation like [DESPOT1](#) this does not necessarily translate into

improved results. Joint reconstruction overcomes this issue, improving the NRMSE of both the SPGR images and the derived T1 map.

Finally, the performance of the [Similarity-promoting operation](#) depends on the shift ratio (β in equation (4.4)), the choice of which is dependent on the application. Nevertheless, once set for a particular application, e.g., [DESPOT1](#) with certain flip angles, the shift ratio can be used for all other such acquisitions.

4.6 Conclusion

I showed that in MRI applications involving multiple acquisitions, e.g., [Quantitative MRI: T1/T2 mapping](#), the structural similarity between the acquisitions can be incorporated as a reconstruction constraint, in addition to the conventional (wavelet) sparsity constraints, for the reconstruction of the MR images from under-sampled k-space data to reduce the acquisition time.

An [Iterative reconstruction](#) algorithm was used to jointly reconstruct the images by alternating between the spatial, wavelet, and frequency domains, in which the similarity, wavelet sparsity, and data consistency constraints are re-enforced respectively.

Without loss of generality, we considered [DESPOT1](#) T1 mapping from two spoiled gradient recalled (SPGR) images, acquired at two optimum flip-angles. Human brain SPGR images were acquired at 3T. K-space data were incoherently under-sampled, and the images were jointly reconstructed from the under-sampled data by the proposed [Iterative reconstruction](#).

Joint reconstructions resulted in significantly lower reconstruction errors compared to a more traditional compressed sensing reconstruction of both SPGR images individually. This improvement became even more important when examining the T1 maps generated from the two under-sampled SPGR reconstructions. While the SPGR individual reconstructions substantially outperformed a low resolution acquisition with the same number of scans lines, the T1 map derived from the individual reconstruction was inferior to the T1 map derived from low resolution acquisitions. This demonstrates the difficulty

in using multiple compressed sensing acquisitions for quantitative calculations. However, the joint reconstruction method, which promotes structural similarity between the acquisitions as well as wavelet sparsity, produced T1 maps with significantly less error than those attained from either individual or low resolution reconstructions for a wide range of under-sampling factors.

4.7 References

- [1] A. Macovski, “Noise in MRI,” *Magn. Reson. Med.*, vol. 36, no. 3, pp. 494–497, 1996.
- [2] Z. Chen, F. S. Prato, and C. McKenzie, “T1 fast acquisition relaxation mapping (T1-FARM): an optimized reconstruction,” *IEEE Trans. Med. Imaging*, vol. 17, no. 2, pp. 155–160, Apr. 1998.
- [3] C. A. McKenzie, Z. Chen, D. J. Drost, and F. S. Prato, “Fast acquisition of quantitative T2 maps,” *Magn. Reson. Med. Off. J. Soc. Magn. Reson. Med. Soc. Magn. Reson. Med.*, vol. 41, no. 1, pp. 208–212, Jan. 1999.
- [4] S. C. L. Deoni, B. K. Rutt, and T. M. Peters, “Rapid combined T1 and T2 mapping using gradient recalled acquisition in the steady state,” *Magn. Reson. Med.*, vol. 49, no. 3, pp. 515–526, Mar. 2003.
- [5] M. Lustig, D. Donoho, and J. M. Pauly, “Sparse MRI: The application of compressed sensing for rapid MR imaging,” *Magn. Reson. Med.*, vol. 58, no. 6, pp. 1182–1195, Dec. 2007.
- [6] E. J. Candes and M. B. Wakin, “An Introduction To Compressive Sampling,” *Signal Process. Mag. IEEE*, vol. 25, no. 2, pp. 21–30, 2008.
- [7] D. L. Donoho, “Compressed sensing,” *IEEE Trans. Inf. Theory*, vol. 52, no. 4, pp. 1289–1306, Apr. 2006.
- [8] M. Doneva, P. Börnert, H. Eggers, C. Stehning, J. Sénégas, and A. Mertins, “Compressed sensing reconstruction for magnetic resonance parameter mapping,” *Magn. Reson. Med. Off. J. Soc. Magn. Reson. Med. Soc. Magn. Reson. Med.*, vol. 64, no. 4, pp. 1114–1120, Oct. 2010.
- [9] J. V. Velikina, A. L. Alexander, and A. Samsonov, “Accelerating MR parameter mapping using sparsity-promoting regularization in parametric dimension,” *Magn. Reson. Med.*, p. n/a–n/a, 2012.
- [10] C. Huang, C. G. Graff, E. W. Clarkson, A. Bilgin, and M. I. Altbach, “T2 mapping from highly undersampled data by reconstruction of principal component coefficient

maps using compressed sensing,” *Magn. Reson. Med.*, vol. 67, no. 5, pp. 1355–1366, 2012.

- [11] F. H. Petzschner, I. P. Ponce, M. Blaimer, P. M. Jakob, and F. A. Breuer, “Fast MR parameter mapping using k-t principal component analysis,” *Magn. Reson. Med.*, vol. 66, no. 3, pp. 706–716, 2011.
- [12] I. Daubechies, M. Defrise, and C. De Mol, “An iterative thresholding algorithm for linear inverse problems with a sparsity constraint,” *Commun. Pure Appl. Math.*, vol. 57, no. 11, pp. 1413–1457, Nov. 2004.
- [13] D. Ma, V. Gulani, N. Seiberlich, K. Liu, J. L. Sunshine, J. L. Duerk, and M. A. Griswold, “Magnetic resonance fingerprinting,” *Nature*, vol. 495, no. 7440, pp. 187–192, Mar. 2013.
- [14] D. L. Donoho, “De-noising by soft-thresholding,” *IEEE Trans. Inf. Theory*, vol. 41, no. 3, pp. 613–627, May 1995.
- [15] K. Fukunaga and L. Hostetler, “The estimation of the gradient of a density function, with applications in pattern recognition,” *IEEE Trans. Inf. Theory*, vol. 21, no. 1, pp. 32 – 40, Jan. 1975.
- [16] B. W. Silverman, *Density Estimation for Statistics and Data Analysis*. Taylor & Francis, 1986.
- [17] L. Birge and P. Massart, “From model selection to adaptive estimation,” *Festschr. Lucien Cam Res. Pap. Probab. Stat.*, pp. 55–87, 1997.
- [18] N. Otsu, “A threshold selection method from gray-level histograms,” *IEEE Trans. Syst. Man Cybern.*, vol. 9, no. 1, pp. 62–66, Jan. 1979.

5 Driven equilibrium single pulse observation of T1 with high-speed incorporation of RF field inhomogeneities (DESPOT1-HIFI)

During the course of these PhD studies, [DESPOT1/DESPOT2 T₁ and T₂ mapping](#) were frequently used. This inevitably involved a closer inspection of the pulse sequences, which resulted in a modification to an extension of DESPOT, known as *DESPOT-HIFI*, which addresses some limitations of the conventional DESPOT due to RF field inhomogeneities at high magnetic fields (3T and above). In this chapter, a modified version of DESPOT-HIFI resulting in more accurate estimation of T1 values at high magnetic fields is presented.

5.1 Introduction

As noted in section [1.3.1](#), The driven equilibrium single pulse observation of T1 ([DESPOT1](#)) is a fast and robust T1 mapping technique based on acquisition of spoiled gradient echo images [1]–[3]. This technique is currently considered the most efficient quantitative mapping technique [4].

In conventional DESPOT1 a T1 map is derived from two spoiled gradient recalled (SPGR) images acquired at optimal flip angles [2], [3]. The SPGR signal intensity, S_{SPGR} , is a function of the longitudinal relaxation time, T_1 , repetition time, TR , flip angle, α :

$$S_{SPGR} = \frac{\rho(1-E_1)\sin\alpha}{1-E_1\cos\alpha} \quad (5.1)$$

Where $E_1 = \exp\left(-\frac{TR}{T_1}\right)$, and ρ is a factor proportional to the longitudinal magnetization.

By holding TR constant and incrementally increasing α , a curve characterized by T_1 is generated, which can be represented in a linear form ($Y = mX + b$) as:

$$\frac{SPGR}{\sin \alpha} = E_1 \frac{SPGR}{\tan \alpha} + \rho(1 - E_1) \quad (5.2)$$

The slope, m , and intercept, b , can be estimated by linear regression, from which T_1 and ρ can be extracted:

$$T_1 = -TR/\ln(m) \quad (5.3)$$

and

$$\rho = b/(1 - m) \quad (5.4)$$

While this approach permits rapid T1 mapping, the estimated T_1 and ρ values are very sensitive to the variations of the transmitted flip angle from the prescribed value, which can result in inaccuracies due to RF field inhomogeneity. In particular, at high magnetic field strengths, such as 3T or above, or when nonsymmetrical RF surface coils are used, the homogeneity of the RF B_1 field cannot be ensured. In such cases, the variations of the transmitted flip angle with respect to the prescribed value is often modeled as $\alpha_T = \kappa\alpha_p$, where κ denotes the spatial variations of the RF field [5].

In order to account for the spatial inhomogeneity of the RF field, and therefore achieve improved accuracy in the computed T1 map, in [5] Deoni proposed to acquire an additional inversion-recovery SPGR (IR-SPGR) image, and solve for κ , T_1 , and ρ with the combined SPGR and IR-SPGR data. This method is called Driven equilibrium single pulse observation of T1 with high-speed incorporation of RF field inhomogeneities (DESPOT1-HIFI).

Although this approach provides a promising solution for RF field inhomogeneity, the IR-SPGR signal equation used in [5] is incorrect. In IR-SPGR the inversion pulse is followed by a train of spoiled gradient echo pulses. Nevertheless, the signal equation

used in [5] is that of an inversion-recovery spin echo (IR-SE) sequence, which does not apply to IR-SPGR.

This chapter provides a modified IR-SPGR signal equation. The modification is evaluated by phantom and in vivo imaging experiments at 3T.

5.2 Theory

IR-SPGR involves the application of a 180° pulse followed by a delay of TI , and a train of low-angle SPGR pulses, which sample successive lines of k-space [5]. The perturbation due to the SPGR pulse train causes the longitudinal magnetization to recover with a different effective time constant [6], [7]. Nonetheless, if the center of k-space is acquired immediately after the inversion pulse, and a moderate number of RF pulses (up to 128) with a low flip angle ($<10^\circ$) is applied after each inversion, the longitudinal recovery can be assumed to follow the regular T_1 recovery [5]. Therefore,

$$M_z(Tr^-) = M_z(0^+)e^{-Tr/T_1} + M_0(1 - e^{-Tr/T_1}) \quad (5.5)$$

where Tr is the time between successive inversion pulses.

Assuming an adiabatic inversion:

$$M_z(0^+) = -M_z(0^-) \quad (5.6)$$

Additionally, at steady state:

$$M_z(0^-) = M_z(Tr^-) \quad (5.7)$$

Combining equations (5.5), (5.6), and (5.7), the longitudinal magnetization at the beginning of each inversion cycle at steady state is calculated:

$$M_z(0^+) = -\frac{1 - e^{-Tr/T_1}}{1 + e^{-Tr/T_1}} M_0 \quad (5.8)$$

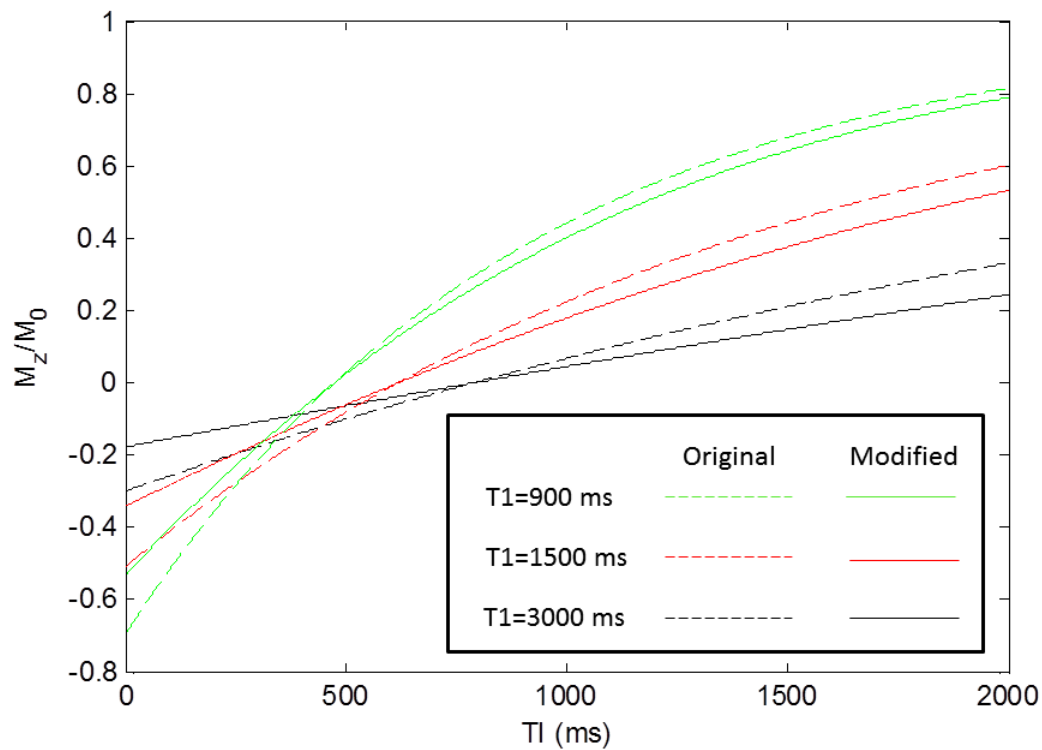


Figure 5.1- Comparison of the original and the modified IR-SPGR equations for three T_1 values representative of the white matter ($T_1=900\text{ms}$), grey matter ($T_1=1500\text{ms}$), and the cerebrospinal fluid ($T_1=3000\text{ms}$) at 3T. The longitudinal magnetization normalized by M_0 is plotted for different values of TI for each case.

based on which, the longitudinal magnetization at time TI at each inversion cycle is derived:

$$M_z(TI^-) = -M_0 \frac{1 - e^{-T_r/T_1}}{1 + e^{-T_r/T_1}} e^{-TI/T_1} + M_0 (1 - e^{-TI/T_1}) \quad (5.9)$$

The IR-SPGR signal is consequently derived. With some algebraic simplifications:

$$S_{IR-SPGR} = \rho \left(1 - \frac{2e^{-TI/T_1}}{1 + e^{-T_r/T_1}} \right) \sin \kappa \alpha_p \quad (5.10)$$

where ρ is a factor proportional to M_0 , and includes T_2^* transverse decay term, e^{-TE/T_2^*} , and B_1 receive field effects.

Figure 5.1 compares the original and the modified IR-SPGR equations for three T1 values representative of the white matter, grey matter, and the cerebrospinal fluid at 3T.

A unique solution for κ , T_1 , and ρ is derived by least squares minimization of the combined SPGR and IR-SPGR data to equations (5.1) and (5.10), i.e., minimization of the function:

$$f(\rho, T_1, \kappa) = \sum_{i=1}^{NTI} \left[\rho \left(1 - \frac{2e^{-TI/T_1}}{1 + e^{-Tr/T_1}} \right) \sin \kappa \alpha_{p,i} - S_{IR-SPGR,i} \right]^2 + \sum_{j=1}^{N\alpha} \left[\frac{\rho(1 - E_1) \sin \alpha_{p,j}}{1 - E_1 \cos \alpha_{p,j}} - S_{SPGR,j} \right]^2$$

5.3 Materials and Methods

Phantom experiments were carried out using a custom made agarose gel phantom comprising 9 nickel chloride doped agarose tubes with the following concentrations: {0, 0.47, 0.7, 1.06, 1.58, 2.37, 3.56, 5.34, 8} mM/l. Reference T1 values were determined by acquiring 2D inversion-recovery fast spin echo (IR-FSE) data at 3T with the following parameters: matrix: 256x256, TE/TR=11.24 ms/5000 ms, TI={100, 400, 800, 1500, 3000} ms, ETL= 16, BW= \pm 15.63 kHz, NEX=0.5. DESPOT1-HIFI data were acquired at 3T with the following parameters: matrix: 256x256x160, resolution = 1mm isotropic, TE/TR = 3.71ms/8.36ms, BW = \pm 19.23 kHz, NEX=1. IR-SPGR data were acquired with TI=450 ms, and $\alpha_p=5^\circ$. SPGR data were acquired with $\alpha_p=4^\circ$ and 18° .

Reference T1 maps were computed by a 3-parameter fit to the IR-FSE data [8]. T1 maps were computed by the conventional DESPOT1 (i.e., DESPOT1 with no RF inhomogeneity correction) with the two SPGR acquisitions, as well as by DESPOT-HIFI based on the modified and the original IR-SPGR signal intensity equations. The former is

referred to as the modified DESPOT-HIFI and the latter is referred to as the original DESPOT-HIFI. The results were compared against the reference IR-FSE T1 values over each of the 9 tubes.

Human brain data of two healthy volunteers were acquired using the same pulse sequences described above at 3T. Human data used in this work were acquired using a protocol approved by the University of Western Ontario Office of Research Ethics.

Similar to the phantom experiments, T1 maps were computed by the conventional DESPOT1 and by the original and modified DESPOT-HIFI and compared against the reference IR-FSE T1 values for different tissues.

5.4 Results

T1 values computed over each of the tubes in the agarose phantom by the conventional DESPOT and by the original and modified DESPOT-HIFI are compared against the reference IR-FSE values in [Figure 5.2](#). While the conventional DESPOT and the original DESPOT-HIFI result in underestimated and overestimated T1 values respectively, the modified DESPOT-HIFI results in the most consistent values with the gold standard.

[Figure 5.3](#) compares the computed T1 values with the contrast concentration for each tube. The T1 values obtained by the modified DESPOT-HIFI follow those of the reference IR-FSE very closely. Additionally, DESPOT-HIFI results in higher correlation between the T1 values and the contrast concentration than the conventional DESPOT.

[Figure 5.4](#) plots T1 values computed by the conventional DESPOT and the original and modified DESPOT-HIFI versus reference values computed based on the IR-FSE acquisitions over three regions of interests (ROI) on white matter, grey matter, and the cerebrospinal fluid for each volunteer. The results generally show the same trend observed with the phantom data. Computed T1 values with different methods are also compared against each other over a few anatomies of interest in [Figure 5.5](#). Sample T1 maps, computed by the original and modified DESPOT-HIFI, and the conventional DESPOT, for one of the healthy volunteers are shown in [Table 5.1](#). The results confirm

that the modified DESPOT-HIFI results in T1 estimates most consistent with the reference T1 values.

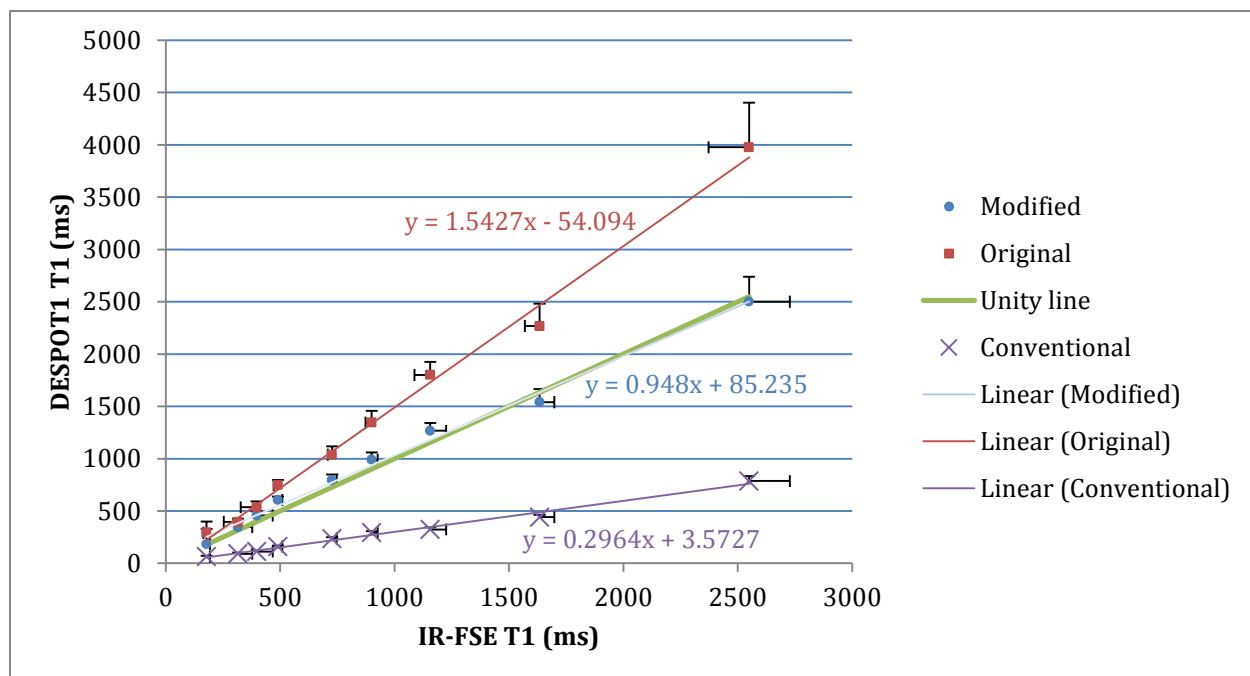


Figure 5.2- Mean T1 values for each tube in the agarose phantom, computed by conventional DESPOT1 and by the original and modified DESPOT1-HIFI versus reference values determined by IR-FSE. The errorbars denote one standard deviation. Linear regressions and the line of unity with the reference T1 values are also shown.

5.5 Discussion and conclusion

While the conventional DESPOT provides an efficient way of computing T1 maps based on the acquisition of two SPGR images at optimal flip angles, it often results in consistently under-estimated T1 values at high magnetic fields, i.e., 3T and above, due to RF field inhomogeneities causing deviations of the transmitted flip angle from that prescribed. To address this problem, Deoni proposed the acquisition of an additional IR-SPGR image to account for the RF field inhomogeneities simultaneous with T1/M0 estimation through least squares minimization of the combined SPGR and IR-SPGR data to the corresponding signal intensity equations. However, the assumed signal intensity equation for the IR-SPGR acquisition is incorrect resulting in consistently overestimated

T1 values. In this chapter, we proposed a modification by deriving the correct IR-SPGR signal intensity equation. The proposed modification was validated on a custom made agarose gel phantom doped with different concentration of nickel chloride resulting different T1 values as well as for *in vivo* human brain T1 mapping. The modified DESPOT-HIFI results in T1 values much more consistent with the reference values computed based on a number of IR-FSE acquisitions.

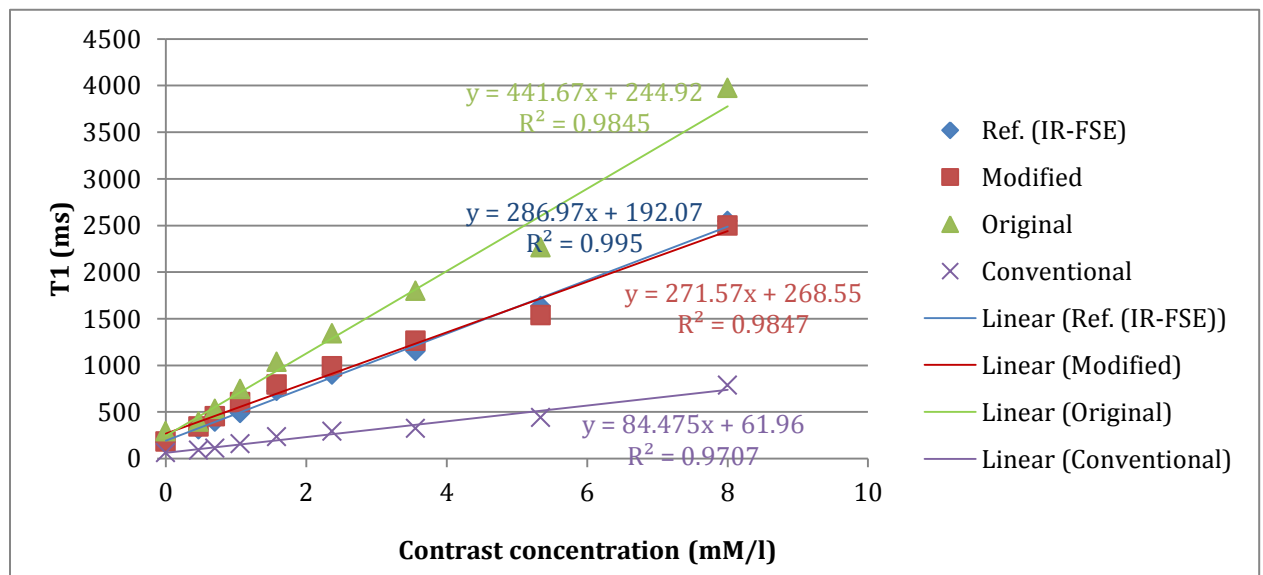


Figure 5.3- Mean T1 values, computed by the conventional DESPOT1, the original and modified DESPOT1-HIFI, and the IR-FSE reference, for each tube in the agarose phantom, versus nickel chloride concentration of the tube.

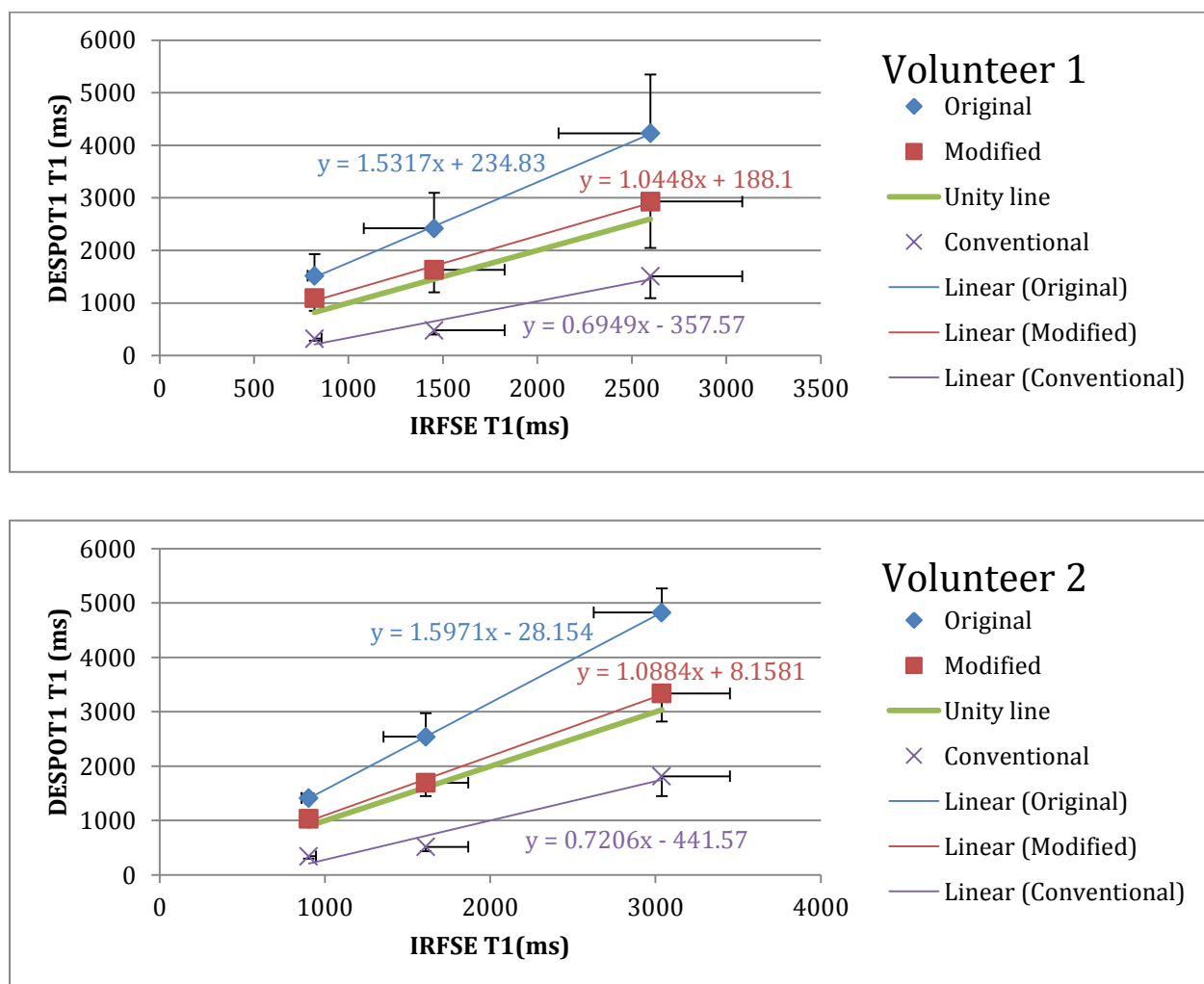


Figure 5.4- Mean T1 values computed by the conventional DESPOT and by the original and modified DESPOT-HIFI versus reference values computed based on IR-FSE acquisitions over three regions of interests (ROI) on white matter (WM), grey matter (GM) and cerebrospinal fluid (CSF). WM ROI includes areas on the frontal lobe, parietal lobe, and corpus callosum, GM ROI includes areas on the cerebral cortex and the caudate nucleus, and CSF ROI includes areas on the lateral ventricle. The errorbars denote one standard deviation. Linear regressions and the line of unity with the reference T1 values are also shown.

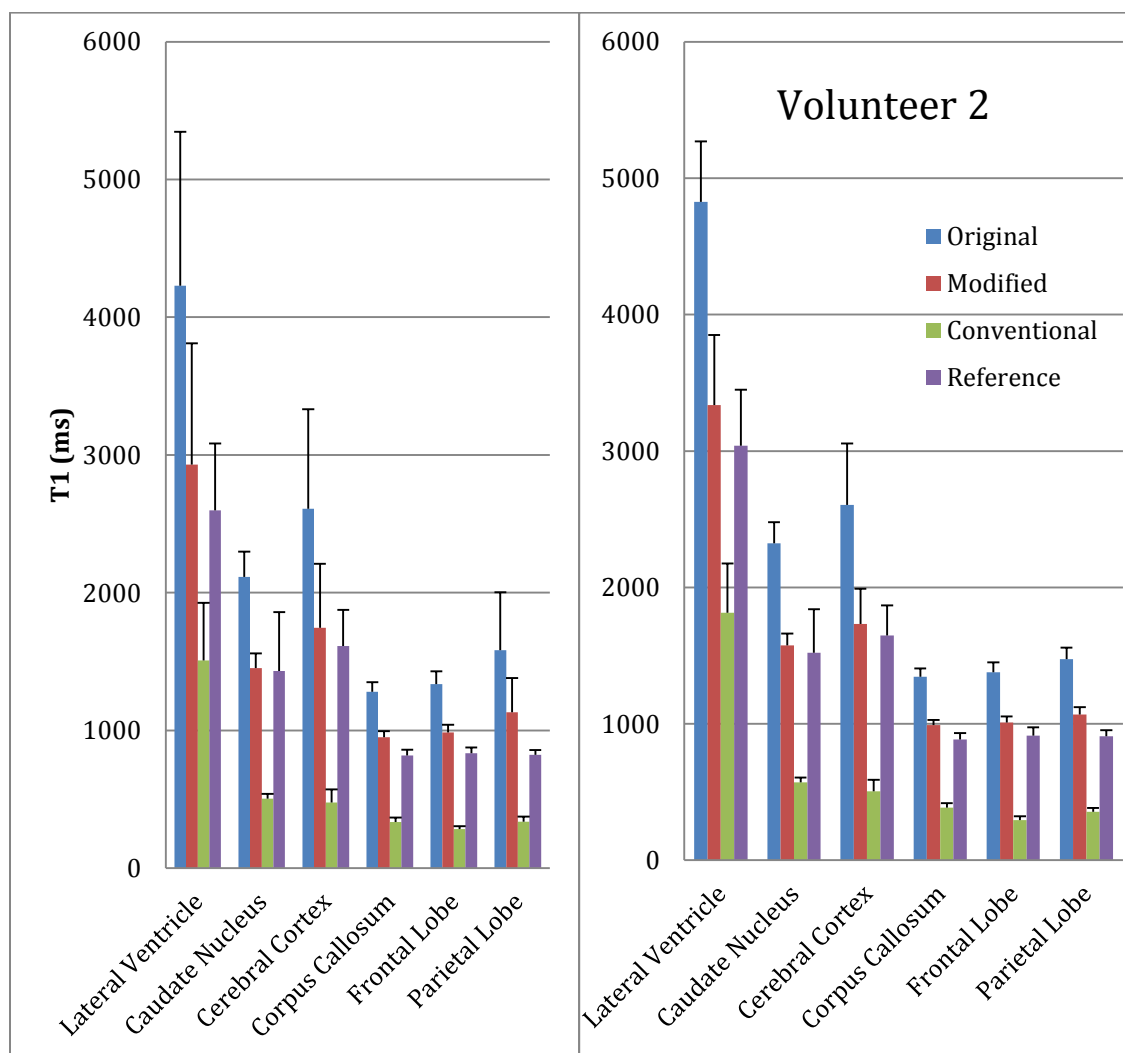


Figure 5.5- Mean T1 values with the errorbars of one standard deviation computed by the conventional DESPOT1, the original and modified DESPOT1-HIFI, and the IR-FSE reference over some anatomies of interest.

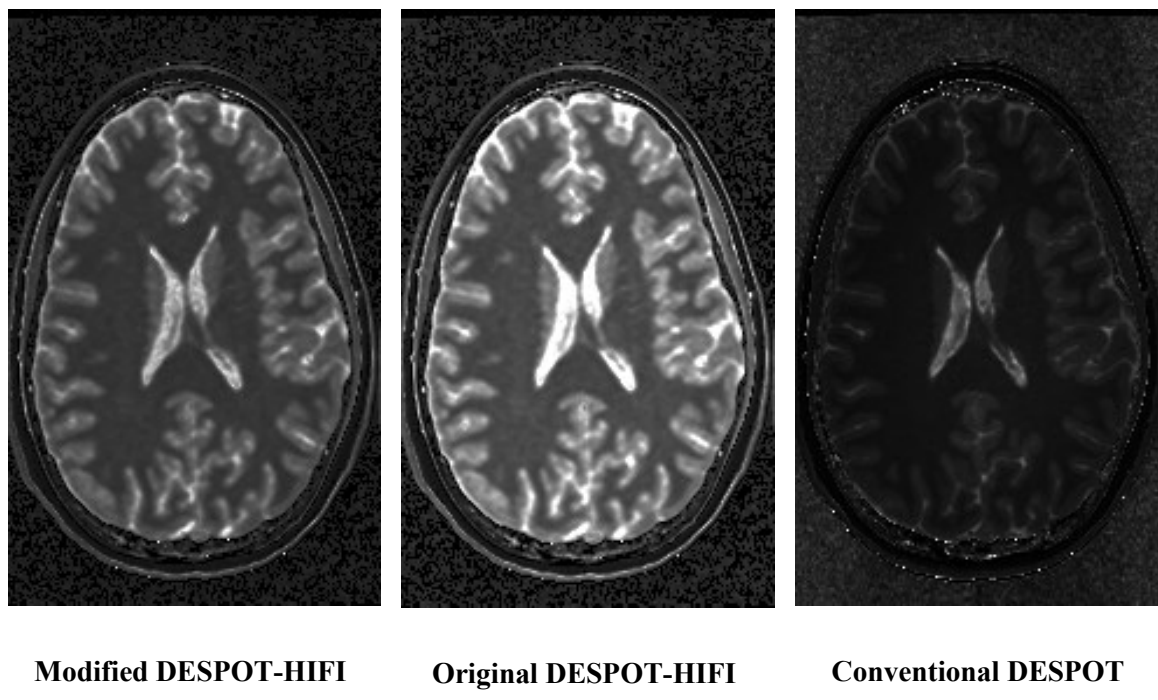


Table 5.1- Sample T1 maps computed by the original and modified DESPOT-HIFI and by the conventional DESPOT1 for a healthy volunteer.

5.6 References

- [1] J. Homer and M. S. Beevers, "Driven-equilibrium single-pulse observation of T1 relaxation. A reevaluation of a rapid 'new' method for determining NMR spin-lattice relaxation times," *J. Magn. Reson.* 1969, vol. 63, no. 2, pp. 287–297, Jun. 1985.
- [2] H. Z. Wang, S. J. Riederer, and J. N. Lee, "Optimizing the precision in T1 relaxation estimation using limited flip angles," *Magn. Reson. Med.*, vol. 5, no. 5, pp. 399–416, 1987.
- [3] S. C. L. Deoni, B. K. Rutt, and T. M. Peters, "Rapid combined T1 and T2 mapping using gradient recalled acquisition in the steady state," *Magn. Reson. Med.*, vol. 49, no. 3, pp. 515–526, Mar. 2003.
- [4] D. Ma, V. Gulani, N. Seiberlich, K. Liu, J. L. Sunshine, J. L. Duerk, and M. A. Griswold, "Magnetic resonance fingerprinting," *Nature*, vol. 495, no. 7440, pp. 187–192, Mar. 2013.

- [5] S. C. L. Deoni, "High-resolution T1 mapping of the brain at 3T with driven equilibrium single pulse observation of T1 with high-speed incorporation of RF field inhomogeneities (DESPOT1-HIFI)," *J. Magn. Reson. Imaging JMRI*, vol. 26, no. 4, pp. 1106–1111, Oct. 2007.
- [6] D. C. Look and D. R. Locker, "Time Saving in Measurement of NMR and EPR Relaxation Times," *Rev. Sci. Instrum.*, vol. 41, no. 2, pp. 250–251, Feb. 1970.
- [7] G. Brix, L. R. Schad, M. Deimling, and W. J. Lorenz, "Fast and precise T1 imaging using a TOMROP sequence," *Magn. Reson. Imaging*, vol. 8, no. 4, pp. 351–356, 1990.
- [8] C. Y. Tong and F. S. Prato, "A novel fast T1-mapping method," *J. Magn. Reson. Imaging*, vol. 4, no. 5, pp. 701–708, 1994.

6 Subjective reconstruction quality assessment

So far throughout this thesis the assessment of the quality of reconstruction achieved by different methods and how different reconstructions compare against each other was solely based on quantitative measures, e.g., the reconstruction error with respect to the fully-sampled reference. However, although useful to some extent, these quantitative measures do not necessarily correlate completely with the perceptual quality judgment made by radiologists and other expert end users. Consequently, unless accompanied by subjective clinical evidence, any conclusion solely based on quantitative evidence is of limited clinical impact. Therefore, a number of experiments were carried out with the help collaborating radiologists, aiming at subjective quality assessment and comparison of under-sampled reconstruction techniques, the results of which is presented in this chapter.

6.1 Introduction

As described in the previous chapters, which were primarily focused on [Under-sampled MRI reconstruction](#), signal-to-noise ratio (SNR) in magnetic resonance imaging (MRI) is proportional to the voxel volume and the square root of the acquisition time [1], which implies that reasonably high resolution and SNR are only achieved at the expense of long acquisition times. Therefore, acceleration of MRI acquisitions without compromising the resolution and/or SNR has been an active field of research since the introduction of this modality [2] (and references therein). In addition to advancements in hardware and pulse sequence design, two major categories of acceleration techniques are [Parallel imaging](#) [3]–[5] and [Compressed sensing](#) [6], both of which reduce the acquisition time by acquiring under-sampled k-space data. However, in the former approach missing k-space data are interpolated based on the knowledge of the coil sensitivity profiles, while the latter interpolates the missing data by imposing a sparsity constraint in a transform

domain on the image. Under-sampled reconstruction techniques based on joint application of parallel imaging and compressed sensing have also been developed [7].

Although quantitative quality measures, such as the normalized root mean square error (NRMSE), contrast-to-noise ratio (CNR), and SNR, are commonly used to assess the reconstruction quality of these techniques, these measures do not necessarily completely correlate with the practical image quality as perceived by radiologists and other expert end users. A few authors have attempted to assess the under-sampled reconstruction quality based on subjective scoring of the images for parallel imaging [8], [9] and compressed sensing [10].

In this chapter we present the results of my study on the subjective quality measurement of compressed sensing, and combined compressed sensing and parallel imaging (where multiple-channel data are available) reconstructions.

6.2 Methods

6.2.1 Study design

While the performance of parallel imaging techniques generally depends on hardware specifications of the imaging system, e.g., number of channels and the g-factor [2], the performance of compressed sensing reconstructions is determined by the underlying image- it is known that compressed sensing generally does better with images with a sparser representation in the sparse transform domain, an example of which is magnetic resonance angiography (MRA) images, which often result in very sparse transform-domain representations [6]. Furthermore, clinical applications vary in terms of their resolution requirements and susceptibility to reconstruction artifacts. Therefore, it is expected to achieve varying degrees of performance/improvement by compressed sensing depending on the application. In this chapter three common clinical applications of MRI in neuroradiology are considered: detection of white matter lesions, cranial nerve imaging, and magnetic resonance angiography (MRA).

6.2.1.1 Detection of white matter lesions

This task involves detection of small non-specific white matter lesions on T2-FLAIR images. Artificial but realistic white matter lesions were incorporated onto FLAIR brain images of a healthy volunteer as follows:

A typical white matter lesion was identified on T2-FLAIR brain image of a multiple sclerosis patient by a senior neuroradiology resident. The lesion was cropped from a 2D slice (approximate lesion size = 2.5mm in diameter). Whole-brain T2-FLAIR images of a healthy volunteer were also acquired (TR/TE=8000ms/120.9ms, TI=2250ms, flip angle=90°, matrix=256x256, BW = 0.86mm isotropic), slice thickness=2mm, slice spacing=2.5, BW=31.3kHz, NEX=1), based on which test images were generated by artificially incorporating the lesion into the acquired axial 2D FLAIR images in random locations in the cerebral white matter where these lesions are commonly seen clinically, with a probability of 50%. In order to preserve the SNR on the destination image, merging was carried out by manipulating the intensity levels on the destination image to match those of the lesion relative to its background. [Figure 6.1](#) shows a sample test image generated in this manner. Human data used in this work were acquired using a protocol approved by the University Of Western Ontario Office Of Research Ethics.

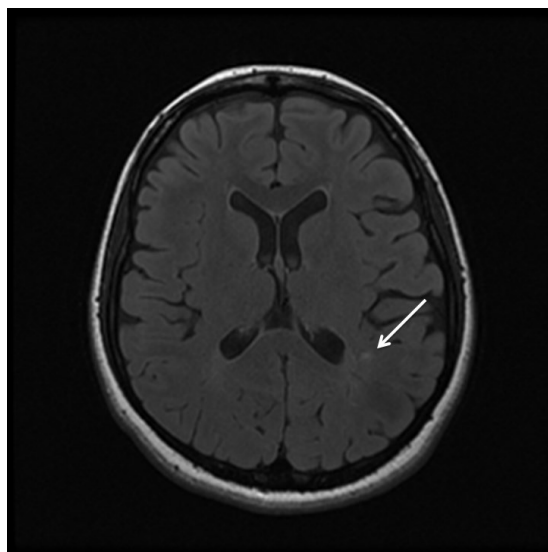


Figure 6.1- Sample white matter lesion artificially incorporated in a FLAIR image.

The test images, generated as described above, were under-sampled in the Fourier domain to generate low-resolution and compressed sensing under-sampled reconstructions. Low-resolution reconstruction was used as a control baseline. For compressed sensing, under-sampling was done based on a variable density scheme appropriate for compressed sensing [6]. Compressed sensing reconstruction was carried out using [Iterative stationary wavelet transform thresholding](#). The set of test images included under-sampling factors 1, i.e., no under-sampling, 2, 3, 4, and 5, each with 30 images for each reconstruction (low-resolution and compressed sensing) totaling to 300 images.

The images were viewed by 3 senior radiology residents in randomized orders. The experiments involved identification of the lesion or declaring there is none, while the participants also indicate their level of confidence using a 4-score ranking system (1: non diagnostic; 2: low confidence; 3: moderately confident; 4: high confidence).

6.2.1.2 Cranial nerve imaging

Whole brain 3D images of a healthy volunteer were acquired at 3T using a 32-channel head coil with a multiacquisition SSFP (or CISS, also known as FIESTA-C) pulse sequence with the following parameters: TR/TE=5.5 ms/2.4 ms, flip angle=55°, matrix: 288x288 (pixel spacing=0.63mm isotropic), slice thickness=1 mm, slice spacing=1 mm, BW=46.9 kHz, NEX=1. A sample multiacquisition SSFP image is shown in [Figure 6.2](#).

Raw k-space data were retrospectively under-sampled with under-sampling factors 2, 3, 4, and 5, for [GRAPPA](#) parallel imaging, [Iterative stationary wavelet transform thresholding](#) ([Table 6.1](#)), and low-resolution reconstruction, obtaining a total of 12 whole brain under-sampled datasets, which were then reconstructed by the corresponding reconstruction technique.

The reconstructions were viewed and scored by three senior radiology residents. The fully-sampled image was presented to each participant followed by the reconstructed images presented at random orders. The participant was requested to score each

reconstruction based on the diagnostic quality of the cranial nerves, with a 5-point scoring system (1: not interpretable, 2: severely degraded, 3: moderately degraded, 4: mildly degraded, 5: no significant artifacts).

Furthermore, in another set of experiments, the three reconstructions at each under-sampling factor were presented to the participant side-by-side, with randomized orders, and the participant was requested to rank them based on the diagnostic quality of the cranial nerves (1 being the best and 3 the worst.)



Figure 6.2- Sample multiacquisition SSFP image (fully-sampled reconstruction).

6.2.1.3 Magnetic resonance angiography (MRA)

Whole brain 3D time of flight (TOF) MR angiogram of a healthy volunteer was acquired at 3T using a 32-channel head coil with the following parameters: TR/TE=20 ms/2.6 ms, flip angle=15°, matrix=216x168 (pixel spacing=1.1mmx1.4mm), slice thickness=1.4 mm, slice spacing= 1.4 mm, BW=10.3 kHz, NEX=1.

Similar to the FIESTA experiments, raw k-space data were retrospectively under-sampled and reconstructed by parallel imaging, combined parallel imaging and compressed sensing (Table 6.1), and the low-resolution reconstruction. The reconstructed

images were scored and ranked similar to the FIESTA reconstructions, based on the diagnostic quality of the vessels.

All the images were viewed by the participants on a commercial LCD display in a room with normal lighting. While this inevitably imposes some limitations since the images are usually viewed in a dark room in the radiology department, due to space constraints, we were unable to perform the experiments in a dark room.

Multiple-coil iterative thresholding reconstruction algorithm

Inputs:

$F_{u,i}$: Under-sampled k-space data ($i = 1, \dots, N_c$, where N_c is the number of coils)

s_i : Coil sensitivities

U_F : Under-sampling operations selecting k-space data

Output:

F_i : Reconstructed k-space data

Algorithm:

// Initialize to the minimum energy reconstruction

for $i \leftarrow 1:N_c$ do

$F_i \leftarrow F_{u,i}$

end

//Reconstruct through iterative thresholding

while *not converged* do

//combine multiple channel data

$f_{opt} \leftarrow \sum_{i=1}^{N_c} \omega_i \frac{f_i}{s_i}$ //where $f_i = \mathcal{F}^{-1}F_i$ and $\omega_i = \frac{s_i^2}{\sum_{j=1}^{N_c} s_j^2}$

//thresholding

$\tilde{f} \leftarrow \Gamma f_{opt}$

//data consistency

for $i \leftarrow 1:N_c$ do

$\tilde{F}_i \leftarrow \mathcal{F}(s_i \tilde{f})$

$F_i \leftarrow \tilde{F}_i - U_F \tilde{F}_i + F_{u,i}$

end

end

Table 6.1- Multiple-coil iterative thresholding reconstruction algorithm. \mathcal{F} and Γ denote the Fourier transform and wavelet thresholding operations, respectively.

6.3 Results

6.3.1 Detection of white matter lesions

Figure 6.3 shows the pooled (i.e., cumulative) results of the lesion detection task for the low-resolution and compressed sensing reconstructions. The low-resolution reconstructions resulted in higher true positive and lower false negative fractions.

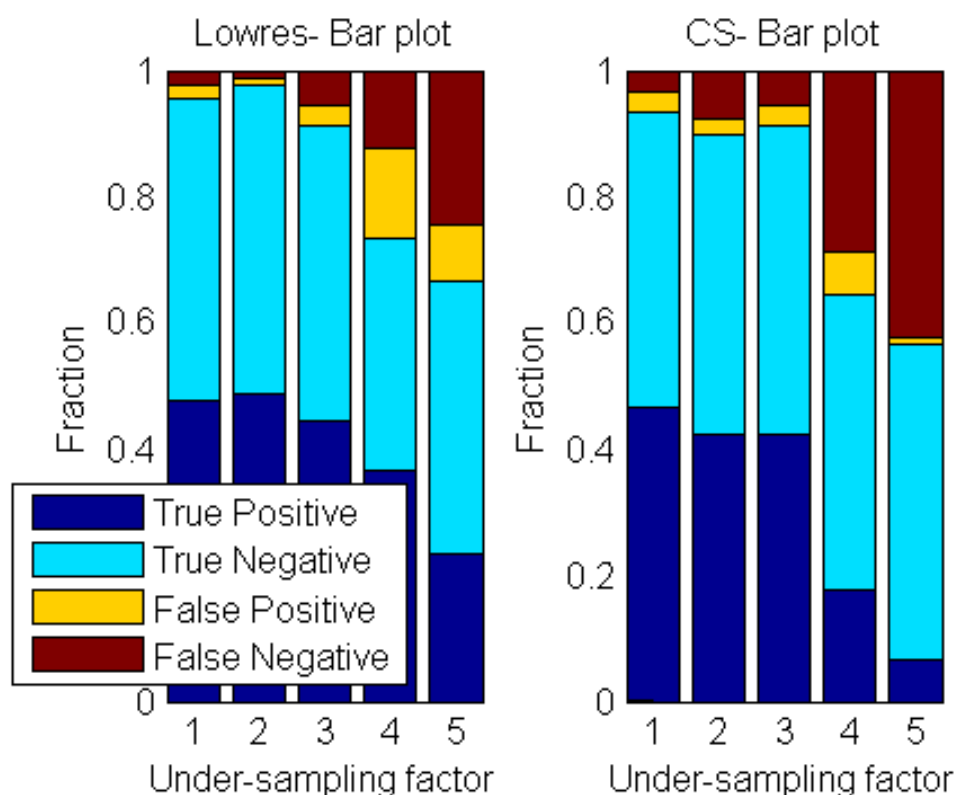


Figure 6.3- Lesion detection performance (pooled) for the compressed sensing (CS) and low-resolution (lowres) reconstructions.

Corresponding ROC curves were computed based on the confidence levels indicated by the participants, following the methodology of Metz [16]. The ROC curves are shown in Figure 6.4. The area under the ROC curves (AUC) and the average of normalized root mean square errors (NRMSE) with respect to the fully-sampled reference images for different under-sampling factors are shown in Table 6.2. The low-resolution reconstructions generally resulted in higher lesion detection accuracy in term of the area

under the ROC curves. However, in terms of the reconstruction errors, compressed sensing reconstructions resulted in lower average NRMSE values.

The reconstruction errors with respect to the fully-sampled reference, measured in terms of the normalized mean square error (NRMSE), are statistically compared in [Table 6.3](#). Compressed sensing reconstructions resulted in significantly lower error values than the low-resolution reconstructions for under-sampling factors 1 to 4.

U.F.	AUC		NRMSE	
	lowres	CS	lowres	CS
1	0.99	0.96	0	0
2	1.0	0.97	0.013	0.0082
3	0.96	0.97	0.024	0.012
4	0.81	0.77	0.033	0.023
5	0.78	0.67	0.042	0.038

Table 6.2- Area under ROC curves (AUC) and the average normalized mean square error (NRMSE) for different under-sampling factors (UF) in the lesion detection task (pooled results). Corresponding ROC curves are shown in [Figure 6.4](#).

The area under the ROC curves (AUC) is compared against the average normalized root mean square error (NRMSE) of the low-resolution and compressed sensing reconstructions for each under-sampling factor in [Figure 6.5](#).

While compressed sensing reconstructions resulted in significantly lower error values than the corresponding low-resolution reconstructions ([Table 6.3](#)), no improvement in lesion detection accuracy was observed with compressed sensing over the simple low-resolution reconstructions. In fact, better detection performance was observed with a simple low-resolution reconstruction.

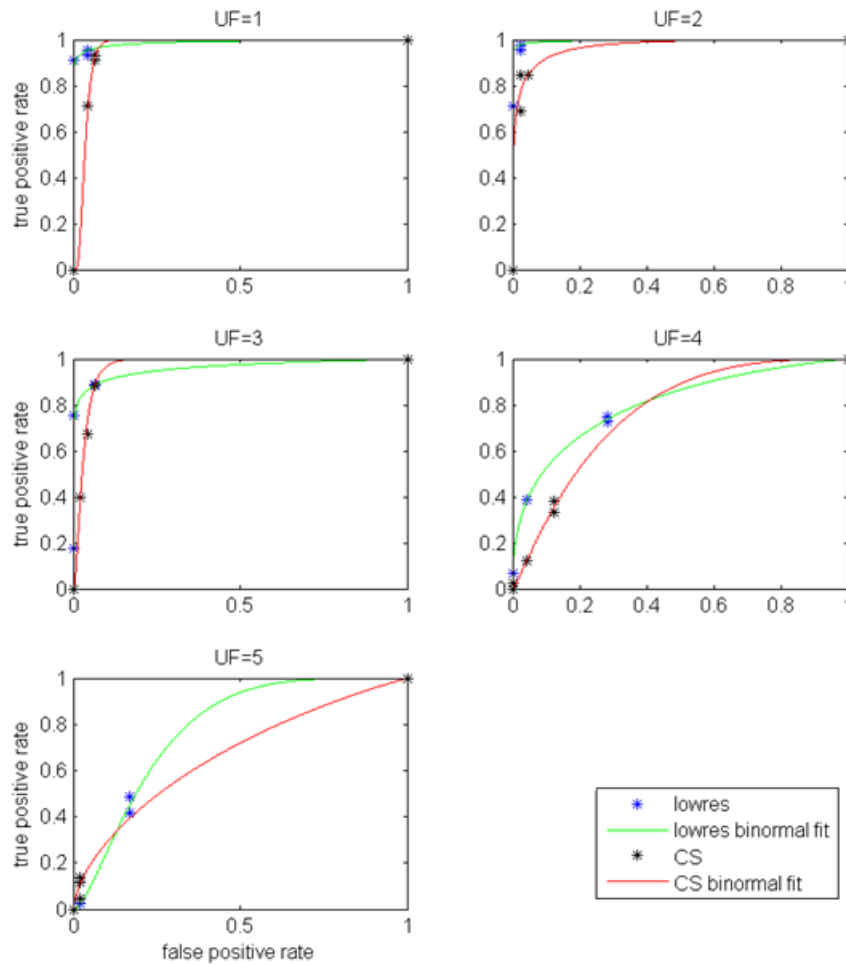


Figure 6.4- ROC curves corresponding to the lesion detection task (pooled results).

Two-sample t test ($\overline{NRMSE}_{CS} - \overline{NRMSE}_{lowres}$)

U.F.	Confidence Interval	P-value
1	0	1
2	$-4.5e-03 \pm 7.7e-04$	$4.9e-13$
3	$-1.2e-02 \pm 1.9e-03$	$4.7e-14$
4	$-9.8e-03 \pm 5.0e-03$	$2.0e-04$
5	$-4.5e-03 \pm 7.0e-03$	$1.0e-01$

Table 6.3- Statistical comparison of the low-resolution (lowres) and compressed sensing (CS) reconstruction errors (NRMSE) in terms of the confidence intervals and the p-values corresponding to a two-sample t test, for different under-sampling factors.

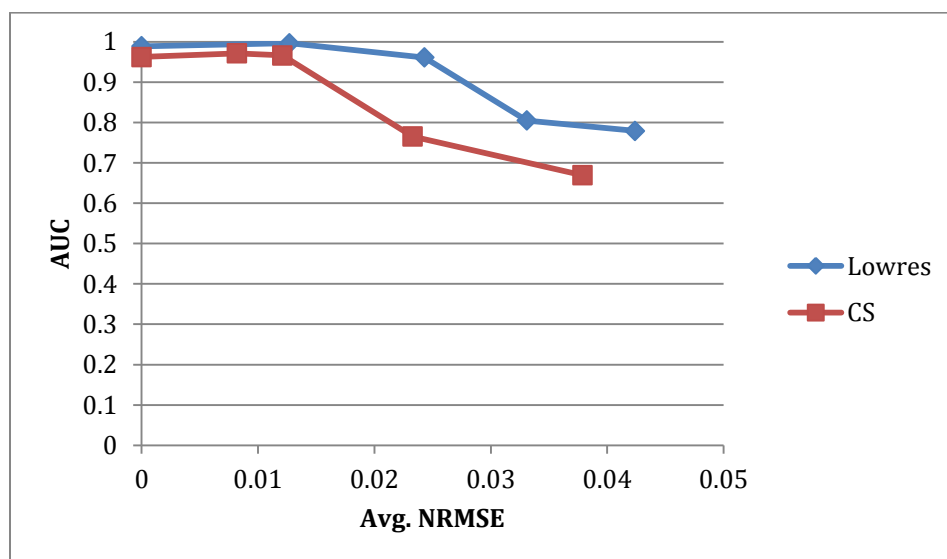


Figure 6.5- Area under ROC curves (AUC) versus average normalized root mean square error for each under-sampling factor for the lesion detection task with compressed sensing (CS) and low-resolution (lowres) reconstructions.

6.3.2 Cranial nerve imaging

The results of the cranial nerve imaging ranking task are shown in [Table 6.4](#), and those of the scoring task are shown in [Table 6.5](#) and [Figure 6.6](#). Except for the low under-sampling factor of 2, combined compressed sensing and parallel imaging is generally ranked the best reconstruction at each under-sampling factor. At under-sampling factor 2, the GRAPPA and CS+PI reconstructions are very similar, as one of the participants ranked them both 1. However, GRAPPA receives slightly better ranking and scoring. Furthermore, while the subjective diagnostic quality score drops for the GRAPPA and low-resolution reconstructions very rapidly with increasing under-sampling factor, the combined CS+PI reconstruction maintains a reasonably high score up to under-sampling factor 4, suggesting that diagnostic quality (i.e., a subjective score of 4 or higher) images are achievable with under-sampling factors as high as 4 by combined compressed sensing and parallel imaging. Also, it is interesting to observe that while for each reconstruction the subjective quality score shows high correlation with the reconstruction error, measured in terms of NRMSE, the correlation follows different trend for different reconstructions.

U.F.	Participant #	GRAPPA	lowres	CS+PI
2	1	1	3	2
	2	1	3	1
	3	1	3	2
3	1	2	3	1
	2	2	3	1
	3	1	3	2
4	1	2	3	1
	2	1	3	1
	3	2	3	1
5	1	2	3	1
	2	2	3	1
	3	3	2	1

Table 6.4- Results of the cranial nerve imaging ranking task for three participants.

6.3.3 Magnetic resonance angiography (MRA)

Table 6.6 shows the results of the MRA ranking task, with those of the scoring task shown in Table 6.7 and Figure 6.8. Sample projection reconstructions at x5 under-sampling are shown in Figure 6.7. The results generally conform to those of the cranial nerve imaging experiments. However, the subjective scores drop more rapidly with increasing under-sampling factor than those of the cranial nerve imaging experiments.

Also, the GRAPPA reconstructions show the most drastic decrease in the subjective score (and increase in the NRMSE) with increasing under-sampling factor. (In terms of the quantitative reconstruction errors, while the NRMSE values of the CS+PI and lowres reconstructions remain within the same range as those of the cranial nerve imaging experiments, GRAPPA results in a noticeable increase in the NRMSE at under-sampling factors 3 and above.) At under-sampling factors 3 and above, GRAPPA performance falls even below the low-resolution reconstruction both in terms of the subjective scores and the NRMSE. In general, for cranial nerve imaging and MRA, while the GRAPPA reconstruction is very effective (in terms of the resulting diagnostic performance) for very low under-sampling factors (2), its limits are reached very fast by increasing the under-sampling factor (3 and above).

U.F.	reconstruction	Avg. score	NRMSE
2	Grappa	5	0.0081
	Lowres	4.7	0.035
	CS+PI	5	0.017
3	Grappa	4.3	0.013
	Lowres	3.3	0.043
	CS+PI	4.7	0.021
4	Grappa	3	0.022
	lowres	2	0.053
	CS+PI	4.3	0.024
5	grappa	2	0.050
	lowres	1	0.060
	CS+PI	3.3	0.026

Table 6.5- Average scores given by three participants for the cranial nerve imaging scoring task and the normalized root mean square error (NRMSE) of the corresponding reconstructions.

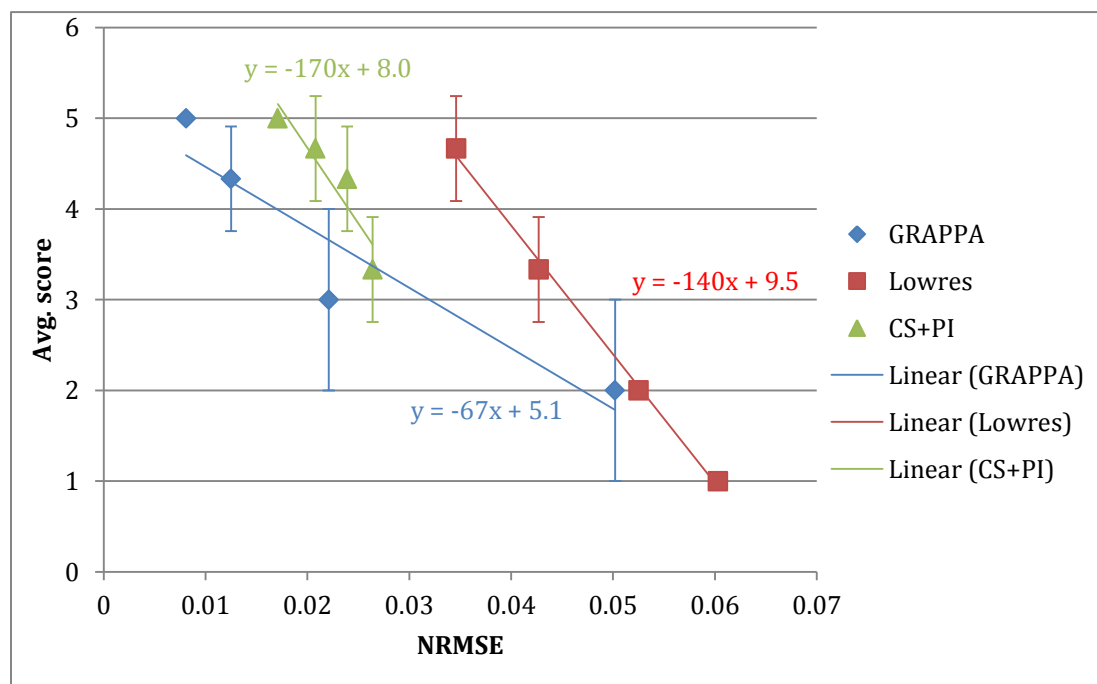


Figure 6.6- Average score (given by three participants) versus the normalized root mean square error (NRMSE) for the cranial nerve imaging scoring task. The error bars show one standard deviation, if non-zero.

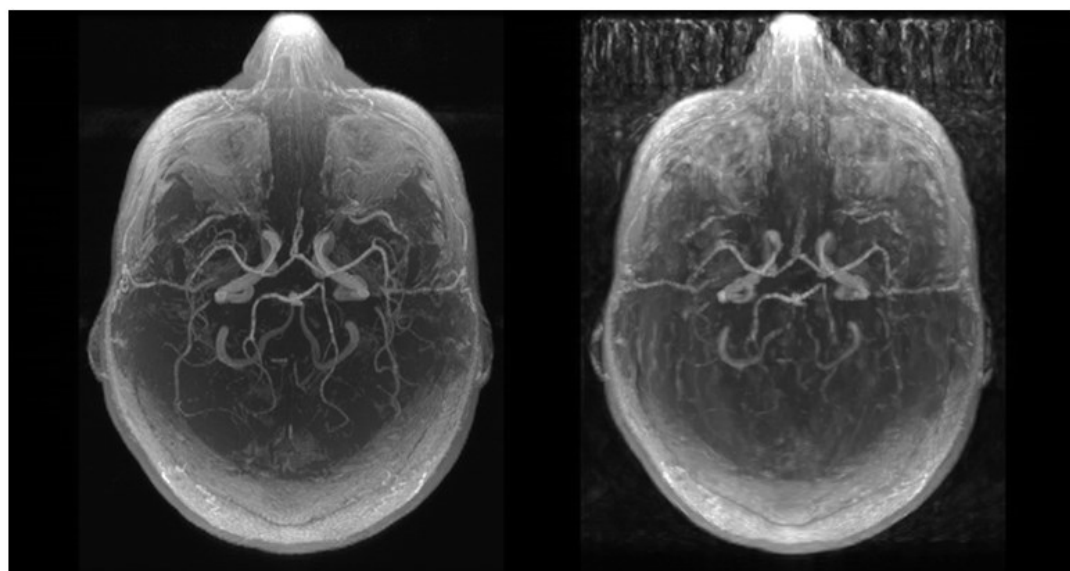
U.F.	Participant #	GRAPPA	lowres	CS+PI
2	1	1	3	2
	2	1	3	1
	3	1	3	2
3	1	3	2	1
	2	3	2	1
	3	3	2	1
4	1	3	2	1
	2	3	2	1
	3	3	2	1
5	1	3	2	1
	2	3	2	1
	3	3	2	1

Table 6.6- Results of the MRA ranking task for three participants.

Although at higher under-sampling factors (3 and above) the subjective scores are generally lower than those of the cranial nerve imaging experiments, the results still suggest that higher under-sampling factors can be achieved by the combined CS+PI reconstruction while maintaining diagnostic quality. (For example, in Table 6.7 CS+PI receives an average score of 4 or higher for under-sampling factors up to 3, while other reconstructions receive a subjective score of 3 or less at under-sampling factor 3 and above.)

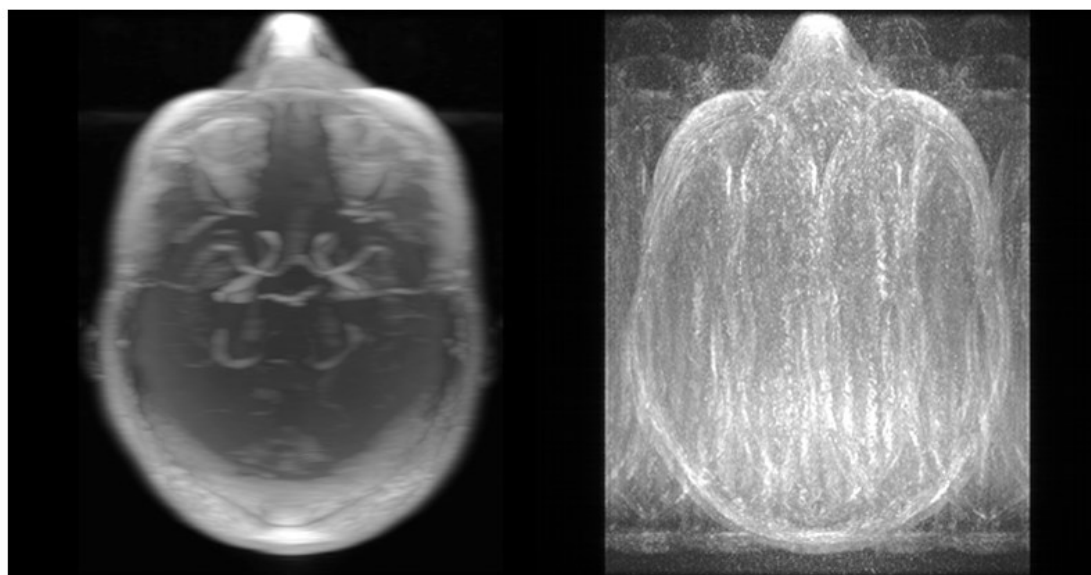
U.F.	reconstruction	Avg. score	NRMSE
2	grappa	5	0.0082
	lowres	4	0.029
	CS+PI	4.7	0.014
3	grappa	1.7	0.11
	lowres	3	0.037
	CS+PI	4	0.025
4	grappa	1	0.14
	lowres	2	0.045
	CS+PI	3.3	0.027
5	grappa	1	0.15
	lowres	2	0.051
	CS+PI	3	0.030

Table 6.7- Average scores given by three participants for the MRA scoring task and the normalized root mean square error (NRMSE) of the corresponding reconstructions.



(a) Fully-sampled

(b) CS+PI



(c) lowres

(D) GRAPPA

Figure 6.7- Maximum intensity projection- Axial view: (a) fully-sampled (b,c,d) 5x under-sampled.

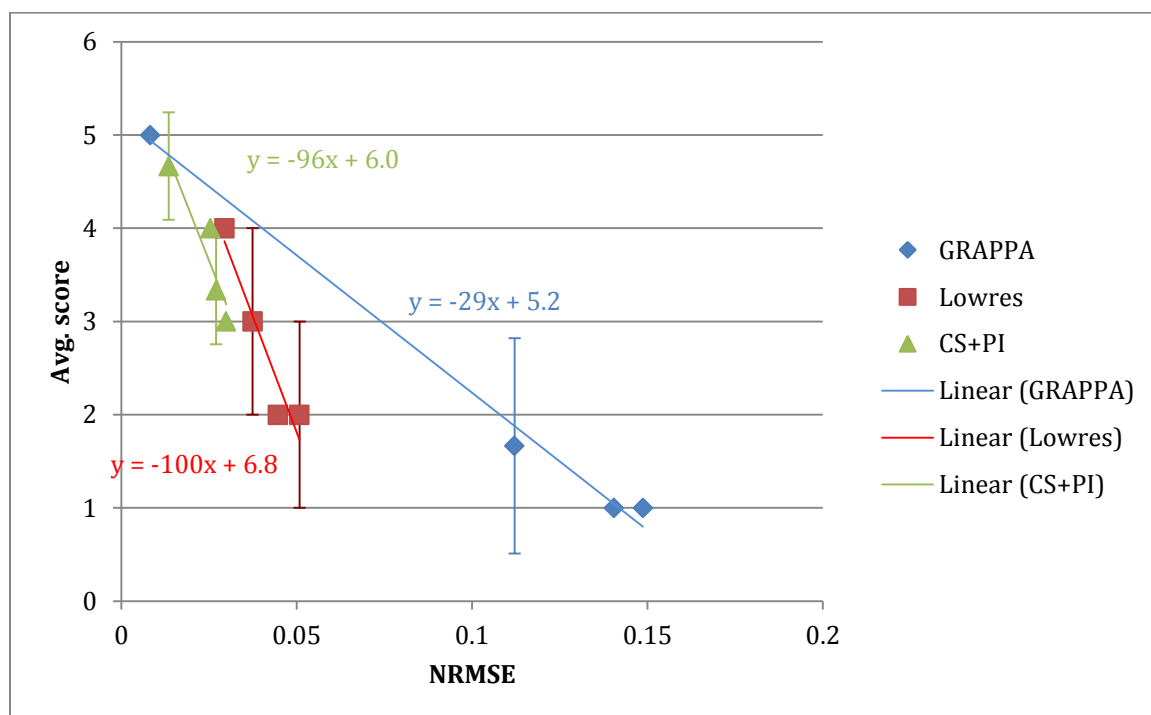


Figure 6.8- Average score (given by three participants) versus the normalized root mean square error (NRMSE) for the MRA scoring task. The error bars show one standard deviation, if non-zero.

6.4 Discussion and conclusion

The results primarily suggest that the advantages of compressed sensing depend on the application. For example, while the results suggest that higher under-sampling factors while maintaining the diagnostic quality are reached with combined CS+PI for cranial imaging and MRAs, as noted in the previous section, no improvement over a simple low-resolution acquisition is achieved by compressed sensing in the lesion detection task, involving identification of relatively large lesions.

Compressed sensing generally improves the resolution by interpolating the under-sampled data based on an *a priori* sparsity reconstruction constraint. This, however, sometimes results in visual reconstruction artifacts, i.e., the under-sampling aliasing artifacts that are not completely removed during the reconstruction, in spite of the increased resolution. This is illustrated in [Figure 6.9](#) with a simple test image. As

suggested by the lesion detection results, this task does not require high resolution images, as lesions are usually large enough distinct areas to be detected on a simple low-resolution reconstruction. However, the aliasing artifacts on the compressed sensing reconstructions may interfere with the detection of the true lesions, resulting in overall detection performance even worse than the simple low-resolution reconstruction, as suggested by the results above. For example, as shown in Table 6.2, while compressed sensing results in lower reconstruction error (NRMSE) than low-resolution, the lesion detection performance in terms of the area under the ROC curve is generally better for low-resolution compared to compressed sensing.

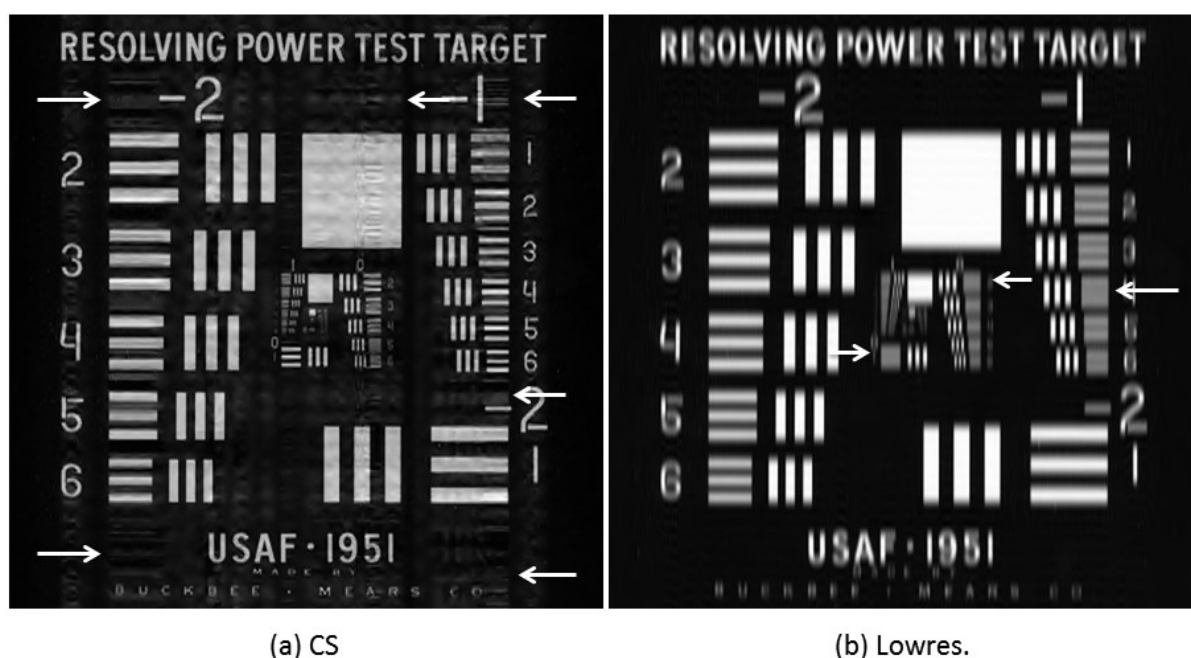


Figure 6.9- Compressed sensing (a) and low-resolution (b) reconstruction of a simple test image by under-sampling in the frequency domain (under-sampling factor 5). While compressed sensing results in higher resolution (finer lines are resolved in the left image) it also results in some aliasing visual artifacts. The arrows point to examples of aliasing artifacts on the compressed sensing reconstruction and loss of resolution in the lowres reconstruction.

It is known that compressed sensing performs very well with very sparse images, e.g., MRAs, which is consistent with our results. However, as noted in the previous section, under-sampled MRA reconstructions generally received lower subjective scores than the FIESTA cranial nerve images at the corresponding under-sampling factor. This can partly be attributed to the fact that the FIESTA cranial nerve images are intrinsically very high SNR images. Additionally the arteries in the MRA have more complex courses and are scrutinized to a higher degree than cranial nerves by radiologists to look for more subtle abnormalities in contour.

In summary, while for some applications, especially those requiring/relying on high resolution, CS may be of advantage, for some others, e.g., certain lesion detection tasks, one might simply reduce the acquisition time by reducing the resolution to a certain amount without affecting the diagnostic performance.

6.5 Reference

- [1] A. Macovski, "Noise in MRI," *Magn. Reson. Med.*, vol. 36, no. 3, pp. 494–497, 1996.
- [2] D. J. Larkman and R. G. Nunes, "Parallel magnetic resonance imaging," *Phys. Med. Biol.*, vol. 52, no. 7, pp. R15–55, Apr. 2007.
- [3] K. P. Pruessmann, M. Weiger, M. B. Scheidegger, and P. Boesiger, "SENSE: Sensitivity encoding for fast MRI," *Magn. Reson. Med.*, vol. 42, no. 5, pp. 952–962, 1999.
- [4] D. K. Sodickson and W. J. Manning, "Simultaneous acquisition of spatial harmonics (SMASH): Fast imaging with radiofrequency coil arrays," *Magn. Reson. Med.*, vol. 38, no. 4, pp. 591–603, 1997.
- [5] M. A. Griswold, P. M. Jakob, R. M. Heidemann, M. Nittka, V. Jellus, J. Wang, B. Kiefer, and A. Haase, "Generalized autocalibrating partially parallel acquisitions (GRAPPA)," *Magn. Reson. Med.*, vol. 47, no. 6, pp. 1202–1210, 2002.
- [6] M. Lustig, D. Donoho, and J. M. Pauly, "Sparse MRI: The application of compressed sensing for rapid MR imaging," *Magn. Reson. Med.*, vol. 58, no. 6, pp. 1182–1195, Dec. 2007.

- [7] M. Lustig and J. M. Pauly, "SPIRiT: Iterative self-consistent parallel imaging reconstruction from arbitrary k-space," *Magn. Reson. Med.*, vol. 64, no. 2, pp. 457–471, 2010.
- [8] B. J. Wintersperger, S. B. Reeder, K. Nikolaou, O. Dietrich, A. Huber, A. Greiser, T. Lanz, M. F. Reiser, and S. O. Schoenberg, "Cardiac CINE MR imaging with a 32-channel cardiac coil and parallel imaging: Impact of acceleration factors on image quality and volumetric accuracy," *J. Magn. Reson. Imaging*, vol. 23, no. 2, pp. 222–227, 2006.
- [9] J. H. Lee, S. S. Lee, J. Y. Kim, I. S. Kim, J. H. Byun, S. H. Park, and M.-G. Lee, "Parallel imaging improves the image quality and duct visibility of breathhold two-dimensional thick-slab MR cholangiopancreatography," *J. Magn. Reson. Imaging*, p. n/a–n/a, 2013.
- [10] S. D. Sharma, C. L. Fong, B. S. Tzung, M. Law, and K. S. Nayak, "Clinical Image Quality Assessment of Accelerated Magnetic Resonance Neuroimaging Using Compressed Sensing," *Invest. Radiol.*, Mar. 2013.
- [11] M. Lustig, D. L. Donoho, J. M. Santos, and J. M. Pauly, "Compressed Sensing MRI," *IEEE Signal Process. Mag.*, vol. 25, no. 2, pp. 72–82, Mar. 2008.
- [12] E. J. Candes and M. B. Wakin, "An Introduction To Compressive Sampling," *Signal Process. Mag. IEEE*, vol. 25, no. 2, pp. 21–30, 2008.
- [13] D. L. Donoho, "Compressed sensing," *IEEE Trans. Inf. Theory*, vol. 52, no. 4, pp. 1289–1306, Apr. 2006.
- [14] S. S. Chen, D. L. Donoho, and M. A. Saunders, "Atomic Decomposition by Basis Pursuit," *SIAM Rev.*, vol. 43, no. 1, pp. 129–159, Jan. 2001.
- [15] I. Daubechies, M. Defrise, and C. De Mol, "An iterative thresholding algorithm for linear inverse problems with a sparsity constraint," *Commun. Pure Appl. Math.*, vol. 57, no. 11, pp. 1413–1457, Nov. 2004.
- [16] C. E. Metz, "Applications of Roc Analysis in Diagnostic Image Evaluation," Chicago Univ., IL (USA); Franklin McLean Memorial Research Inst., Chicago, IL (USA), CONF-790783-1, Jan. 1979.

7 Summary and future directions

7.1 Thesis summary

The primary objective of this thesis was to study MRI acceleration techniques based on the acquisition of under-sampled k-space data followed by interpolation of the missing samples. Although with advancements in MRI hardware, e.g., new scanners with higher strength static magnetic field and gradients, as well as advancements in pulse sequence design, e.g., echo train imaging techniques [1]–[7], faster acquisitions have become possible, due to physical and biological constraints the acquisition time is still relatively long for typical clinically used pulse sequences [8]. Furthermore, while the acquisition time can be reduced by trading off the resolution and/or signal-to-noise ratio (SNR) of the acquired images [9], practical limits are very soon reached due to the minimum requirements on resolution and/or SNR in many applications. On the other hand, patient comfort and cost considerations limit the acceptable clinical scan times, which in turn limits the number of pulse sequences that can be run in a single clinical examination. However, because of MR's versatility in acquiring multiple tissue-related parameters, e.g., T1 and T2, the patient is being subjected to increasing number of imaging sequences. Therefore, reducing the acquisition time in magnetic resonance imaging, while maintaining an acceptable image quality, i.e., resolution and SNR, remains a primary field of research [8].

A major class of MRI acceleration techniques is based on the acquisition of under-sampled k-space data (therefore, reducing the acquisition time) and interpolation of the missing samples to generate a full-resolution image. Two major categories of under-sampled MRI reconstructions are [Compressed sensing](#) [10], [11] and [Parallel imaging](#) [12]–[14]. The former involves interpolation of under-sampled k-space data by assuming an *a priori* sparsity constraint on the image, while in the latter interpolation is based on the knowledge of the coil sensitivities. When multiple-channel data available, the best reconstruction performance is achieved by a combined

compressed sensing and parallel imaging reconstruction [15], [16]. The main approaches taken in this thesis to acceleration of MRI acquisitions fall under these two categories.

The specific objectives of this thesis can be summarized as follows:

1. **Compressed sensing reconstruction by penalizing the stationary wavelet transform coefficients:** While the discrete wavelet transform is commonly used as the sparsifying transform in compressed sensing, reconstruction is traditionally carried out by penalizing the decimated wavelet transform coefficients (DWT) [10]. However, penalizing the decimated wavelet transform coefficients often results in visual reconstruction artifacts, which are mainly associated with the lack of translation-invariance of the wavelet basis in the decimated form [17]. A major contribution of this thesis was to show that these reconstruction artifacts can be eliminated or greatly reduced by penalizing the translation invariant version of the discrete wavelet transform, i.e., penalizing the stationary wavelet transform coefficients for [Stationary wavelet transform sparse recovery](#). Additionally, a practical [Iterative stationary wavelet transform thresholding](#) algorithm allowing for simultaneous incorporation of coil sensitivity profiles for combined compressed sensing and parallel imaging reconstruction was developed.
2. **Joint under-sampled reconstruction of multiple-acquisition datasets:** Some applications of MRI, e.g., [Quantitative MRI: T1/T2 mapping](#) [18]–[22], involve multiple sequential acquisitions that exhibit high correlation, or low joint entropy, since they are often acquired by only changing an imaging parameter. In this thesis it was shown that such correlation can be incorporated in [Under-sampled MRI reconstruction](#) problems to improve the reconstruction quality, or increase the under-sampling factor while maintaining the reconstruction quality.
3. **Driven equilibrium single pulse observation of T1 with high-speed incorporation of RF field inhomogeneities (DESPOT1-HIFI):** While [DESPOT1/DESPOT2 T₁ and T₂ mapping](#) techniques [23] provide efficient ways of computing T1/T2 maps [24], at high (3T and above) magnetic some inaccuracies are observed due to the deviations of the transmitted flip angle from the prescribed values. In order to address this problem, an extension to the DESPOT known as DESPOT-HIFI [22] was proposed. Another

contribution of this thesis was a modification to DESPOT-HIFI resulting in more accurate computation of the quantitative T1 and T2 maps.

4. **Subjective quality assessment of the under-sampled reconstructions:** While quantitative quality metrics, e.g., the normalized mean square error (NRMSE), have been commonly used to evaluate and compare the quality of different under-sampled reconstructions, it was shown in this thesis that such quantitative measures do not necessarily correlate with the perceptual quality as perceived by radiologists (Chapter 5). Therefore, any quantitative assessment of the reconstruction quality is of limited clinical impact unless accompanied by subjective assessments directly related to the diagnostic quality of the images. This problem was addressed in the thesis through a number of subjective experiments, carried out with the help of collaborating radiologists, aimed at subjective clinical evaluation of different under-sampled reconstructions for different applications.

7.1.1 Stationary wavelet transform penalization

Traditionally wavelet-based compressed sensing reconstructions involve penalizing the decimated wavelet transform (DWT) coefficients [10], [11], [25], [26]:

$$\min_{f^*} \|\psi_{DWT} f^*\|_{l_1} \text{ s.t. } \|U_F \mathcal{F} f^* - F_u\|_{l_2} < \varepsilon \quad (7.1)$$

where ψ_{DWT} denotes the decimated wavelet transform (DWT) and \mathcal{F} the Fourier transform. U_F is the k-space under-sampling operation and F_u the originally acquired (under-sampled) k-space data. The solution is denoted by f^* .

Chapter 3 of this thesis demonstrated that some of the reconstruction artifacts, associated with the lack translation of the wavelet basis in the decimated (DWT) form, can be eliminated or reduced by penalizing the undecimated discrete wavelet transform, i.e., the stationary wavelet transform (SWT), which provides a translation-invariant basis. That is, $\min_{f^*} \|\psi_{SWT} f^*\|_{l_1} \text{ s.t. } \|U_F \mathcal{F} f^* - F_u\|_{l_2} < \varepsilon$, where ψ_{SWT} is now the stationary wavelet transform (SWT).

It was shown that SWT-penalized reconstructions result in fewer visual artifacts, as well as significantly lower reconstruction error with respect to the fully-sampled reference compared to the corresponding DWT-penalized reconstructions. Furthermore, SWT reconstructions generally converged faster, i.e., in fewer iterations, than the corresponding DWT reconstructions. Additionally, while DWT-penalized reconstructions often over-converged, in many cases no over-convergence was observed with SWT.

These characteristics were demonstrated for compressed sensing reconstructions with different additional constraints, including DWT/SWT-penalized reconstructions with additional total variation (TV), and coil sensitivity, i.e., combined parallel imaging and compressed sensing reconstruction. The latter is of particular practical interest since it is expected to achieve the best reconstruction performance by combined parallel imaging and compressed sensing reconstruction, when multiple-channel data available.

In Chapter 2 an [Iterative stationary wavelet transform thresholding](#) reconstruction algorithm was presented. Iterative thresholding algorithms are commonly used to find a solution to the aforementioned l_1 -regularized reconstruction problem (equation 7.1) [25], [27], [28]. While traditionally thresholding is performed on the decimated wavelet transform (DWT) coefficients corresponding to a DWT-penalized reconstruction, as shown in chapter 2, SWT-penalized reconstruction can be achieved through iterative SWT thresholding. Furthermore, an extension of the iterative thresholding reconstruction for simultaneous incorporation of multiple-coil data was presented.

7.1.2 Joint under-sampled reconstruction of multiple-acquisition datasets

Some MR applications, e.g., [Quantitative MRI: T1/T2 mapping](#) [18]–[22], involve multiple sequential acquisitions of an object. These images are often acquired by changing a single imaging parameter. Consequently, while the intensity levels of these acquisitions are manipulated, they exhibit high structural similarity, i.e., low joint entropy. In chapter 4, this similarity was incorporated as an additional constraint in the under-sampled reconstruction problem to improve reconstruction quality, or increase under-sampling while maintaining the quality. To this end, a [Similarity-promoting operation](#) was developed, which was then

incorporated in an [Iterative stationary wavelet transform thresholding](#) reconstruction algorithm, in addition to the conventional thresholding, i.e., sparsity-promoting, operation.

While incoherent under-sampling is important for compressed sensing reconstruction of individual images [10], in the joint reconstruction case, under-sampling incoherence between different acquisitions becomes crucial in addition to the individual under-sampling incoherence. While the latter is achieved by random under-sampling of each k-space dataset, the former is achieved by making the individual under-sampling operations in different acquisitions independent of each other.

Without loss of generality, the methods and results were demonstrated for the [DESPOT1](#) T1 mapping technique, in which the quantitative T1 map is computed from two spoiled gradient recalled (SPGR) acquisitions at optimal flip angles [23].

Joint reconstructions resulted in significantly lower reconstruction error compared with the traditional individual reconstructions as well as the low-resolution reconstructions, in terms of both the reconstruction of individual SPGR images and the computed T1 map.

In addition to the reconstruction error in individual SPGR images, DESPOT1 error also depends on the correlation between the individual errors. For example, while the individual reconstructions resulted in significantly lower reconstruction error of the individual SPGR images than the low-resolution reconstructions, the error in the T1 map computed from the low-resolution images was significantly lower than that computed from individual reconstructions. This decrease in the DESPOT1 error is mainly associated with the high correlation between the errors in the low-resolution images- the main source of error in the low-resolution reconstructions is the blurring due to the low-pass filtering of the images, which is the same for both of the images. Nevertheless, random under-sampling in the compressed sensing reconstructions results in less correlated errors of the individual reconstructions, which in turn results in increased DESPOT1 error. However, the joint reconstruction exhibited significantly lower SPGR and DESPOT1 error compared to the individual and low-resolution reconstructions.

7.1.3 Driven equilibrium single pulse observation of T1 with high-speed incorporation of RF field inhomogeneities (DESPOT1-HIFI)

Driven equilibrium single pulse observation of T1/T2 (DESPOT1/DESPOT2 T_1 and T_2 mapping) is currently the most efficient T1/T2 mapping technique. In DESPOT1 a T1 map is computed from two spoiled gradient recalled (SPGR) acquisitions at *optimal* flip angles. Once the T1 map is computed, it is used with DESPOT2 to compute the T1 map from steady state free precision (SSFP) acquisitions [23]. However, deviations of the transmitted flip angle, α_T , from the prescribed value, α_P , introduce inaccuracies in the computed T1 values due to inhomogeneities of the RF (B_1) field at high magnetic fields (3T and above). The transmitted flip angle is generally related to the prescribed flip angle as $\alpha_T = \kappa\alpha_P$, where κ is a parameter denoting the spatial variations of the B_1 field.

The Driven equilibrium single pulse observation of T1 with high-speed incorporation of RF field inhomogeneities (DESPOT1-HIFI) addresses this problem by an additional inversion recovery spoiled gradient echo (IRSPGR) acquisition. The combined SPGR and IRSPGR data are then used to simultaneously estimate κ , M_0 , and T_1 .

In chapter 5 a modification to DESPOT-HIFI was proposed resulting in more accurate estimation of κ , M_0 , and T_1 . In particular, this modification involved rederivation of the IRSPGR signal intensity equation used in DESPOT-HIFI. The proposed modification was validated on phantom and *in vivo* human brain data.

7.1.4 Subjective quality assessment of under-sampled reconstructions

Validation of results is an important aspect of the under-sampled reconstructions. While quantitative quality metrics, such as the reconstruction error with respect to fully-sampled data, are commonly used for the purpose of evaluation of the performance of under-sampled reconstruction techniques, as well as their comparison, as shown in Chapter 5, such quantitative measures do not always conform to subjective quality as perceived by radiologists and other expert end users. Consequently, these quantitative evaluations/comparisons are of limited clinical impact, unless accompanied by subjective results related to the clinical diagnosis.

The problem of subjective quality assessment and comparison of under-sampled reconstructions was addressed in Chapter 5, where we reported the results of the subjective experiments performed with the assistance of collaborating radiologists in order to assess/compare the performance of different under-sampled reconstruction techniques for different specific applications. In particular, three common applications of MRI in neuroradiology were considered:

1. **Detection of white matter lesions:** In this task the participant was asked to identify white matter lesions on reconstructed FLAIR images. Artificial but realistic white matter lesions were placed on FLAIR brain images of a healthy volunteer in random locations with a probability of 50% to generate test images. These images were then under-sampled in the frequency domain at a range of under-sampling factors from 1, i.e., no under-sampling, to 5, for compressed sensing and low-resolution reconstructions. The quality of the reconstructions was evaluated based on the lesion detection performance achieved by the participants for each reconstruction and different under-sampling factors. The results generally suggested no improvement in the lesion detection performance achieved by compressed sensing over a simple low-resolution reconstruction.
2. **Cranial nerve imaging:** In this task the participants were asked score under-sampled reconstructed multiacquisition SSFP (or CISS, also known as FIESTA-C) images based on the diagnostic quality of the cranial nerves. The dataset consisted of low-resolution, GRAPPA, and combined compressed sensing and parallel imaging (reconstruction through the multiple-coil iterative stationary wavelet transform thresholding algorithm presented in Chapter 2), each at under-sampling factors 2, 3, 4, and 5. The reconstructions were also ranked by the participants at each under-sampling factor. The results generally suggested that combined compressed sensing and parallel imaging reconstructions receive the highest scores/ranks.
3. **Magnetic resonance angiography (MRA):** This task involved presenting the participants with time of flight (TOF) MRA images along with the corresponding projection reconstructions, based on which different reconstructions at different under-sampling factors were subjectively scored and ranked. Similar to the previous task, low-resolution, GRAPPA, and combined compressed sensing and parallel imaging

reconstructions were evaluated at under-sampling factors 2, 3, 4, and 5. Similar to cranial nerve imaging, the results generally suggested that combined compressed sensing and parallel imaging reconstructions receive the highest scores/ranks.

Performance of the compressed sensing reconstructions depends on the clinical application. In particular, compressed sensing reconstructions lead to improved diagnostic performance in applications involving fine features requiring high resolution, e.g., the cranial nerve imaging and MRA tasks described above. Nevertheless, it is also known that while improving the resolution, compressed sensing often results in visual reconstruction artifacts. Consequently, for applications such as the lesion detection task described above, which do not require high resolution, one may simply reduce the acquisition time by appropriately reducing the resolution.

7.2 Future work

7.2.1 Computation time

As emphasized throughout this thesis, one of the main motivations behind accelerated acquisitions is either to allow more data to be acquired in a single imaging session or to reduce motion artifacts. However, if the reconstruction is not performed in real-time it is impossible to know if the data need to be reacquired until after the patient is out of the scanner. Therefore, while theoretically the reconstruction can be performed off-line, in practice an accelerated acquisition will be of limited use if it cannot be reconstructed in real-time.

As noted, the execution time of the MATLAB implementation of the iterative-thresholding-based reconstructions presented in this thesis is in the order of a few seconds for a 256x256 matrix. Although this can be considered close to real-time the execution time can potentially be greatly reduced by more efficient and/or multi-thread GPU-based implementations of the algorithms. Nevertheless, as noted, the execution time is far less than that of the similar MATLAB implementation of other state-of-the-art reconstruction algorithms producing comparable results, with execution times in the order of thousands of seconds for a similar image (see, for example, section 3.4). The interested reader is referred to [29], in which a GPU-based implementation of under-sampled MRI reconstruction has recently been developed.

7.2.2 Other clinical applications

Although the methods and results in this thesis were primarily presented for magnetic resonance brain imaging, they are directly applicable to other clinical applications. Figure 7.1 shows an example of under-sampled reconstruction of SPGR foot images at x3 under-sampling. As this figure clearly shows, higher resolution is achieved by combined compressed sensing and parallel imaging reconstruction through the multiple-coil iterative SWT thresholding algorithm presented in section 2.2.1, compared with a simple low-resolution reconstruction.

As noted previously, subjective clinical assessment of the under-sampled reconstruction methods is essential for the translation of these techniques to real clinical applications. Also, as discussed previously, the performance of the reconstruction techniques to a great extent depends on the underlying clinical application. Obviously, each new application calls for a new set of experiments aimed at subjective quality assessment of the reconstruction techniques.

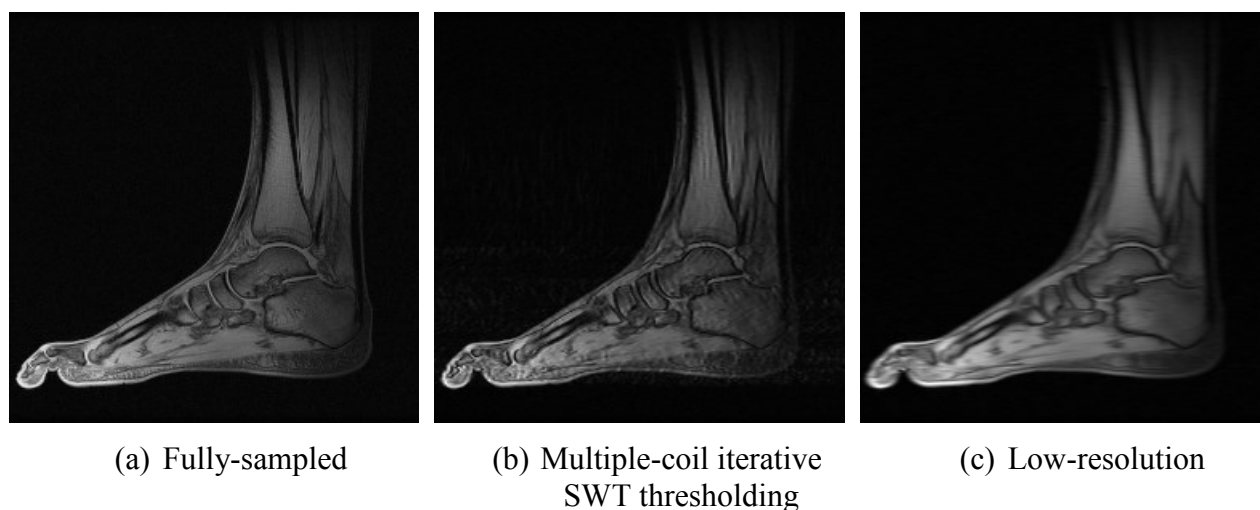


Figure 7.1- Reconstruction of 8-channel spoiled gradient recalled foot images at x3 under-sampling.

7.2.3 Cardiac Cine MRI

Chapter 4 of this thesis presented the idea of exploiting the correlation between multiple successive acquisitions as an additional reconstruction constraint. Cardiac cine MRI is another major category of MR imaging techniques that can particularly benefit from the correlation

between successive acquisitions. While several approaches to incorporating the correlation between successive acquisitions in cardiac cine MRI have been proposed by different authors (see [30] and references therein), this area still remains an active field of research.

7.3 Reference

- [1] P. Mansfield, "Multi-planar image formation using NMR spin echoes," *J. Phys. C Solid State Phys.*, vol. 10, no. 3, p. L55, Feb. 1977.
- [2] D. A. Feinberg and K. Oshio, "GRASE (gradient- and spin-echo) MR imaging: a new fast clinical imaging technique.," *Radiology*, vol. 181, no. 2, pp. 597–602, Nov. 1991.
- [3] K. Oshio and D. A. Feinberg, "GRASE (Gradient-and Spin-Echo) imaging: A novel fast MRI technique," *Magn. Reson. Med.*, vol. 20, no. 2, pp. 344–349, 1991.
- [4] C. T. W. Moonen, G. Liu, P. V. Gelderen, and G. Sobering, "A fast gradient-recalled MRI technique with increased sensitivity to dynamic susceptibility effects," *Magn. Reson. Med.*, vol. 26, no. 1, pp. 184–189, 1992.
- [5] G. Liu, G. Sobering, A. W. Olson, P. Van Gelderen, and C. T. W. Moonen, "Fast echo-shifted gradient-recalled MRI: Combining a short repetition time with variable T2* weighting," *Magn. Reson. Med.*, vol. 30, no. 1, pp. 68–75, 1993.
- [6] J. Hennig, "Multiecho imaging sequences with low refocusing flip angles," *J. Magn. Reson. 1969*, vol. 78, no. 3, pp. 397–407, Jul. 1988.
- [7] J. Hennig, A. Nauerth, and H. Friedburg, "RARE imaging: A fast imaging method for clinical MR," *Magn. Reson. Med.*, vol. 3, no. 6, pp. 823–833, 1986.
- [8] D. J. Larkman and R. G. Nunes, "Parallel magnetic resonance imaging," *Phys. Med. Biol.*, vol. 52, no. 7, pp. R15–55, Apr. 2007.
- [9] A. Macovski, "Noise in MRI," *Magn. Reson. Med.*, vol. 36, no. 3, pp. 494–497, 1996.
- [10] M. Lustig, D. Donoho, and J. M. Pauly, "Sparse MRI: The application of compressed sensing for rapid MR imaging," *Magn. Reson. Med.*, vol. 58, no. 6, pp. 1182–1195, Dec. 2007.
- [11] E. J. Candes and M. B. Wakin, "An Introduction To Compressive Sampling," *Signal Process. Mag. IEEE*, vol. 25, no. 2, pp. 21–30, 2008.
- [12] K. P. Pruessmann, M. Weiger, M. B. Scheidegger, and P. Boesiger, "SENSE: Sensitivity encoding for fast MRI," *Magn. Reson. Med.*, vol. 42, no. 5, pp. 952–962, 1999.
- [13] D. K. Sodickson and W. J. Manning, "Simultaneous acquisition of spatial harmonics (SMASH): Fast imaging with radiofrequency coil arrays," *Magn. Reson. Med.*, vol. 38, no. 4, pp. 591–603, 1997.

- [14] M. A. Griswold, P. M. Jakob, R. M. Heidemann, M. Nittka, V. Jellus, J. Wang, B. Kiefer, and A. Haase, "Generalized autocalibrating partially parallel acquisitions (GRAPPA)," *Magn. Reson. Med.*, vol. 47, no. 6, pp. 1202–1210, 2002.
- [15] M. Lustig and J. M. Pauly, "SPIRiT: Iterative self-consistent parallel imaging reconstruction from arbitrary k-space," *Magn. Reson. Med.*, vol. 64, no. 2, pp. 457–471, 2010.
- [16] S. S. Vasanawala, M. J. Murphy, M. T. Alley, P. Lai, K. Keutzer, J. M. Pauly, and M. Lustig, "Practical parallel imaging compressed sensing MRI: Summary of two years of experience in accelerating body MRI of pediatric patients," in *Biomedical Imaging: From Nano to Macro, 2011 IEEE International Symposium on*, 2011, pp. 1039–1043.
- [17] R. R. Coifman and D. L. Donoho, "Translation-invariant de-noising," *Wavelets Stat. Springer Lect. Notes Stat.*, vol. 103, pp. 125–150, 1995.
- [18] Z. Chen, F. S. Prato, and C. McKenzie, "T1 fast acquisition relaxation mapping (T1-FARM): an optimized reconstruction," *IEEE Trans. Med. Imaging*, vol. 17, no. 2, pp. 155–160, Apr. 1998.
- [19] C. Y. Tong and F. S. Prato, "A novel fast T1-mapping method," *J. Magn. Reson. Imaging*, vol. 4, no. 5, pp. 701–708, 1994.
- [20] C. A. McKenzie, Z. Chen, D. J. Drost, and F. S. Prato, "Fast acquisition of quantitative T2 maps," *Magn. Reson. Med. Off. J. Soc. Magn. Reson. Med. Soc. Magn. Reson. Med.*, vol. 41, no. 1, pp. 208–212, Jan. 1999.
- [21] S. Meiboom and D. Gill, "Modified Spin-Echo Method for Measuring Nuclear Relaxation Times," *Rev. Sci. Instrum.*, vol. 29, no. 8, pp. 688–691, Aug. 1958.
- [22] S. C. L. Deoni, "High-resolution T1 mapping of the brain at 3T with driven equilibrium single pulse observation of T1 with high-speed incorporation of RF field inhomogeneities (DESPOT1-HIFI)," *J. Magn. Reson. Imaging JMRI*, vol. 26, no. 4, pp. 1106–1111, Oct. 2007.
- [23] S. C. L. Deoni, B. K. Rutt, and T. M. Peters, "Rapid combined T1 and T2 mapping using gradient recalled acquisition in the steady state," *Magn. Reson. Med.*, vol. 49, no. 3, pp. 515–526, 2003.
- [24] D. Ma, V. Gulani, N. Seiberlich, K. Liu, J. L. Sunshine, J. L. Duerk, and M. A. Griswold, "Magnetic resonance fingerprinting," *Nature*, vol. 495, no. 7440, pp. 187–192, Mar. 2013.
- [25] I. Daubechies, M. Defrise, and C. De Mol, "An iterative thresholding algorithm for linear inverse problems with a sparsity constraint," *Commun. Pure Appl. Math.*, vol. 57, no. 11, pp. 1413–1457, Nov. 2004.
- [26] D. L. Donoho, "Compressed sensing," *IEEE Trans. Inf. Theory*, vol. 52, no. 4, pp. 1289–1306, Apr. 2006.
- [27] M. Fornasier and H. Rauhut, "Iterative thresholding algorithms," *Appl. Comput. Harmon. Anal.*, vol. 25, no. 2, pp. 187–208, Sep. 2008.

- [28] T. Blumensath and M. E. Davies, "Iterative hard thresholding for compressed sensing," *Appl. Comput. Harmon. Anal.*, vol. 27, no. 3, pp. 265–274, Nov. 2009.
- [29] M. Murphy, M. Alley, J. Demmel, K. Keutzer, S. Vasanawala, and M. Lustig, "Fast -SPIRiT Compressed Sensing Parallel Imaging MRI: Scalable Parallel Implementation and Clinically Feasible Runtime," *IEEE Trans. Med. Imaging*, vol. 31, no. 6, pp. 1250–1262, 2012.
- [30] P. Zamani, M. Kayvanrad, and H. Soltanian-Zadeh, "Using learned under-sampling pattern for increasing speed of cardiac cine MRI based on compressive sensing principles," *EURASIP J. Adv. Signal Process.*, vol. 2012, no. 1, p. 82, Apr. 2012.

Appendix A: Erroneous DESPOT-HIFI equation

It was noted in chapter 5 that although DESPOT-HIFI is based on an additional IR-SPGR acquisition, in which the inversion pulse is followed by a train of spoiled gradient echo pulses, the IR-SPGR signal equation used in the original DESPOT-HIFI paper [1] is that of an inversion-recovery spin echo (IR-SE) sequence, which results in inaccuracies in the computed T1 values. The nature of the erroneous assumption is outlined below:

An IR-SE sequence involves successive applications of a 180° -pulse, i.e., the inversion pulse, followed by a 90° -pulse, i.e., the RF refocusing pulse. The time between two successive inversion pulses is referred to as the *repetition time* (TR) and the time between the 180° inversion pulse and the 90° refocusing pulse is referred to as the *inversion time* (TI).

At time $t = 0^-$, immediately prior to the application of the inversion pulse, the magnetization vector is equal to the equilibrium magnetization, M_0 :

$$M_z(0^-) = M_0 \quad (1)$$

Assuming the inversion pulse is applied at $t = 0$:

$$M_z(0^+) = -M_0 \quad (2)$$

Therefore, at $t = TI^-$, right before the application of the 90° RF refocusing pulse (see section 1.2.4):

$$M_z(TI^-) = M_0(1 - 2e^{-\frac{TI}{T_1}}) \quad (3)$$

The 90° RF refocusing pulse flips the longitudinal magnetization vector onto the transverse plane. Therefore, after the application of the 90° pulse:

$$M_z(TI^+) = 0 \quad (4)$$

The longitudinal magnetization recovers towards M_0 until time $t = Tr^-$, just prior to the application of the next inversion pulse:

$$M_z(Tr^-) = M_0 \left(1 - e^{-\frac{(Tr-TI)}{T_1}} \right) \quad (5)$$

Since M_z recovers from zero after the 90° pulse at each cycle, $M_z(Tr^-)$ is the same at the end of each cycle. Therefore, for each cycle but the very first one, $M_z(0^-) = M_0 \left(1 - e^{-\frac{(Tr-TI)}{T_1}} \right)$, based on which $M_z(TI^-)$ is derived:

$$M_z(TI^-) = -M_0 \left(1 - 2e^{-TI/T_1} + e^{-Tr/T_1} \right) \quad (6),$$

which is the assumed IR-SPGR signal intensity equation in the original DESPOT-HIFI paper. The main discrepancy is the assumption of the 90° RF refocusing pulse, which is crucial in the above derivation. However, the IR-SPGR sequence involves a 180° inversion followed by gradient echoes, i.e., SPGR, acquisitions, which do not involve RF refocusing.

Reference

[1] S. C. L. Deoni, "High-resolution T1 mapping of the brain at 3T with driven equilibrium single pulse observation of T1 with high-speed incorporation of RF field inhomogeneities (DESPOT1-HIFI)," *J. Magn. Reson. Imaging JMRI*, vol. 26, no. 4, pp. 1106–1111, Oct. 2007.

Appendix B: Human ethics approval

FORM 2FOO1 UWO HSREB FULL BOARD SUBMISSION (December 2008)

CONFIDENTIAL

PAGE 1

SECTION 1 PROJECT REGISTRATION

1.1a	Project Title
⇒ Structural and Functional MR imaging in Frontal and Temporal Lobe Epilepsy at 1.5T, 3T, and 7T	
1.1b	Sponsor or Agency Reference Number or Identifier if known.
⇒ N/A	

1.2	Is this a US Food and Drug Administration (FDA) monitored study and/or a study funded or supported by a US government agency?	YES	
		NO	✓

1.3	<i>When will recruitment of research participants start?</i> Start Date	June 1st 2009
	<i>When will all contact and follow up with study subjects and/or data collection be concluded?</i> End Date	July 31st 2015

1.4	Principal or Lead Investigator at this site. (PI must be a faculty or staff member at UWO or affiliated institutions. Supervisor for student or resident projects must be a faculty or clinical advisor.)		
	Name	Terence M. Peters	
	Title & Position	Professor, Medical Imaging and Medical Biophysics, University of Western Ontario	
	Degrees	PhD	
	Departmental Affiliation	Robarts Research Institute - Imaging Research Laboratories	
Mailing Address	Building & Street Address	Robarts Research Institute - Imaging Research Laboratories P.O. Box 5015, 100 Perth Drive,	
	City, Province	London, ON	
	Postal Code	N6A 5K8	
	Telephone	██████████	Fax
	Email (required)	██████████	
For security purposes please provide your hospital, institute or UWO email address whenever possible.			

1.5	_____ Date: _____
	Signature of Local Principal Investigator attesting that:

- a) all co-investigators have reviewed the protocol contents and are in agreement with the protocol as submitted;
- b) all investigators have read the Tri-Council Policy Statement: Ethical Conduct in Research Involving Humans and the UWO Guidelines on Health Sciences Research Involving Human Subjects and agree to abide by the guidelines therein;
- c) the investigator(s) will adhere to the Protocol and Consent Form as approved by the HSREB;
- d) the Principal Investigator will notify the HSREB of any changes or adverse events/experiences in a timely manner;
- e) the study will not start until the contract/ agreement has been approved by the appropriate university, hospital or research institute official;
- f) if the study is funded by Industry the investigators will adhere to the conditions described in Section 3.2: and
- g) if external regulatory approval is required, the investigators will not start the study until all approvals are in place.

1.6 List all local co-investigators and collaborators. Include research personnel only if they have a significant role in the conduct of the study. Expand chart as required.			
Name	Title/Position	Degrees	Role
Donald H. Lee	Professor, Medical Imaging, UWO	MB, Bch, FRCPC	Radiologist
Seyed M Mirsattari	Assistant Professor in the Department of Clinical Neurological Sciences. University of Western Ontario.	MD, FRCPC	- Recruiting patients. - Perform neurological examination - Interpret EEG and clinical data from the patient's chart. - Urgent neurological assessment when patients are in the MR scanners.
Frank Bihari	Electrophysiology Technologist. Department of Clinical Neurological Sciences, UWO.	BSc	Data analyst
Andrew Parrent	Neurosurgeon, LHSC; Associate Professor, UWO	MD, FRCSC	Will perform some of the neurosurgeries and provide consultation.
Robert Hammond	Neuropathologist, Professor, Pathology, UWO	MD, FRCPC	Provide pathology consultation.
Zhongjun Hou	Radiologist, LHSC	MD	Image Analysis
Diego Cantor-Rivera	Graduate Student UWO	MSC (PhD Candidate)	Image Analysis
Cyndi Harper-Little	MRI Technologist		Will perform the MRI Scans
Kevin Wang	Graduate Student UWO	MESc (PhD Candidate)	Data Collection and Image Analysis
David Steven	Neurosurgeon LHSC; Associate Prof. UWO	MD, FRCSC	Will perform some of the neurosurgeries and provide consultation.

Sandrine de Ribapierre	Neurosurgeon LHSC; Assistant Prof. UWO	MD, FRCSC	Will perform some of the neurosurgeries and provide consultation.
Jorge Burneo	Neurosurgeon LHSC; Assistant Prof. UWO	MD, FRCSC	- Recruiting patients. - Perform neurological examination - Interpret EEG and clinical data from the patient's chart. - Urgent neurological assessment when patients are in the MR scanners.
Mohammad Kayvanrad	Graduate Student UWO	MSc Graduate Student	Data Collection and Image Analysis
Robert Mayer	LHSC Clinical trials Coordinator	BA HR Dip	Management of patient scanning at Robarts

17a	Is this a multi-centred study?	YES	
		NO	✓
1.7b	If YES, who is the Principal Investigator or Project Leader for the entire study? Provide name and complete contact information.		
	⇒		
1.7c	If YES, if the study is administered by a Coordinating or Contract Research Organization (CRO) provide the name and contact information.		
	⇒		

1.8a	To whom should REB notices and correspondence regarding this protocol be sent – the PI or an Administrative Contact? <i>Note that this must be a local person within the institution. The Local Principal Investigator is ultimately responsible for all aspects of the project and is required to sign-off on all requests for changes and modifications to the protocol. In some instances the REB may override the naming of an administrative contact but will notify the Principal Investigator of this determination and that materials will be sent directly to him/her instead.</i>	PI (default option)	✓
		Admin Contact	
1.8b	If Administrative Contact selected provide name and contact information below.		
	Contact Name		
	Title & Position		
	Department		
	Building & Street Address		
	City, Province		
	Postal Code		
	Telephone	Fax	
	Email (required) For security purposes please provide your hospital, institute or UWO email address whenever possible.		

1.9a	What is the status of the funding or support for this project? <i>The HSREB strongly recommends waiting to apply for ethics approval until after a project submitted for funding has received notification that the funding has been approved. It is very wasteful of the researcher's and the REB's time to prepare/review a protocol that may not proceed or may require significant revision and re-review as a result of receiving less funding than anticipated.</i>	Funding not required	
		Application Pending	
		Funded	✓
		In-Kind contribution only describe (e.g. drugs, devices)	
If Application Pending; Funded; or In-Kind Contribution fill in chart below.			
1.9b	Name of funding agency(s) or sponsor(s) In the case of grant funding also provide the grant or proposal number if known.	CIHR grant: Image-guided Surgery for Epilepsy PI: Terry Peters MOP # 89844	
1.9c	Name of investigator receiving/applying for funding	Terence Peters	

1.10a	Will the research utilize patients (or their records), resources or staff at any of these sites and/or is the researcher associated with one of these sites? If YES to any item, please note that the UWO Office of Research Ethics will routinely share information as to the ethics approval status and other ethics-related or conduct-of-research issues of this submission with the LHRI Grants & Contracts Office. In some instances it may be necessary to also inform the LHSC/SJHC Privacy Office.	NONE of the following sites are involved with this research	
		(check all that apply)	
		LHSC – Victoria Hospital - YES	
		LHSC – University Hospital - YES	✓
		LHSC – South Street Hospital - YES	
		LHSC - London Regional Cancer Program - YES	
		Children's Hospital of Western Ontario - YES	
		UWO Fowler Kennedy Clinic - YES	
		St. Joseph's Health Care London - YES	
		Parkwood Hospital - YES	
		Regional Mental Health Care (London) - YES	
		Regional Mental Health Care (St. Thomas) - YES	
		Byron Family Medical Centre - YES	
		Victoria Family Medical Centre - YES	
St. Joseph's Family Medical Centre - YES			

1.11a	Does this project require Health Canada approval?	NO	✓
		YES – Drug Clinical Trial	
		YES – Natural Product	
		YES – Medical Device	
1.11b	If YES, what is the status of that application? You will be required to provide a copy of the "Letter of No Objection" or a comparable document to the Office of Research Ethics before you may start the research.	Approval received (attach a copy of No Objection letter or comparable document)	
		Submitted to Health Canada but not yet approved	
		Not yet submitted – sole Canadian site therefore require UWO HSREB approval prior to submission to Health Canada	
		Not yet submitted by sponsor or other Canadian site	

1.12a	Clinical Trial Registration Has this clinical trial been (or will it be) registered with a registry that meets the ICMJE standards? What is a clinical trial? A clinical trial is a research study designed to test the safety and/or effectiveness of drugs, devices, treatments, or preventive measures in humans. The HSREB strongly supports the recommendations of the International Committee of Medical Journal Editors (ICMJE) regarding the requirement for registration of all clinical trials on a publicly accessible and recognized registry. Check the following website for some FAQ's regarding registration: http://www.lhronhealth.ca/LHRI/opportunities/clinical_trials.html	NOT APPLICABLE - not a Clinical Trial	✓
		YES – Has been registered	
		YES – Will be registered	
		NO – Will not be registered	
1.12b	If NO , indicate why inclusion in a registry is not possible or desirable. If the reason is not sufficient the HSREB may decide that the following statement must be in the Informed Consent documentation. "This clinical trial will not be registered with a recognized, publicly-accessible clinical trial registry and therefore it is unlikely the study results will be published by established medical journals." ⇒		
1.13a	Dissemination of Clinical Trial Results Is there an intention to make the results of this clinical trial publicly available through one or some of the following methods (select all that apply). The HSREB feels that every effort should be made to make clinical trial results public. The HSREB recognizes that not all submissions get accepted for publication or presentation.	NOT APPLICABLE Not a Clinical Trial	✓
		NOT APPLICABLE Preliminary or Feasibility Study	
		NO public release of study results planned	
		YES - peer reviewed journal publication and/or presentation at conference or scientific meeting	
		YES - clinical trial registry	
		YES - other (describe)	
1.13b	If NO , indicate why public dissemination of study results is not possible or desirable. Note that reasons based solely on the need to protect proprietary information are not sufficient justification. If the reason is not sufficient the HSREB may decide that the following statement must be in the Informed Consent documentation. "There are no intentions to make the results of this study publicly available. You should know that when the presence or outcomes of selected trials are not made public, these studies cannot influence the thinking of patients, clinicians, other researchers and experts who write practice guidelines or decide on insurance-coverage policy." ⇒		

SECTION 2 CONFLICT OF INTEREST

2.1	Conflict of Interest - General This section to be completed for <u>all</u> submissions not just those funded by industry. Note also that this declaration applies to <u>all</u> co-investigators as well as the Principal Investigator.		
2.1a	Do any of the investigators or their immediate families have any proprietary interests in the product under study or the outcome of the research including patents, trademarks, copyrights and licensing agreements?	YES	
		NO	✓
2.2	Conflict of Interest - Industry Sponsored Protocols Only Note also that this declaration applies to <u>all</u> co-investigators as well as the Principal Investigator.	NOT APPLICABLE ✓	
		YES	NO
2.2a	Are any of the investigators or their immediate families receiving any personal remuneration (including investigator payments and recruitment incentives) from industry sponsors for taking part in this investigation?		
2.2b	Is there any compensation for this study that is affected by the study outcome?		
2.2c	Do any of the investigators or their immediate families have equity interest in the sponsoring company? (this does not include Mutual Funds)		
2.2d	Do any of the investigators or their immediate families receive payments of other sorts from this sponsor (e.g. grants, compensation in the form of equipment or supplies, retainers for ongoing consultation and honoraria)?		
2.2e	Are any of the investigators or their immediate families members of the sponsor's Board of Directors (or comparable body)?		
2.3	If YES to any of the above in 2.1 or 2.2 please describe the arrangement, including the monetary value of any consulting or share holdings, and discuss the implications of a potential conflict of interest. If the conflict of interest cannot be eliminated, what the conflict is and how that conflict is being managed should be discussed below and disclosed in the Letter of Information. The discussion and disclosure should explain what additional protections have been put in place to protect the study subject.		
	⇒		

SECTION 3 INDUSTRY FUNDED PROTOCOLS ONLY

3.1	REB Administration Fee The University requires an administration fee for industry funded protocols submitted for ethical review. Please select billing option A) or B). <i>Note: It is ultimately the responsibility of the local investigator to ensure the fee is paid. In the event the Office of Research Ethics is not able to recover the fee in a timely manner from the party named below, an invoice will be sent to the Local Principal Investigator for payment. Failure on the part of the Sponsor or the Investigator to pay the fee in a timely manner may result in the withholding or withdrawal of ethics approval until such time as the matter is resolved.</i>		
A)	The funds for this study will be administered by Lawson Health Research Institute (LHRI) The fee will be paid from a LHRI research account. If NO, please provide complete billing information below in part "B".	YES	
		NO	
B)	The funds for this study will not be administered by LHRI. Send invoice to:		
BILLING INFORMATION – COMPLETE ALL SECTIONS			
Company or Institution			
Contact Person			
Street Address			

City		Province / State	
Country		Postal Code	
Telephone Number		Fax	
CONTRACT &/OR PROTOCOL REFERENCE NUMBER REQUIRED To ensure the sponsor is able to match the invoice for the ethics administration fee with the contract you must provide the contract and/or protocol reference number.			

If you feel that due to extenuating circumstances the REB fee should be waived or adjusted, provide a brief written explanation to the Office of Research Ethics *prior* to the submission of this protocol. Include the following:

- Indicate how the funding will be used (budget)
- Identify who will own the data or any intellectual property arising from the agreement
- Indicate if there are any restrictions (e.g. publication delays) imposed upon the investigator by the sponsor and if so, what they are.

Do not assume that prior waivers or discounts will also apply to this submission. (Email tfletch6@uwo.ca or write to Office of Research Ethics Room 4180 Support Services Building UWO)

3.2	Conditions for Industry Funded Research
<p>Investigators are reminded of the following requirements :</p> <ul style="list-style-type: none"> ▪ all agreements and contracts must be approved by the appropriate research administration office for their institution prior to starting the study (e.g. LHRI Clinical Research Office of Grants and Contracts; UWO Offices of Research Development Services or Industry Liaison etc.); ▪ contracts and agreements must not put undue limitations on an investigator's right to publish; ▪ contracts and agreements must not prohibit a study investigator from informing research participants of any risks that may arise during a study; ▪ investigators and their staff are not permitted to accept 'finders fees' for subject recruitment, nor accept compensation for services rendered that is significantly greater than their normal wages or fees for time spent; and, ▪ research related expenses should be covered by the project Sponsor or other research funds not by OHIP, the participant's health insurance or the institution's operating budget. 	

SECTION 4 PROJECT DESCRIPTION

Complete each section under the appropriate heading. Be succinct and adhere to the page limitations. DO NOT DIRECT THE COMMITTEE TO 'SEE ATTACHED'. DO NOT USE TEXT COPIED FROM FUNDING APPLICATIONS OR STUDY PROTOCOLS UNLESS IT PROVIDES A SUCCINCT SUMMARY OF THE METHODOLOGY APPROPRIATE FOR ETHICAL REVIEW AND DEALS WITH ETHICAL ISSUES. Copies of detailed proposals submitted to a funding agency (e.g. CIHR, Heart & Stroke) will not be reviewed as the ethical issues are not often adequately addressed in such documents and they frequently do not provide a succinct summary as noted above. Your protocol will be RETURNED UNREVIEWED if the project description information is incomplete, illegible or improperly filled out. **Please adhere to the page limitations.**

4.1a	Provide a brief one or two sentence overview of the proposed research describing the population, intervention and outcome. <i>e.g. Patients with stage 4 colon cancer will be randomized to treatment A or treatment B to assess survival. Healthy volunteers will have a 4.0 Tesla head MRI with a new coil to assess picture quality (pilot).</i>
<p>⇒ A group of 100 patients with frontal or temporal lobe epilepsy who are scheduled for frontal or temporal lobectomy, and another group of healthy volunteers will undergo high resolution magnetic resonance imaging (MRI), magnetic resonance spectroscopy (MRS), and diffusion tensor imaging (DTI) on 1.5, 3, and 7 Tesla MR scanners to localize the site of the seizure focus in the patient group, in which the imaging findings will be correlated with clinical and EEG data. After surgery, the excised temporal lobe tissue from 50 patients will be imaged in the 9.4T MRI scanner at Robarts Research Institute.</p>	
4.1b	Provide KEYWORDS about the research. (Max 5) Frontal Lobe Epilepsy; 7T MRI; 3T MRI; Seizure Focus

4.2a	Is this a sequel to previously approved research?	YES	✓
		NO	
4.2b	If YES, indicate the previous ethics review number(s):		
⇒			
REB # 11155			
4.2c	If YES, describe differences from the previously approved protocol(s):		
⇒			
MRI scanning at 7 Tesla in addition to previously approved scanning at 3Tesla. Also, the excised brain tissue will be scanned at 9.4Tesla in addition to 3 Tesla.			
4.3	Background & Justification – Briefly summarize knowledge base and past human and/or animal research which has led to this project. When describing previous human studies or trials indicate the number of participants. (1 page maximum– adhere to page limitations)		

⇒

Epilepsy is a chronic neurological disorder with repeated unprovoked seizures that affect up to 1% of the general population with a large economic and social burden to society. More than 30% of patients with epilepsy have inadequate control of seizures with drug therapy and are considered to have intractable epilepsy (1). Frontal lobe epilepsy accounts for 20-30% of operative procedures involving intractable epilepsy. Anatomic localization of the site of seizures focus is crucial in the evaluation and management of epilepsy patients. Lesional frontal epilepsy has been associated with a better surgical outcome than non-lesional epilepsy. Prognosis is best if the epileptogenic lesion can be surgically removed completely (2).

While anatomic magnetic resonance imaging is reasonably good for detecting temporal lobe epilepsy, it is not as good for detecting abnormalities in seizures originating from the frontal lobes in the absence of structural abnormalities such as tumours (3, 4). High resolution imaging using local surface coils was found to be effective in demonstrating the normal grey-white matter junction, and due to its 3-dimensional acquisition, images can be reformatted into coronal, sagittal, and surface-rendered views. These have been shown to be effective in demonstrating cortical dysplasia, a potential occult epileptogenic focus (5).

Unlike conventional MRI, which provides structural information based on signals from water protons, proton magnetic resonance spectroscopy (MRS) provides information about

the chemical composition of the brain. The MRS spectrum of the brain is characterized by three major peaks: N-acetylaspartate (NAA), a neuronal marker, creatine (Cr) and choline (Cho). The most common application of MRS in epilepsy has been the non-invasive lateralization of the epileptic focus. MRS reveals abnormally low resonance intensities of NAA/Cr within the temporal lobes of temporal lobe epilepsy patients (6). Functional MRI (fMRI) and MR spectroscopy (MRS) have matured in recent studies to suggest that they increase the sensitivity and specificity in localizing the seizure focus in frontal lobe epilepsy (7).

Diffusion Tensor Imaging (DTI) is a new acquisition MRI technique that can be used to demonstrate fibre tracts within the brain (white matter). DTI can identify the motion of water molecules in the brain and it has been recently added to the armamentarium of methods for investigating the cause and consequences of epilepsy. DTI has shown to identify abnormalities that can not be detected on conventional MRI. Serial DTI scans could also have the potential to detect subtle changes secondary to seizures. However, the degree of reliability and the reproducibility of DTI data remain to be determined (9).

The standard care for patients with frontal lobe epilepsy involves MR imaging in a clinical 1.5T MR scanner. The great appeal of 3T and 7T MRI is the improvement in image quality, contrast, and resolution. Because the signal-to-noise ratio (SNR) correlates in approximately linear fashion with field strength, 3T imaging is roughly twice as great as at 1.5 T, and 7T is almost 5 times greater. The time necessary to acquire satisfactory images using 3T and 7T can be substantially reduced, which has the added advantage of minimizing motion artefacts. More and thinner slices can also be obtained at 3T and 7T in the same scan time required at 1.5T, and functional MRI and MRS benefit significantly from being performed at 3T and 7T. Images of the brain acquired at 3T have been rated as significantly superior in lesion conspicuity and diagnostic value (10, 11), and we expect 7T images to be even more so.

4.4	Study Design: Indicate which of the following best describes the type of investigation proposed. (select all that apply)		
	Clinical Trial		Pilot Study
	Drug or Natural Product Study (Phase I)		Qualitative Study
	Drug or Natural Product Study (Phase II)		Epidemiological Study
	Drug or Natural Product Study (Phase III)		Device Assessment/Development
	Drug or Natural Product Study (Phase IV)		Open-Label Extension Study
	Placebo Control		Other-Specify
	Randomized		Academic Research Study

4.5	Objectives and Hypotheses: Provide a clear statement of the purpose and objectives of the project. (i.e. Why are you doing the study?) State hypotheses and/or research question(s). (1 page maximum – adhere to page limitations)
-----	--

⇒ The research proposal will focus on the structural localization and functional changes in frontal and temporal lobe epilepsy. High-resolution MR imaging will be utilized to try to demonstrate areas of brain abnormalities at 1.5, 3 and 7T scanners using the appropriate MRI coils, including local surface coils and MR techniques, including Diffusion Tensor Imaging (DTI). The data from the patients and the healthy volunteers will form a clinical database, which will help neurosurgeons and neurologists to plan the most effective surgical interventions in the future.

Hypothesis:

Combined functional and high resolution anatomic MRI can depict the site of seizures focus with greater than 90% sensitivity and 90% specificity.

4.6	Methodology - Describe the study design and what will be done to the participants at each stage of the research. Investigators are encouraged to use flow charts or diagrams in their descriptions. For clinical trials (if applicable) include a description of "stopping rules" or "discontinuation criteria". (2 page maximum – adhere to page limitations)
-----	--

**Imaging methods:**

One hundred patients with frontal or temporal lobe epilepsy will be recruited into the experimental arm of the study over a five-year period, and 100 healthy volunteers into the Control Group. All patients will be subjected to the routine MR examination scheduled for epileptic patients in LHSC on a 1.5 T MR scanner. The routine MRI protocol includes the following sequences: multi-planar spin echo images (SE), fluid attenuation inversion recovery (FLAIR), diffusion tensor images (DTI), functional MRI (fMRI) and MRS.

Similar imaging techniques will be performed on high-resolution MR scanners at 3T and 7T recently installed at the Imaging Laboratory of Robarts Research Institute, to demonstrate areas of cortical dysplasia or other abnormalities in the frontal or temporal lobes in patients in whom conventional anatomic MR is negative or inconclusive.

During the scanning, the patient will be monitored for seizure activity. If a convulsive seizure or prolonged non-convulsive seizure occurs during the scanning, the study will be terminated and the patient will receive immediate on-site medical attention by the study epileptologist (SMM). The imaging findings will be correlated with clinical and EEG data.

We are seeking permission from the Tissue Use Committee to scan the resected brain tissue in the 9.4T MR Scanner immediately following surgery, and just prior to clinical pathological and histological analysis. A well established scanning sequence that allows for extremely high resolution image data will be used to scan the resected brain tissue, which will then be compared to the clinical pathology results. This will allow a better understanding of the anatomical and structural organization of the brain, a more precise localization of the seizure focus, and more detailed identification of certain cortical regions and associated functional pathways. We will correlate histological findings from excised tissue with high-resolution in vivo and ex vivo imaging of the affected brain tissue. This research is intended ultimately to eliminate the need for invasive and traumatic procedures, such as the Wada Test (that anesthetizes a hemisphere) and the application of cortical and deep brain EEG electrodes commonly employed to lateralize epileptogenic activity and identify seizure foci.

4.7	Scientific validity of the study design: Address the strengths and weaknesses of the selected design. Specifically indicate why a particular design was selected. (1 page maximum – adhere to page limitations)
-----	---



We use a standard MRI protocol for epilepsy that employs data analysis comparable to published work in this area. In addition, high-resolution imaging is expected to demonstrate

areas of cortical dysplasia or other abnormalities in the frontal lobes in patients in whom conventional anatomic MR (using the standard head coil) is negative or inconclusive.

We expect Diffusion Tensor Imaging (DTI) to show fibre tract derangements in frontal lobe epilepsy that are not visible on anatomic MR images. This will be especially important in patients with cortical dysplasia, where tracts can be disrupted when studied pathologically. The 3 and 7T MR scanners, with their improved signal levels are expected to improve spatial and temporal resolution of anatomical and functional studies.

This study will build on the strength of the world-renowned epilepsy program currently in place at LHSC, based on patients from a busy epilepsy unit, which is the largest in Canada. The research fits well with the fMRI program currently in place, and uses expertise, equipment, and facilities currently present in the Robarts Research Institute. If certain sequences prove to be more helpful in localizing the side of abnormality in frontal epilepsy based on this research, these will be incorporated into the routine imaging of patients with epilepsy. Lastly, this research offers an opportunity to develop new imaging sequences (DTI) for evaluation of epilepsy, which may be carried over to other Neurologic problems e.g. Alzheimer disease. It will also provide the first neurological images obtained with a 7T MRI in Canada.

4.8	References – If possible please restrict the list to ten (10) of the most relevant references. References must be properly cited and contain the author, title of article, journal and page number(s).
-----	--

⇒

1. Wiebe S, Blume WT, Grivin JP, et al. A randomized controlled trial of surgery for temporal lobe epilepsy. *N Engl J Med* 2001; 345:311-8.
2. Sheryl Haut. <http://www.emedicine.com/NEURO/topic141.htm>. Last updated on March 2002.
3. So EL. Role of neuroimaging in the management of seizure disorders. *Mayo Clin Proc* 2002; 77: 1251-1264.
4. Lee DH, Gao F-Q, Rogers JM et al. MR in temporal lobe epilepsy: analysis with pathologic confirmation. *Am J Neuroradiol* 1998; 19:19-27.
5. Bernasconi A, Antel SB, Collinis DL, et al. Texture analysis and morphological processing of magnetic resonance imaging assist detection of focal cortical dysplasia in extra-temporal epilepsy. *Ann Neurol* 2001; 49:770-775.
6. Cendes F, Caramanos Z, Andermann F et al. Proton magnetic resonance spectroscopic imaging and magnetic resonance imaging volumetry in the lateralization of temporal lobe epilepsy: a series of 100 patients. *Ann Neurol* 1997; 42:737-746.
7. Namer IJ, Bolo NR, Sella F et al. Combined measurements of hippocampal N-acetyl aspartate and T2 relaxation time in the evaluation of mesial temporal epilepsy: correlation with clinical severity and memory performance. *Epilepsia* 1999; 40: 1424-1432.
8. Rugg-Gunn FJ, Eriksson SH, Symms MR et al. Diffusion tensor imaging in refractory epilepsy. *Lancet* 2002; 359(9319):1748-1751.
9. Thulborn KR, Davis D. Clinical MRI at 3.0 Tesla: performance and safety. *Proc Int Soc Magn Reson Med*. 1999; 7: 828.
10. Price SJ, Burnet NG, Donovan T et al. Diffusion tensor imaging of brain tumors at 3T: a potential tool for assessing white matter tract invasion? *Clin Radiol*. 2003;58:455-462.

Sample Size:		
4.9a	Number of subjects at this centre	200
4.9b	Number of subjects in entire study	200
4.9c	Number of centres participating	1

For all study types (including pilot studies), justify the sample size on scientific grounds.

4.10	If a formal sample size calculation was not performed , justify why a formal sample size calculation is not required or possible; and give a rationale for the proposed number of subjects.
------	--

⇒

The MRI data from the patients and volunteers will form the basis for a clinical database. It is feasible to collect such data from 100 patients with frontal and temporal lobe epilepsy and 100 healthy volunteers over a five-year period. This database will give more information to surgeons to make clinical decisions better for their patients with frontal and temporal lobe epilepsy.

OR

4.11a	If a formal sample size calculation was performed , complete the following:	
4.11b	Alpha error and indicate if one- or two-sided	
4.11c	Statistical power	
4.11d	Estimated value of outcome measure in the CONTROL GROUP	
4.11e	Difference which can be detected with specified sample size	
4.11f	Primary outcome measure	

The HSREB no longer requires the actual sample size calculation or sample size reference be submitted to the HSREB for clinical trials that require a "No Objection Letter" from Health Canada. In lieu of providing the actual calculation investigators **MUST** provide a comprehensive rationale for the sample size selected (Section 4.11g). However, the HSREB reserves the right to request the calculation, formula or reference if it deems it necessary. Please note, investigators are encouraged to submit the calculation and references whenever possible as it may aid the HSREB in its decision-making.

4.11g	In lieu of the actual sample size calculation, provide a comprehensive reason or rationale for the choice of sample size, including reflections on the power of the study and when appropriate, clinical justification.
-------	---

⇒

All other research studies in which a sample size calculation was done must complete Sections 4.12a and 4.12b

4.12a	Sample Size Calculation – give the actual calculation
⇒	

4.12b	Sample Size Reference: Give a reference for the formula or method used. If a table in a published source was used instead of a calculation, provide the reference(s) and table reference numbers. If a sample size calculator was used, provide a description of the software package used and/or the URL for internet-based calculators.
⇒	

4.13	Analysis - State how the data will be analyzed to fulfil each objective or to test each hypothesis. Please state specific primary and secondary end points if appropriate. (1 page maximum– adhere to page limitations)
⇒ MRI data will be compared qualitatively and quantitatively to the pathology findings to demonstrate that multimodality MRI is equivalent to pathology in distinguishing epileptic areas in the brain. ROC analysis will be performed to compare the sensitivity and specificity of the different MRI modalities to that of the current gold standard - the histological analysis of the pathology report. <u>The MRI data from the healthy volunteers will also be compared qualitatively with that from patients with frontal or temporal lobe epilepsy, to record any distinguishing features that might cause epileptic seizures.</u>	

SECTION 5 RESEARCH PARTICIPANTS

5.1	To assist the HSREB in determining vulnerability and risk indicate if the research <i>specifically</i> targets or recruits the following persons: (check all that apply)
✓	Healthy Volunteers
✓	Patients
	Pregnant women
✓	Minors (under 18)
	Participants with language or comprehension barriers (e.g. illiterate, non-English speaking, dysphasic)
	Employees or students of UWO or the institution where the study is being carried out
	Incompetent or unconscious participants

	Institutionalized persons (e.g. prison, extended care facility)
	Participants recruited in emergency or life-threatening situations or other very stressful situations

5.2a	Will the study involve males AND females?	YES	✓
		NO	
5.2b	If NO, explain why only one gender is being selected. (e.g. condition under study is gender specific)		
⇒			

5.3a	What is the age range of the participants?	LOWER AGE LIMIT	40-16
		UPPER AGE LIMIT	65

5.4	Participant Inclusion and Exclusion Criteria: List all inclusion/exclusion criteria and indicate with an asterisk (*) those criteria which will be included in the Letter of Information.		
5.4a	Inclusion Criteria		

⇒

1. Patients, male or female with history of frontal or temporal lobe epilepsy aged ~~40~~ 16-65 years old.
2. For the healthy volunteers, no history of epilepsy or head injury.
3. Patients must have had comprehensive EEG studies to identify the site of their epileptogenic region.
4. Women of childbearing potential must be using an acceptable method of birth control if sexually active.

5.4b	Exclusion Criteria		
------	--------------------	--	--

⇒

1. People with severe coexisting or terminal systemic disease.
2. People with history of ventricular arrhythmia, myocardial infarction, unstable angina, decompensated congestive heart failure or any other acute, severe, uncontrollable or sustained cardiovascular condition.
3. Claustrophobic subjects.
4. People with pacemakers or other electronic implants
5. People who have had an operation where a metallic implant was used (i.e. clips, pins, staples, etc)
6. People who are welders, military or armed forces personnel if skeletal survey reveals metallic particles.
7. People injured by a metallic object that was not removed.
8. People who are pregnant or trying to conceive.
9. People who have an immediately evident need for surgery.
10. People with pre-existing medical conditions (e.g. significant renal or hepatic disease) which, in the investigator's opinion, may interfere with the patient's suitability and participation in the study.

5.5a	Are these participants also taking part in other research?	YES	
------	--	-----	--

	<i>If you discover that a person is already participating in another study and your study involves any type of medical or physical procedure, it is recommended that you contact the other study's principal investigator to ensure that enrollment in your study will not disadvantage the participant. Some clinical trials prohibit participation in more than one study even though there is no risk or medical contraindication.</i>	NO	
		UNKNOWN	✓
5.5b	If YES or UNKNOWN, explain any risks associated with participation in multiple studies.		
⇒ There are no known risks to the patient or healthy volunteer in participating in other research studies.			

SECTION 6 RESEARCH PROCEDURES AND PATIENT CARE

Note: All research costs must be covered by research funds.

6.1	Indicate which of the following interventions, testing or procedures are to be performed on the human participants <i>as part of this research study</i> .		
	Drugs or Natural Products		Analysis of existing data
	Devices		Analysis of existing biological specimens
	Radiation		Cognitive or perceptual experiment
	Magnetic Resonance Imaging	✓	Chart or document review
	PET Scans		Evaluation of program or services
	Surgery		Observation of behaviour
	Non-surgical manipulation (e.g. physiotherapy)		Interview/survey/questionnaire/diaries
	Collection of blood		Audio or video taping
	Non-invasive physical measurements (e.g. BP, weight)		Gene therapy - <i>If the study uses a gene transfer vector, the vector is considered to be a drug and must be reported in drug section.</i>
	Collection of other bodily materials or tissues		Other

6.2a	Describe the standard of care for the condition under study if the study involves patient care.	Not applicable	
⇒ Standard of care for patients with epilepsy undergoing surgery for frontal or temporal lobectomy involves magnetic resonance imaging at 1.5 Tesla magnet field strength. The MR imaging includes T1 and T2-weighted imaging, and sometimes Diffusion Tensor Imaging (DTI) and functional MRI (fMRI) if the neurosurgeon requests them.			
6.2b	List all procedures, tests, drugs etc. utilized for the purpose of this study which are <i>not part of ordinarily accepted care</i> of the participant and which are being done for research purposes only. If additional or extended hospitalization or outpatient visits are required include the number of days or visits.		
⇒ The research part of this study is the addition of 3 and 7 Tesla Magnetic Resonance Imaging. The scanners operate under an Investigational Testing Authorization from Health Canada and operating parameters adhere to current FDA and IEC guidelines. There will be required one or two sessions of approximately 1 hour each.			

6.3	Complete the chart below and describe all drugs or natural products that will be used in the study. If an investigational drug or natural product is being used submit one copy of the Investigator's Brochure or for approved drugs under study in this protocol submit Product Monograph – this document will be retained by the Office of Research Ethics. Expand chart as required. <i>If the study uses a gene transfer vector, the vector is considered to be a drug and must be reported in this section.</i> <i>If a contrast agent is being used during imaging it should be listed below.</i>	Not applicable: No drugs used in study	✓
	DRUG or NATURAL PRODUCT NAME (& IND number if appropriate)	DOSE	STATUS Investigational Marketed Cleared New Drug

6.4	Complete the chart below and describe all devices that are being assessed in the study. If investigational device is being used provide one copy of the Investigator's Brochure – this document will be retained by the Office of Research Ethics. Expand chart as required.	Not applicable: No devices under study	✓
	DEVICE NAME	STATUS Investigational Approved	

If radiological testing or therapy (including Xray, CT, MRI, ultrasound etc) is being used, researchers may find the following website a useful resource in determining the appropriate language for Informed Consent documentation to explain these procedures and their risks to participants. <http://www.radiologyinfo.org/>

6.5a	Will any radioactive material be used?	YES	
		NO	✓
6.5b	If YES, describe the Radioisotopes, how they will be introduced into the body and provide an assessment of risk.		
	⇒		
6.6a	Will the participant be exposed to x-rays?	YES	
		NO	✓

6.6b	If YES, describe the X-ray Exposure, describe the assessment of risk and give the dose equivalents (background radiation).
⇒	

6.7a	Will any Magnetic Resonance Imaging (MRI) or Positron Emission Tomography (PET) scans be used?	YES	✓
		NO	

6.7b	If YES indicate the type of machine (e.g. 3T); describe the exposure and give an assessment of risk.
------	--

⇒ The study will utilize a 3T GE 750 or a 3T Siemens Tim Trio, and a Varian/Siemens 7T human MRI system. The risks to participants in this study are minimal. To date, in the absence of ferromagnetic materials, there has been no replicated evidence of specific acute or cumulative health hazards associated with magnetic field exposure as collected from static fields up to 8 Tesla. Safety concerns also exist due to (i) specific absorption rate (SAR) of power to tissue from coils producing RF fields, (ii) time varying magnetic field rate of change from gradient coils (dB/dt) and (iii) sound pressure levels (SPL) from MRI gradient coils. The 7 Tesla MRI system at Robarts is equipped with all the safety monitoring systems, equivalent to the 3 Tesla Siemens Tim Trio commercial clinical system, which ensure that levels of SAR, dB/dt and sound pressure level are not exceeded and pose an insignificant risk to human subjects.

N.B. If an MRI is being used the following wording MUST be included in the Informed Consent documentation. Additional wording is required for MRI's on children - see HSREB Guideline 2-G-004 (formerly Appendix 3) <http://www.uwo.ca/research/ethics/med/hsreb-guidelines.htm>

"The Food & Drug Administration (USA) has indicated that for clinical diagnosis an 'insignificant' risk is associated with human MRI exposure at the intensities used in this project. Current Canadian guidelines follow the USA guidelines. Although very rare, injury and deaths have occurred in MRI units from unsecured metal objects being drawn at high speeds into the magnet or from internal body metal fragments of which the subject was unaware or had not informed MRI staff. To minimize this latter possibility it is essential that you complete a screening questionnaire. Other remote but potential risks involve tissue burns and temporary hearing loss from the loud noise inside the magnet. The latter can be avoided with ear headphone protection that also allows continuous communication between the subject and staff during the study.

MRI exclusion criteria

If you have any history of head or eye injury involving metal fragments, if you have ever worked in a metal shop or been a soldier, if you have some type of implanted electrical device (such as a cardiac pacemaker), if you have severe heart disease (including susceptibility to arrhythmias), if you are wearing metal braces on your teeth, or [for women] if you could be pregnant, or have an intrauterine device, you should not have an MRI scan."

SECTION 7 BIOLOGICAL SPECIMENS TO BE COLLECTED FROM SUBJECTS

7.1a	Are biological specimens (e.g. blood, tissue, muscle biopsies or tumor samples) to be taken or analyzed for the purposes of this research protocol?	YES	✓
		NO	

7.1b	Are any biological specimens (blood, tissue etc.) being taken for future genetic testing or other unspecified testing or studies? <i>N.B. If YES, a separate information/consent document will be required.</i>	YES	
		NO	✓

If YES to either 7.1a or 7.1b complete the balance of this section.

7.2a	Describe what specimens will be taken and what they will be used for. In the case of blood samples also provide the total amount of blood that will be taken.
------	--

⇒

Resected Temporal lobes from 50 patients who have undergone temporal lobectomy for relief of intractable epilepsy.

7.2b	Indicate how and when the specimen will be collected and by whom. Describe facilities and procedures to protect the physical comfort and safety of the participants from whom samples will be taken. In the case of invasive sampling e.g. taking blood, biopsies indicate who will take the sample and give their qualifications to do so.
------	--

⇒

The specimens will be harvested by each patient's Neurosurgeon during standard care temporal lobectomy for relief of intractable epilepsy. All normal hospital procedures will be followed. These specimens normally go straight to pathology for clinical histopathological analysis, but we have obtained permission from the Tissue Use Committee in the past to image these specimens in the 9.4T MRI immediately prior to the pathology exam, and we are currently applying for this same permission.

7.2c	Explain who will control or own the specimens?
------	--

⇒

The specimens will be owned and controlled by the hospital, as standard post-operative pathology specimens.

7.2d	Explain how and where the specimens will be stored.
------	---

⇒

The specimens will be owned and controlled by the hospital, as standard post-operative pathology specimens.

7.2e	Describe how long the specimens will be retained and how they will be destroyed.
------	--

⇒

The specimens will be owned and controlled by the hospital, as standard post-operative pathology specimens.

7.3.a	What was the original purpose or use of the tissue or specimens?	Collected specifically for research purposes	
		Originally collected for diagnostic purposes	✓
		No purpose or use - unwanted or discarded tissue or biomaterials	

7.3b	The subsequent use of tissue or biomaterials (except blood) originally collected for diagnostic purposes must, be approved by the Department of Pathology Tissue Use Committee prior to submission to the HSREB and a copy of their approval appended to this form. If the Tissue Committee approval is not available at the time of submission to the HSREB, ethics approval will be withheld until a copy of Tissue Committee approval is received.									
	<table border="1"> <tr> <td>Tissue Use Committee approval</td> <td>Not applicable</td> <td></td> </tr> <tr> <td></td> <td>Pending</td> <td>✓</td> </tr> <tr> <td></td> <td>Approval attached</td> <td></td> </tr> </table>	Tissue Use Committee approval	Not applicable			Pending	✓		Approval attached	
Tissue Use Committee approval	Not applicable									
	Pending	✓								
	Approval attached									

SECTION 8 QUESTIONNAIRES, FORMS & OTHER DATA TO BE USED IN STUDY

Questionnaires, forms, assessment forms, scales, interviews, surveys and diaries etc.

8.1	<p>In the chart below list all questionnaires and forms etc. that will be used in the study and indicate who will be completing or administering the form. (e.g. subject , interviewer, nurse, spouse, caregiver, physician etc). Expand chart as required.</p> <p>Attach a copy of the data collection forms. E.g. Chart abstraction sheets, questionnaires, surveys, interview outlines etc. If you will be using standard, previously validated or widely accepted instruments provide FIVE (5) copies. If the instruments have been developed or adapted for this project, provide SEVENTEEN (17) copies. Do not insert copies of instruments in this chart; append them at the end of the protocol submission form.</p> <p>If there are no actual forms, you must append a comprehensive list of data to be collected or topics to be covered.</p>																		
	<table border="1"> <thead> <tr> <th>TITLE OF QUESTIONNAIRE, SURVEY, SCALE, DATA COLLECTION FORM ETC. (do <u>not</u> insert the questions or actual instrument here, append to the end of the submission)</th> <th>STATUS Standard New Adapted</th> <th>WHO WILL COMPLETE OR ADMINISTER THE FORM?</th> </tr> </thead> <tbody> <tr><td></td><td></td><td></td></tr> <tr><td></td><td></td><td></td></tr> <tr><td></td><td></td><td></td></tr> <tr><td></td><td></td><td></td></tr> <tr><td></td><td></td><td></td></tr> </tbody> </table>	TITLE OF QUESTIONNAIRE, SURVEY, SCALE, DATA COLLECTION FORM ETC. (do <u>not</u> insert the questions or actual instrument here, append to the end of the submission)	STATUS Standard New Adapted	WHO WILL COMPLETE OR ADMINISTER THE FORM?															
TITLE OF QUESTIONNAIRE, SURVEY, SCALE, DATA COLLECTION FORM ETC. (do <u>not</u> insert the questions or actual instrument here, append to the end of the submission)	STATUS Standard New Adapted	WHO WILL COMPLETE OR ADMINISTER THE FORM?																	

8.2	Indicate all sources of data	<table border="1"> <tr><td>Patient HOSPITAL chart or clinical record</td><td></td></tr> <tr><td>Other HOSPITAL departmental records e.g. Pharmacy, Physiotherapy, Laboratory</td><td></td></tr> <tr><td>Directly from research participant or other informant</td><td></td></tr> <tr><td>NON-HOSPITAL clinician records e.g. Family Physician office</td><td></td></tr> <tr><td>NON-HOSPITAL laboratories or treatment sites e.g. physiotherapy clinic, laboratory</td><td></td></tr> <tr><td>Departmental or clinic (clinical) database</td><td></td></tr> <tr><td>Other (specify) 1.5, 3, and 7 Tesla MRI data (1.5T is the standard clinical MRI that patients undergo as part of their preoperative care)</td><td>✓</td></tr> </table>	Patient HOSPITAL chart or clinical record		Other HOSPITAL departmental records e.g. Pharmacy, Physiotherapy, Laboratory		Directly from research participant or other informant		NON-HOSPITAL clinician records e.g. Family Physician office		NON-HOSPITAL laboratories or treatment sites e.g. physiotherapy clinic, laboratory		Departmental or clinic (clinical) database		Other (specify) 1.5, 3, and 7 Tesla MRI data (1.5T is the standard clinical MRI that patients undergo as part of their preoperative care)	✓
Patient HOSPITAL chart or clinical record																
Other HOSPITAL departmental records e.g. Pharmacy, Physiotherapy, Laboratory																
Directly from research participant or other informant																
NON-HOSPITAL clinician records e.g. Family Physician office																
NON-HOSPITAL laboratories or treatment sites e.g. physiotherapy clinic, laboratory																
Departmental or clinic (clinical) database																
Other (specify) 1.5, 3, and 7 Tesla MRI data (1.5T is the standard clinical MRI that patients undergo as part of their preoperative care)	✓															

SECTION 9 DECEPTION OR PARTIAL DISCLOSURE TO BE USED IN THE STUDY

9.1a	Do any of the procedures in this study include the use of deception or partial disclosure of information to participants? <i>This section refers to instances of deliberate deception or the withholding of key information that may influence a participant's performance or responses. Deception does not include randomization, double blind or placebo controlled procedures unless the subject is not told that these procedures will be used.</i>	YES	
		NO	✓
9.1b	If YES, provide a rationale for the planned deception or partial disclosure. ⇒		
9.1c	If YES, describe the procedures for a) debriefing the participants and b) giving them a second opportunity to consent to participate after debriefing. If debriefing and re-consent are not viable options please explain. ⇒		

SECTION 10 RISKS AND BENEFITS OF THE RESEARCH

10.1a	RISKS & DISCOMFORTS: Discuss the overall risks of the proposed research, and specify the particular risks and discomforts associated with each research procedure, drug test, or other aspect of the protocol, including combinations of these. Consider privacy, confidentiality, psychological, emotional, social, economic etc. risks and stressors. Risks in clinical trials are sometimes more easily described in terms of therapeutic or non-therapeutic risks.		
	<p>⇒</p> <p>The risks to participants in this study are minimal. Magnetic resonance imaging employs strong static magnetic fields along with switching gradient and rapidly oscillating radio frequency (RF) fields to obtain tissue specific information from the spin properties in nuclei of different molecules. MRI is a routine test done on millions of North Americans every year with well over 150 million studies performed since the early 1980s. This study utilizes a static magnetic field strength of 1.5 Tesla, 3 Tesla and 7 Tesla. With 12 years experience of human imaging at 4 Tesla in our laboratory at the Robarts Research Institute and with over 10 years experience with human imaging at 7 Tesla and higher worldwide (University of Minnesota – 7T, 9.4T, Ohio State University – 8T, University of Illinois – 9.4T) there have been no serious side effects documented.</p> <p>To date, in the absence of ferromagnetic materials, there has been no replicated evidence of specific acute or cumulative health hazards associated with magnetic field exposure as collected from static fields up to 8 Tesla. As a result of these findings, the <i>Criteria for Significant Risk Investigations of Magnetic Resonance Diagnostic Devices</i> as issued by the FDA in July 2003 has issued a revision increasing the limit of the static magnetic field strength to 8 Tesla for most populations superseding the previous document <i>Guidance for Magnetic Resonance Diagnostic Devices – Criteria for Significant Risk Investigations</i>, issued September 1997. The aforementioned FDA document also mandates three other parameters for human safety, that being (i) specific absorption rate (SAR) of power to tissue from coils producing RF fields, (ii) time varying magnetic field rate of change from gradient coils (dB/dt) and (iii) sound pressure level (SPL) also produced from MRI gradient coils.</p>		

Acoustic noise level may increase as magnetic field increases. However, the noise level is also dependent on the specific data acquisition techniques that are used. In this study, acoustic noise is well below the FDA guidelines and subjects are given earplugs to reduce any annoyance, our safety monitoring systems are the same as those found on the 1.5 Tesla GE scanners at LHSC-UC. Subjects are also monitored by video camera and intercom throughout each study.

10.1b Describe facilities and procedures to protect the physical and mental health, comfort and safety of the participants.

⇒

The 7 Tesla MRI at Robarts is equipped with all the safety monitoring systems, equivalent to 3 Tesla GE 750 or 3Tesla Siemens Tim Trio commercial clinical system, which ensure that levels of SAR, dB/dt and sound pressure level not exceeded and pose an insignificant risk to human subject. The subject will also be able to communicate with the MRI operator during the entire study in the event he/she becomes uncomfortable or wishes to terminate participation in the study. The human MRI labs at Robarts also have full code support through the facilities at LHSC in the event of a cardiac arrest (ie. Code Blue).

Risk of seizure in the magnet:

Epilepsy patients may have a seizure during scanning. During focally originating seizures, patients are usually awake with some altered awareness, but are not in contact with others in their environment and do not respond normally to instructions or questions. They often stare into space and either remain motionless or engage in repetitive behaviors called automatisms. Complex partial seizures typically last less than three minutes and may be immediately preceded by simple partial seizures. Afterward, these patients experience postictal changes, often characterized by somnolence, confusion or headache for several minutes. The patient has no memory of what took place during the seizures other than, perhaps, the aura. Focal originating seizures are usually self limiting. Some seizures may progress to generalized tonic seizures. The likelihood that the patient will have a seizure in the magnet is small because of the selection criteria. However, there is a possibility that the patient can have a seizure in the magnet, as can happen at any time and will depend on the frequency of the seizure activity for such particular patient. However, the potential for injury to the patient is minimal, since there is no significant abnormal movement that can lead to injury. In addition, there is a "help" call button in the MR scanner; if the patient feels any abnormal aura, he/she can press on the button to notify us before he/she will be removed from the scanner and the epileptologist will attend to him/her. The clinician will make a decision to terminate the study and treat the patient. Patients are routinely treated with fast acting anti-convulsants (e.g. sublingual lorazepam 1-2 mg or buccal midazolam 10 mg) if the seizure lasts for longer than two minutes. Oxygen and a crash cart are available in the MR suite if needed. Also, the Emergency Room of the London Health Sciences Centre is less than 300 meters from the Robarts MR suite, therefore we can transfer the patient there if aggressive treatment is needed.

10.2	BENEFITS: Discuss any possible direct benefits to the research participants as a result of their participation in the study. Please note that monetary compensation is not considered a benefit. If applicable, discuss possible benefits to society at large or the patient/participant population being studied.
⇒ There will likely be no direct benefit to the participants in this study. The sequences could be helpful in localizing the epileptogenic focus in frontal lobe epilepsy that would affect each patient's management.	

10.3	Delays or withholding of standard care	YES	NO
10.3a	Are any standard therapies or diagnostic procedures to be withheld during the course of the study?		✓
10.3b	Will a placebo be used in lieu of standard care?		✓
10.3c	Will management or treatment of the participant's condition be prolonged or delayed because of the research?		✓
10.3d	If YES to any of the above, discuss the potential risks and benefits to the participants and provide a rationale why standard care must be withheld or delayed.		
⇒			

10.4a	If the research subject is/or becomes pregnant, breastfeeds a child or fathers a child while in the study, does their participation in the study pose a possible risk to the foetus or child?	YES	✓
		NO	
10.4b	If YES, please discuss these risks and indicate what monitoring will be undertaken during the study and following the study conclusion? N.B. this information must be included in the participant's Information & Consent documentation and if access to the records of the female partner and her child is required, separate consent forms must be signed by the pregnant partner at the start of the study or whenever they become a partner to the research participant. These documents should be submitted to the HSREB at the same time as the primary informed consent documentation. (See HSREB Guideline 2-G-028 Female Partner)		
⇒ The inclusion criteria state that women of childbearing age who are sexually active must use an effective form of birth control to ensure they are not pregnant when they undergo MRI Scanning. As MRI scanning is part of standard care for these patients, they will be well aware of the risks and will be monitored as part of standard care practices.			
10.4c	If the research subject fathers a child while in the study, will access to the health records of the 'pregnant' partner and/or her child be required and/or will the woman or child be monitored by this study during and/or after the pregnancy? If YES, separate informed consent documentation must be provided to and signed by the partner at the start of the study or whenever they become a partner to the research participant. These documents should be submitted to the HSREB for approval at the same time as the main informed consent documentation. (See HSREB Guideline 2-G-028 Female Partner)	YES	
		NO	✓

10.5a	The TCPS requires that researchers propose a continuing review process appropriate for the risk of this project. The higher the risk the more frequent the review. Please indicate your recommendation as to the frequency of the REB's continuing review. At a minimum, all protocols will require the completion of the REB's Surveillance Report Form annually.	ANNUAL (default)	<input checked="" type="checkbox"/>
		EVERY 6 MONTHS	<input type="checkbox"/>
		EVERY 3 MONTHS	<input type="checkbox"/>
		EVERY MONTH	<input type="checkbox"/>
10.5b	If the risks associated with this project are such that they warrant more than an annual review please discuss what type of reports in addition to the usual REB Surveillance Report that you will provide the REB. e.g. DSMB reports, interim analyses etc.		
⇒			

10.6a	Is there a formal Data Safety Monitoring Committee (or comparable body) in place for this study?	YES	<input type="checkbox"/>
		NO	<input checked="" type="checkbox"/>
10.6b	If YES, is this Committee independent of the study Sponsor(s)? I.e. Is it an external committee able to provide an unbiased assessment?	YES	<input type="checkbox"/>
		NO	<input type="checkbox"/>
10.6c	NEW **If YES – please note you must submit the Data Safety Monitoring Committee report(s) to the Office of Research Ethics using Form 2-F-014 **		

10.7a	Are there plans to conduct formal Interim Analyses at prescribed times during the study?	YES	<input type="checkbox"/>
		NO	<input checked="" type="checkbox"/>
10.7b	If YES, indicate when these will take place and if they will be conducted by persons independent of the study sponsor.		
⇒			

SECTION 11 COMPENSATION AND COSTS

11.1a	Will the participants be compensated or reimbursed for their time, expenses and/or contribution to the research?	YES	<input checked="" type="checkbox"/>
		NO	<input type="checkbox"/>
11.1b	If YES, provide details. Specify the amount, what the compensation or reimbursement is for, and how payment will be determined for participants who do not complete the study. This information must be included in the Information/Consent documentation. At a minimum, protocols funded by industrial sponsors are expected to cover parking and other incidental costs.		
⇒ Participants will be reimbursed \$20 for any expenses incurred as a result of this study, such as travel and parking.			

11.2a	Are the participants likely to incur any additional expenses as a result of their participation in this study?	YES	<input type="checkbox"/>
		NO	<input checked="" type="checkbox"/>
11.2b	If YES, describe If YES, this information must be included in the Information/Consent documentation.		

⇒			
11.3a	If the drug is marketed before a trial is complete will study participants be required to pay for the drugs if they want to continue with the study? If YES, this information must be included in the Information/Consent documentation.	YES	
		NO	
		NOT APPLICABLE	✓
11.3b	If YES, give an estimate of the costs to the patient.		
⇒			

SECTION 12 PRIVACY & CONFIDENTIALITY ISSUES

LHSC and SJHC require that all persons accessing patient information complete the hospital Privacy & Confidentiality Education Program. Contact the LHSC-SJHC Privacy Office (x32996) for more information.

If research data are lost, stolen or accessed inappropriately, it must be reported to the HSREB immediately. If the data relate to hospital patients or records, a report must also be made to the hospital's Privacy Office AND Lawson Administration (x77749).

12.1a	Indicate if any of the following personal identifiers will be collected for research purposes during the course of the research. (Excluding the consent form which will contain the participant's name.) If any are to be collected, indicate which will be retained with the research data set or biological specimen once data or biological specimen collection is complete? Indicate "Retained" if there will be a Master list kept after data collection is complete that links participant identifiers to de-identified data.	Researchers may find it helpful to consult the CIHR Best Practices for Protecting Privacy in Health Research. http://www.cihr-irsc.gc.ca/e/29138.html	Collected	Retained
		No personal identifiers		
		Full or Partial Name or Initials	✓	
		Location or Contact info: address, phone, postal code etc		
		Full or Partial Date of Birth or Death		
		Personal Numbers: e.g. OHIP Health Card, SIN		
		Institutional / Hospital Chart or Record #	✓	
		Facilities and service providers		
	Other personal identifiers(specify)			
12.1b	IF ANY OF THE ABOVE IDENTIFIERS WILL BE COLLECTED give the level of detail to be collected. E.g. full name or initials only; full date of birth or year only; full postal address or 3 digit postal code; names of service providers or type of institution only etc.			

⇒ The full names and the Hospital Numbers will be collected on a Master List for each patient, which links them to their study code number. No personal identifiers will be collected for the healthy volunteers.

12.1c IF ANY OF THE ABOVE IDENTIFIERS WILL BE **COLLECTED** provide a comprehensive rationale explaining why it is necessary to collect this information.
IF ANY OF THE ABOVE IDENTIFIERS WILL BE **RETAINED** once data collection is complete provide a comprehensive rationale explaining why it is necessary to retain this information. (Including the retention of master lists that link participant identifiers with de-identified data.)

Acceptable reasons will generally be limited to the following purpose and investigators will need to defend their reasons for collecting and/or retaining identifiers and how the identifiers will be used to achieve the stated purpose.

- Contact or linkage for follow up or ongoing data collection
- Provide data for clinical monitoring of the participant
- Enable data to be withdrawn from data set if participant withdraws consent
- Return individual results to participant
- Conduct a data linkage with a high degree of accuracy

Do not just copy one of the above reasons into the box below. Investigators must, in their own words, explain fully and defend their reasons for collecting and/or retaining identifiers and explain how the identifiers will be used to achieve the stated purpose.

⇒ The full names and the Hospital Numbers of each patient will be linked to their study codes on a Master List in order to access their clinical data in their hospital charts.

12.2 In addition to the UWO HSREB, identify all agencies or individuals other than the local research team who, for **monitoring or auditing purposes**, may require access to identifiable or confidential data collected for this research or database/registry/bank, now or in the future. e.g. the Sponsor(s), CRO's, regulatory agencies such as Health Canada or the FDA etc.

Include the following sentence into all recruitment informed consent materials where the participant's identity is known and access to the records or follow up by the HSREB is possible.
"Representatives of The University of Western Ontario Health Sciences Research Ethics Board may contact you or require access to your study-related records to monitor the conduct of the research."

⇒ None

12.3 Describe the procedures to be used for preserving the confidentiality of data or specimens both during the data or specimen collection and in the release of the findings. e.g. all identifiers removed once data collected, data coded by unique identifiers with master list held separate from data etc. If a device has a serial or code number that will allow the sponsor to identify individual patients this should be noted in the Letter of Information.

⇒ All identifiers will be removed from the MRI data, and the data from individual patients will only be identified by a study code number. The full names and the Hospital Numbers of each patient will be linked to their study codes on a Master List, so that their clinical data can be accessed. The Master List will be kept in a separate, secure location. No personal identifiers will be collected for the healthy volunteers.

12.4a	Will anyone other than employees, clinical staff or students of the institution where the patients' original records or samples are located, approach participants or have direct access to a subject or their records for purposes of collecting data or conducting this research?	YES	
		NO	✓
12.4b	If YES indicate who these people are, what their role is, why they need access and what safeguards have been instituted to ensure they adhere to acceptable security practices and maintain confidentiality.		
⇒			

12.5a	<p>What security measures are in place locally to ensure protection of the data, records or specimens?</p> <ul style="list-style-type: none"> Describe local procedures for securing and storing written records, videotapes, computer discs, recordings and questionnaires, specimens etc. Provide details as to where the data or specimens will be located locally and who will have access to them. Describe what local organizational, technological and physical measures are in place to protect security of data, specimens, servers and portable media or devices? (locked doors, coded restricted access, encryption etc) <p>At a minimum it is required that all hard copy records be maintained in secure offices and locked filing cabinets and all electronic records and data sets will be password protected and access limited to approved persons only. Enhanced security measures such as encryption should also be considered.</p> <p>Master lists must be stored separately from the data. E.g. data files and the master list should not be stored on the same portable device.</p>		
	Indicate which of the following security measures will be/have been undertaken to protect the data and records	(check all that apply)	
		All hospital and research staff accessing patient information have completed the hospital Privacy & Confidentiality Education Program	✓
		Data will be encrypted	
		Data will be password protected	✓
		Data will be stored on a hospital or other institutional network drive that has firewalls and security measures in place	✓
		Hard copy records will be stored in a locked cabinet in a secure location	✓
		Access to records and data limited to authorized persons	✓
		All identifiers to be removed once data collected/verified	
		Master list linking data with identifiers stored separately from data.	
		Consultation with hospital Privacy Office or LHRI Research Office re privacy and security issues	✓
12.5b	Describe these measures in more detail.		
⇒ Only the patient's study code will be input in the original source data from the MRI machines. Their name or other personal identifiers will not be used at all. <u>Dr. Mirsattari will keep the Master List in a locked filing cabinet in his office.</u>			

12.6	Indicate how long the specimens and/or data will be retained and if not being kept indefinitely; describe the method of disposal or destruction.		
⇒ The de-identified MR images will be stored indefinitely as electronic files, as they will form part of an ongoing clinical database.			

--

12.7a	Are participant data or biological specimens being sent or taken off-site to a sponsor, co-investigator or central data collection site or registry? NB a formal contract or data or material transfer agreement must be in place between the local institution and the recipient before data or specimens are sent.	YES	
		NO	✓
12.7b	Will data be taken off site for analyses? E.g. In the case of patient information is there plans for the researcher to conduct analyses away from the site? E.g. at home?	YES	
		NO	✓

If YES to either 12.7a or 12.7b complete the balance of this section.

If NO go to Section 13.

12.8a	Will personal identifiers be included with the data or specimens sent or taken off-site ? Note: Data and specimens that leave the site should not include the patient's name or other identifiers unless there is a compelling reason. Data that includes identifiable personal health information MUST be encrypted before being sent or taken off site or utilized via secure remote access. Master lists must be stored separately from the data. E.g. data files and the master list should not be stored on the same portable device.	YES	
		NO	
12.8b	If YES, indicate which, if any, of these participant identifiers will be included with the data or specimens sent off-site?	Full or Partial Name or Initials	
		Contact info: address, phone, postal code etc	
		Date of Birth or Death	
		Personal Numbers: e.g. OHIP Health Card, SIN	
	Institutional / Hospital Chart or Record #		
12.8c	IF ANY OF THE ABOVE IDENTIFIERS WILL BE SENT OR TAKEN OFF-SITE provide a comprehensive rationale explaining why it is necessary for this information to go off-site. Acceptable reasons will generally be limited to the following purpose and investigators will need to defend their reasons for sending identifiers off-site and how they will be used to achieve the purpose stated. <ul style="list-style-type: none"> • Contact or linkage for follow up or ongoing data collection • Provide data for clinical monitoring of the participant • Enable data to be withdrawn from data set if participant withdraws consent • Return individual results to participant • Conduct a data linkage with a high degree of accuracy • Data analyses Do not just copy one of the above reasons into the box below. Investigators must defend their reasons for collecting and/or retaining identifiers and explain how the identifiers will be used to achieve the stated purpose.		
⇒			
12.9d	If NO, will there be a code or identifiers that allow linkage of the data and/or specimens back to the study and/or the research participant?	No personal identifiers sent/taken off-site but data and/or specimens are coded and linkage is possible.	
		Data and/or specimens completely de-identified and no linkage is maintained.	

12.9e	If a LINKAGE IS POSSIBLE describe how the data and/or specimens are to be coded to allow the linkage and who will retain a master list linking participants and their data. Note that in most instances the master list should remain in a secure location at the local site.	
⇒		
12.9f	Indicate which of the following security measures will be/has been undertaken to protect the data and records	(check all that apply)
Data will be encrypted		
Data will be password protected		
Data will be de-identified		
Data will be shipped by courier or other bonded shipping method		
Data will be personally delivered by researcher or research staff or picked up by co-investigator or sponsor		
All identifiers to be removed prior to shipping		
Master list linking data with identifiers retained at local site.		
Data sent by fax to a secure location		

12.10	If YES to either 12.7a or 12.7b, indicate where data, records or specimens are sent or taken. Be as specific as possible.
⇒	

12.11	If YES, describe how data or specimens are sent or taken off-site or accessed from off-site ? (E.g. hard copy, fax, electronic transmission email/web site, portable media devices, secure remote access, courier etc.) and describe transmission safeguards and security measures i.e. Are data encrypted prior to transmission? If yes describe level of encryption? Physical security (private faxes, shipping of disks etc)? Note that data containing identifiable personal health information MUST be encrypted to an appropriate level.
⇒	

12.12	If YES, Describe the off-site procedures for securing and storing written records, videotapes, computer discs, recordings and questionnaires, data and specimens.
⇒	

12.13	If YES, indicate how long the data or specimens will be retained off-site and describe the method of disposal if data or specimens are not returned to the local site or not retained indefinitely.
⇒	

SECTION 13 PARTICIPANT RECRUITMENT & CONSENT PROCESS

Disclaimer: The Review Board does not assess the legal validity of the consent form nor does it provide any other legal advice.

13.1 Describe the method of recruiting and sampling participants.

⇒ Epileptic patients with suggested frontal or temporal epileptogenic regions by clinical data (semiology), neurological examination or/and EEG findings, will be recruited from the Epilepsy Unit at London Health Sciences Centre (LHSC) or the epilepsy out-patient clinics at LHSC. Their routine clinical investigations including neurological examination and EEG will be reviewed by the study epileptologist (Dr. Mirsattari).

Patients with other active neurological or systemic disease that would impair their ability to participate in the study or data interpretation will be excluded. A control group of healthy adult volunteers (aged 18-65) will undergo the MRI examinations only. Written informed consent will be obtained from all patients and volunteers prior to testing.

13.2 Identify **who** will be contacting the potential participants to recruit them. *In the case of patients, initial contact must be made by a member of the patient's health care team, circle of care or someone the patient would expect to have relevant information about them.*

⇒ Dr. Mirsattari, the epileptologist, will be the person who contacts patients to recruit them for the study. The group of healthy volunteers will be recruited by advertisements at Robarts Research Institute, and the University of Western Ontario.

13.3 Indicate where the research will be conducted.

⇒ The standard clinical care of the patients will be performed at LHSC-UH, but the research MR Imaging for patients and volunteers will be carried out in the MRI suites at Robarts Research Institute.

13.4	Will posters, advertisements, public notices or telephone solicitation be used to recruit or notify participants?	YES	✓
		NO	

*If YES, provide **five (5)** copies of audio announcements or telephone recruitment scripts and all hardcopy advertisements, notices and announcements that will be used. If video or electronic media are used e.g. video tape or CD's provide only **one (1)** copy of tape or CD. This will be retained by the Office of Research Ethics and will not be returned to the Investigator.*

13.5	What type of consent(s) to participate was or will be obtained from participants?	Explicit written consent – use of formal consent documentation	✓
		Explicit verbal consent e.g. telephone recruitment	
		Explicit consent - other e.g. completion of questionnaire, survey evidence of consent	
		Passive consent e.g. notices posted with option to opt out	
		Prior consent e.g. other research consent	

13.6	If written consent cannot be obtained from potential participants prior to the intervention or written consent is not appropriate, provide a justification. (E.g. completion of a questionnaire in a survey study is evidence of compliance; emergency health situation etc.)
⇒	

13.7a	Will minors or persons not able to consent for themselves be included in the study?	YES	✓
		NO	
13.7b	If YES, describe the consent process and indicate who will be asked to consent on their behalf and discuss what safeguards will be employed to ensure the rights of the research participant are protected. Whether or not a separate assent form is used, investigators and parents or guardians should discuss the study with the person (when appropriate) and explain exactly what will happen and what the person's rights are. In certain circumstances, the REB may find it acceptable for mature or emancipated minors to give consent without also requiring consent from parents or guardians.		
⇒ The lower age limit is age 16 as there are some younger patients with epilepsy scheduled for surgery and it would be useful to have data from these patients. The parents or legal guardian will be asked to consent on behalf of their children in consultation with their neurosurgeon. No person under the age of 18 will be recruited for the control group of healthy volunteers.			

13.8	Briefly describe plans (if any) for provision of feedback to participants.
⇒ There is no feedback planned to be provided for participants.	

13.9	Describe opportunities (if any) available to participants to consent to future, as yet unknown, research on their data or specimens.	Not Applicable	✓
In the case of de-identified data this is not an option, but researchers need to think carefully about the logistics and likelihood of being able to contact participants in the future if they promise contact for future consent.			
⇒			

13.10	<p>Describe what opportunities (if any) will be available to participants to withdraw their data or specimens in the future.</p> <p>Please note that it may be necessary to deny participants the right to withdraw data or specimens to protect the integrity of research already using the data. If this is the case, this limitation on their ability to withdraw must be made clear in the Letter of Information.</p> <p>In the case of de-identified data withdrawal is not an option.</p>	Not Applicable	✓
⇒			

13.11	<p>Attach a copy of all documentation (separate from the example in the Sponsor documents) that will be used to inform and obtain consent from the potential participants about the research. Separate Information/Consent documents or a combined Information/Consent document may be used. Wording regarding the participant's consent <u>must</u> comply with the UWO guidelines, be relevant to the Canadian and Ontario scene and participants <u>must</u> be given a copy of the Letter of Information or combined Information/Consent document to keep for reference.</p> <p>THE CHECKLIST ON NEXT PAGE IS DESIGNED TO ASSIST YOU IN THE PREPARATION OF THE INFORMED CONSENT DOCUMENTATION. WHEN USED IN CONJUNCTION WITH THE GUIDELINES FOR PREPARATION OF INFORMED CONSENT DOCUMENTATION IT WILL ENSURE YOUR MATERIALS MEET THE REB'S MINIMUM REQUIREMENTS.</p> <p>CHECK THE DOCUMENTS CAREFULLY FOR COMPLETENESS. IT IS THE INVESTIGATOR'S RESPONSIBILITY TO CORRECT ALL SPELLING OR GRAMMATICAL ERRORS AND ENSURE THE DOCUMENTS MEET UWO HSREB SPECIFICATIONS BEFORE SUBMITTING THE PROTOCOL TO THE HSREB. INCOMPLETE OR POORLY PREPARED CONSENT DOCUMENTATION IS A MAJOR REASON WHY ETHICS APPROVAL IS DELAYED.</p> <p>See Guideline 2-G-005 (formerly Appendix 4) on the following website. http://www.uwo.ca/research/ethics/med/hsreb-guidelines.htm</p> <p>If you can not, or do not want to include a 'required' item provide a rationale why.</p>		
⇒			

These are the contact persons for participants who have questions regarding their rights and the conduct of the research. The correct person must be inserted into this sentence and this phrase included in the Letter of Information.

"If you have any questions about your rights as a research participant or the conduct of the study you may contact..."

If participants are recruited from within the LHSC or SJHC system or research is taking place at LHSC or SJHC sites	Dr. David Hill, Scientific Director, Lawson Health Research Institute at [REDACTED]
If participants recruited from sites other than LHSC or SJHC and research not taking place at LHSC or SJHC sites.	The Office of Research Ethics at [REDACTED] or by email at [REDACTED]

CHECKLIST – INFORMATION & CONSENT DOCUMENTATION	
<i>To be used in conjunction with the Guidelines for preparation of Information & Consent documentation. See 2-G-005 on the following website. http://www.uwo.ca/research/ethics/med/hsreb-guidelines.htm</i>	
HAVE YOU INCLUDED OR ADDRESSED THE FOLLOWING ISSUES?	
<i>Required</i>	Title of the research
<i>Required</i>	Identity of researchers & sponsors
<i>Required</i>	Invitation to participate in research
<i>Required</i>	Information/consent documents addressed to research participant
<i>Required</i>	Provide summary explanation of research
<i>Required</i>	Indicate number of participants – total & local
<i>When appropriate</i>	Describe inclusion & exclusion criteria
<i>Required</i>	Describe the research and any experimental procedures
<i>Required</i>	Explain specific research techniques
<i>Required</i>	Estimate of participant's time commitment
<i>Required</i>	Location of the research
<i>Required</i>	Describe Risks / Harms / Benefits even if there are none
<i>When appropriate</i>	Discuss special risks re Pregnancies or breastfeeding
<i>Required</i>	Voluntary participation, can refuse to participate, withdraw from study at any time etc.
<i>When appropriate</i>	Participation in concurrent or future studies?
<i>When appropriate</i>	Collection of Specimens or Human Tissues (<i>separate consent documentation required for banking and unspecified future research</i>)
<i>When appropriate</i>	Notification of new findings to be provided
<i>Required</i>	Discuss anonymity &/or confidentiality of information
<i>When appropriate</i>	Describe alternative treatments or options
<i>Required</i>	Contact person(s) for participants re questions about study and/or treatment and care
<i>Required</i>	Contact person(s) for participants re subject rights
<i>When appropriate</i>	Discuss compensation & costs to subjects
<i>When appropriate</i>	Tell subject to ask if private health or life insurer will continue to cover
<i>Required</i>	No waiver of rights
<i>Required</i>	No indication of institutional approval
<i>Required</i>	Statement that participant will receive copy of Information/consent document to keep
<i>Required</i>	Non identification in publication of results
<i>When appropriate</i>	Conflict of Interest declared
<i>Required</i>	Consent statement as per UWO standard
<i>Required</i>	Signatures for appropriate persons
<i>Required</i>	Language Level - lay language, grade 8 level for general population
Formatting – pages numbered, appropriate type size, page layout, header/footer, headings etc.	
<p>Separate assent forms for children 7+ are optional and not always appropriate, but if used, should include these items. Include an assent form only if it will enhance a child's understanding of what they will have to do. It must be short and written in very simple language. Whether or not a separate assent form is used, investigators and parents or guardians should discuss the study with the child and explain exactly what will happen and what the child's rights are.</p>	
	<ul style="list-style-type: none"> ▪ what the study is about ▪ why the child is eligible to participate ▪ procedures, what will happen ▪ voluntary participation, withdrawal ▪ risks, discomforts ▪ benefits ▪ contacts ▪ an invitation to ask questions ▪ signature

Curriculum Vitae

EDUCATION

- 2009-
Present PhD (Biomedical Engineering), Terry M. Peters, In progress
The University of Western Ontario, London, Canada
- 2007-2009 M.Eng. (Electrical Engineering), Ashraf A. Kassim, 2010
National University of Singapore (NUS), Singapore
- 2003-2007 B.Sc. (Electrical Engineering), 2007
University of Tehran, Tehran, Iran

HONORS AND AWARDS

- 2011-2013 NSERC CREATE Computer Assisted Medical Intervention (CAMI)
Scholarship
The University of Western Ontario
- 2009-2013 Western Graduate Research Scholarship (WGRS)
Western Graduate Research Scholarship International (WGRSI)
The University of Western Ontario
- 2007-2009 A*STAR International Graduate Scholarship
National University of Singapore
- 2003-2004 Distinguished Student Scholarship
2006-2007 *University of Tehran*

Publications, Conference, and Presentation Awards

- Feb. 2012 Second Prize Award
M. H. Kayvanrad, A. J. McLeod, J. S. H. Baxter, C. A. McKenzie, T. M. Peters, "T1 map reconstruction from under-sampled k-space data using a similarity constraint," presented at Imaging Network of Ontario (ImNO), Toronto, Canada, 2012.

THESES

- 2009 Iterative thresholding for sparse recovery
M.Eng., Ashraf A. Kassim, National University of Singapore
- 2007 **Reduced reference estimation of image transmission quality**
B.Sc., Alireza Nasiri-Avanaki, University of Tehran

PUBLICATIONS

Journal Papers

P. Zamani, M. H. Kayvanrad, and H. Soltanian-Zadeh, "Using learned under-sampling pattern for increasing speed of cardiac cine MRI based on compressive sensing principles," *EURASIP Journal on Advances in Signal Processing*, vol. 2012, no. 1, p. 82, Apr. 2012.

Conference Papers

M. H. Kayvanrad, C. A. McKenzie, T. M. Peters, "MRI reconstruction from partial k-space data by iterative stationary wavelet transform thresholding," 2012 Sparsity Techniques in Image Processing (STMI), 2012, Nice, France.

M. H. Kayvanrad, A. J. McLeod, J. S. H. Baxter, C. A. McKenzie, and T. M. Peters, "T1 Map Reconstruction from Under-sampled KSpace Data using a Similarity Constraint," in *International Society of Magnetic Resonance in Medicine*, 2012 (20), p. 15.

M. H. Kayvanrad, C. A. McKenzie, and T. M. Peters, "Iterative wavelet thresholding for rapid MRI reconstruction," *Proceedings of Medical Imaging 2011: Image Processing*, Lake Buena Vista, Florida, USA, 2011, p. 79624S-79624S-10.

P. Zamani, M. H. Kayvanrad, and H. Soltanian-Zadeh, "Cardiac Cine MRI using Compressive Sensing principles," in *2010 17th Iranian Conference of Biomedical Engineering (ICBME)*, 2010, pp. 1-4.

M. H. Kayvanrad, "Reconstruction from random measurements," in *9th International Conference on Signal Processing, 2008. ICSP 2008*, 2008, pp. 2697-2701.

M. H. Kayvanrad, S. Sodagari, A. Nasiri Avanaki, and H. Ahmadi-Noubari, "Reduced reference watermark-based image transmission quality metric," in *3rd International Symposium on Communications, Control and Signal Processing, 2008. ISCCSP 2008*, 2008, pp. 526-531.

PROFESSIONAL WORK EXPERIENCE

- 2006 Researcher, National AIS Networking plan
Internship, Ports and Maritime Organization, Tehran, Iran
- 2001-2002 Developer, *BWR Analyst* software for Analysis and Management of Ballast Water Records
Global Ballast Water Management (Globallast) program, under the supervision of GEF, UNDP, and IMO, Tehran, Iran
- 2001 Developer, *HEAT* software for simulation of ships' Ballast Water thermal behavior in order to evaluate the Heating treatment of Ballast Water- Introduced in the 1st R&D on Ballast Water Management, International Maritime Organization (IMO), London, March 2001
Global Ballast Water Management (Globallast) program, under the supervision of GEF, UNDP, and IMO, Tehran, Iran

ACADEMIC TEACHING EXPERIENCE

- Winter 2013 Teaching Assistant, Programming Fundamentals, Q. M. Rahman
Winter 2012 *The University of Western Ontario*
Fall 2010
- Fall 2012 Teaching Assistant, Medical Imaging, M. Drangova
Fall 2011 *The University of Western Ontario*
- Winter 2011 Teaching Assistant, Electronics Lab, L. Marinov
The University of Western Ontario
- Spring 2006 Teaching Assistant, Engineering Mathematics, J. Rashed-Mohassel
Fall 2005 *University of Tehran*

MEMBERSHIPS

- 2012 Student Member, IEEE
2006
- 2012 Student member, ISMRM
- 2010-2012 Member, IEEE UWO student chapter
- 2011 Student member, SPIE
- 2008-2009 Member, *Alliance Française de Singapour*

2005-2007 Member, IEEE Iran section

2003- Present Member, Alumni Association of Faculty of Engineering, University of Tehran